Role of predisposing genetics, telomere signaling and crosstalk of cardiac fibroblasts and cardiomyocytes in a pluripotent stem cell model of dilated cardiomyopathy

Dissertation

for the award of the degree

"Doctor rerum naturalium" (Dr. rer. nat.)

of the Georg-August-Universität Göttingen
within the doctoral program
Cardiovascular Science
of the Göttingen Graduate Center for Neurosciences, Biophysics, and Molecular Biosciences (GGNB)

submitted by

Wiebke Maurer
from Göttingen

Göttingen, 2022

Thesis Committee

Prof. Dr. rer. nat. Katrin Streckfuß-Bömeke (Reviewer), Clinic for Cardiology and Pneumology, University Medical Center Göttingen

Prof. Dr. rer. nat. Susanne Lutz (Second reviewer), Clinic for Pharmacology and Toxicology, University Medical Center Göttingen

Prof. Dr. med. Bernd Wollnik, Human Genetics, University Medical Center Göttingen

Members of the Examination Board

Prof. Dr. rer. nat. Katrin Streckfuß-Bömeke (Reviewer), Clinic for Cardiology and Pneumology, University Medical Center Göttingen

Prof. Dr. rer. nat. Susanne Lutz (Second reviewer), Clinic for Pharmacology and Toxicology, University Medical Center Göttingen

Prof. Dr. med. Bernd Wollnik, Human Genetics, University Medical Center Göttingen

Prof. Dr. med. Ralf Dressel, Institute for Cellular and Molecular Immunology, University Medical Center Göttingen

PD Dr. Laura Zelarayán-Behrend, Clinic for Pharmacology and Toxicology, University Medical Center Göttingen

Prof. Dr. Rüdiger Behr, German Primate Center, Leibniz Institute for Primate Research

Date of oral examination: September 26th, 2022

“Nothing in life is to be feared, it is only to be understood. Now is the time to understand more, so that we may fear less.” – Marie Curie

Table of contents

List of Figures i
List of Tables iii
Abbreviations iv
Summary xii
1 Introduction 1
1.1 The heart 1
1.1.1 Cellular composition of the heart 1
1.1.1.1 Cardiomyocytes and its contractile unit – the sarcomere 2
1.1.1.1.1 Ca^{2+}cycling in cardiac excitation-contraction coupling 3
1.1.1.2 Cardiac fibroblasts 4
1.2 Cardiomyopathies 6
1.2.1 Dilated cardiomyopathy 6
1.2.1.1 Causes of DCM 6
1.2.1.1.1 DCM genetics 7
1.2.1.2 Pathophysiology of DCM 9
1.2.1.2.1 Fibrosis as a hallmark of DCM 9
1.2.1.2.2 Oxidative stress as a hallmark of DCM 10
1.2.1.2.3 Telomere shortening as a hallmark of DCM 10
1.3 Filamin C 11
1.3.1 Structure and function of FLNC 12
1.3.2 FLNC variants and cardiomyopathies 13
1.4 Stem cells 15
1.4.1 Human induced pluripotent stem cells 16
1.4.1.1 Reprogramming into iPSC 16
1.4.1.2 Cardiac differentiation and maturation of iPSC-cardiomyocytes 18
1.4.1.3 iPSC-cardiomyocytes and iPSC-CFB in research and disease modeling 21
1.5 Gene editing of iPSC 23
1.5.1 CRISPR/Cas9 technology 24
1.5.2 CRISPR/Cas9 gene editing in iPSC with high efficiency 25
1.6 Aims 28
2 Materials 29
2.1 Cell lines 29

2.2 Basal Media and Supplements 31
2.3 Cell culture media 31
2.4 CRISPR/Cas9 cell manipulation 33
2.5 Buffers and Solutions 33
2.6 Commercial kits 36
2.7 Chemicals, Reagents, Enzymes 37
2.8 Laboratory equipment 39
2.9 Consumables 40
2.10 Antibodies 41
2.11 Oligonucleotides 42
2.12 Software 44
2.13 Online Programs 44
3 Methods 45
3.1 Cell culture 45
3.1.1 Coating cell culture plates with Geltrex 45
3.1.2 Glass coverslip preparation 45
3.1.3 Feeder-free cultivation of human iPSC on Geltrex 45
3.1.4 Cryopreservation of hiPSC on Geltrex 45
3.1.5 Thawing hiPSC on Geltrex 46
3.1.6 Spontaneous *in vitro* differentiation of iPSC 46
3.1.7 Directed differentiation into iPSC-stromal cells 47
3.1.8 Directed differentiation into ventricular iPSC-cardiomyocytes 47
3.1.9 Digestion of iPSC-cardiomyocytes 48
3.1.10 Pellet collection of cells 49
3.1.11 Fixation of cells on coverslips 49
3.1.12 Cell size measurement using CASY 49
3.1.13 CRISPR/Cas9 genome editing 50
3.2 Molecular biology 52
3.2.1 Genomic DNA isolation 52
3.2.2 RNA isolation 52
3.2.3 DNase I digestion 52
3.2.4 Reverse transcription of RNA 53
3.2.5 Semi-quantitative PCR 53
3.2.6 Quantitative PCR 54

3.2.7 Agarose gel electrophoresis 55
3.2.8 Gel extraction 55
3.2.9 Sanger sequencing 55
3.2.10 Alkaline phosphatase staining 55
3.2.11 Immunofluorescence (IF) staining of 2D cells 56
3.2.12 Immunofluorescence staining of paraffin-embedded tissue sections 57
3.2.13 Analysis of sarcomeric regularity 58
3.2.14 Detection of hydrogen peroxide activity 59
3.2.15 Treatment of cells with Angiotensin Receptor-Neprilysin Inhibitor (ARNi) 59
3.2.16 Western blot analysis 59
3.2.16.1 Protein isolation from iPSC-cardiomyocytes pellets 59
3.2.16.2 SDS-polyacrylamide electrophoresis 60
3.2.16.3 Protein transfer and detection 60
3.2.17 Flow cytometry 61
3.2.18 Quantitative fluorescent *in situ* hybridization to analyze telomere length 62
3.2.19 Telomerase Repeated Amplification Protocol (TRAP) assay 62
3.3 Functional analysis 63
3.3.1 Engineered Human Myocardium (EHM) 63
3.3.1.1 Generation of EHM 63
3.3.1.2 Optical imaging of EHM 63
3.3.1.3 Analysis of EHM contractile function 63
3.3.2 Engineered connective tissue 64
3.3.2.1 Generation of ECT 64
3.3.2.2 Contraction analysis of ECT 65
3.3.2.3 Determination of cross-sectional area (CSA) of ECT 65
3.3.2.4 Destructive tensile strength measurement and stress strain analysis 65
3.3.3 FURA-2AM Ca^{2+} measurements 66
3.3.4 Fluo-4 Ca^{2+} measurements 67
3.4 Statistical analysis 68
4 Results 69
4.1 Recruitment of DCM index family 69
4.1.1 Pedigree analysis reveal *de novo* appearance of DCM in index family 69

4.1.2 Identification of potentially predisposing new variants in FLNC and integrin-linked kinase within the DCM family 70
4.1.3 Generated patient-specific iPSC of all DCM family members display full pluripotency 75
4.1.4 Successful directed differentiation into patient-specific iPSC-cardiomyocytes 79
4.1.4.1 Quality control of generated iPSC-cardiomyocytes 80
4.1.4.2 Decreased differentiation efficiency of DCM1 iPSC into iPSC-cardiomyocytes 81
4.2 Cellular analysis of DCM iPSC-cardiomyocytes 82
4.2.1 Dysregulated sarcomere structure in DCM iPSC-cardiomyocytes 82
4.2.2 Differences in cell size of DCM iPSC-cardiomyocytes 84
4.3 FLNC gene editing 85
4.3.1 Successful generation of isogenic control iPSC lines using CRISPR/Cas9 85
4.3.2 Generated isogenic control iPSC display full pluripotency 86
4.3.3 Absence of off-target effects in CRISPR/Cas9 generated FLNC-rescue isogenic control iPSC 88
4.3.4 Quality control of gene edited isogenic control iPSC-cardiomyocytes 92
4.3.5 Differentiation efficiency of isogenic control DCM1_FLNC2 iPSC into iPSC-cardiomyocytes is improved compared to DCM1-iPSC 93
4.3.6 Rescue of sarcomeric regularity in isogenic control iPSC-cardiomyocytes 94
4.3.7 Rescue of cell size of DCM1 iPSC-cardiomyocytes after FLNC gene editing 95
4.4 Molecular analysis of DCM and isogenic control iPSC-cardiomyocytes 96
4.4.1 FLNC rescue enhances maturation state of iPSC-cardiomyocytes 96
4.4.2 Unaffected expression and localization of mutated FLNC 97
4.4.3 Unaffected expression of FLNC interaction partners 100
4.4.4 Downregulation of Connexin43 protein expression in DCM iPSC-cardiomyocytes 101
4.4.5 DCM1 and DCM3 iPSC-cardiomyocytes show different regulation of genes and proteins important for Ca^{2+} handling 102
4.5 Functional analysis of DCM and FLNC-rescue iPSC-cardiomyocytes 107
4.5.1 Aberrant Ca^{2+} handling in DCM iPSC-cardiomyocytes 107
4.5.1.1 Classical heart failure phenotype and slower Ca^{2+} kinetics of DCM iPSC-cardiomyocytes 107
4.5.1.2 FLNC-dependent increased SERCA activity in DCM3 iPSC-cardiomyocytes 110
4.5.1.3 Pro-arrhythmic potential in DCM1 iPSC-cardiomyocytes 111

4.5.2 Increased reactive oxygen species in DCM1 iPSC-cardiomyocytes can be reduced by ARNi treatment ... 112
4.5.3 Increased tissue stiffness and decreased contractile function in DCM EHM can partially be restored upon *FLNC* rescue ... 113
4.6 Role of CFB in DCM development and pathophysiology ... 116
4.6.1 Isolated CFB express several specific CFB marker ... 116
4.6.2 Establishment of protocol for directed differentiation into iPSC-Stromal cells (StC) ... 119
4.6.3 Analysis of 3D ECT ... 122
4.6.3.1 Reduced contraction in DCM1 ECT is restored upon FLNC rescue ... 122
4.6.3.2 Increased CSA in DCM1 ECT is restored upon FLNC rescue ... 123
4.6.3.3 Increased tissue stiffness and decreased elasticity in ECT of primary DCM CFB ... 124
4.7 Role of telomere length in development and pathophysiology of DCM ... 126
4.7.1 Increased telomere shortening in DCM iPSC-cardiomyocytes ... 127
4.7.2 Unaffected telomerase activity ... 128
5 Discussion ... 130
5.1 Identified FLNC missense variant is in a mutation and interaction hotspot of FLNC, the ROD2 domain ... 131
5.2 iPSC of all family members show full pluripotency ... 135
5.3 Differentiated iPSC-cardiomyocytes show high purity and ventricular subtype-specificity but decreased differentiation efficiency of DCM1 iPSC ... 135
5.4 FLNC rescue genome editing ... 137
5.5 FLNC-dependent dysregulated sarcomeric structure in DCM iPSC-cardiomyocytes ... 140
5.5.1 Restored sarcomeric regularity enhances iPSC-cardiomyocyte maturation ... 142
5.5.2 FLNC-dependent reduction in cell size of DCM1 iPSC-cardiomyocytes as a consequence of sarcomeric disarray ... 144
5.6 Downregulation of CX43 as a marker for heart failure ... 145
5.7 Aberrant Ca^{2+} handling in DCM iPSC-cardiomyocytes ... 147
5.7.1 Reduced transient Ca^{2+} amplitude and slower Ca^{2+} kinetics as a hallmark of DCM phenotype improve upon FLNC rescue ... 147
5.7.2 CaMKIIδ-dependent phosphorylation of RYR2 and PLN in DCM1 iPSC-cardiomyocytes to compensate for slower Ca^{2+} kinetics ... 149
5.7.3 Increased SERCA activity in DCM3 affects alterations in Ca^{2+} handling ... 150

5.8 FLNC-independent elevated levels of ROS in DCM1 iPSC-cardiomyocytes can be treated with the Angiotensin Receptor-Neprilysin Inhibitor Entresto 151
5.9 Mechanical impairment in DCM EHM is partially restored by FLNC rescue ... 153
5.10 Role of CFB in DCM pathophysiology 156
5.10.1 Characterization of primary CFB and their activation state 156
5.10.2 Directed differentiation of CFB-like cells from iPSC 158
5.10.3 Analysis of 3D ECT 160
5.10.3.1 FLNC-dependent decrease in ECT contraction and compaction 160
5.10.3.2 Increased tissue stiffness and reduced elasticity in diseased ECT 161
5.11 Telomere shortening as a cause for DCM 163
5.12 Limitations of this work 165
5.13 Conclusion 166
5.14 Outlook 168
6 References 172
7 Appendix 199
8 Acknowledgments i
9 Affidavit iii

List of Figures

FIG. 1: SCHEMATIC STRUCTURE OF CARDIAC SARCOMERE WITH COMPONENTS OF THIN AND THICK FILAMENTS. 3
FIG. 2: SCHEMATIC OVERVIEW OF CA^{2+} CYCLING DURING SYSTOLE AND DIASTOLE. 4
FIG. 3: SCHEMATIC AND EXEMPLARY OVERVIEW OF CARDIOMYOAPTHY CAUSING GENE VARIANTS. 9
FIG. 4: STRUCTURE OF FLNC PROTEIN AND IDENTIFIED PATHOGENIC VARIANTS IN FLNC. 12
FIG. 5: SCHEMATIC OVERVIEW OF FLNC INTERACTION NETWORK WITHIN CARDIOMYOCYTES. 13
FIG. 6: SCHEMATIC OVERVIEW OF IN VIVO AND IN VITRO CARDIOMYOCYTE DIFFERENTIATION. 19
FIG. 7: SCHEMATIC OVERVIEW OF IN VIVO AND IN VITRO CFB DIFFERENTIATION. 21
FIG. 8: SCHEMATIC OVERVIEW OF EUKARYOTIC DSB REPAIR USED FOR CRISPR/CAS9 GENOME EDITING. 25
FIG. 9: PLATING SCHEME FOR SPONTANEOUS IN VITRO DIFFERENTIATION DAY 8. 46
FIG. 10: SCHEMATIC OVERVIEW OF DIRECTED DIFFERENTIATION INTO STROMAL CELLS. 47
FIG. 11: SCHEMATIC OVERVIEW OF DIRECTED DIFFERENTIATION INTO VENTRICULAR IPSC-CARDIOMYOCYTES. 48
FIG. 12: CRISPR STRATEGY TO RESCUE FLNC VARIANT IN DCM IPSC PATIENT LINES. 52
FIG. 13: WORKFLOW FOR ANALYSIS OF SARCOMERIC REGULARITY USING FFT. 58
FIG. 14: STRESS-STRAIN CURVE OF ECT AFTER DESTRUCTIVE TENSILE STRENGTH MEASUREMENT SHOWING THE MAIN MEASURED PARAMETERS. 66
FIG. 15: OVERVIEW OF DCM INDEX FAMILY. 69
FIG. 16: FAMILY PEDIGREE OF INDEX PATIENT DCM1. 70
FIG. 17: IDENTIFICATION AND VERIFICATION OF DCM-ASSOCIATED SNPS AND VARIANTS WITHIN THE DCM FAMILY. 74
FIG. 18: PLURIPOTENCY CHARACTERIZATION BY CELL MORPHOLOGY AND SPECIFIC PROTEIN EXPRESSION. 76
FIG. 19: EXPRESSION OF ENDOGENOUS PLURIPOTENCY-ASSOCIATED MARKERS ON MRNA LEVEL. 77
FIG. 20: EXPRESSION OF GERM LAYER-SPECIFIC PROTEINS AFTER SPONTANEOUS IN VITRO DIFFERENTIATION OF IPSC. 78
FIG. 21: EXPRESSION OF GERM LAYER-SPECIFIC GENES AFTER SPONTANEOUS IN VITRO DIFFERENTIATION OF IPSC. 79
FIG. 22: REPRESENTATIVE QUALITY CONTROL ANALYSES OF IPSC-CARDIOMYOCYTES. 81
FIG. 23: ANALYSIS OF DIFFERENTIATION EFFICIENCY OF IPSC INTO IPSC-CARDIOMYOCYTES. 82
FIG. 24: SARCOMERIC REGULARITY IS DECREASED IN DCM IPSC-CARDIOMYOCYTES. 83
FIG. 25: CELL SIZE OF IPSC-CARDIOMYOCYTES DIFFERS AMONG FAMILY MEMBERS. 84
FIG. 26: GENERATION OF ISOGENIC FLNC-RESCUE IPSC. 86
FIG. 27: PLURIPOTENCY CHARACTERIZATION OF FLNC GENE EDITED IPSC CLONES. 87
FIG. 28: SPONTANEOUS IN VITRO DIFFERENTIATION OF FLNC GENE EDITED IPSC CLONES. 88
FIG. 29: OFF TARGET ANALYSIS OF FLNC GENE EDITED IPSC CLONES. 92
FIG. 30: SEQUENCE COMPARISON OF WILDTYPE, PATIENT, AND ISOGENIC CONTROL LINES OF GFPT2 OFF-TARGET SITE. 92
FIG. 31: REPRESENTATIVE QUALITY CONTROL ANALYSES OF GENE EDITED IPSC-CARDIOMYOCYTES. 93
FIG. 32: ANALYSIS OF DIFFERENTIATION EFFICIENCY OF ISOGENIC CONTROL IPSC OF DCM1 INTO IPSC-CARDIOMYOCYTES. 94
FIG. 33: SARCOMERIC REGULARITY IS RESCUED IN ISOGENIC CONTROL IPSC-CARDIOMYOCYTES. 95
FIG. 34: CELL SIZE OF IPSC-CARDIOMYOCYTES CHANGES AFTER FLNC GENE EDITING. 96
FIG. 35: EXPRESSION ANALYSIS OF CARDIOMYOCYTE MATURATION MARKERS MYH6 AND MYH7 IN DCM IPSC-CARDIOMYOCYTES. 97
FIG. 36: EXPRESSION ANALYSIS OF FLNC IN DCM AND ISOGENIC CONTROL IPSC-CARDIOMYOCYTES. 98
FIG. 37: LOCALIZATION OF FLNC IN DCM AND ISOGENIC CONTROL (IPSC-) CM. 100
FIG. 38: EXPRESSION ANALYSIS OF FLNC INTERACTION PARTNERS IN IPSC-CARDIOMYOCYTES. 101
FIG. 39: EXPRESSION OF CX43 IN DCM AND ISOGENIC CONTROL IPSC-CARDIOMYOCYTES. 102

FIG. 40: EXPRESSION OF IMPORTANT CA^{2+} HANDLING PROTEINS IN DCM1 AND ISOGENIC CONTROL IPSC-CARDIOMYOCYTES. 105
FIG. 41: EXPRESSION OF IMPORTANT CA^{2+} HANDLING PROTEINS IN DCM3 AND ISOGENIC CONTROL IPSC-CARDIOMYOCYTES. 106
FIG. 42: EXPRESSION OF IMPORTANT CA^{2+} HANDLING GENES IN DCM AND ISOGENIC CONTROL IPSC-CARDIOMYOCYTES. 107
FIG. 43: FURA-2AM MEASUREMENTS TO EVALUATE CA^{2+} HANDLING OF DISEASED AND FLNC RESCUED IPSC-CARDIOMYOCYTES. 109
FIG. 44: FLUO-4 MEASUREMENTS TO EVALUATE CA^{2+} HANDLING OF DISEASED AND FLNC RESCUED IPSC-CARDIOMYOCYTES. 110
FIG. 45: FURA-2AM MEASUREMENTS TO EVALUATE CA^{2+} HANDLING OF DISEASED AND FLNC RESCUED IPSC-CARDIOMYOCYTES. 111
FIG. 46: FLUO-4 MEASUREMENTS TO EVALUATE CA^{2+} SPARKS OF DISEASED AND FLNC RESCUED IPSC-CARDIOMYOCYTES. 112
FIG. 47: ANALYSIS OF OXIDATIVE STRESS OF DCM IPSC-CARDIOMYOCYTES. 113
FIG. 48: ANALYSIS OF DISEASED, ISOGENIC AND CONTROL EHM. 116
FIG. 49: CHARACTERIZATION OF DIFFERENT FIBROBLAST LINEAGES BY MRNA MARKER EXPRESSION. ... 118
FIG. 50: DIRECTED DIFFERENTIATION OF IPSC INTO IPSC-STC. 120
FIG. 51: CHARACTERIZATION OF IPSC-DERIVED STC BY MRNA MARKER EXPRESSION. 121
FIG. 52: IF STAINING OF IPSC-STC. 122
FIG. 53: CONTRACTION ANALYSIS OF ECT. 123
FIG. 54: CSA ANALYSIS OF ECT. 124
FIG. 55: STRESS-STRAIN ANALYSIS OF ECT. 126
FIG. 56: QFISH ANALYSIS OF TELOMERE LENGTH OF IPSC AND IPSC-CARDIOMYOCYTES. 128
FIG. 57: TRAP ASSAY TO ANALYZE TELOMERASE ACTIVITY OF DCM IPSC. 129
FIG. 58: SUMMARY OF DCM PATHOPHYSIOLOGY IN INDEX FAMILY. 167

SUPPL. FIG. 1: SUMMARY OF SCN10A KNOCK-OUT IPSC LINES AND SUBSEQUENT QUALITY CONTROL ANALYSIS. 201
SUPPL. FIG. 2: OFF TARGET ANALYSIS OF $NA_V1.8$ KO GENE EDITED IPSC CLONES. 201
SUPPL. FIG. 3: PLURIPOTENCY CHARACTERIZATION OF FLNC GENE EDITED IPSC CLONES. 204
SUPPL. FIG. 4: SPONTANEOUS IN VITRO DIFFERENTIATION OF FLNC GENE EDITED IPSC CLONES. 205
SUPPL. FIG. 5: FULL WESTERN BLOT MEMBRANES FOR ALL DCM1/DCM1_RES WESTERN BLOTS. 207
SUPPL. FIG. 6: FULL WESTERN BLOT MEMBRANES FOR ALL DCM3/DCM3_RES WESTERN BLOTS. 208

List of Tables

TAB. 1: LIST OF SOMATIC, REPROGRAMMED OR GENETICALLY MODIFIED CELLS AND CELL LINES USED. . 29
TAB. 2: LIST OF ALL BASAL MEDIA AND SUPPLEMENTS USED. 31
TAB. 3: COMPOSITION OF CELL CULTURE MEDIA. 31
TAB. 4: LIST OF CRISPR/CAS9 COMPONENTS FOR CELL MANIPULATION. 33
TAB. 5: CRRNA AND HDR TEMPLATE OF CRISPR STRATEGY USED TO RESCUE FLNC MUTATION. 33
TAB. 6: COMPOSITION OF BUFFERS AND SOLUTIONS. 33
TAB. 7: LIST OF ALL COMMERCIAL KITS USED. 36
TAB. 8: LIST OF ALL CHEMICALS, REAGENTS AND ENZYMES USED. 37
TAB. 9: LIST OF ALL LABORATORY EQUIPMENT USED. 39
TAB. 10: LIST OF ALL CONSUMABLE MATERIAL USED. 40
TAB. 11: LIST OF PRIMARY ANTIBODIES. 41
TAB. 12: LIST OF SECONDARY ANTIBODIES. 41
TAB. 13: LIST OF PRIMERS USED. 42
TAB. 14: LIST OF ALL SOFTWARE USED. 44
TAB. 15: LIST OF ALL ONLINE PROGRAMS USED. 44
TAB. 16: NUMBER OF IPSC-CARDIOMYOCYTES USED FOR DIFFERENT READ-OUTS. 49
TAB. 17: REACTION PROTOCOL FOR REVERSE TRANSCRIPTION USING THE ISCRIPT CDNA SYNTHESIS KIT (BIORAD). 53
TAB. 18: MASTER MIX FOR SEMI-QUANTITATIVE PCR. 53
TAB. 19: REACTION PROTOCOL FOR SEMI-QUANTITATIVE PCR 54
TAB. 20: MASTER MIX FOR QUANTITATIVE PCR. 54
TAB. 21: REACTION PROTOCOL FOR QUANTITATIVE PCR. 54
TAB. 22: ANTIBODIES AND RESPECTIVE CONDITIONS USED FOR IF STAINING OF IPSC-CARDIOMYOCYTES. 56
TAB. 23: DEWAXING PROTOCOL FOR PARAFFIN-EMBEDDED TISSUE SECTIONS. 57
TAB. 24: ANTIBODIES USED FOR IF STAINING OF PARAFFIN-EMBEDDED TISSUE SECTIONS. 58
TAB. 25: ANTIBODIES AND RESPECTIVE CONDITIONS USED FOR WESTERN BLOTS 61

SUPPL. TAB. 1: MEAN CT VALUES. 206
SUPPL. TAB. 2: CELL LINES AND DIFFERENTIATION ID-NUMBERS USED IN EXPERIMENTS. 209

Abbreviations

°C	Degree Celsius
αSMA	Alpha-smooth muscle actin
µg	Microgram
µl	Microliter
µm	Micrometer
18S	18S ribosomal RNA
A	Adenine
aa	Amino acid
AAV	Adeno-associated virus
ABD	Actin-binding domain
ACM	Arrhythmogenic cardiomyopathy
ACTA2	Alpha-smooth muscle actin gene
AFP	Alpha-feto protein
ALB	Albumin
ALP	Alkaline phosphatase
AngII	Angiotensin II
ANONA	Analysis of variance
Arg	Arginine
ARNi	Angiotensin Receptor-Neprilysin Inhibitor
ARVC	Arrhythmogenic right ventricular cardiomyopathy
AT1	Angiotensin type I
ATP	Adenosine-triphosphate
BCA	Bicinchoninic acid
BMP	Nodal/bone morphogenic protein
bp	Base pair
BSA	Bovine serum albumin
BSFM	Basal serum-free medium
C	Cytosine
Ca^{2+}	Calcium ion

CaMKII	Ca^{2+}/calmodulin-dependent protein kinase II
Cas	CRISPR-associated protein
CASPF	Ca^{2+} spark frequency
CDM	Cardiac differentiation medium
cDNA	Complementary DNA
CFB	Cardiac fibroblasts
CH	Calponin-homology domain
CICR	Calcium-induced calcium release
cm^2	Square centimeter
c-MYC	V-myc myelocytomatosis viral oncogene homolog
COL1A1	Collagen type I
CRISPR	Clustered regulatory interspaced palindromic repeats
crRNA	CRISPR RNA
CSA	Cross-sectional area
Ct	Cycle threshold
CTGF	Connective tissue growth factor
cTNT/I/C	Cardiac Troponin T / I / C
CTRL	Control
CX43	Connexin43
CYBA	Cytochrome b-245 alpha-chain
d	Day(s)
DAPI	4', 6-Diamidino-2-phenylindole dihydrochloride
DCM	Dilated cardiomyopathy
DMD	Duchenne Muscular Dystrophy
DMEM	Dulbecco's Modified Eagle Medium
DMSO	Dimethyl sulfoxide
DNA	Deoxyribonucleic acid
dNTP	Deoxynucleotide triphosphates
DPBS	Dulbecco`s phosphate-buffered saline
DSB	Double strand break
DSC2	Desmocollin-2

DSG2	Desmoglein-2
DSP	Desmoplakin
DTT	Dithiothreitol
E8	Essential 8
EB	Embryoid body
EC	Endothelial cells
ECM	Extracellular matrix
ECT	Engineered connective tissue
EF	Ejection fraction
EGC	Embryonic germ cell
EHM	Engineered heart muscle
EHT	Engineered heart tissue
EMT	Epithelial-mesenchymal transition
EndMT	Endothelial-mesenchymal transition
ESC	Embryonic stem cell
FACS	Fluorescence-activated cell sorting
FCS	Fetal calf serum
FFT	Fast Fourier Transformation
FGF2	Fibroblast growth factor 2
FGM3	Fibroblast growth medium
FLNA	Filamin A
FLNB	Filamin B
FLNC	Filamin C
FLOW	Fluorescence cytometry
FOC	Force of contraction
FSP1	Fibroblast-specific protein
Fw	Forward
g	Gravitational force
G	Guanine
GAPDH	Glycerinaldehyd-3-phosphat-dehydrogenase
GDF3	Growth differentiation factor-3

GFPT2	Glutamine-Fructose-6-Phosphate Transaminase 2
GJ	Gap junctions
GJA1	Gap Junction Protein Alpha 1 (coding for Connexin43)
Gly	Glycine
GSK3	Glycogen synthase kinase 3
h	Hour
H1/H2	Hinge region 1/2
HCM	Hypertrophic cardiomyopathy
HDR	Homology directed repair
HEK	Human embryonic kidney cells
HEPES	4-(2-hydroxyethyl)-1-piperazineethanesulfonic acid
HFBM	Human fibroblast medium
HRP	Horseradish peroxidase
HUVEC	Human umbilical vein endothelial cells
Hz	Hertz
ICD	Intercalated disc
IF	Immunofluorescence
IgG	Immunoglobulin G
IgM	Immunoglobulin M
ILK	Integrin-linked kinase
IMDM	Iscove`s Modified Dulbecco`s Medium
iPSC	Induced pluripotent stem cells
IWP	Inhibitor of WNT production
IWP2	Wnt antagonist II
JAKMIP3	Janus kinase and microtubule-interacting protein 3
kDa	Kilo Dalton
KLF4	Krüppel-like factor 4
kPa	Kilo Pascal
LGR4	Leucine-rich repeat-containing G-protein coupled receptor 4
LIN28	Cell lineage abnormal 28
LMNA	Lamin A/C

LTCC	Voltage-gated L-type calcium channels
LV	Left ventricle
LVNC	Left ventricular non-compaction
M	Molar
mA	Milliampere
MAP2	Microtubule-associated protein 2
MCU	mitochondrial Ca^{2+} uniporter
MEA	Multi-electrode array
MEF	Mouse embryonic fibroblast
MESP1	Mesoderm posterior1
Met	Methionine
mg	Milligram
mGSC	Multipotent germline stem cell
MHC	Myosin-heavy chain
min	Minute
ml	Milliliter
MLC	Myosin-light chain
mm	Millimeter
MMP	Matrix metalloproteinases
mN	Millinewton
mRNA	Messenger RNA
MTG	Monothioglycerine
MYBPC3	Myosin binding protein C3
MYH6	α-myosin heavy chain gene
MYH7	β-myosin heavy chain gene
MYOT	Myotilin encoding gene
N2B	Stiff titin isoform
N2BA	Elastic titin isoform
$Na_v1.5$	Voltage-gated Na^+ channel 1.5
$Na_v1.8$	Voltage-gated Na^+ channel 1.8
NCX	Na^+/Ca^{2+} exchanger

NEAA	Non-essential amino acid
ng	Nanogram
NGS	Next generation sequencing
NHEJ	Non-homologous end joining
NLRP6	NLR family pyrin domain containing 6
nm	Nanometer
NMD	Non-sense mediated decay
nt	Nucleotides
OCT4	Octamer binding transcription factor 4
OKSM	Yamanaka factors: OCT4-SOX2-KLF4-c-MYC
ON	Overnight
PAM	Protospacer adjacent motif
PAX3	Paired box 3
PAX6	Paired box 6
PBMCs	Peripheral blood mononuclear cells
PBS	Phosphate-buffered saline
PCR	Polymerase chain reaction
PDGFRα	Platelet-derived growth factor receptor alpha
PFA	Paraformaldehyde
PGM5	Aciculin encoding gene
PITX2	Paired-like homeodomain transcription factor 2
PKA	Protein kinase A
PKP2	Plakophilin-2
PLN	Phospholamban
POSTN	Periostin
Pro	Proline
PSC	Pluripotent stem cell
PTM	Post-translational modification
PVDF	Polyvinylidene difluoride
qFISH	Quantitative fluorescent *in situ* hybridization
qPCR	Quantitative real-time PCR

RA	Retinoic acid
RBM20	RNA-binding motif protein 20
Res	Rescue
Rev	Reverse
RNA	Ribonucleic acid
RNP	Ribonucleoprotein
ROS	Reactive oxygen species
RPMI	Roswell Park Memorial Institute Medium
rs	Reference SNP ID number
RT	Room temperature
RYR2	Ryanodine receptor 2
SC	Stem cell
SDS	Sodium dodecyl sulfate
sec	Second
SEM	Standard error of mean
Ser	Serine
SERCA	Sarcoplasmic/endoplasmic reticulum Ca^{2+} ATPase
SFB	Skin fibroblast
SNP	Single-nucleotide polymorphism
SOX2	SRY-box2; SRY: Sex-determining region of Y
SpCas9	*Streptococcus pyogenes* Cas9
SR	Sarcoplasmic reticulum
StC	Stromal cells
StC-EM	Stromal cell expansion medium
StC-IM	Stromal cell induction medium
StC-SM	Stromal cell specification medium
SYNPO2	Myopodin encoding gene
T	Thymin
T3	Triiodothyronine
TB	Turbo transfer
TBE	Tris/Borate/EDTA buffer

TBS	Tris-buffered saline
TCF21	Transcription factor 21
TEMED	Tetramethylethylenediamine
TGFβ	Transforming growth factor beta
Thr	Threonine
TRA1-60	Tumor rejection antigen 1-60
tracrRNA	Trans-activating crRNA
TRAP	Telomerase Repeated Amplification Protocol
TS	Telomere substrate
TTN	Titin
TTS	Takotsubo syndrome
TUBB	Tubulin
TZV	Thiazovivin
UV	Ultraviolet
V	Volt
Val	Valine
VEGF	Vascular endothelial growth factor
VSMC	Vascular smooth muscle cells
VUS	Variant of unknown significance
W	Watt
w/	with
w/o	without
WB	Western blot
WES	Whole exome sequencing
Wt	Wildtype
αSMA	Alpha-smooth muscle actin

Summary

Despite rapid scientific and medical advances, cardiovascular diseases represent a major threat to human health worldwide. Among these, cardiomyopathies are one of the leading causes of heart failure. Dilated cardiomyopathy (DCM) characterized by dilation of the left ventricle and systolic dysfunction but no left ventricular wall thickening, represents one of the most common causes of heart failure and is the leading indication for heart transplantation worldwide. The underlying molecular causes of most DCM cases remain unknown. Nevertheless, it was shown that up to 35% of all DCM cases have a family history and are associated with mutations in more than 50 gene loci. Hence, identifying the underlying molecular mechanisms which contribute to DCM development is indispensable. Hence this project aims to identify disease causing variants and to unravel associated underlying molecular mechanisms contributing to the DCM pathophysiology.

To establish a human *in vitro* DCM model of a four-member index family, containing patients with severe DCM (father and oldest daughter) and healthy controls (mother and second daughter) patient-derived iPSC-cardiomyocytes were used. Generated integration-free iPSC-lines of all four family members displayed full pluripotency. They were differentiated into beating iPSC-cardiomyocytes with high purity. Whole exome sequencing (WES) and panel sequencing identified a new and disease-causing missense variant in the *filamin C (FLNC,* p.R2187P*)* gene. With the use of CRISPR/Cas9 generated isogenic control iPSC lines, a FLNC-dependent dysregulated sarcomeric structure could be identified as main disease phenotype, giving first evidence for the crucial role of the *FLNC* variant within the DCM pathophysiology. Based on this finding we analyzed the role of the *FLNC* variant further on molecular and functional levels. We found no differences in FLNC expression or localization between diseased and control (iPSC-) cardiomyocytes, suggesting impairments of FLNC interactions to important binding partners. Additionally, FLNC-R2187P-dependent contraction defects and increased stiffness were shown in 3D engineered heart muscle, composed of iPSC-cardiomyocytes, fibroblasts, and collagen, in both patients. Furthermore, an impaired Ca^{2+} handling, characterized by decreased systolic Ca^{2+} content and slowed Ca^{2+} kinetics, were demonstrated FLNC-R2187P-dependent in the diseased father and daughter. Interestingly, different possible compensatory mechanisms of Ca^{2+} handling were shown for the two patients. Analysis of iPSC-cardiomyocytes of the diseased daughter identified unusual and significantly increased SERCA expression and activity. However, it remains debatable, whether impaired Ca^{2+} handling or increased SERCA activity was appearing first. iPSC-cardiomyocytes of the diseased father demonstrated CaMKIIδ-dependent, but FLNC-independent increased RYR2-S2814 and PLN-T17 phosphorylation to possibly counteract slowed Ca^{2+} kinetics. Additionally, elevated levels of ROS were identified exclusively in the diseased father. However, both patients displayed FLNC-independent decreased CX43 expression of unknown cause. Moreover, FLNC-dependent compaction and contraction of diseased engineered connective tissue, composed of (iPSC-) cardiac fibroblasts (CFB) and collagen, were decreased. With this, we could – to our knowledge – for the first time demonstrate a role of FLNC within CFB in general and identify

a decisive role of the identified FLNC variant in CFB as an important player in the DCM pathophysiology. Engineered connective tissue of primary CFB additionally displayed increased stiffness, pointing towards fibrotic processes, which is in line with demonstrated increased fibrosis of explanted myocardium of the left ventricle of the father, shown in previous studies. Moreover, for both patients an increased telomere shortening in iPSC-cardiomyocytes, of unknown cause, was observed and remains to be elucidated.

Taken together, these results clearly identified the newly found FLNC missense variant as underlying disease cause within the DCM family, primarily leading to a dysregulated sarcomeric structure, contraction defects and increased stiffness, classical DCM pathomechanisms, which could be linked to the FLNC variant. Besides the shared disease causing FLNC variant and associated pathomechanisms, we identified exclusive phenotypes for each patient, which might be explanatory for different disease onsets. Furthermore, FLNC-dependent functional impairments in CFB were identified pointing to FLNC as a crucial player within the DCM pathophysiology. Based on these findings, future experiments will shed more light onto the exact cause of the missense variant on the FLNC function in detail.

1 Introduction

1.1 The heart

The heart is a big muscle in the center of the human body, ensuring life-long constant pumping of blood throughout the body. To conduct its important functions the human heart consists of four functional different chambers – two small chambers, the left and right atria and two larger chambers, the left and right ventricles. Proper blood pumping function of the heart relies on a highly complex interplay of several cellular mechanisms including mechanisms of electrical stimulation and propagation as well as of force generation and propagation both largely based on Ca^{2+} cycling and orderly structural requirements to yield a balanced and sufficient contraction of the heart.

1.1.1 Cellular composition of the heart

The function of the heart is dependent on its highly diverse cellular composition. The main cell types of the heart are divided into two families – the myocytes and the non-myocytes. The myocyte fraction, comprising up to 30% of the total cell volume, is represented by the cardiomyocytes. The non-myocyte fraction makes up to 70% of the heart cellular composition and is primarily composed of endothelial cells (EC) and fibroblasts but also includes vascular smooth muscle cells (VSMC), pericytes and immune cells (Pinto *et al.*, 2016; Zhou and Pu, 2016). Additionally, the heart is largely innervated by sympathetic and parasympathetic nerves from the autonomic nervous system (Kimura *et al.*, 2012). All different cell types are responsible for individual functions within the heart. Complex and dynamic interaction networks between the cells are formed, allowing propagation and integration of electrical, mechanical, and chemical stimuli throughout the heart (Banerjee *et al.*, 2006; Pinto *et al.*, 2016; Zhou and Pu, 2016). Role and function of cardiomyocytes and fibroblasts will be discussed in the following paragraphs in more detail. Cardiac EC line blood and lymphatic vessels (Lother *et al.*, 2018). In addition to this major function, EC are connected to cardiomyocytes by paracrine signaling. This includes activation of cardiomyocyte hypertrophic growth (Kamo *et al.*, 2015), or initiation of angiogenic signaling of the EC by the cardiomyocytes (Oka *et al.*, 2014). Furthermore, EC are also involved in inflammatory responses and regulation of extracellular matrix (ECM) by interaction with immune cells and fibroblasts (Tirziu *et al.*, 2010). VSMC and pericytes, collectively named mural cells, cover the abluminal surfaces of arteries and veins and contribute to vessel stability due to interactions with EC (Chen *et al.*, 2016). VSMC comprise a myosin/actin network important for arterial contraction and blood pressure regulation (Michel *et al.,* 2012). Additionally, VSMC also secrete important ECM components. Pericytes are reported to be involved in regeneration processes of the heart (Chen *et al.*, 2016). Sympathetic innervation of the heart is largely carried out by secretion of norepinephrine and has effects on increasing heart rate, conduction velocity, as well as contraction and relaxation (Kimura *et al.*, 2012). This is, amongst others, mediated by direct interaction of sympathetic neurons with cardiomyocytes (Zaglia and Mongillo, 2017) or VSMC (Michel *et al.*, 2012).

1.1.1.1 Cardiomyocytes and its contractile unit – the sarcomere

The pumping function of the heart is conducted by the muscular part of the heart – the myocardium. The muscular function of the myocardium is mainly provided by the contractile cells – the cardiomyocytes. Several cardiomyocytes form a functional syncytium connected by intercalated discs (ICD), leading to formation of long muscle fibers. At the ICD, the cardiomyocytes are connected by gap junctions (GJ), desmosomes and adherens junctions allowing ion exchange and electrical coupling from one cardiomyocyte to another (Bers and Borlaug, 2018).

To generate contraction, cardiomyocytes comprise several, repetitively connected sarcomeres. Sarcomeres are the smallest contractile units of the cardiomyocytes. Two sarcomeres are connected at the so called Z-disc, marking the lateral boarder of the sarcomere and leading to the well-known pattern of striated muscle fibers *(Henderson et al.*, 2017). They are composed of a plethora of different proteins arranged in a highly regulated pattern of thin and thick filaments. Due to the highly regulated and repetitive arrangement, the sarcomere appears to be segmented into the I-band, comprising the thin filaments close to the Z-disc, the A-band, representing the region where thin and thick filaments are interacting, and the M-line in the center of the sarcomere (Clark *et al.*, 2002; Gautel and Djinovic-Carugo, 2016; Henderson *et al.*, 2017) (Fig. 1). The thick filament, located in the center of the sarcomere, mainly consists of myosin. Myosin is a huge motor protein composed of two myosin-heavy chain (MHC) and two regulatory myosin-light chain (MLC) proteins. Thick filaments are connected to the M-line by interactions to M-line proteins myomesin and obscurin, providing a cytoskeletal scaffold (Agarkova *et al.*, 2004; Walker and Spinale, 1999). Additionally, the giant protein titin (TTN), which spans the sarcomere by N-terminal interactions to the Z-disc and C-terminal interactions to the M-line, provides structural support and links the thick filaments to the Z-disc (Tajsharghi, 2008; Walker and Spinale, 1999). The thin filament is composed of filamentous actin (F-actin) and its regulatory proteins tropomyosin and troponin forming a helix structure. F-actin is anchored to the Z-disc by α-actinin. There are different cardiac troponins (cTNT, cTNI, cTNC), which prevent the attachment of the myosin heads to actin during the stationary phase (Henderson *et al.*, 2017). Thin and thick filaments act together in the so called cross-bridging cycle, pulling the Z-discs closer together, causing the cell to contract (Huxley, 1969). This cross-bridging cycle is initiated by increasing intracellular Ca^{2+} levels as described below, however correct expression, alignment and function of actin, myosin and many other structural and regulatory sarcomere proteins is the prerequisite for functional contraction of cardiomyocytes.

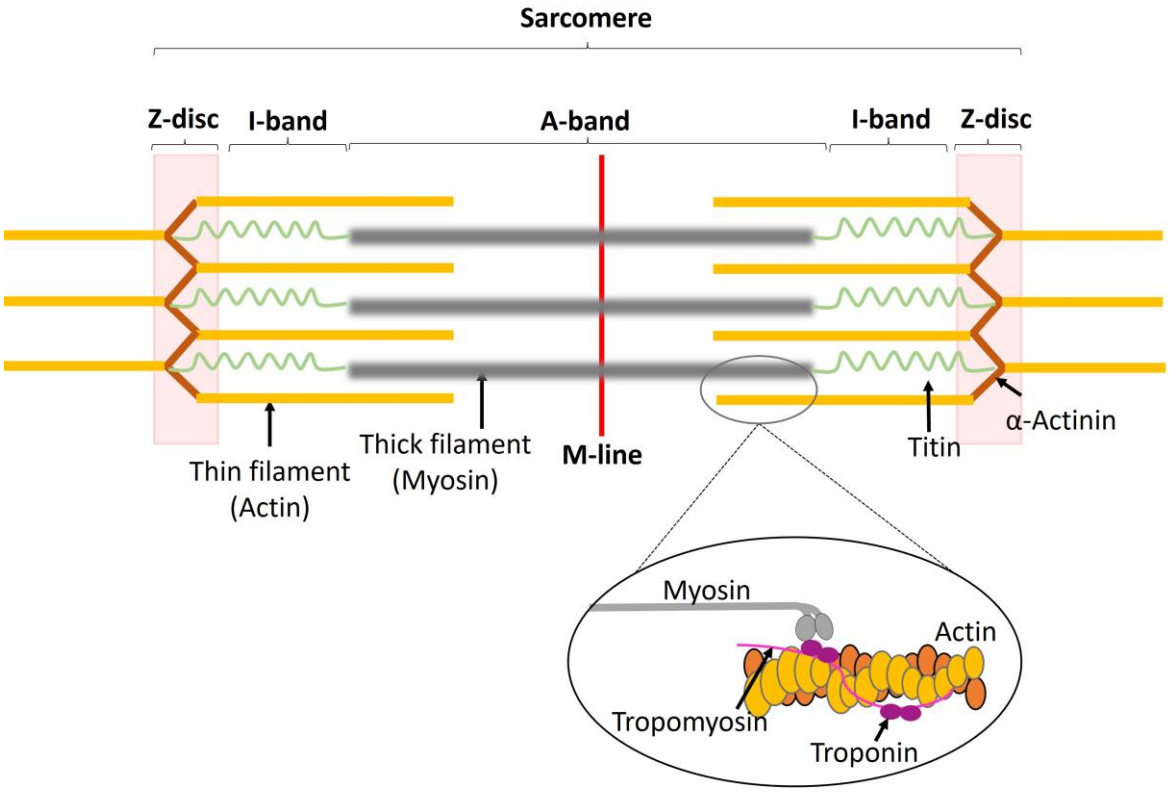

Fig. 1: Schematic structure of cardiac sarcomere with components of thin and thick filaments. The Z-disc marks the lateral ends of each sarcomere. The thin filaments comprise actin, troponin and tropomyosin. Actin filaments are cross-linked by α-actinin at the Z-disc. The thick filaments mainly contain myosin and are located at the center of the sarcomere but are connected to the Z-disc via titin. Contraction is mediated by the cross-bridging cycle via interactions of thick and thin filaments.

1.1.1.1.1 Ca^{2+}cycling in cardiac excitation-contraction coupling

To generate cardiac contraction, action potentials are initiated by cardiac pacemaker cells. These action potentials travel throughout the heart by propagation over atria and ventricles from cell to cell, inducing cross-bridging cycles at the sarcomeres leading to mechanical contraction. This process is called the excitation-contraction coupling (Bers, 2002). Since cardiomyocytes are connected by GJ, forming a syncytium, this contraction is orchestrated in a synchronized manner.

An action potential that is initiated by the pacemaker cells and propagated throughout the heart from cell to cell via GJ, opens voltage-gated Na^+ channels ($Na_v1.5$) in the sarcolemma of cardiomyocytes (Fig. 2). This leads to depolarization of the membrane, marking the start of the systolic phase. Depolarization of the membrane results in opening of voltage-gated L-type Ca^{2+} channels (LTCC), and an initial Ca^{2+} influx into the cardiomyocyte (Fig. 2). This initial small Ca^{2+} influx is sensed by the Ca^{2+}-sensitive Ca^{2+} channel ryanodine receptor 2 (RYR2) located in the sarcoplasmic reticulum (SR) and results in a positive feedback loop. This is known as calcium-induced calcium release (CICR) (Fig. 2) (Bers, 2008). CICR describes the opening of RYR2 and massive Ca^{2+} release from the SR upon initial Ca^{2+} influx through LTCC, which would not be sufficient to induce contraction. This Ca^{2+} influx is sensed by cTNT within the thin filament of the sarcomere and initiates the cross-bridging cycle (Bers, 2002; 2008; Lehman *et al.*, 1994) (Fig. 2). In more detail, upon Ca^{2+} binding to cTNT a

conformational change of the thin filament is induced allowing the myosin heads of the thick filament binding to actin. Under ATP consumption, the myosin heads pull the actin filament towards the M-line, causing contraction of the cardiomyocytes (Bers and Borlaug, 2018; Lehman *et al.*, 1994). The end of the action potential marks the beginning of the diastolic phase, where the heart muscle relaxes again. Hence, the end of the action potential is accompanied with closing of LTCCs and stopping of Ca^{2+} influx. Additionally, the bound Ca^{2+} is released from cTNT and the myofilaments of the sarcomere return to their resting state, leading to relaxation of the muscle. In accordance with this, the remaining cytoplasmic Ca^{2+} is removed. Most of the cytoplasmic Ca^{2+} (~70%) is recycled to the SR via the sarcoplasmic/endoplasmic reticulum Ca^{2+} ATPase (SERCA) located in the SR membrane under ATP consumption (Klabunde, 2012). Ca^{2+} uptake into the SR by SERCA is largely regulated by the transmembrane protein phospholamban (PLN). Unphosphorylated PLN binds SERCA and inhibits the Ca^{2+} reuptake. Upon phosphorylation of PLN the binding to SERCA becomes weakened and SERCA becomes more active (Bers and Borlaug, 2018). The remaining cytoplasmic Ca^{2+} is transported to the extracellular space via the Na^{+}/Ca^{2+} exchanger (NCX) or into the mitochondria via the mitochondrial Ca^{2+} uniporter (MCU) (Dedkova and Blatter, 2013). Hence, Ca^{2+} is a crucial second messenger for cardiac excitation-contraction coupling. Both, proper contraction, and relaxation are crucial for correct heart function.

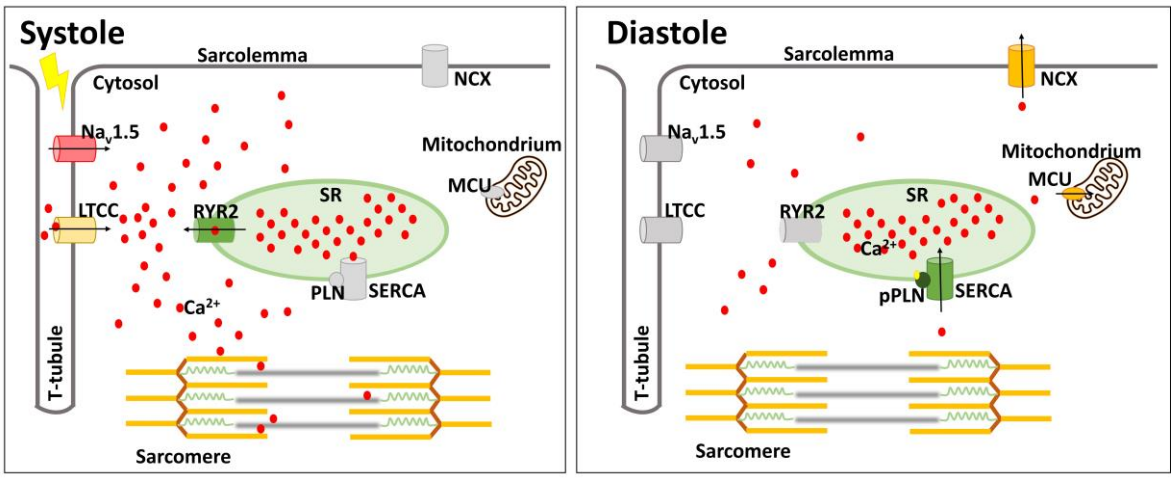

Fig. 2: Schematic overview of Ca^{2+} cycling during systole and diastole. Incoming action potential leads to opening of $Na_v1.5$, inducing membrane depolarization. Subsequently voltage-gated LTCC open. Initial Ca^{2+} influx opens Ca^{2+}-sensitive Ca^{2+} channels RYR2, triggering the release of Ca^{2+} from the SR, initiating cross-bridging cycle in the sarcomere, leading to cardiomyocyte contraction (systole). Relaxation is initiated by recycling of cytosolic Ca^{2+} via SERCA to the SR, NCX to the extracellular space and MCU to the mitochondria (diastole).

1.1.1.2 Cardiac fibroblasts

Amongst the non-myocyte cells of the heart, which make up ~70% of the total cell content (Banerjee *et al.*, 2006; Nag and Zak, 1979), recent studies identified cardiac fibroblasts (CFB) comprising ~20% (Pinto *et al.*, 2016). Although CFB seem to derive from several cellular lineages and the contribution of these lineages to the actual CFB population still needs to be elucidated in more detail, evidence is growing that, at least in the murine heart, the majority of resident CFB is arising from platelet-derived growth factor receptor alpha

(Pdgfrα)-positive and/or periostin (Postn)-positive epicardial-derived cells during heart development (Munoz-Chapuli *et al.,* 2001; Zhou *et al.*, 2010b). This is additionally supported by studies showing that the majority of resident fibroblasts in the murine heart derive from a transcription factor 21 (Tcf21) lineage (Pinto *et al.*, 2016). TCF21 has been shown to be crucial for CFB development from epicardial progenitors (Acharya *et al.*, 2012). Differentiation of CFB from epicardial-derived cells is mediated by epithelial-mesenchymal transition (EMT), which is stimulated by transforming growth factor beta (TGFβ) signaling (Olivey *et al.*, 2006; Smith *et al.*, 2011). In addition to epicardial-derived CFB, a smaller proportion of resident CFB was shown to develop from EC of the endocardium by a process called endothelial-mesenchymal transition (EndMT) (Ali *et al.*, 2014; de Lange *et al.*, 2004).

The main function of CFB in the healthy heart is the regulation of the ECM homeostasis. For this, on the one hand, CFB synthesize and secrete matrix proteins, like collagen or laminin, contributing to the production of ECM (Bosman and Stamenkovic, 2003; Souders *et al.,* 2009). On the other hand, CFB also promote ECM degradation e.g., by production of matrix metalloproteinases (MMP) (Lindner *et al.*, 2012; Souders *et al.*, 2009). Besides regulating ECM homeostasis, CFB do exert direct mechanical forces onto the ECM via interactions with integrins (Manso *et al.*, 2009). Integrins are transmembrane proteins, which serve as mechanical linkage between a cells´ cytoskeleton and the ECM, mediating so called focal adhesions (Ehrlich *et al.*, 2000; Schiro *et al.*, 1991). Hence, CFB have a direct effect on ECM compaction (Mayalu *et al.*, 2019). Moreover, direct interactions of CFB with cardiomyocytes via GJ are currently discussed (Johnson and Camelliti, 2018; Louault *et al.*, 2008). Upon cardiac injury or mechanical stress, activated fibroblasts and progressively myofibroblasts arise. Like resident fibroblasts, the exact origin of activated fibroblasts and myofibroblasts needs to be clarified. However, most activated fibroblasts and subsequent myofibroblasts derive by proliferation and activation from resident fibroblasts of epicardial origin, shown by an increase of $TCF21^{+}$/$POSTN^{+}$ cell populations upon myocardial injury (Kanisicak *et al.*, 2016; Zeisberg and Kalluri, 2010). Nonetheless, smaller proportions of activated fibroblasts/myofibroblasts also derive from secondary sources like EC (Widyantoro *et al.*, 2010), pericytes (Kramann *et al.,* 2015) or blood-born cells (Mollmann *et al.*, 2006). The reason and consequences for this is not unraveled yet. The activation of fibroblasts is a gradual process of transdifferentiation into different cell subtypes marked by rapidly changing marker expression (Stempien-Otero *et al.*, 2016). This starts with development into activated fibroblasts with a pro-inflammatory and pro-survival phenotype. Subsequently activated fibroblasts with a proliferative, pro-fibrotic and pro-angiogenic phenotype develop. Finally, CFB with an anti-angiogenic myofibroblast phenotype, marked by increasing alpha-smooth muscle actin (αSMA) expression arise (Bretherton *et al.*, 2020; Mouton *et al.*, 2019). Myofibroblasts are contractile and largely involved in ECM remodeling e.g., shown by increased expression of collagens (Kanisicak *et al.*, 2016; Tomasek *et al.*, 2002). Hence, activated fibroblasts and myofibroblasts actively drive progression of the fibrotic process.

As a result of diverse developmental origin of resident, activated and myofibroblasts and fast and dynamic changes between subtypes, clear identification of the different CFB subtypes remains difficult. Nevertheless, this clear identification would be important to

assess the disease state, progression, and prognosis. This is further complicated by the absence of unique markers for CFB. As for example, αSMA is expressed by embryonic fibroblasts and myofibroblasts, but also can be found in cardiomyocytes and VSMC (Eschenhagen, 2018; Zeisberg and Kalluri, 2010). Similarly, fibroblast-specific protein (FSP1) is reported as a specific marker for CFB, but is only expressed in certain CFB subpopulations (Ivey and Tallquist, 2016; Kong *et al.,* 2013; Tallquist and Molkentin, 2017). Likewise, connective tissue growth factor (CTGF) was considered to be a myofibroblasts-specific marker but is also expressed by injured cardiomyocytes (Krenning *et al.*, 2010; Souders *et al.*, 2009).

1.2 Cardiomyopathies

Cardiovascular diseases still are, despite rapid scientific and medical progress, a major threat to human health worldwide and account for one in four deaths (Benjamin *et al.*, 2017; Lozano *et al.*, 2012). Among these, cardiomyopathies are one of the leading causes of heart failure (Benjamin *et al.*, 2017; Maron *et al.*, 2006). Cardiomyopathies comprise diseases of the heart muscle or myocardium without coronary artery or valve diseases or hypertension, solely inducing structural and functional myocardial abnormalities (Elliott *et al.*, 2008). Cardiomyopathies are additionally characterized by being non-inflammatory, developing progressively and may worsen rapidly, thereby increasing the risk of arrhythmias and heart failure (Maron *et al.*, 2006). According to their functional and morphological phenotype, cardiomyopathies can be divided into DCM, hypertrophic cardiomyopathy (HCM), restrictive cardiomyopathy (RCM), arrhythmogenic cardiomyopathy (ACM) and unclassified cardiomyopathies. The latter include left ventricular non-compaction (LVNC) and takotsubo syndrome (TTS) cardiomyopathies (Elliott *et al.*, 2008).

1.2.1 Dilated cardiomyopathy

DCM is classified by dilation of the left ventricle and systolic (=contractile) dysfunction, not accompanied by hypertension or coronary artery or valve diseases (Elliott *et al.*, 2008; Weintraub *et al.,* 2017). DCM accounts for 50-60% of all cardiomyopathies and represents one of the most common causes of heart failure. Additionally, DCM is the most frequent reason for heart transplantation worldwide (Michels *et al.*, 1992; Regitz-Zagrosek *et al.*, 2010; Weintraub *et al.*, 2017). DCM occurs with a prevalence of 40 DCM cases per 100,000 individuals and affects patients of all age and gender. However, an onset is most common between 30-40 years and males are more often affected than females (Hershberger and Jordan, 1993; Michels *et al.*, 1992; Weintraub *et al.*, 2017).

1.2.1.1 Causes of DCM

Due to a broad spectrum of symptoms, partially overlapping with other disorders and asymptomatic presentation at early stages, DCM often is difficult to diagnose. DCM onset is linked to an initial event reducing cardiac contractility. This initial trigger, meaning the underlying cause of DCM, remains unknown in many patients, leading to the diagnosis of so-called idiopathic DCM. Although the exact underlying cause often is not identified, DCM

cases in general can be classified into two groups – familial/genetic caused or non-familial/non-genetic caused (Elliott *et al.*, 2008). Familial/genetic causes include DCM cases associated with a genetic mutation that occurs in more than two first-degree family members (Elliott *et al.*, 2008). However, sporadic DCM cases caused by genetic mutations which occurred *de novo,* but also could be transmitted to following generations, are also classified as familial cases (Elliott *et al.*, 2008). Up to 35% of all DCM cases are accounted as familial cases associated with specific gene mutations (Hershberger and Siegfried, 2011). Familial DCM cases are mainly monogenetic and autosomal dominant (Elliott *et al.*, 2008; Hershberger *et al.*, 2013). Non-familial/non-genetic cases of DCM are mainly acquired by secondary causes of non-genetic origin. These secondary causes include inflammation, infectious diseases, drug treatment, toxins, or autoimmune diseases (Elliott *et al.*, 2008; Schultheiss *et al.*, 2019).

1.2.1.1.1 DCM genetics

As described previously, up to 35% of all DCM cases have a family history and are associated with mutations in more than 50 gene loci (Maron *et al.*, 2006; Michels *et al.*, 1992; Rosenbaum *et al.*, 2020; Weintraub *et al.*, 2017). Additionally, it is hypothesized that a large proportion of idiopathic DCM cases is based on unknown genetic variants. The so far described genetic variants associated with DCM are mainly encoding for cytoskeleton, sarcomere, splicing factors, nuclear envelope and desmosome proteins (Dal Ferro *et al.*, 2019; Rosenbaum *et al.*, 2020). The most prominent gene associated with DCM is *TTN*, coding for the largest sarcomeric protein titin and accounting for 12-18% of familial DCM cases (Dal Ferro *et al.*, 2019). Mainly truncating titin variants lead to DCM development (Fomin *et al.*, 2021; Herman *et al.*, 2012). Titin-based DCM cases are characterized by ventricular arrhythmias, enhanced cardiac fibrosis, and a reduced cardiac mass (Verdonschot *et al.*, 2018). A significant proportion of genetic DCM cases is associated with variants in genes encoding for structural proteins, like the cytoskeleton or the Z-disc. Variants in these proteins (e.g. αMHC, βMHC, MYBPC3, titin) mainly affect cardiomyocyte structure, sarcomeric orientation and contraction (Dal Ferro *et al.*, 2019). They account for at least 10% of familial DCM cases. This number is currently increasing, especially due to high numbers of newly identified FLNC variants being associated with DCM (more detailed information see 1.3). Additionally, often variants in sarcomeric proteins with catalytic activity are associated with DCM (10% of familial DCM). This includes variants in αMHC (*MYH6),* βMHC *(MYH7),* MYBPC3*,* cTNT *(TNNT2)*, mainly affecting sarcomeric contraction, force generation and transmission (Dal Ferro *et al.*, 2019; Hershberger *et al.*, 2013). However, MYBPC3 variants being causative for DCM are highly discussed, as it seems more likely, that they rather induce HCM, which develop to a phenotype of dilated ventricle and systolic dysfunction, similar to DCM (Cahill *et al.*, 2013). Proteins of desmosomes, which connect myocardial cells and anchor the cytoskeleton to the cell surface, are associated with ~5% of familial DCM (Elliott *et al.*, 2010). Desmosome proteins harboring DCM causing variants are plakophilin-2 (PKP2), desmoplakin (DSP), desmocollin-2 (DSC2), desmoglein-2 (DSG2). DCM cases based on these variants often are characterized by ventricular arrhythmia and LV fibrosis (Dal Ferro *et al.*, 2019; Elliott *et al.*, 2010). Furthermore, variants in ion channel related genes, which usually are associated with channelopathies, also could

lead to structural defects, as shown for DCM. This includes truncating or missense variants in the voltage-sensitive domain of the voltage-gated sodium channel $Na_v1.5$ or $Na_v1.8$, encoded by *SCN5A* and *SCN10A,* respectively. *SCN5A*-caused DCM cases usually are associated with ventricular arrhythmias and conduction defects (Dal Ferro *et al.*, 2019; Sedaghat-Hamedani *et al.*, 2021). Similarly, SCN10A-associated DCM cases usually are associated with cardiac arrhythmias and sudden cardiac death (Gando *et al.*, 2019; Hayashi *et al.*, 2020; Jabbari *et al.*, 2015; Maltese *et al.*, 2019). Variants in ion channel genes associated with DCM also include variants in RYR2, leading to altered Ca^{2+} handling and impaired sarcomeric function (Dal Ferro *et al.*, 2019). However, RYR2-dependent DCM cases mostly are accompanied by a catecholaminergic polymorphic ventricular tachycardia (CPVT) phenotype (Marjamaa *et al.*, 2009). Genetic variants in LaminA/C (LMNA) localized in the nuclear envelope, account for 4-6% of familial DCM cases, and are characterized by ventricular arrhythmia (Taylor *et al.*, 2003). Additionally, variants in the RNA-binding motif protein 20 (RBM20), which regulates mRNA splicing of many sarcomeric proteins, accounts for 2-3% of familial DCM cases (Brauch *et al.*, 2009; Rebs, 2021). The above-mentioned affected genes causing DCM only are representative examples of all genes associated with DCM. Nevertheless, it shows that a diverse set of genes, located in different subcellular compartments and involved in different cellular pathways and functions, are capable of causing the same cardiac disease phenotype, DCM (summarized in Fig. 3 A). However, it needs to be mentioned, that variants in these genes are not only associated with DCM, but often are also causative for other cardiomyopathies, like HCM, ACM (summarized in Fig. 3 B). Hence, genetic screenings and clinical diagnostic always need to be combined for most efficient diagnosis and treatment. Yet, since genetic causes account for a large amount of DCM cases and especially because early stages often are displayed asymptomatic, genetic screening for pathogenic variants in patients and close relatives could improve individual prognosis and therapy and might reduce the high amount of heart failure and sudden cardiac death. However, this genetic screening faces several difficulties. First, different DCM cases are caused by variants in more than 50 genes and a plethora of different variants within these loci account for DCM phenotypes. Secondly, many of these variants are particular rare or even only occur in individual families or patients. *De novo* occurrence of so far unknow mutations might be possible as well. Hence, only screening for known variants with high population frequency often is not sufficient to identify causative variants. Whole exome/genome sequencing on a patient-specific basis would be most valid, however time and resource consumable. Additionally, validation of pathogenicity of certain variants remains challenging (Cahill *et al.*, 2013).

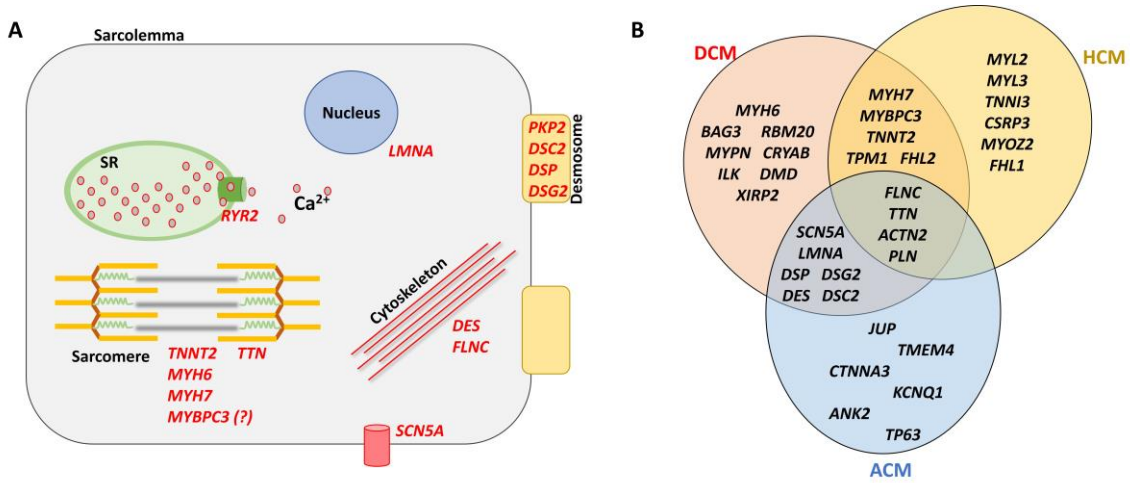

Fig. 3: Schematic and exemplary overview of cardiomyopathy causing gene variants. **A** A diverse set of genes displays variants associated with a DCM phenotype. These genes are often functionally distinct, still result in an indistinguishable phenotype. This includes sarcomeric/contractile genes, like *TTN, TNNT2, MYH6, MYH7*, *MYBPC3*; cytoskeletal genes, like *DES* and *FLNC*; ion channel genes, like *RYR2* and *SCN5A*; genes coding for proteins localized to the nuclear envelope, like *LMNA*; and genes coding for the desmosomes, like *PKP2, DSC2, DSP* and *DSG2*. DCM associated genes are highlighted in red. **B** Genes that are associated with genetic DCM, HCM and ACM. Genes affected in different cardiomyopathies are summarized from (Brodehl *et al.*, 2019a; Grassi *et al.*, 2021)

1.2.1.2 Pathophysiology of DCM

Regardless of the exact underlying cause leading to reduced cardiac contractility, early compensatory mechanisms are initiated including increase in stroke volume and heart rate to maintain the cardiac output. However, with progressing time, these mechanisms are not sufficient and result in elevated end-systolic (afterload) and end-diastolic (preload) volumes. As a consequence, wall stress of the left ventricular wall is increasing (De Paris *et al.,* 2019; Weintraub *et al.*, 2017). With disease progression myocardial stress is increasing further, subsequently damaging the cardiomyocytes and inducing production of reactive oxygen species (ROS), like hydrogen peroxide (H_2O_2) or superoxide (O_2^-) further impairing myocyte function and promoting apoptosis (D'Oria *et al.*, 2020; Mitropoulou *et al.*, 2020). Consequently, a huge myocardial remodeling is initiated involving several cell types, such as cardiomyocytes and CFB. Because of remodeling processes, the number of cardiomyocytes diminishes due to apoptotic processes and the remaining cardiomyocytes undergo phenotypic changes towards eccentric myocyte hypertrophy to compensate for the cardiomyocyte loss (Hong *et al.,* 2000; Kajstura *et al.*, 1995; Olivetti *et al.,* 1997). Subsequently, the left ventricle becomes dilated and thin-walled and the contractile force is decreased dramatically. Together, this myocardial remodeling progressively leads to a decrease in ejection fraction (EF) and severe systolic dysfunction (De Paris *et al.*, 2019). Eventually end-stage DCM can be reached, classified by symptoms of end-stage heart failure, including chest pain, fatigue and fainting, which could result in heart failure, arrhythmia or sudden cardiac death (Seferovic *et al.*, 2019).

1.2.1.2.1 Fibrosis as a hallmark of DCM

In addition to cardiomyocyte remodeling, CFB are important players during myocardial remodeling. Due to increasing myocardial stress (oxidative and mechanical) and paracrine

signals secreted from the cardiomyocytes to the CFB, myofibroblast transdifferentiation and activation is increased (Eijgenraam *et al.*, 2020). Although not fully understood, it is thought that mechanically stressed cardiomyocytes release angiotensin II (AngII) which acts as a paracrine factor on CFB and induces canonical and non-canonical TGFβ signaling, activating myofibroblast transdifferentiation and activation (Bouzegrhane and Thibault, 2002; Eijgenraam *et al.*, 2020; Rosenkranz, 2004). Activated myofibroblast induce excessively increased collagen secretion leading to fibrosis (Mihl *et al.*, 2008). Myocardial fibrosis can account for up to 36% of the total LV mass (Eijgenraam *et al.*, 2020). Initially, fibrosis will compensate for cardiomyocyte loss to myocardial integrity and structure. However, in heart failure conditions, like in end-stage DCM the fibrotic response is not downregulated anymore (Piek *et al.*, 2016). Consequently, sustained increasing fibrosis occur, the myocardium becomes stiffer, and the ventricular compliance is reduced. Additionally, not only by increasing mechanical stress based on stiffening of the myocardium but also by active secretion of paracrine factors secreted by CFB, cardiomyocyte hypertrophy and cell death are enhanced, further worsening the overall myocardial function (Eijgenraam *et al.*, 2020; Mihl *et al.*, 2008; Piek *et al.*, 2016). Presence and severity of fibrosis has consequences on the prognosis of cardiomyopathy progression, as fibrosis is associated with higher risks to develop arrhythmia, atrial fibrillation or even experience sudden cardiac death (Eijgenraam *et al.*, 2020).

1.2.1.2.2 Oxidative stress as a hallmark of DCM

ROS display a group of oxygen containing, highly reactive chemical species. This includes O_2^-, OH^- and H_2O_2. Low levels of ROS occur under physiological conditions and have important roles to maintain different levels of cell homeostasis (D'Oria *et al.*, 2020; Munzel *et al.*, 2015). This includes functions in excitation-contraction coupling, since they modify important Ca^{2+} handling proteins, like Ca^{2+}/calmodulin-dependent protein kinase II (CaMKII), SERCA, RYR2, and PLN (Burgoyne *et al.*, 2012). Additionally, physiological ROS also is important in cardiomyocyte differentiation and proliferation processes (Buggisch *et al.,* 2007; Hom *et al.*, 2011). However, upon myocardial stress, based on cardiac remodeling and contractile dysfunction, dysregulation of the balance of ROS production and removal can occur, leading to high levels of ROS, which is called oxidative stress (D'Oria *et al.*, 2020; Munzel *et al.*, 2015; Sam *et al.*, 2005). The resulting dysregulation of otherwise physiological important redox signaling might result in cellular and overall myocardial dysfunction. Processes like dysregulated protein oxidation, lipid peroxidation, gene expression and DNA damage will impair several cardiac functions. This includes contractile dysfunction by impaired Ca^{2+} handling for example, and cardiomyocyte death by inducing apoptosis, arrhythmia and ventricular dilation (Burgoyne *et al.*, 2012; Sabri *et al.*, 2003; Wencker *et al.*, 2003).

1.2.1.2.3 Telomere shortening as a hallmark of DCM

During the past years, an unconventional idea was rising in the field of cardiomyopathy research: Is telomere shortening a hallmark of genetically induced cardiomyopathy? Telomeres are short DNA repeats at the end of each chromosome protecting the genomic DNA. The telomeric repeats get shortened with each cell division, which is an important

marker for cell senescence (Okamoto and Seimiya, 2019; Saliques *et al.*, 2010). Dysregulation of naturally occurring telomere shortening is associated with oncogenic pathophysiological mechanisms, where telomeres do not shorten by cell division, due to an enhanced telomerase activity maintaining telomere length (Okamoto and Seimiya, 2019). In contrast to this, recent studies revealed shortened telomeres in age-related, diseased cardiac tissue (Saliques *et al.*, 2010). That aging seems to be a major risk factor for cardiovascular diseases is known for a long time (Saliques *et al.*, 2010). However, since cardiomyocytes are largely non-proliferative, the telomere shortening is unlikely caused only by recurred cell divisions simply based on the patient`s age (Saliques *et al.*, 2010). Nevertheless, a telomere shortening of roughly 20bp per year was reported for human cardiomyocytes, and hence might also drive the development of age-dependent forms of cardiomyopathies (Chang *et al.*, 2016; Saliques *et al.*, 2010). Subsequent studies identified cardiomyocyte-specific telomere shortening also in young patients with Duchenne Muscular Dystrophy (DMD), that was absent in equally affected vascular smooth muscle cells of the same patients (Chang *et al.*, 2016). More recent studies reported cardiomyocyte-specific telomere shortening in patients with genetically inherited, isolated, end-stage HCM and DCM associated with mutations in proteins important for contractile function (Chang and Blau, 2018; Chang *et al.*, 2018). The same group now hypothesizes a link of cardiomyocyte-specific telomere shortening in DMD patients with classical molecular symptoms of DCM. They postulate that cardiomyocyte-specific telomere shortening is contraction-dependent and mechanosensitive (Chang *et al.*, 2021).

1.3 Filamin C

The actin cytoskeleton is essential for several cellular functions. This includes maintenance of cell shape, adhesion, or signal transduction. Actin is indispensable for formation of the sarcomere in cardiomyocytes, and hence influences contraction properties. To fulfill all these important functions actin needs to be organized into functional bundles and networks. This is mediated by dynamic cross-linking via specialized actin cross-linkers, like spectrin, fimbrin, α-actinin and filamins (Popowicz *et al.*, 2006; Zhou *et al.*, 2010a). In addition to form parallel actin bundles, filamins are capable of forming orthogonal actin networks (Popowicz *et al.*, 2006). The filamin family contains three isoforms (A, B, C), which are all encoded by separate genes (*FLNA, FLNB*, and *FLNC*) and on different chromosomes – X-chromosome, chromosome 3 and chromosome 7, respectively (Himmel *et al.*, 2003; Stossel *et al.*, 2001). All three family members are highly homologous and show 70% sequence similarity (van der Flier and Sonnenberg, 2001). *FLNA* and *FLNB* are reported to be expressed ubiquitously, whereas expression of *FLNC* seems to be restricted to striated skeletal and cardiac muscle (van der Flier and Sonnenberg, 2001). Filamins form homodimers and in addition to their main function of crosslinking actin they act as multi-adaptor proteins e.g., anchoring transmembrane proteins to the cytoskeleton or serving as scaffold for signaling proteins (van der Flier and Sonnenberg, 2001; Zhou *et al.*, 2010a).

1.3.1 Structure and function of FLNC

Human *FLNC* is encoded on chromosome 7q32.1, contains 48 coding exons and is translated to the high molecular mass (~290kDa) protein FLNC. Similar to the two family members FLNA and FLNB, FLNC has a conserved actin-binding domain (ABD, Fig. 4), comprising two N-terminal calponin-homology domains (CH1 and CH2, Fig. 4), which are found in other actin cross-linking proteins as well, and are necessary to cross-link actin filaments (Mao and Nakamura, 2020; van der Flier and Sonnenberg, 2001). The ABD is followed by two ROD domains (ROD1 and ROD2, Fig. 4) containing 24 highly homologous repeats, each of ~96aa in an immunoglobulin-like fold. The two ROD domains are divided by a hinge region (H1) between repeat 15 and 16 (Fig. 4). This hinge region, however, is spliced out during myogenesis in the mostly expressed splice variant of FLNC (Mao and Nakamura, 2020). A second hinge region (H2) is located between repeat 23 and 24, separating the most C-terminal repeat, which serves as the dimerization domain of FLNC to form homodimers important for FLNC function (Mao and Nakamura, 2020). Notably, FLNC contains a unique, intrinsically disordered 82aa insertion in domain 20, which is absent in otherwise highly homologous family members FLNA and FLNB and was reported to be sufficient for targeting FLNC to the sarcomeric Z-disc (Mao and Nakamura, 2020). This 82aa insertion is 100% conserved in mammals and even highly conserved among all vertebrates, highlighting its importance in FLNC structure (Fig. 4).

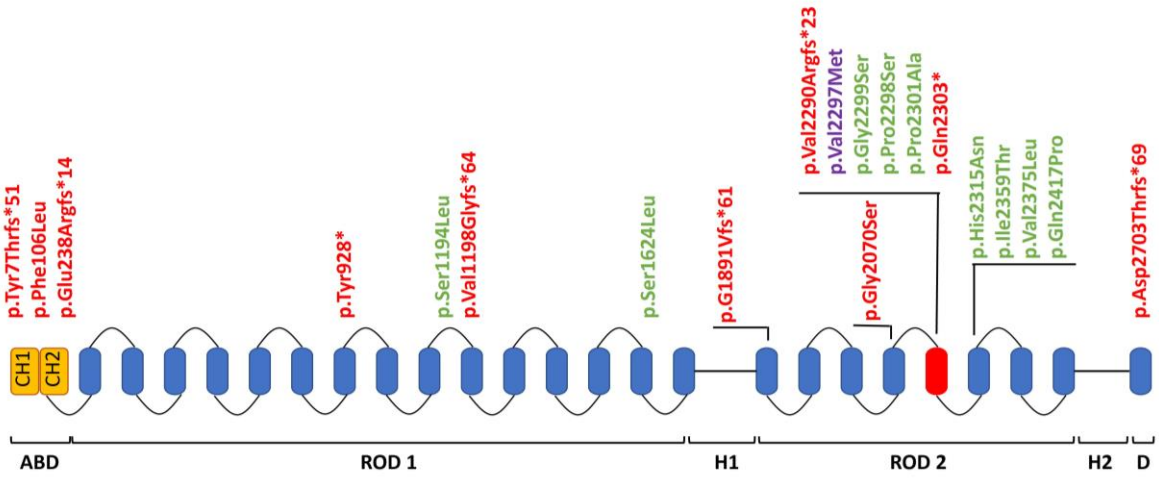

Fig. 4: Structure of FLNC protein and identified pathogenic variants in FLNC. The N-terminal ABD consists of two CH domains, which mediate actin binding. The ABD is followed by 24 immunoglobulin-like repeats. The first rod (ROD1) spans from repeat 1-15 and is separated from the second rod (ROD2) by a hinge (H1) domain. The last, 24th repeat is separated by a second hinge domain (H2) and functions as a dimerization domain to form FLNC homodimers, important for crosslinking function. Domain 20 (red) harbors a unique 82 amino acid insertion, not found in highly homologous family members – FLNA and FLNB. A small collection of pathogenic variants and their location within the protein are shown for DCM (red), HCM (green) and Arrhythmogenic right ventricular cardiomyopathy (ARVC, purple).

Within cardiomyocytes FLNC is located at the Z-disc, the ICD and to lesser extend to the sarcolemma (Mao and Nakamura, 2020). Its main function is the cross-linking of sarcomeric actin, and hence it is necessary for muscle differentiation and maintenance of elongated myofibrils (Popowicz *et al.*, 2006; van der Flier and Sonnenberg, 2001; Zhou *et al.*, 2010a). Additionally, FLNC acts as a multi-adaptor protein interacting with a plethora of proteins,

like receptors, transmembrane proteins, signaling molecules, and ion channels (Fig. 5). Hence, FLNC is integrated into a complex interaction network important for cardiomyocyte structure and function. In more detail, FLNC interacts with several Z-disc proteins, like aciculin (Molt *et al.*, 2014), myopodin (Linnemann *et al.,* 2010), myotilin (van der Ven *et al.*, 2000), xin (van der Ven *et al.,* 2006), and myozenin (Gontier *et al.*, 2005), supporting proper sarcomere assembly and stability (Fig. 5). Furthermore, FLNC interacts with γ-/δ-sarcoglycans and β1-integrin at the sarcolemma (Gontier *et al.*, 2005; Loo *et al.*, 1998; Thompson *et al.*, 2000) (Fig. 5). These interactions link the cytoskeleton to the ECM and stabilize the sarcolemma. Hence, it enables force and signaling transduction from the myofibrils to the ECM and neighboring cells, like cardiomyocytes and CFB. Several of the above-mentioned interactions are mediated by interaction with the 82aa insertion in domain 20, including myotilin, myopodin, aciculin, xin and β1-integrin (Loo *et al.*, 1998; Thompson *et al.*, 2000) (Fig. 5). Uniqueness, high conservation between species, indispensability for Z-disc targeting and importance for interaction with several proteins forming highly complex structural and functional networks, highlight the important role of this 82aa insertion of FLNC domain 20.

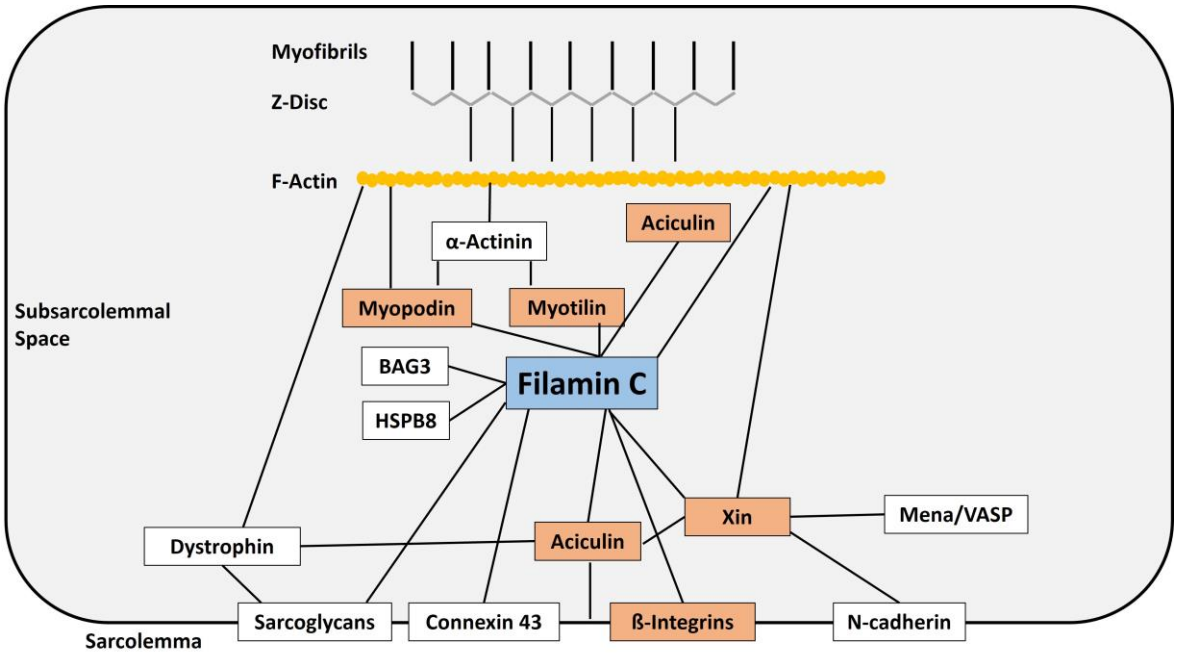

Fig. 5: Schematic overview of FLNC interaction network within cardiomyocytes. Shown are direct and indirect interactions of FLNC to an exemplarily chosen set of interaction partners. This highlights its role as multi-adaptor protein, important for sarcomere assembly and stability, ECM interaction as well as force and signaling transduction. Interaction partners highlighted in orange depend on the 82aa insertion in FLNC domain 20 for proper interaction.

1.3.2 FLNC variants and cardiomyopathies

FLNC variants have already been associated with skeletal myopathies for some time (Ader *et al.*, 2019; Furst *et al.,* 2013; Mao and Nakamura, 2020). These were mainly missense variants located in the ABD or dimerization domain of FLNC, leading to generation of large insoluble FLNC aggregates in the cytoplasm (Furst *et al.*, 2013; Leber *et al.*, 2016). Recent studies also identified *FLNC* variants linked to isolated cardiac phenotypes, like HCM (Valdes-Mas *et al.,* 2014), ARVC (Brodehl *et al.*, 2016), DCM (Begay *et al.*, 2016) and LVNC

(Ader *et al.*, 2019; Miszalski-Jamka *et al.*, 2017). *FLNC* variants associated with cardiomyopathies occur with a prevalence of 3-4% in DCM, 1-8% in HCM, 2-8% in ARVC and 1% in LVNC and hence are among the more prevalent causes for genetic cardiomyopathies (Ader *et al.*, 2019; Ortiz-Genga *et al.*, 2016). Furthermore, FLNC-dependent cardiomyopathies are classified as being more malignant than many other genetic-based cardiomyopathies and are associated with higher risks for arrhythmias and sudden cardiac death (Begay *et al.*, 2016; Eden and Frey, 2021; Ortiz-Genga *et al.*, 2016; Verdonschot *et al.,* 2020). FLNC-dependent cardiomyopathies often are characterized by a Z-disc disarray, and impaired mechanotransduction (Verdonschot *et al.*, 2020).

In more detail, isolated cardiomyopathy-associated FLNC variants can be largely clustered into two, most frequently identified groups – truncating variants and missense variants. Interestingly, truncating variants cluster all over the FLNC protein (Fig. 4) and hence can be found in the ABD (p.Tyr7Thrfs*51), the ROD1 domain (p.Tyr928*), the ROD2 domain (p.Gln2303*), as well as the dimerization domain (p.Asp2703Thrfs*61) (Ader *et al.*, 2019). This suggests, that for truncating variants the location only has limited impact on disease. This is largely explained as FLNC truncating variants were shown to induce non-sense mediated decay (NMD) of the FLNC mRNA leading to haploinsufficiency (Ader *et al.*, 2019; Eden and Frey, 2021; Verdonschot *et al.*, 2020). Based on haploinsufficiency, amount of normal FLNC protein is less, leading to a Z-disc disarray and weakened binding of the Z-disc to the membrane as well as impaired cell-cell adhesion. Consequently, truncating variants result in an impaired mechanotransduction. Hence, these patients often are susceptible to develop arrhythmia and fibrosis (Ader *et al.*, 2019; Eden and Frey, 2021; Verdonschot *et al.*, 2020). Missense variants in contrast, rather cluster to the ROD2 domain (Fig. 4), which is highly important for targeting FLNC to the Z-disc and is required for interaction with many, especially Z-disc proteins (Ader *et al.*, 2019; Eden and Frey, 2021). This for example includes variants found in Ig-domain 20 (p.Pro2298Ser, p.Pro2301Ala) (Gomez *et al.*, 2017) or Ig-domain 21 (p.His2315Asn, p.Val2375Leu) (Ader *et al.*, 2019; Valdes-Mas *et al.*, 2014). Such missense variants often lead to changes in secondary protein structure or impair the binding to important interaction partners. As a result of these missense variants, often insoluble cytoplasmic protein aggregates are formed based on the abnormal FLNC protein composition. Additionally, missense variants are often associated with sarcomeric abnormalities, as abnormal FLNC protein might not be directed to Z-disc or interactions to the FLNC protein are impaired. Both would have consequences on muscle maintenance and mechanosensing (Verdonschot *et al.*, 2020). In addition to a classification of FLNC variants as truncating or missense variants, the resulting cardiomyopathy subtype can be grouped accordingly. FLNC-related HCM is mainly associated with missense mutations and consequently usually displays cytoplasmic FLNC aggregate formation as described before (Ader *et al.*, 2019; Eden and Frey, 2021; Valdes-Mas *et al.*, 2014). In contrast to this, FLNC-related DCM predominantly is associated with truncating mutations, more often displaying arrhythmia and fibrosis (Ader *et al.*, 2019; Eden and Frey, 2021). These DCM cases, associated with truncating FLNC variants, generally display a more severe phenotype and worse prognosis with significant LV dilation and systolic dysfunction, but also with high levels of myocardial fibrosis and conduction abnormalities (Begay *et al.*, 2016; Eden and Frey, 2021; Ortiz-Genga *et al.*, 2016). A truncating variant (p.G1891Vfs*61) for example was

associated with a familial DCM case (Begay *et al.*, 2018). These patients had a severe LV dysfunction and arrhythmogenic phenotype, as well as increased fibrosis. A degeneration of cardiomyocytes within this tissue could be identified, and remaining cardiomyocytes displayed hypertrophy. Although the sarcomeric structure was not affected, the Z-disc appeared less clear structured, but thicker (Begay *et al.*, 2018). Although FLNC missense variants are largely found in HCM, and truncating FLNC variants are enriched in DCM, there are also two DCM cases reported being associated with FLNC missense variants. For example, a FLNC missense variant (p.Phe106Leu) was identified in addition to a truncating FLNC variant on the second allele, leading to compound heterozygosity with a very early onset of DCM (Reinstein *et al.*, 2016). An additional FLNC missense variant (p.Gly2070Ser) was shown to be associated with DCM (Ortiz-Genga *et al.*, 2016), resulting in an altered splice site and a lower amount of FLNC protein, similar as described for truncating FLNC variants.

Since identifying FLNC variants being causative for several isolated cardiomyopathy phenotypes and its inclusion into standard screening panels in 2014, the number of identified pathogenic FLNC variants is dramatically increasing. However, most variants are only identified and classified as pathogenic by bioinformatic pipelines in combination with clinical diagnostic. Hence, the underlying molecular mechanisms by which individual FLNC variants affect the cardiomyopathy phenotype are mostly unknown. Only larger concepts, as described above, are known for general effects of truncating or missense variants. Hence, regarding the high prevalence and severity described, more detailed analysis of these mechanism specific for certain variants would have huge impact on disease treatment and prognosis.

1.4 Stem cells

Stem cells (SC) display a special type of cells important for the development and maintenance of whole organisms, since they are characterized by the ability of unlimited self-renewal and the capacity to differentiate into other cell types (Hall and Watt, 1989). Based on their differentiation potential SC can be grouped into toti-, pluri-, multi-, and unipotent SC (Jaenisch and Young, 2008). Totipotent SC have the unique ability to form a whole organism as they can differentiate into any cell type including extraembryonic placental cells and can only be found in very early zygote and 8-cell morula stages (Kelly, 1977; Worku, 2021). Pluripotent SC, also called embryonic stem cells (ESC), are found in the inner cell mass of the blastocyst. They can differentiate into all cells of all three germ layers (endoderm, mesoderm, and ectoderm), as well as into all germline cells. However, they cannot form a whole organism because they cannot differentiate into cells of the extraembryonic placental tissue (Jaenisch and Young, 2008; Worku, 2021). Multi- and unipotent SC are found in the adult organism and are important for tissue repair after injury and to maintain tissue homeostasis. Multipotent SC can only differentiate into several cell types of a specific cell lineage and not into cells of all three germ layers. A classic example for multipotent SC are hematopoietic cells, which give rise to different blood cells (Ogawa, 1993). Unipotent SC have the smallest differentiation potential and can give rise to only

one cell type, like spermatogonial SC differentiating only into sperm cells (Phillips *et al.*, 2010).

1.4.1 Human induced pluripotent stem cells

The extraordinary developmental potential of pluripotent stem cells (PSC) made them an interesting platform for medical research on cell-based therapy and tissue engineering. Hence, major effort was done to make these cells available and eventually the ability of isolation of ESC from murine (Evans and Kaufman, 1981) and human (Thomson *et al.*, 1998) blastocysts marked a tremendous breakthrough. Both, murine and humane ESC showed differentiation potential in cells of all three germ layers (Nagy *et al.*, 1990) and showed unlimited self-renewal *in vitro*. Additionally, expression of classical pluripotency genes, like Octamer binding transcription factor 4 (*OCT4)*, SRY: Sex-determining region of Y-box 2 (*SOX2*), and *NANOG* and expression of alkaline phosphatase (ALP) was reported (Hanna *et al.,* 2010). After obtaining ESC from the murine and human blastocyst, several other approaches were established to generate PSC from different tissue. This includes embryonic germ cells (EGC) from primordial germ cells (Matsui *et al.,* 1992) or multipotent germline stem cells (mGSC) from adult mouse spermatogonial cells (Guan *et al.*, 2006). Although the aforementioned approaches of generation/isolation of PSC hold many opportunities for medical research and translational application, the use of human ESC raises huge ethical issues as it is dependent on the terminal use of early embryos. On the other hand, usage of animal models is limited in the use for translational medicine, based on species differences. Alternative use of adult stem cells (e.g., multipotent SC) would imply a minor differentiation potential compared to PSC and additionally their use in cell-based therapy might be limited due to rejection reactions. In 2006 the first paper of the generation of induced pluripotent stem cells (iPSC) was published by Yamanaka and Takahashi (Takahashi and Yamanaka, 2006). For the first time they could reprogram terminally differentiated, somatic mouse fibroblasts into PSC (Takahashi and Yamanaka, 2006). One year later, they already could transfer the system to the human model (Takahashi *et al.*, 2007). Like ESC, iPSC show comparable self-renewal and differentiation capacity and expression of classical pluripotency markers. These findings paved the way for patient-specific translational medical research and therapy, without the need for highly discussed embryo-derived ESC.

1.4.1.1 Reprogramming into iPSC

In general, reprogramming into iPSC is based on the activation of expression of certain genes in somatic cells to re-induce a pluripotent state. Yamanaka and Takahashi identified a minimal set of necessary genes by testing a diversity of 24 pluripotency-associated genes from which they eliminated one factor after another, testing if reprogramming was still possible. With this approach they defined a set of only four factors – Oct4, Sox2, V-myc myelocytomatosis viral oncogene homolog (c-Myc) and krüppel-like factor 4 (Klf4) – being sufficient to reprogram murine fibroblasts (Takahashi and Yamanaka, 2006). These four factors were also sufficient to reprogram human fibroblasts and were termed OKSM or Yamanaka factors (Takahashi *et al.*, 2007). Simultaneously, another group demonstrated reprogramming of human mesenchymal cells by transduction of OCT4, SOX2, NANOG and

cell lineage abnormal 28 (LIN28) *(Yu et al., 2007)*. However, only Yamanaka was awarded the Nobel prize for his work in 2012. Conclusively, both studies showed that OCT4 and SOX2 were indispensable for the reprograming process. However, recent studies suggest, that OCT4 is not needed for reprogramming of somatic cells (Velychko *et al.*, 2019). Hence, the role and necessity of OCT4 during the reprograming process remains debatable. Finally in 2008, reprogramming of fibroblasts obtained from patient material by skin biopsy using the Yamanaka factors was shown for the first time (Park *et al.*, 2008). However, the exact molecular mechanisms underlying the reprograming process are not fully elucidated yet. Nevertheless, reprogramming is known to be a multi-step process. In the early phases of reprogramming, cell cycle genes, as well as metabolic regulators are upregulated, which results in increased proliferation (Adachi and Scholer, 2012). This process is largely mediated by MYC binding to genes with histone H3 lysine 4 trimethylation (H3K3me3)-modified promoters (Adachi and Scholer, 2012). Additionally, expression of somatic genes is repressed by cooperative binding of several transcription factors. Moreover, cooperative binding of Yamanaka factors also activates expression of further endogenous pluripotency genes. However, especially binding of OCT4 plays a crucial role. It is involved in establishing required chromatin states at respective enhancer/promoter regions. Additionally, this OCT4 binding is reported to recruit further factors, like SOX2 and KLF4 to the enhancer regions of pluripotency genes (Adachi and Scholer, 2012). Together, suppression of somatic genes and activation of pluripotency genes will promote mesenchymal-to-epithelial transition, when reprogramming fibroblasts for example (Adachi and Scholer, 2012; Samavarchi-Tehrani *et al.,* 2010). Furthermore, this induces changes from oxidative phosphorylation-based metabolism towards a glycolysis-based metabolism (Zhang *et al.*, 2012). Subsequently, Yamanaka factors also induce the expression of further endogenous pluripotency-related genes (Takahashi and Yamanaka, 2016). Notably, during the reprograming process, ectopic expression of Yamanaka factors will also induce their own endogenous expression in a positive feedback loop (Takahashi and Yamanaka, 2016). Hence, once the cells are reprogrammed, they are no longer dependent on functional expression of externally introduced factors. Consequently, in late phases of reprogramming the initiated upregulation of the cell cycle and the metabolism, the repression of somatic genes, and parallel activation of expression of pluripotency genes is maintained by expression of endogenous transcription factors and pluripotency regulators (Adachi and Scholer, 2012). Additionally, it was shown, that introduction of the Yamanaka factors in certain stoichiometry ratio and not in equimolar amounts was increasing reprogramming efficiency (Tiemann *et al.*, 2011).

In early reprogramming approaches lentiviral or retroviral transduction was used to stably integrate the reprogramming factors into the genome of somatic cells. However, integration into the genome occurs randomly and thus holds the risk of insertional mutagenesis affecting expression and function of random genes. To circumvent this risk several integration-free reprogramming approaches were established. This includes viral transduction of adenovirus (Zhou and Freed, 2009) or Sendai virus (Fusaki *et al.*, 2009), which do not integrate into the genome and the expression of reprogramming factors is only transiently. Additionally, non-viral integration-free methods have been described based on transfection of DNA plasmids (Okita *et al.*, 2008), mRNA (Warren *et al.,* 2010) or

proteins (Kim *et al.,* 2009). With progress in more efficient and safe delivery methods for reprogramming, also further research enabled reprogramming of other somatic cells than fibroblasts. Hence, reprogramming of keratinocytes, bone marrow-derived mesenchymal cells and blood cells was reported until now (Staerk *et al.*, 2010; Streckfuss-Bomeke *et al.*, 2013).

With increasing knowledge on iPSC their long-term culture conditions did improve as well. Where iPSC primarily were cultured in serum-harboring media on feeder layer cells, like mitotically inactivated mouse embryonic fibroblasts (MEF) (Yu *et al.*, 2007), iPSC culture was developing towards animal-free conditions. This was important, since animal-based products are largely varying between batches, which affects iPSC culture consistency (Chen *et al.*, 2011). Furthermore, animal-free culture conditions made iPSC cell culture more translatable for clinical applications. Now, highly chemically defined, animal-free media are used, and iPSC are cultured on recombinant matrix variants, like Geltrex or Matrigel instead of MEF.

1.4.1.2 Cardiac differentiation and maturation of iPSC-cardiomyocytes

Cardiac diseases are a major threat to human health worldwide. The exact underlying causes of most diseases remain unknown. Especially, due to the high prevalence and severe outcome of DCM, it is highly important to unravel the exact underlying molecular mechanisms which contribute to DCM development. Such experiments ideally would require patient-derived cardiomyocytes. However, adult cardiomyocytes are characterized by very low proliferation potential and thus, culturing and expanding those cells in the laboratory remains difficult (Yutzey, 2017). PSC therefore represent an interesting alternative as they can be differentiated to cardiomyocytes *in vitro*, avoiding the obstacles faced by patient-derived cardiomyocytes mentioned earlier (Batalov and Feinberg, 2015; Burridge and Zambidis, 2013). Besides ethical issues, ESC-derived cardiomyocytes usually do not represent a diseased phenotype and hence are not suitable to analyze the actual underlying cause of a certain disease. In contrast to this, the model of iPSC can use patient-derived somatic cells, like fibroblasts, directly and reprogram them to PSC, which can be differentiated to cells of all three germ layers afterwards, including cardiomyocytes. Hence, iPSC-derived cardiomyocytes serve as a suitable model to study human cardiac diseases in a patient-specific context, making it the most translatable model.

However, iPSC differentiation into cardiomyocytes is a highly complex process and hence, several approaches were established to enhance specificity and efficiency of differentiating iPSC to iPSC-cardiomyocytes. In first approaches, iPSC-cardiomyocytes were generated by embryoid body (EB) formation. For this, iPSC were cultured in suspension, where they form 3D non-adherend aggregates – the EBs. Within the EBs the iPSC spontaneously differentiate, developing into cells of all three germ layers (Mummery *et al.,* 2012). However, the overall yield of iPSC-cardiomyocytes within this spontaneous differentiation process was very low and not consistent. To make iPSC-cardiomyocytes differentiation more efficient and reproducible and to yield higher purity, direct differentiation approaches were developed by modulation of signaling pathways recapitulating *in vivo* cardiogenesis.

In vivo cardiogenesis (Fig. 6) is initiated in early embryogenesis during gastrulation. First a mesodermal cell fate is induced in the posterior epiblast via the activation of Wnt-signaling by nodal/bone morphogenic protein 4 (BMP4) (Burridge *et al.,* 2012). The mesodermal fate can be identified by presence of brachyury^{+} cells. Subsequently, cardiac mesodermal cells are induced by inhibition of canonical Wnt signaling and can be identified by mesoderm posterior1 (MESP1) expression (Burridge *et al.*, 2012). These cells further differentiate into cardiac progenitor cells via inhibitory effect of BMP and the canonical Wnt pathway which promotes the cardiac phenotype. The inhibited notch signaling, and the activated fibroblast growth factor (FGF) are the main drivers of the development into (immature) cardiomyocytes.

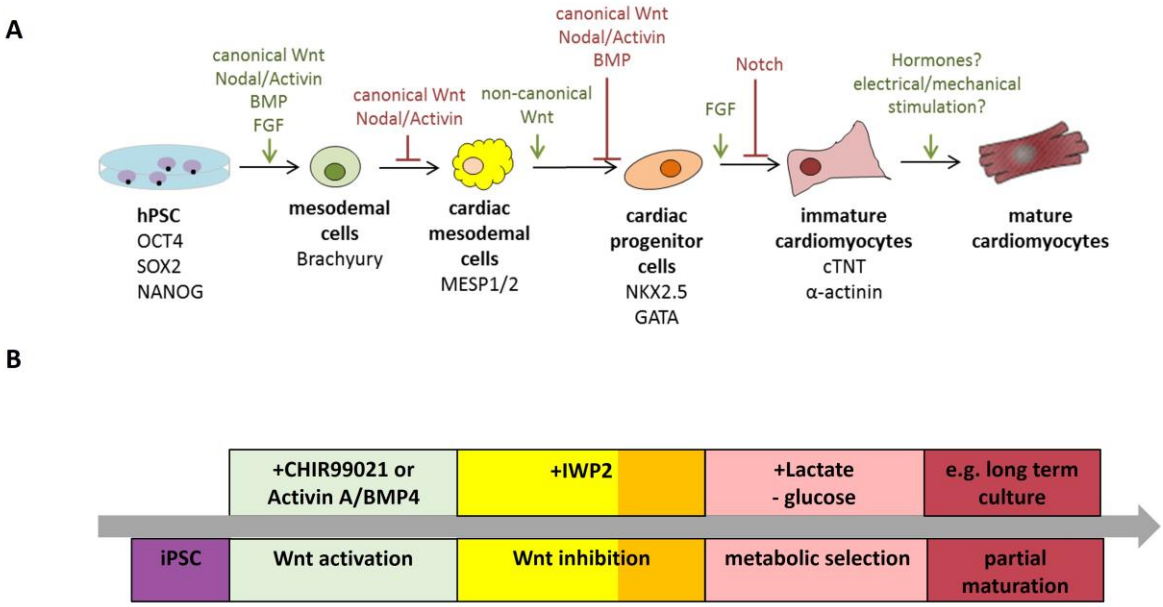

Fig. 6: Schematic overview of *in vivo* and *in vitro* cardiomyocyte differentiation. **A** Schematic overview of *in vivo* cardiogenesis. Activation of Wnt and BMP signaling induced differentiation towards brachyury^{+} mesodermal cells. Upon subsequent inhibition of Wnt signaling a cardiac fate is induced. Immature cardiomyocytes arise during the chamber morphogenesis which undergo several processes to finally result in mature cardiomyocytes. **B** Schematic overview of *in vitro* differentiation of iPSC into iPSC-cardiomyocytes by manipulation of Wnt signaling. Cardiomyocytes are metabolically selected after differentiation and are matured by prolonged culture.

Consequently, in order to translate the *in vivo* cardiogenesis into *in vitro* directed iPSC-cardiomyocytes differentiation, Wnt signaling is modulated by addition of several small molecules, as it was proven as most efficient in 3D EBs (Laflamme *et al.*, 2007; Yang *et al.,* 2008) and 2D monolayer differentiation (Lian *et al.*, 2012) (Fig. 6). For this, a mesodermal fate of iPSC is initiated by activation of Wnt signaling. This is either achieved by addition of an activin A/BMP4 combination or alternatively by blocking the glycogen synthase kinase 3 (GSK3, a Wnt inhibitor) via addition of the small molecule CHIR99021. Like in *in vivo* development, subsequently Wnt signaling is inhibited, to induce a cardiac lineage. This is achieved by inhibition of Wnt signaling. For this, small molecules, like inhibitors of WNT production (IWPs) can be added (Burridge *et al.*, 2014; Lian *et al.*, 2012). To enrich purity of the obtained iPSC-cardiomyocytes cultures, a metabolic selection step is conducted, as it was shown to be most efficient compared to other purification methods (Burridge and Zambidis, 2013; Lian *et al.*, 2013; Tohyama *et al.*, 2013). Metabolic selection is based on

the ability of cardiomyocytes to metabolite lactate, if glucose is not available. Hence, glucose depletion and lactate supplementation are applied onto the cells, which will lead to starvation and subsequent death of glucose-dependent non-cardiomyocytes. These direct differentiation protocols followed by metabolic selection achieve iPSC-cardiomyocytes yields of up to 90% (Burridge *et al.*, 2014). However, the predominant cardiomyocyte subtype within the resulting iPSC-cardiomyocytes population are ventricular cardiomyocytes, with only lower amounts of atrial or nodal cardiomyocytes. To obtain predominantly atrial cardiomyocytes, retinoic acid (RA) is added in parallel to IWP2, which was shown to be highly efficient (Cyganek *et al.*, 2018). Establishment of efficient and robust protocols for achieving other cardiomyocyte subtypes is still ongoing (Schweizer *et al.,* 2017).

So far, all described differentiation protocols only yield immature cardiomyocytes with a rather fetal/neonatal than adult phenotype. Especially in the early days of cardiomyocyte differentiation, iPSC-cardiomyocytes expressed most cardiac genes, like RYR2, SERCA, NCX, however expression levels were decreased compared to adult cardiomyocytes (Yang *et al.*, 2014c). Furthermore, during *in vivo* development isoform switches of certain genes are observed which are used as markers of maturation. One of this is the isoform switch from the predominant expression of α-MHC (encoded by *MYH6*) in the fetal heart to the predominant expression of βMHC (encoded by *MYH7*) in the adult heart (Guo and Pu, 2020; Reiser *et al.*, 2001; Zhao *et al.*, 2020b). In the beginning of cardiomyocyte differentiation, iPSC-cardiomyocytes rather expressed the fetal isoforms of such genes. Since the immature phenotype might hold drawbacks in comparison of iPSC-cardiomyocytes and adult cardiomyocytes and impair the translation of results obtained from iPSC-cardiomyocytes research to the adult organism and into clinics, a lot of effort was done and still is ongoing to improve the maturation state of iPSC-cardiomyocytes. This today already allows a huge step forwards and generated iPSC-cardiomyocytes are approaching a more neonatal and more mature phenotype. The most straight forward and easy approach is prolonged culture of iPSC-cardiomyocytes exceeding a culture time of minimum eight weeks, since it was shown to enhance gene expression, cell size, sarcomeric structure, metabolic behavior and even electrophysiological properties towards a more mature state (Emanuelli *et al.*, 2022; Kamakura *et al.*, 2013; Lewandowski *et al.,* 2018). Further, more complex approaches include addition of triiodothyronine (T3), which was shown to yield longer sarcomeres and enhanced Ca^{2+} handling resulting in improved contraction (Ahmed *et al.*, 2020; Funakoshi *et al.*, 2021; Yang *et al.*, 2014d). Another approach is focusing on the metabolism, since it was shown that adult cardiomyocytes switch from glycolysis to fatty acid oxidation (Yang *et al.*, 2019). Hence, removal of glucose from the medium and replacement by fatty acids, like palmitate or linoleic acid was shown to enhance maturation, shown by improvement of structural as well as physiological changes (Correia *et al.*, 2017; Funakoshi *et al.*, 2021; Horikoshi *et al.*, 2019; Thomas *et al.*, 2022b; Vuckovic *et al.*, 2022). Other approaches rather concentrate on the fact, that in the adult heart cardiomyocytes are included into a functional, 3D environment and hence apply functional stress onto the iPSC-cardiomyocytes by electrical stimulation or mechanical stretch (LaBarge *et al.*, 2019), introduce cellular communication with other cell types by co-culture with for example mesenchymal cells (Yoshida *et al.*, 2018), or enable maturation in larger 3D structures or

organoids (Ahmed *et al.*, 2020; Hofbauer *et al.*, 2021; Tiburcy *et al.,* 2017). Despite all the efforts and achievements that were made to enhance iPSC-cardiomyocytes maturation, none of the above-mentioned approaches could enhance iPSC-cardiomyocytes maturity to a level comparable of adult cardiomyocytes (Feyen *et al.*, 2020). Hence, more research is required to overcome this drawback in iPSC-cardiomyocytes research.

In addition to iPSC-derived cardiomyocytes, other non-cardiomyocyte cells, like CFB or EC can be differentiated from iPSC (Iyer *et al.*, 2016; Natividad-Diaz *et al.*, 2019; Zhang *et al.*, 2019). CFB can be generated by recapitulation of their *in vivo* development from epicardial-derived cells as well (Iyer *et al.*, 2016; Zhang *et al.*, 2019) (Fig. 7). For this, like generation of iPSC-derived cardiomyocytes, first a mesodermal fate is induced by addition of activin A/BMP4 and/or CHIR99021 (Giacomelli *et al.*, 2020; Guadix *et al.*, 2017) (Fig. 7). To induce a cardiac fate, again, WNT signaling is inhibited by addition of small molecule IWPs (Iyer *et al.*, 2016; Zhang *et al.*, 2019) (Fig. 7). Subsequently differentiation into epicardial-like cells is initiated by addition of BMP4, RA and CHIR99021, which were shown to act synergistically to efficiently induce epicardial differentiation (Guadix *et al.*, 2017; Iyer *et al.*, 2016) (Fig. 7). The obtained iPSC-derived epicardial-like cells are subsequently treated with FGF) to induce CFB differentiation (Bao *et al.*, 2016; Giacomelli *et al.*, 2020; Iyer *et al.*, 2016; Zhang *et al.*, 2019; Zhao *et al.,* 2017) (Fig. 7).

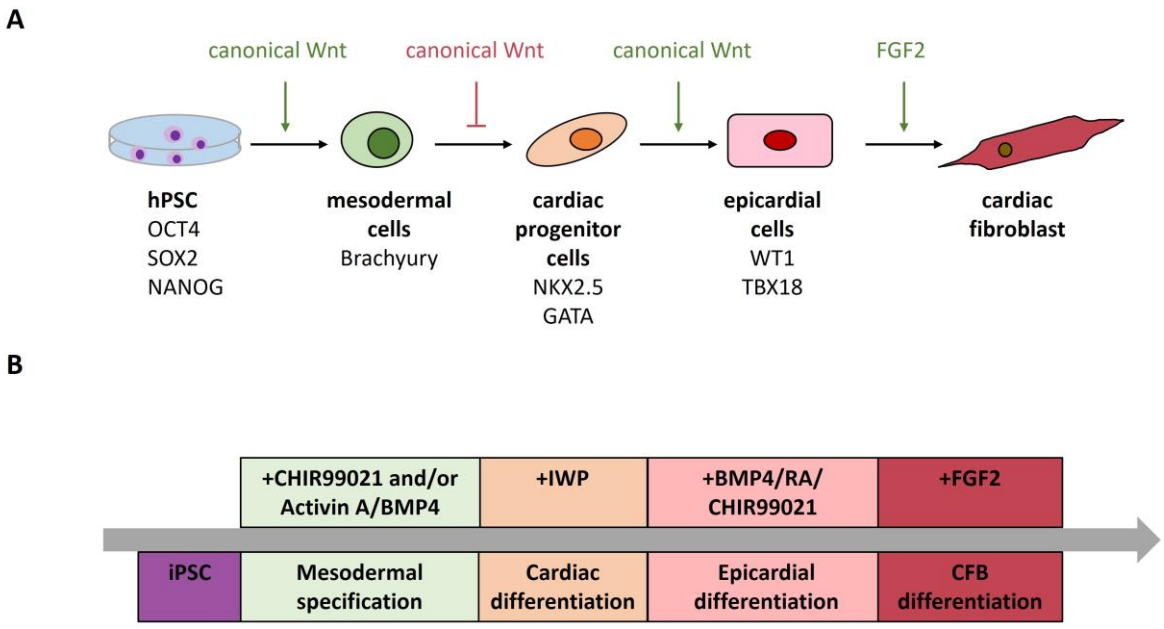

Fig. 7: Schematic overview of *in vivo* and *in vitro* CFB differentiation. **A** Schematic overview of *in vivo* CFB specification. Activation of Wnt and BMP signaling induces differentiation towards brachyury^{+} mesodermal cells. Upon subsequent inhibition of Wnt signaling a cardiac fate is induced. Reactivation of Wnt signaling induces differentiation into epicardial cell. FGF2 signaling enables CFB specification. **B** Schematic overview of previously published *in vitro* differentiation of iPSC into iPSC-CFB via epicardial differentiation (Giacomelli *et al.*, 2020; Iyer *et al.*, 2016; Zhang *et al.*, 2019).

1.4.1.3 iPSC-cardiomyocytes and iPSC-CFB in research and disease modeling

Patient-specific iPSC and its various deriving cardiac cell types (e.g., cardiomyocytes and CFB) provide a powerful tool for cardiac research. They represent a human model and hence overcome the obstacles faced by animal models which often cannot recapitulate the

exact human phenotype. Additionally, they are characterized by unlimited proliferation potential and can be cultured comparably easily, both being advantageous compared to patient-derived adult cardiomyocytes with very low proliferation potential (Yutzey, 2017). Furthermore, iPSC-cardiomyocytes/CFB are favorable compared to ESC. Besides avoiding ethical concerns faced by ESC-derived cardiomyocytes, iPSC-derived cardiomyocytes represent a patients geno- and phenotype and hence provide a suitable tool for disease modeling, especially for monogenetic diseases like DCM (Ebert *et al.*, 2012).

The suitability of iPSC-cardiomyocytes to study monogenetic cardiac diseases was shown several times by identifying structural or functional impairments and mechanisms in iPSC-cardiomyocytes recapitulating the patients diseased phenotype (Karakikes *et al.*, 2014; Rebs, 2021; Schick *et al.*, 2018; Sun *et al.*, 2012). With the achievement of generating isogenic control iPSC lines using gene editing methods like CRISPR/Cas9, monogenetic, as well as polygenetic diseases could be studied in more detail. Since certain genetic variants can be repaired in patient lines or introduced into control lines, the contribution of such variants thought to be associated with certain diseases can be studied in more detail (Guo *et al.*, 2019; Karakikes *et al.*, 2015). In addition to monogenetic diseases, iPSC-derived cells were also shown to model even multifactorial diseases with unknown genetic predisposition, like TTS (Borchert *et al.*, 2017). In this study, higher sensitivity, and impaired desensitization of patient-derived iPSC-cardiomyocytes to β-adrenergic signaling was identified as underlying driver for the TTS (Borchert *et al.*, 2017). By unraveling the causative mechanism, future studies could further concentrate on underlying genetic predispositions, which are remained within the patient-derived iPSC cells. Moreover, the possibility to integrate the iPSC-derived cardiac cells into 3D models, disease modeling is raised to a next level. This 3D modeling allows analysis of function of different cells in a more realistic 3D environment. It enables analysis of cell-cell interactions and communications, which might be affected in a highly complex organ, like the heart, also driving the onset and progression of certain diseases. This includes generation of matrix-free cardiac organoids which could be constructed from single cell types or combinations of cell types, like cardiomyocytes, CFB and/or EC (Thomas *et al.*, 2022a; Zhu *et al.*, 2022). Additionally, matrix-containing approaches lead to tissue formation not only studying cell-cell but also cell-matrix interaction and communication (Thomas *et al.*, 2022a). This for example includes approaches, like engineered heart tissue (EHT)/engineered heart muscle (EHM) (Borchert *et al.*, 2017; Mannhardt *et al.*, 2016; Tiburcy *et al.*, 2017), or engineered connective tissue (ECT) (Santos *et al.*, 2021).

By modeling patient-specific diseases, iPSC-derived cardiac cells provide a powerful tool for high-throughput drug screening to discover new drugs or to evaluate potential cardiotoxicity. On the one hand, using iPSC-derived cardiac cells for drug screening and testing, the number of animal studies is reduced. On the other hand, since patient-derived iPSC cardiac disease models resemble human disease conditions with high accuracy, specific drug testing becomes more efficient and accurate (Dick *et al.*, 2010; Ebert *et al.*, 2012). Beneficial effects of certain drugs onto iPSC-cardiomyocytes function were shown several times (Jung *et al.*, 2012; Sasaki *et al.*, 2016; Yoshida and Yamanaka, 2017).

Additionally, by harboring a patient-specific geno- and phenotype iPSC-derived cardiac cells are ideal for personalized medicine in drug screening.

Not only in disease modeling or (personalized) drug screening iPSC-derived cardiac cells provide an interesting platform for translational approaches from bench to bedside, but also in regenerative medicine the use of iPSC-derived cells is a promising tool. A major drawback in any type of organ transplantation or cell therapy is the risk of potential immune reactions, leading to rejection reactions in the worst case. Additionally, the limited number of healthy organs for organ transplantation is a huge issue. The use of patient-specific iPSC-derived cells in regenerative medicine could overcome these problems and would reduce the need of immunosuppressive therapy. Especially in the cardiovascular field, usage of iPSC-based cell therapy is of high interest. This is because many cardiac diseases are accompanied by cell death, which could not be replaced by largely non-proliferative cardiomyocytes and hence often leads to scar formation, impairing overall heart muscle function. However, the risk of teratoma formation induced by undifferentiated cells needs to be monitored very closely when using iPSC-derived cardiac cell therapy. Additionally, the reported immaturity of iPSC-derived cardiac cells might hold difficulties about electrophysiological properties. Nevertheless, first studies in animal models showed beneficial effects of iPSC-derived cardiomyocytes after myocardial infarction (Romagnuolo *et al.*, 2019; Shiba *et al.*, 2016; Ye *et al.*, 2013). Within the BIONAT-HF (Biological Ventricular Assist Tissue in terminal Heart Failure, ClinicalTrials.gov Identifier: NCT04396899) study the first early clinical trial is ongoing to test for beneficial effects of iPSC-derived heart patches in patients with severe heart failure with reduced EF. These used heart patches derived from EHM, which were generated from iPSC-derived cardiomyocytes and stromal cells incorporated into a collagen hydrogel. This clinical study marks a huge progress in iPSC-based cardiovascular regenerative medicine. Based on this, it is most likely that the iPSC-based cardiac system will be a crucial part in regenerative medicine in the future.

1.5 Gene editing of iPSC

As already described, the identification and generation of patient-specific iPSC and their differentiation capacity into a versatile set of cells paved the way towards patient-specific cardiovascular research, among others allowing or improving research on genetically inherited cardiac diseases, since they harbor the complete patient`s genetic background. However, varying genetic background of different individuals complicated the choice of meaningful controls to decipher the role of specific genetic variants. With the identification of the clustered regulatory interspaced palindromic repeat (CRISPR)/ **C**RISPR-**as**sociated protein (Cas) (CRISPR/Cas9) gene editing tool, now generation of more suitable controls is possible. This is because either single genetic variants of patient lines can be reverted to wildtype sequences while maintaining the rest of the genetic background or certain genetic variants can be introduced into external control lines. This allows analysis of the contribution of certain genetic variants to disease pathophysiology in a new and more precise way.

1.5.1 CRISPR/Cas9 technology

Originally, the CRISPR/Cas system was detected as a RNA-mediated defense mechanism of bacterial and archaeal adaptive immunity (Bhaya *et al.*, 2011; Fineran and Charpentier, 2012). The CRISPR/Cas system relies on RNA as well as protein components. For this, the CRISPR locus comprises alternating repeat (23-50nt) and spacer (17-84nt) sequences. Although highly variable, the spacer sequences were shown to have high sequence similarity to viral or phage genomes and the repeat sequences are characterized by the unifying ability to form loop structures (Bolotin *et al.*, 2005; Ishino *et al.*, 1987; Mojica *et al.*, 1993). Additionally, a Cas, characterized by two catalytic endonuclease domains, can introduce double strand breaks (DSB) (Richter *et al.*, 2012). The crRNA (transcribed repeat and spacer RNA) binds to a trans-activating crRNA (tracrRNA) (Chylinski *et al.*, 2014). Subsequently, the tracrRNA:crRNA molecule associates with the Cas enzyme, forming a ribonucleoprotein (RNP) complex (Chylinski *et al.*, 2014). This RNP complex then is guided to target site by sequence specificity of the crRNA. At the site of action, the Cas protein will introduce several DSB. For initiation of the DSB the Cas enzyme needs to recognize a certain motif, the so-called protospacer adjacent motif (PAM), with in the target genome. The PAM site is a 3nt sequence, located adjacently to the sequence complementary to the crRNA (Deveau *et al.*, 2008). Due to excessive research and the availability of large databases, several different CRISPR/Cas systems have been identified. These in general can be grouped into two different classes which differ in their effector module composition. Where in class I multiple Cas proteins are encoded with distinct functions on crRNA processing and interference, class II systems are classified by a single, but multidomain Cas protein (Makarova *et al.*, 2020). These two classes are further divided into six types (I-VI), two in each class and up to 33 subtypes. The class 2 type II system is the by far best characterized system, comprising the Cas9 as effector module for crRNA and target binding, since it is the most frequently used system for eukaryotic gene editing (Makarova *et al.*, 2020).

Rapid research identified this bacterial system as a powerful tool to desirable manipulate genomes. Hence, the first bacterial genome was experimentally edited by CRISPR/Cas9 in 2012 (Jinek *et al.*, 2012). Further studies soon translated this system to eukaryotic cells (Cong *et al.*, 2013). Like the bacterial system, the CRISPR/Cas technology is used to introduce DNA double-strand breaks in eukaryotic cells. By designing crRNAs with complementary sequences to the region of interest, site-specific DSB are achieved. The DNA DSB initiate the cells endogenous repair mechanisms, which in eukaryotic cells can be divided into two groups – non-homologous end joining (NHEJ) and homology directed repair (HDR) (Fig. 8). NHEJ simply ligates the resulting DNA ends after the DSB. Although, NHEJ is a very fast repair, it often leads to random insertions and deletions, since the DNA ends are not ligated perfectly after DSB (Gottlich *et al.*, 1998). Due to insertions or deletions, NHEJ often results in frameshifts and even could lead to premature stop codons, potentially resulting in gene knockouts (Gottlich *et al.*, 1998). With regard to cardiac research, Maurer *et al.* used the NHEJ repair in gene editing to generate iPSC with a homozygous $Na_v1.8$ knock-out (Maurer *et al.*, 2022). With subsequent differentiation into iPSC-cardiomyocytes and functional analyses, Bengel *et al.* could prove a cardiomyocyte-

driven role of $Na_v1.8$ to enhanced persistent Na^+ current (late I_{Na} or I_{NaL}) in HF conditions (Bengel *et al.*, 2021). In contrast to this, HDR is less error prone since it uses a homologous DNA sequence template to complementary regenerate the DSB (Ranjha *et al.*, 2018). Endogenous HDR typically uses the second allele naturally occurring within the genome (Ranjha *et al.*, 2018). However, in gene editing approaches, specifically designed exogenous HDR templates can be introduced to the cell in addition to the CRISPR/Cas complex (Trevino and Zhang, 2014). Nucleotides could be exchanged, which is suitable to study the role of certain single-nucleotide polymorphisms (SNPs) on certain diseases. Either a diseased variant in a patient line can be exchanged by a wildtype variant or vice versa generating so called isogenic controls, which are perfect controls in iPSC research as mentioned above (Hamrick *et al.*, 2022; Kim *et al.*, 2021; Rebs, 2021). So far, the CRISPR/Cas system holds a plethora of gene editing methods of eukaryotic cells. This includes the availability of different Cas enzymes with different PAM recognition motifs or the modulation of the Cas enzymes to expand their function beyond only introducing DSB, to introduce single-strand breaks, regulating gene expression or tagging genes with reporter systems (Barrangou and Doudna, 2016; Pickar-Oliver and Gersbach, 2019).

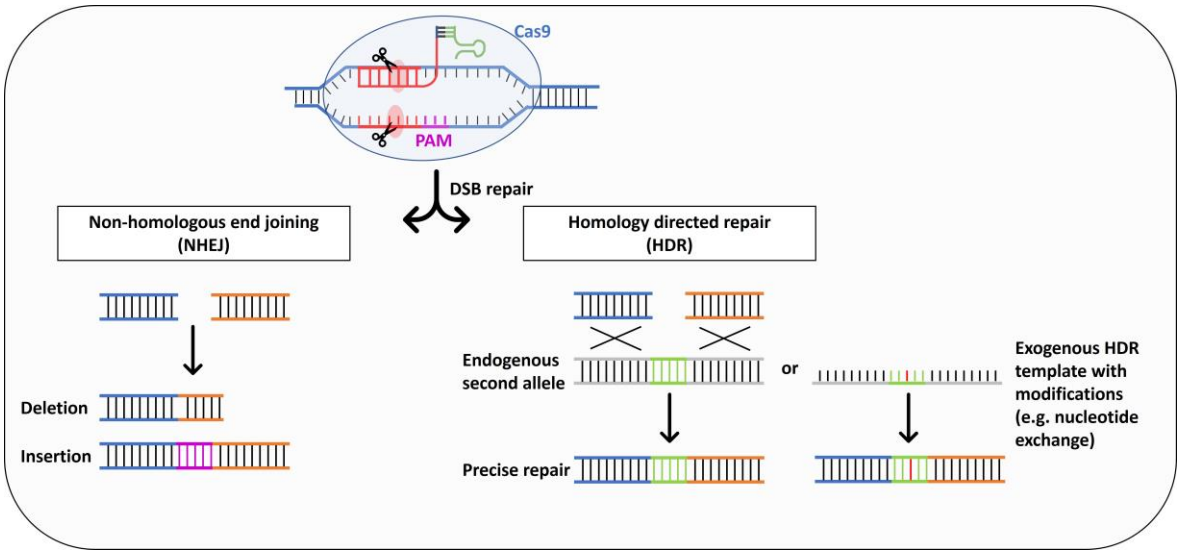

Fig. 8: Schematic overview of eukaryotic DSB repair used for CRISPR/Cas9 genome editing. Upon site-specific binding the Cas9 protein will introduce DSB to the target sequence. These DSB can be repaired by NHEJ that leads to random insertions or deletions of nucleic acids. The second possibility to repair the DSB is the HDR which utilizes a template DNA to remodel the DSB. The template DNA could be the endogenous second allele. For genome editing an HDR template can be provided exogenously. With this specific nucleotide changes can be induced (red line).

1.5.2 CRISPR/Cas9 gene editing in iPSC with high efficiency

CRISPR/Cas9 is an ideal model for gene editing in eukaryotic cells and even holds several opportunities in iPSC research as mentioned earlier. When applying CRISPR/Cas9 gene editing to iPSC there are several challenges faced that need to be considered. First of all, several huge components, including the tracrRNA, crRNA, Cas enzyme and in some cases a HDR template need to be introduced to the cells for CRISPR/Cas9 action. Hence, two things have to be considered for delivery. On the one hand, it needs to be considered in which molecular form these components should be introduced. Cas9, tracrRNA, and crRNA could be delivered as DNA plasmids, or as mRNA for Cas9 in addition to the tracrRNA:crRNA, or

direct delivery of the Cas9 protein alongside with the tracrRNA:crRNA (Lino *et al.*, 2018). Direct delivery of the Cas9 protein holds the advantage that the amount of active protein can be determined more precisely, it is stably active for a shorter time (preventing off-target cutting) and also was shown to be less toxic in stem cells (Okamoto *et al.*, 2019). On the other hand, it needs to be considered how these components should be delivered, meaning considering a suitable vector. This includes two major methods shown suitable for iPSC – viral transduction of adeno-associated viruses (AAV) or electroporation (Lino *et al.*, 2018). Electroporation is a straightforward approach, fast and easy to conduct and the Cas9 protein can be introduced directly within a RNP complex, being advantageous as mentioned earlier and hence is the best choice for *in vitro* applications. In contrast to this, AAV transduction is a promising approach for *in vivo* application. This is based on the tissue tropism of specific AAV serotypes. For example, AAV6 and AAV9 specifically deliver cargos to cardiomyocytes, and hence holds a huge advantage for direct and specific gene therapy in human (Ambrosi *et al.*, 2019; Moretti *et al.*, 2020). Nevertheless, AAVs only have low packaging capacity, as a consequence the huge Cas9 would need to be spilt to several vectors (Maeder *et al.*, 2019). In addition to the most suitable delivery method, the efficiency of CRISPR/Cas9 also is affected by other factors. One of these includes the selection and design of crRNA/target site. On the one hand, this is limited by position of PAM sites within the targeted genome, necessary for Cas9 active cleavage. For the originally identified *Streptococcus pyogenes* Cas9 (SpCas9) the PAM site is denoted as NGG triplet, a motif occurring every eight base pairs in average (Ramakrishna *et al.*, 2014). For being more flexible in crRNA design, Cas9 of different species could be used, which recognize other PAM sites (Jiang *et al.*, 2013). On the other hand, editing efficiency is also directly influenced by the design of the crRNA itself, which is reported to be highly difficult and often not clearly predictable. This is why it is advised to use one out of several crRNA design tools, monitor the outcome cautiously and when in doubt test several crRNAs (Lino *et al.*, 2018). These design tools also include risk calculation of off-target cutting, meaning Cas9-mediated DSB at genomic locations distinct from the desired one. Off-target cutting is mediated by binding of the crRNA to non-intended genomic locations, which could lead to Cas9 cutting even in the presence of a small number of mismatches. Hence, the number of potential off-target sites should be reduced by most specific design of the crRNA (Lino *et al.*, 2018). Especially when single nucleotides should be exchanged, HDR templates are used harboring the desired “new” nucleotide that should be introduced. However, HDR is very low in mammalian cells, even when HDR-templates are introduced and NHEJ remains the predominant form of DNA repair after DSB (Maruyama *et al.*, 2015). Hence, to enhance HDR and with it the overall CRISPR/Cas9 efficiency, several approaches are reported. These include addition of small molecules during the CRISPR/Cas9 experiment which inhibit NHEJ and promote HDR (Srivastava *et al.*, 2012; Vartak and Raghavan, 2015). To further enhance HDR, or more precisely prevent re-cutting, the HDR template is designed to harbor silent mutations in addition to the desired nucleotide, which should be exchanged. Introduction of these silent mutations will lead to synonymous amino acids and hence should not influence resulting protein structure and function. However, they introduce mismatches for crRNA or PAM site binding. This reduces rebinding of the crRNA to the template after successful HDR and hence prevents Cas9 re-cutting (Paquet *et al.*, 2016). So far, several

studies reported successful gene editing of iPSC lines, including knockout based on NHEJ, leading to loss-of-function or gain-of-function or single nucleotide exchanges generating isogenic controls to patient lines or introducing pathogenic SNPs in control lines using HDR (Ben Jehuda *et al.*, 2018; Bengel *et al.*, 2021; Horii *et al.*, 2013; Young *et al.*, 2016). These studies impressively showed, how CRISPR/Cas9 genome editing further diversifies the use of iPSC in research and translational medicine. Notably, the first clinical trials applying CRISPR/Cas strategies to treat certain diseases are already ongoing (Frangoul *et al.*, 2021; Hamrick *et al.*, 2022; Lacey and Fraietta, 2020).

1.6 Aims

For this project, a four-member family was recruited containing patients with severe DCM and external controls. The father and the older daughter were identified with sudden onset DCM at the age of 40 years and 6 months, respectively, both needed heart transplantation. The mother and the second daughter did not show any cardiac phenotype. Since two first-degree family members were affected, the DCM is hypothesized to be of familial/genetic cause. However, the underlying causative gene variant was not identified so far. To unravel the underlying genetic predisposition and potential functional effects of the DCM pathophysiology within this family the patient-specific iPSC model was used, generated from somatic cells of all family members. For this, the main objectives of this study were defined as follows:

1. Identification of underlying predisposing genetics by sequencing approaches

2. Pluripotency characterization and subsequent direct differentiation into functional beating ventricular cardiomyocytes of previously reprogrammed iPSC

3. Generation of isogenic control iPSC and iPSC-cardiomyocytes of diseased family members based on the results of identification of potential disease-causing variants and subsequent pluripotency characterization of iPSC

4. Molecular and functional analysis of healthy, diseased, and isogenic iPSC-cardiomyocytes to identify an *in vitro* disease phenotype and evaluate the contribution of the identified variant to the DCM pathophysiology, this includes:

    a. Analysis of sarcomeric regularity
    b. Analysis of cell size
    c. Gene expression analysis of important cardiac players
    d. Analysis of Ca^{2+} homeostasis (including Ca^{2+} load and kinetics)
    e. Analysis of oxidative stress
    f. Analysis of contraction capacity and Ca^{2+} response in EHM

5. Investigation of the role of CFB within the DCM pathophysiology

    a. Cellular and molecular characterization of primary CFB
    b. Testing and adapting a protocol for directed differentiation into iPSC-CFB and subsequent characterization
    c. Functional analysis of primary and iPSC-derived CFB within 3D ECT to identify a potential disease phenotype and evaluate a putative contribution of the identified variant

6. Investigation of the role of cardiomyocyte-specific telomere shortening within the DCM pathophysiology

2 Materials

2.1 Cell lines

Tab. 1: List of somatic, reprogrammed or genetically modified cells and cell lines used. *already established prior to the start of the project in the lab for Translational stem cell research, Clinic for Cardiology and Pneumology, UMG Göttingen

Cell type	Internal name	Specification
Primary cells		
Human primary dermal fibroblasts	DCM1*	Derived from skin biopsy of a 40-year-old male patient (father, DCM1) with DCM and a *FLNC* mutation (c.6560G>C het, p.Arg2187Pro) and *ILK* mutation (c.1274T>C, het; p.Met425Thr)
Human primary cardiac fibroblasts	DCM1_LV/CFB1*	Extracted from explanted heart tissue of male DCM patient (DCM1), with a *FLNC* mutation (c.6560G>C het, p.Arg2187Pro) and *ILK* mutation (c.1274T>C, het; p.Met425Thr)
Human primary cardiac fibroblasts	CFB2*	Extracted from explanted heart tissue of male DCM patient
Human primary cardiac fibroblasts	CFB3*	Extracted from explanted heart tissue of male DCM patient
Human primary cardiac fibroblasts	CFB9*	Extracted from explanted heart tissue of male control
Peripheral blood mononuclear cells (PBMCs)	DCM2*	Isolated from blood sample of a 39-year-old healthy female (mother, DCM2)
Peripheral blood mononuclear cells (PBMCs)	DCM3*	Isolated from blood sample of a 9-year-old female patient (daughter 1, DCM3) with DCM and a *FLNC* mutation (c.6560G>C het, p.Arg2187Pro) and *ILK* mutation (c.1274T>C, het; p.Met425Thr)
Peripheral blood mononuclear cells (PBMCs)	DCM4*	Isolated from blood sample of a 5-year-old healthy female (daughter 2, DCM4)
Human primary dermal fibroblasts	CTRL1*	Derived from skin biopsy of a 25-year-old healthy female
Peripheral blood mononuclear cells (PBMCs)	WT4*	Isolated from blood sample of a 34-year-old healthy male
Reprogrammed cells		
iPSC	ssDCM1.4*	iPSC line generated by reprogramming of dermal fibroblasts

		of DCM1 by transduction of non-integrating sendai virus
iPSC	ssDCM1.6*	iPSC line generated by reprogramming of dermal fibroblasts of DCM1 by transduction of non-integrating sendai virus
iPSC	ssDCM2F1*	iPSC line generated by reprogramming of PBMCs of DCM2 by transduction of non-integrating sendai virus
iPSC	ssDCM2F2*	iPSC line generated by reprogramming of PBMCs of DCM2 by transduction of non-integrating sendai virus
iPSC	ssDCM3.4*	iPSC line generated by reprogramming of PBMCs of DCM3 by transduction of non-integrating sendai virus
iPSC	ssDCM3.7*	iPSC line generated by reprogramming of PBMCs of DCM3 by transduction of non-integrating sendai virus
iPSC	ssDCM4A2*	iPSC line generated by reprogramming of PBMCs of DCM4 by transduction of non-integrating sendai virus
iPSC	ssDCM4A4*	iPSC line generated by reprogramming of PBMCs of DCM4 by transduction of non-integrating sendai virus
iPSC	pCTRL1.1*	iPSC line generated by reprogramming of dermal fibroblasts of CTRL1 by transfection with plasmids
iPSC	isWT4bld6*	iPSC line generated by reprogramming of PBMCs of WT4 by transduction of non-integrating sendai virus
Genetically modified cells		
iPSC	DCM1.4_FLNC2_K1	Isogenic iPSC clone 1 of ssDCM1.4 generated by CRISPR/Cas9 with rescued *FLNC* mutation, c.6560G, p.Arg2187
iPSC	DCM1.4_FLNC2_K5	Isogenic iPSC clone 5 of ssDCM1.4 generated by CRISPR/Cas9 with rescued *FLNC* mutation, c.6560G, p.Arg2187

iPSC	DCM1.4_FLNC2_K9	Isogenic iPSC clone 9 of ssDCM1.4 generated by CRISPR/Cas9 with rescued *FLNC* mutation, c.6560G, p.Arg2187
iPSC	DCM3.7_FLNC2_K19	Isogenic iPSC clone 19 of ssDCM3.7 generated by CRISPR/Cas9 with rescued *FLNC* mutation, c.6560G, p.Arg2187
iPSC	DCM3.7_FLNC2_K23	Isogenic iPSC clone 23 of ssDCM3.7 generated by CRISPR/Cas9 with rescued *FLNC* mutation, c.6560G, p.Arg2187
iPSC	DCM3.7_FLNC2_K24	Isogenic iPSC clone 24 of ssDCM3.7 generated by CRISPR/Cas9 with rescued *FLNC* mutation, c.6560G, p.Arg2187

2.2 Basal Media and Supplements

Tab. 2: List of all basal media and supplements used.

Name	**Manufacturer**
B27 serum-free supplement w/ insulin	Thermo Fisher Scientific (#17504-044)
B27 supplement w/o insulin	Thermo Fisher Scientific (#A1895601)
Dulbecco`s Modified Eagle Medium (DMEM) powder, high glucose	Thermo Fisher Scientific (#12100061)
Dulbecco`s Modified Eagle Medium (DMEM) w/o GlutaMAX	Thermo Fisher Scientific (#11960-044)
Essential 8 (E8) Kit	Thermo Fisher Scientific (#A1517001)
Fetal calf serum (FCS)	Thermo Fisher Scientific (#10270-106)
Fibroblast Growth Medium 3 Kit	Promocell (#C-23130)
Iscove`s Modified Dulbecco`s Medium (IMDM) with GlutaMAX	Thermo Fisher Scientific (#31980022)
KnockOut DMEM	Thermo Fisher Scientific (#10829018)
RPMI 1640 w/ GlutaMAX, w/o HEPES	Thermo Fisher Scientific (#61870010)
RPMI 1640 w/HEPES/GlutaMAX	Thermo Fisher Scientific (#72400021)
RPMI 1640 w/o glucose	Thermo Fisher Scientific (#11879020)
StemFlex	Thermo Fisher Scientific (#A3349401)

2.3 Cell culture media

Tab. 3: Composition of cell culture media. *FCS used after heat inactivation at 56°C for 30min.

Name	**Composition**	
Basal serum-free medium (BSFM)	2% 1% 10µl/ml	RPMI 1640 w/o HEPES B27 supplement w/o insulin Sodium Pyruvat L-ascorbic acid 2-phosphate (20mM)

Cardiac differentiation medium (CDM)	1µl/ml	BSFM IWP2 (5mM)
Cardio culture medium	1x	RPMI 1640 w/ HEPES/GlutaMax B27/insulin supplement (50x)
Cardio differentiation medium	500mg/l 200mg/l	RPMI 1640 w/ HEPES/GlutaMax Human recombinant albumin L-ascorbic acid 2-phosphate
Cardio digest medium	80% 1µl/ml 20%	Cardio culture medium TZV (2mM) FCS*
Cardio selection medium	4ml/L 500mg/l 200mg/l	RPMI w/o Glucose Lactate/HEPES (1M) Albumin L-ascorbic acid 2-phosphate
E8/TZV medium	1µl/ml	E8 medium TZV (2mM)
Essential 8 medium (E8 medium)	1x	E8 basal medium E8 supplement (50x)
Human fibroblast medium (HFBM)	10% 1% 1% 1% 10ng/ml	DMEM w/o Glucose FCS* L-Glutamine (200mM) NEAA (100x) β-Mercaptoethanol (100x) hbFGF
Iscove differentiation medium	20% 1% 3µl/ml	IMDM with GlutaMax FCS* NEAA (100x) MTG stock
Lactate/HEPES (1M)	3ml 18ml	Sodium DL-lactate solution 60% HEPES sodium salt solution
MTG stock	1ml 13µl	IMDM MTG
StC-EM with CHIR (StC-EM+C)	0.0825µl/ml	StC-EM CHIR99021 (12mM)
StemFlex	1x	StemFlex basal medium StemFlex supplement (50x)
Stromal cell expansion medium (StC-EM)	1% 10% 50ng/ml 25ng/ml	KnockOut DMEM L-Glutamine (200mM) FCS* hbFGF VEGF
Stromal cell induction medium (StC-IM)	0.0825µl/ml 5ng/ml 9ng/ml 5ng/ml	BSFM CHIR99021 (12mM) BMP4 Activin A hbFGF

Stromal cell specification medium (StC-SM)	50ng/ml 4µl/ml 0.0825µl/ml	BSFM BMP4 Retinoic acid (1mM) CHIR99021 (12mM)
2x DMEM	20% 20% 2%	ddH_2O 10x DMEM FCS* Penicillin/Streptomycin

2.4 CRISPR/Cas9 cell manipulation

Tab. 4: List of CRISPR/Cas9 components for cell manipulation.

Name	Manufacturer
Cas9 nuclease V3	IDT (#1081058)
crRNA	IDT (Individual design)
HDR enhancer	IDT (#232809511)
HDR-template	IDT (Individual design)
tracrRNA	IDT (#1072532)

Tab. 5: crRNA and HDR template of CRISPR strategy used to rescue FLNC mutation.

Name	Sequence
crRNA 1 (FLNC1)	5´- TGATCTCCGTGCGCTCCGTG-3`
crRNA 2 (FLNC2)	5´- CTGATCTCCGTGCGCTCCGT-3`
HDR template	5´-AGCGCCTGACACGCACCTTCACACGCAGCAGCCACACCTAC ACCCGCACCGAGCGCACGGAGATAAGCAAGACGCGGGGCGGG GAGACAAA-3`

2.5 Buffers and Solutions

Tab. 6: Composition of buffers and solutions. *FCS used after heat inactivation at 56°C for 30min

Name	Composition	
1% BSA/PBS	1%	1x DPBS (1x) BSA (7.5%)
15% Separation gel (2 gels)	3ml 6ml 3ml 48µl 18µl	ddH_2O Rotiphorese Gel 30 (37.5:1) Tris-HCl / SDS, pH 6.8 10 % APS TEMED
4% Stacking gel (2 gels)	4.62ml 1ml 1.88ml 37.5µl 15µl	ddH_2O Rotiphorese Gel 30 (37.5:1) Tris-HCl / SDS, pH 6.8 10 % APS TEMED
5% BSA	5%	TBS-T buffer BSA (w/v)
5% Milk	5%	TBS-T buffer milk (w/v)

6% Separation gel (2 gels)	6.6ml 2.4ml 3ml 48µl 18µl	ddH_2O Rotiphorese Gel 30 (37.5:1) Tris-HCl / SDS, pH 6.8 10 % APS TEMED
AmplexRed working solution 1 (per 6 well)	630.4µl 6.4µl 3.2µl	1x Reaction buffer 10 U/ml Horseradish peroxidase 10 mM AmplexRed reagent stock solution
AmplexRed working solution 2	630.5µl 13µl 6.5µl	1x Reaction buffer 10 U/ml Horseradish peroxidase 10 mM AmplexRed reagent stock solution
Anode buffer	 36.4g/l 17.9g/l	ddH_2O Tris base Tricine (adjusted to pH=8.8)
Caffeine solution (10mM)	10ml 19.42mg	1x Tyrode`s solution (FURA) Caffeine
Calcium imaging staining solution - FURA-2AM - Fluo-4	 1ml 1.3µl 5µl 1.5ml 0.9µl 3.8µl	 1x Tyrode`s solution (FURA) Pluornic-F127 FURA-2AM solution  1x Tyrode`s solution (Fluo) Pluoronic-F127 Fluo-4 solution
Cathode buffer	 36.3g/l 3.6g/l	ddH_2O Amino caproid acid Tris base (adjusted to pH=8.7)
Citratpuffer	 2.94g/l 0.5ml/l	ddH_2O Sodium Citrate Dihydrate Tween20 (adjusted to pH=6)
CHIR (12mM)	894µl 5mg	DMSO CHIR99021
FACS B10 buffer	 0.5% 10% 2.2ml/l	1x DPBS (1x) BSA (w/v) FCS* 0.5M EDTA pH=8.0
FACS buffer/ Staining buffer for IF	 1% 0.1%	1x DPBS (1x) BSA (w/v) Triton-X_{100} (v/v)
Fluo-4 solution	44µl 50µg	DMSO Fluo-4
Fluo-4 Tyrode solution (10x)	 81.8g/l	ddH_2O NaCl

	4.026g/l 0.952g/l 23.831g/l	KCl $MgCl_2$ HEPES (adjusted to pH=7)
Fluo-4 Tyrode solution (1x)	 1x 1.8g/l 1.8g/l	ddH_2O 10x Tyrode`s solution Glucose Calcium (adjusted to pH=7.4)
Fura-2AM solution	44µl 50µg	DMSO FURA-2AM
FURA-2AM Tyrode solution (10x)	 81.816g/l 2.982g/l 0.952g/l 23.831g/l	ddH_2O NaCl KCl $MgCl_2$ HEPES (adjusted to pH=7)
FURA-2AM Tyrode solution (1x)	 1x 1.8016g/l 1.25µl/ml	ddH_2O 10x Tyrode`s solution Glucose Calcium (1M)
FURA-2AM Caffeine Tyrode solution	 1.942g/L	1x Tyrode`s solution Caffeine
IWP2 (5mM)	4.28ml 10mg	DMSO IWP2
Lactate/HEPES (1M)	3ml 18 ml	Sodium DL-lactate solution 60% (w/w) 1M HEPES sodium salt solution
Laemmli buffer	 10%	Laemmli buffer (4x) β-Mercaptoethanol
Protein lysis buffer	 20mM 200mM 20mM 1% 1mM 1mM 1x 1x	ddH_2O Tris-HCl (pH 7.4) NaCl NaF Igepal Na_3VO_4 DTT PhosSTOP cOmplete, EDTA-free Protease Inhibitor
Running buffer (10x)	 30.2g/L 144g/L 10g/L	ddH_2O Tris base Glycine SDS
TBE buffer	 10.8g/l 5.5g/l 4ml/l	ddH_2O Tris base Boric acid 0.5 M EDTA pH=8

TBS with Tween-20 (TBST) buffer	0.1%	TBS buffer Tween-20
Tris-buffered saline (TBS) buffer	24g/L 80g/L	ddH_2O Tris base NaCl (adjusted to pH=7.6)
4x Tris/ SDS, pH 6.8	60.5g/L 4g/L	ddH_2O Tris SDS (adjusted to pH=6.8)
4x Tris/ SDS, pH 8.8	182,16g/l 4g/L	ddH_2O Tris SDS (adjusted to pH=8.8)
Turbo transfer (TB) buffer (1x)	20%	ddH_2O Trans-Blot Turbo 5x Transfer buffer
TZV (2mM)	6.8ml 10mg	DMSO TZV

2.6 Commercial kits

Tab. 7: List of all commercial kits used.

Kit	**Manufacturer**
Alkaline phosphatase (ALP) staining kit	Sigma-Aldrich (#86R-1KT)
AmplexRed Hydrogen Peroxide Assay Kit	Thermo Fisher Scientific (#A22188)
DNase I Set	Zymo Research (#E1010)
Human stem cell nucleofector Kit 2	Lonza (#VPH-5022)
Immobilon Western Kit	Millipore (#WBKLS0500)
iQ SYBR Green Supermix	BioRad (#170-8882)
iScrpit cDNA Synthesis Kit	BioRad (#1708891)
MycoAlert Plus Mycoplasma Detection Kit	Lonza (#LT07-710)
Pierce BCA protein assay kit	Thermo Fisher Scientific (#23225)
QIAamp DNA Mini Kit	Qiagen (#51306)
QIAquick Gel Extraction Kit	Qiagen (#28706)
ReliaPrep RNA Miniprep Systems	Promega (#Z6112)
RNA Clean & Concentrator-5 Kit	Zymo Research (#R1016)
SuperSignal West Femto Maximum Sensitivity Substrate	Thermo Fisher Scientific (#34095)
SV total RNA isolation system	Promega (#Z3105)

2.7 Chemicals, Reagents, Enzymes

Tab. 8: List of all chemicals, reagents and enzymes used.

Name	Manufacturer
4', 6-Diamidino-2-phenylindole dihydrochloride (DAPI)	Sigma-Aldrich (#D9542)
6-Aminohexanoic Acid	AppliChem (#63B764.0914F)
Activin A	R&D (#338-AC-010)
Agarose, universal	VWR (#35-1020)
Albumin, human recombinant	Sigma-Aldrich (#A9731)
Amino caproid acid	Applichem (#A2266.0500)
Bambanker Cryopreservation Medium	Nippon Genetics (#BB02)
BMP4, human recombinant, animal-free	Peprotech (#AF-120-05ET)
Boric acid	Roth (#6943.1)
Bovine Collagen type I	LLC Collagen Solutions (#CB-024)
Bovine serum albumin (BSA) Fraction 7.5%	Thermo Fisher Scientific (#152600037)
BSA powder Albumin Fraction V	Roth (#8076.3)
Caffeine powder	Sigma-Aldrich (#C0750)
Calcium chloride solution ($CaCl_2$) solution	Sigma-Aldrich (#21115)
CASY ton	OLS OMNI Life Science (#2501037)
CHIR99021	Merck (#361559)
cOmplete, EDTA-free Protease Inhibitor	Roche (#04693132001)
Dimethyl sulfoxide (DMSO)	Sigma-Aldrich (#D2650)
Dithiothreitol (DTT)	Carl Roth (#6908)
dNTP mix (100 mM)	Bioline (#Bio-39029)
Dulbecco`s phosphate-buffered saline (1x DPBS) 1x	Thermo Fisher Scientific (#14190144)
Dulbecco`s phosphate-buffered saline (1x DPBS) 10x	Thermo Fisher Scientific (#70011-044)
EDTA 0.5 M pH=8.0	AppliChem (#A3145.0500)
Ethanol	Chemsolute (#2236.1000)
FGF-basic, human recombinant	PeproTech (#100-18B)
Fluo-4 probe	Thermo Fisher Scientific (#F14201)
Fluoromount-G Mounting Medium	Southern Biotech (#0100-01)
Formalin (37%)	Merck (#1039991000)
FURA-2-AM, cell permanent	Thermo Fisher Scientific (#F1221)
Geltrex	Thermo Fisher Scientific (#A1413302)
Gene ruler 100 bp Plus DNA Ladder	Thermo Fisher Scientific (#SM0241)
Glycine	Roth (#3908.2)
GoTaq G2 Polymerase	Promega (#M784B)
Green buffer 5x	Promega (#M7911)
HEPES sodium salt solution (1M)	Sigma-Aldrich (#H3662)
Hydrochloric acid (HCl), fuming37 %	Merck (#1.00314.1000)
Igepal	Sigma-Aldric, (#I3021)
Inhibitor of Wnt Production-2 (IWP2)	Merck (#681671)
Isopropanol	Merck (#109634)

Laemmli buffer 4x	Biorad (#1610747)
L-ascorbic acid 2-phosphate	Sigma-Aldrich (#A8960)
L-Glutamine (200mM)	Thermo Fisher Scientific (#25030081)
Magnesium chloride ($MgCl_2$)	Sigma-Aldrich (#M8266)
Methanol	Merck (#106009)
Midori Green Advance	Nippon Genetics (#MG04)
Milk powder	Roth (#T145)
Monothioglycerine (MTG)	Sigma-Aldrich (#M6145-25ML)
Non-essential amino acid (NEAA) solution (100x)	Thermo Fisher Scientific (#11140035)
Nuclease-free water	Thermo Fisher Scientific (#AM9932)
PageRuler Plus Prestained Protein Ladder	Thermo Fisher Scientific (#26620)
Paraformaldehyde 4% (PFA) (ROTI Histofix)	Carl Roth (#P087.1)
PBS 1x	Thermo Fisher Scientific (#14190144)
Penicillin/Streptomycin 100x	Thermo Fisher Scientific (#15140122)
PhosSTOP tablets	Roche (#04906837001)
Pluronic F-127	Merck (#540025)
Ponceau S solution 0.1%	Sigma-Aldrich (#P7170)
Potassium chloride (KCl)	Sigma-Aldrich (#P9541)
Retinoc acid ≥98%	Sigma-Aldrich (#R2625)
Roti Histol	Roth (#6640.5)
Rotiphorese Gel 30 (37.5:1)	Roth (#3029.1)
Sacubitrilat	Aobious (#AOB9326)
SDS	Roth (#0183.1)
Sodium chloride (NaCl)	Roth (#9265.1)
Sodium DL-lactate solution 60% (w/w)	Sigma-Aldrich (#L4263)
Sodium fluoride (NaF)	Roth (#P756.2)
Sodium orthovanadate (Na_3VO_4)	Sigma-Aldrich (#S6508)
Sodium Pyruvat 100x	Thermo Fisher Scientific (#11360070)
StemPro Accutase	Thermo Fisher Scientific (#A1110501)
Thiazovivin (TZV)	Merck (#420220)
Trans-Blot Turbo transfer (TB) buffer 5x	Biorad (#10026938)
Tricine	Biochemika (#A1085.0250)
Tris base	Roth (#5429.2)
Triton-X-100	Sigma-Aldrich (#3051.3)
Trypsin/EDTA 0.25	Thermo Fisher Scientific (#25200056)
Tween-20	Biorad (#170-6531)
Valsartan	Sigma-Aldrich (#SML0142)
VEGF-A165, human recombinant	R&D systems (#293-VE-010)
Versene (0.48 mM EDTA)	Thermo Fisher Scientific (#15040066)
β-mercaptoethanol (Cell culture)	Promega (#Z523A)
β-mercaptoethanol (WesternBlot)	BioRad (#1610710)

2.8 Laboratory equipment

Tab. 9: List of all laboratory equipment used.

Name	Manufacturer
Agarose gel chamber (Sub-Cell GT)	BioRad
Amaxa Nucleofectot II Device	Lonza
Balance EWJ	Kern
Centrifuge 5415 R	Eppendorf
Centrifuge 5810 R	Eppendorf
Centrifuge Cytospin 4	Thermo Fisher Scientific
FACS Canto II	BD Bioscience
Freezer -20°C	Liebherr
Freezer -80°C	Thermo Fisher Scientific
Fridge 4°C	Liebherr
Gas burner (gasprofi 1)	W. Kranich GmbH + Co. KG
Glas bottles (50ml - 1000ml)	Schott
Heat sterilization	Memmert
Heatblock Thermomixer comfort, 1.5ml	Eppendorf
Hemocytometer Thoma	Marienfeld superior
Ice boxes	Neolab
Imager ChemiDoc XRS	BioRad
Incubator HERACELL	Thermo Fisher Scientific
Micropipettes Reference/Research plus (2.5/10/100/1000µl)	Eppendorf
Microscope Axiovert 25	Zeiss
Microscope Observer A1	Zeiss
Microscope Observer Z1	Zeiss
Microscope Olympus Motic AE31	Olympus
Microwave	AEG
Milli-Q water preparation system	Merck
Mini-PROTEAN Tetra Vertical Electrophoresis Cell	BioRad
Mr. Frosty Freezing Box	Thermo Fisher Scientific
Nanodrop	Implen
PCR Cycler Thermocycle 48	SensoQuest
pH meter	InoLab
Pipette Accu-jet Pro	Brand
Power supply NanoPac 500	Cleaver Scientific
Power supply PowerPac 3000	BioRad
qPCR CFX connect Real-time system	BioRad
Sterile work bench HERASAFE	Thermo Fisher Scientific
Stereomicroscope, Stereo Lumar.V12	Zeiss
Rheometer RSA-G2	TAinstruments
Transfer System Trans-Blot Turbo	BioRad
Vortex Genie 2	Schütt Labortechnik
Waterbath	Memmert

2.9 Consumables

Tab. 10: List of all consumable material used.

Name	Manufacturer
12-well CytoOne plate, TC-treated	Starlab (#CC7682-7512)
6-cm dish, TC-treated	Nunc (#150288)
6-Well CytoOne plate, TC-treated	Starlab (#CC7682-7506)
96-well plate, u-shaped bottom, clear	Brand (#781600)
96-well plate, white, qPCR	BioRad (#HSP9601)
Aluminium foil	Roth (#2596.1)
Cell scraper, 2-position blade, size M	Sarstedt (#83.3951)
Cover slips, round, 20mm	Menzel (#CB00200RA1)
Cryotube	Nunc (#377224)
FluoroDish cell culture dish, 35mm	WPI (#FD35-100)
Microseal B PCR plate seals	BioRad (#MSB1001)
Multiply-µStrip Pro 8	Sarstedt (#72.991.002)
Nitrocellulose membrane	Sigma-Aldrich (#GE10600002)
Pasteur pipettes	Th. Geyer (#7691061)
Pipette filter tips (10/200/1250µl)	Starlab (#S1120-3710, S1120-1740, S1182-1730)
Pipette tips (10/200/1250µl)	Starlab (#S1111-3700-C, S1111-1706-C, S1112-1720-C)
Polystyrene test tube, 5 ml, round bottom	BD Falcon (#352058)
Polyvinylidene difluoride (PVDF) membrane	Sigma-Aldrich (#GE10600023)
Reaction tube 0.5ml	Eppendorf (#0030121023)
Reaction tube 0.5ml, brown	Eppendorf (#30121155)
Reaction tube 1.5ml	Eppendorf (#0030120086)
Reaction tube 1.5ml, brown	Eppendorf (#0030120191)
Reaction tube 15ml	Sarstedt (#62.554.002)
Reaction tube 2.0ml	Eppendorf (#0030120094)
Reaction tube 2.0ml, brown	Eppendorf (#0030120248)
Reaction tube 5.0ml	Th. Geyer (#7696741)
Reaction tube 50ml	Sarstedt (#62.547.004)
Scalpel No. 22	Feather (#02.001.30.022)
Serological pipettes 10ml	Sarstedt (#86.1254.001)
Serological pipettes 25ml	Sarstedt (#86.1685.001)
Serological pipettes 50ml	Sarstedt (#86.1256.001)
Serological pipettes 5ml	Sarstedt (#86.1253.001)
Sterile filter Steriflip 50ml	Merck (#SCGP00525)
Sterile filter Steritop 250ml	Millipore (#SCGPT02RE)
Superfrost plus adhesion microscope slides	Thermo Scientific (#J1800AMNZ)
T25 flask, TC-treated	Sarstedt (#833910002)
T75 flask, TC-treated	Sarstedt (#833911002)
Whatman blotting paper	Sigma-Aldrich (#WHA10426890)

White filter cards	Thermo Scientific (#5991022)
Wipes precision and task	Kimtech (#05511, #7558)

2.10 Antibodies

Tab. 11: List of primary antibodies.

Name	Host species, isotype	Manufacturer
AFP	Rabbit, IgG	Dako (#A0008-4oC)
CAMK2δ	Rabbit, IgG	Thermo Fisher Scientific (#PA5-22168)
CAMK2δ ox	Rabbit, IgG	Biozol GmbH (#GTX36254-50)
Col1A1	Mouse, IgG	Abcam (#ab90395)
CX43	Rabbit, IgG	Abcam (#ab11370)
cTNT	Mouse, IgG	Thermo Fisher Scientific (#12699030)
FLNC	Rabbit, IgG	Sigma Aldrich, (#HPA006135)
LIN28	Goat, IgG	R&D systems (#AF3757)
MLC2v	Rabbit, IgG	Proteintech (#10906-1-AP)
NANOG	Goat, IgG	Abcam (#PA5-18406)
NCX	Mouse, IgG	Swant AG (#R3F1)
OCT4	Goat, IgG	R&D systems (#AF1759)
PLN	Mouse, IgG	Thermo Fisher Scientific (#MA3-922)
PLN_pSer16	Rabbit, IgG	Badrilla (#A010-12AP)
PLN_pThr17	Rabbit, IgG	Badrilla (#A010-13)
RYR2	Rabbit, IgG	Sigma-Aldrich (#HPA020028)
RYR2_pSer2808	Rabbit, IgG	Badrilla (#A010-30)
RYR2_pSer2814	Rabbit, IgG	Badrilla (#A010-31)
SERCA2a	Mouse, IgG	Thermo Fisher Scientific (#MA3-919)
SOX2	Mouse, IgG	R&D systems (#MAB2018)
Titin M8/M9	Rabbit, IgG	Myomedix Order form
TRA1-60	Mouse, IgG	R&D systems (#MAB4770)
Vinculin	Mouse, IgG	Abcam (#ab130007)
α-Actinin	Mouse, IgG	Sigma-Aldrich (#A7811)
α-SMA	Mouse, IgG	Sigma-Aldrich (#A2547)
β-III-Tubulin	Mouse, IgG	Covance (#MMS-435P)

Tab. 12: List of secondary antibodies.

Name	Manufacturer
Alexa488 Donkey-anti mouse IgG	Thermo Fisher Scientific (#A21202)
Alexa488 Goat-anti mouse IgG, IgM	Thermo Fisher Scientific (#A10680)
Alexa555 Donkey-anti rabbit IgG	Thermo Fisher Scientific (#A31572)
Alexa555 Donkey-anti goat IgG	Thermo Fisher Scientific (#A21432)
Cy3 goat-anti mouse IgG, IgM	Jackson ImmunoResearch Laboratories (#115-165-068)
HRP Donkey-anti mouse IgG	Thermo Fisher Scientific (#A16011)
HRP Donkey-anti rabbit IgG	Thermo Fisher Scientific (#A16023)

2.11 Oligonucleotides

All primer sequences were designed with the NCBI Primer Blast software and generated at Microsynth Seqlab.

Tab. 13: List of primers used.

Gene		Sequence 5´- 3´	Ann./ Cyc.	Method	bp
Pluripotency markers					
OCT4	fw	GACAACAATGAAAATCTTCAGGAGA	60°C/40	qPCR	473
	rev	TTCTGGCGCTTACAGAACCA			
SOX2	fw	GCTACAGCATGATGCAGGACCA	60°C/40	qPCR	135
	rev	TCTGCGAGCTGGTCATGGAGTT			
NANOG	fw	AGTCCCAAAGGCAAACAACCCACTTC	60°C/40	qPCR	164
	rev	ATCTGCTGGAGGCTGAGGTATTTCTGTCTC			
LIN28	fw	AGTAAGCTGCACATGGAAGG	60°C/40	qPCR	410
	rev	ATTGTGGCTCAATTCTGTGC			
GDF3	fw	GTCTCCCGAGACTTATGCTACG	60°C/40	qPCR	136
	rev	AGTAGAGGAGCTTCTGCAGGCA			
Germ layer markers					
AFP	fw	ACTCCAGTAAACCCTGGTGTTG	60°C/36	RT-PCR	255
	rev	GAAATCTGCAATGACAGCCTCA			
ALB	fw	CCTTTGGCACAATGAAGTGGGTAACC	60°C/40	RT-PCR	355
	rev	CAGCAGTCAGCCATTTCACCATAGG			
cTNT	fw	GACAGAGCGGAAAAGTGGGA	62°C/32	RT-PCR	305
	rev	TGAAGGAGGCCAGGCTCTAT			
αMHC	fw	GTCATTGCTGAAACCGAGAATG	60°C/35	RT-PCR	413
	rev	GCAAAGTACTGGATGACACGCT			
MAP2	fw	CCACCTAGAATTAAGGATCA	55°C/35	RT-PCR	479
	rev	GGCTTACTTTGCTTCTCTGA			
PAX3	fw	AGAAGCCGAACCACCTTCAC	56°C/35	RT-PCR	383
	rev	GGGTTGGAAGGAATCGTGCT			
Housekeeping genes					
GAPDH	fw	GTCTCCTCTGACTTCAACAGCG	60°C/40	qPCR	110
	rev	ACCACCCTGTTGCTGTAGCCAA			
GAPDH	fw	AGAGGCAGGGATGATGTTCT	60°C/32	RT-PCR	258
	rev	TCTGCTGATGCCCCCATGTT			
18S	fw	ACCCGTTGAACCCCATTCGTGA	60°C/40	qPCR	159
	rev	GCCTCACTAAACCATCCAATCGG			
TUBB5	fw	CTGGACCGCATCTCTGTGTACT	60°C/40	qPCR	117
	rev	GCCAAAAGGACCTGAGCGAACA			
Fibroblast specific markers					
Col1A1	fw	AGACAGTGATTGAATACAAAACCA	60°C/40	qPCR	130
	rev	GGAGTTTACAGGAAGCAGACA			
FSP1	fw	TCTTTCTTGGTTTGATCCTGACT	60°C/40	qPCR	130
	rev	AGTTCTGACTTGTTGAGCTTGA			
TCF21	fw	CAACCTGACGTGGCCCTTTA	60°C/40	qPCR	86

	rev	TGGTTCCACATAAGCGGCTC			
CTGF	fw	TTGGCAGGCTGATTTCTAGG	60°C/40	qPCR	193
	rev	GGTGCAAACATGTAACTTTTGG			
POSTN	fw	ACAAGAAGAGGTCACCAAGGTC	60°C/40	qPCR	109
	rev	CTTCCTCACGGGTGTGTCTC			
Cardiac markers					
ACTA2	fw	AAGCACAGAGCAAAAGAGGAAT	60°C/40	qPCR	76
	rev	ATGTCGTCCCAGTTGGTGAT			
ACTA2	fw	CAGCCAAGCACTGTCAGGAAT	58°C/50	RT-PCR	477
	rev	CATAGAGAGACAGCACCGCC			
βMHC	fw	AGACTGTCGTGGGCTTGTATCAG	60°C/40	qPCR	101
	rev	GCCTTTGCCCTTCTCAATAGG			
MLC2v	fw	GGCGAGTGAACGTGAAAAAT	60°C/40	qPCR	200
	rev	CAGCATTTCCCGAACGTAAT			
PITX2	fw	AGCCATTCTTGCATAGCTCG	60°C/40	qPCR	108
	rev	GTGTGGACCAACCTTACGGA			
GJA1	fw	GGGTTAAGGGAAAGAGCGACC	60°C/40	qPCR	248
	rev	CCCCATTCGATTTTGTTCTGC			
PLN	fw	AGCACGTCAAAAGCTACAGAATCT	60°C/40	qPCR	132
	rev	CTGATGTGGCAAGCTGCAGATC			
FLNC	fw	ATGGTAGCTGCACCGTGGAGTA	60°C/40	qPCR	121
	rev	TCCACCACATCCTTCACTGGCA			
FLNC_seq	fw	CTCCCTTGACCACACAGGAA	56°C/36	Sanger seq	207
	rev	AAGTCCCCAAACACAGCAGG			
ILK_seq	fw	GGCCAGTGGCTTCTCTCTAC	56°C/36	Sanger seq	251
	rev	GACACCTCTGGAGTTCAGGC			
SERCA	fw	GGACTTTGAAGGCGTGGATTGTG	60°C/40	qPCR	129
	rev	CTCAGCAAGGACTGGTTTTCGG			
NCX	fw	AAGTGACTGAAAATGACCCTGTTAG	60°C/40	qPCR	401
	rev	AAAAATAGTTACAGTGGCAGTGGAG			
CaMKIIδ	fw	ACACGGTGACTCCTGAAGCCAA	60°C/40	qPCR	145
	rev	GTCTCCTGTCTGTGCATCATGG			
Off-target analysis					
GFPT2	fw	GAGGGCTCCGGGTTATAAGG	50°C/36	Sanger seq	155
	rev	CTGCTTCTCGGGCTCCTTC			
IGSF11	fw	AGCTGGGTAGCATGCTCACT	50°C/36	Sanger seq	260
	rev	TGTCACGATGGCCTGACCAT			
JAKMIP3	fw	TTGCCTCTTCCACATCAGGT	50°C/36	Sanger seq	298
	rev	AGTTTTGTTCACATTTGCCC			
LGR4	fw	GATCAGGTCGGGTTGCTAGT	50°C/36	Sanger seq	563
	rev	TCTAATTCCTCTAACCTCCAGCAAA			
NLRP6	fw	CAAAACAACTGCCAGCCTCC	50°C/36	Sanger seq	321
	rev	TGCTTTCCACTCACCAGGAC			

2.12 Software

Tab. 14: List of all software used.

Software	Supplier
AxioVision software	Carl Zeiss Microscopy GmbH, Germany
BioEdit	http://www.mbio.ncsu.edu/BioEdit/bioedit.html
CFX Connect Real-time PCR system	Bio-Rad Laboratories Inc.
EndNote basic	Thomson ISI ResearchSoft, CA, USA
Flowing Software	Perttu Terh
Image Lab Software	Bio-Rad Laboratories Inc.
ImageJ/Fiji	National Institutes of Health
IonWizard	IonOptix
Lab Chart	AD Instruments
Microsoft Office	Microsoft Co., Redmond, USA
Mikrowin 2000/2010	Mikrotek Laborsysteme GmbH
Prism 6/8/9	GraphPad Software Inc.
ZEN	Carl Zeiss Microscopy GmbH, Germany

2.13 Online Programs

Tab. 15: List of all online programs used.

Program	Website
Basic Local Alignment Search Tool (BLAST)	https://blast.ncbi.nlm.nih.gov/Blast.cgi
CRISPOR	http://crispor.tefor.net/
Ensemble	https://www.ensembl.org/index.html
Jefferson Off-Spotter	https://cm.jefferson.edu/Off-Spotter/
National Center for Biotechnology Information (NCBI)	http://www.ncbi.nlm.nih.gov/
Reverse Complement	http://www.bioinformatics.org/sms/rev_comp.html

3 Methods

3.1 Cell culture

All cells were cultured in a humidified atmosphere at 37°C, 5% CO_2 and 95% humidity. All cell culture handling was performed under sterile conditions using a laminar flow workbench.

3.1.1 Coating cell culture plates with Geltrex

In order to cultivate human iPSC, iPSC-cardiomyocytes and iPSC-CFB, cell culture plates needed to be coated with Geltrex before passaging the cells. For this purpose, frozen Geltrex aliquots (2mg) were thawed and resuspended thoroughly in cold DMEM (12ml; 167mg/l). 1ml/6-well, 0.5ml/12-well, 2ml/T25 flask, 4ml/T75 flask and 1ml/FluoroDish of the Geltrex/DMEM solution were added and distributed properly. The coated plates were incubated 30min at 37°C or overnight (ON) at 4°C before usage. Coated plates could be stored at 4°C for up to 1.5 weeks.

3.1.2 Glass coverslip preparation

For certain experiments, e.g., IF staining, iPSC, iPSC-cardiomyocytes or iPSC-CFB were digested onto round glass cover slips with a diameter of 20mm for 12-well plates or 25mm for 6-well plates. Before usage, the coverslips needed to be cleaned and sterilized properly. Hence, they were incubated for 1h in 0.1M hydrochloric acid and in 70% ethanol for 30min. Afterwards, the coverslips were dried with lint-free paper and sterilized for 2h at 200°C.

3.1.3 Feeder-free cultivation of human iPSC on Geltrex

Human iPSC were cultured in 1.5ml E8 medium on Geltrex-coated 6-well plates, with a daily medium change. To maintain the iPSC over time, they needed to be passaged twice a week or when reaching 80-90% confluency. To passage human iPSC the cells were washed once with 1ml/6well Versene. Afterwards, they were incubated in 1ml/6well Versene for 3-5min (depending on iPSC line) at room temperature (RT). As soon as the cells started to detach the Versene solution was aspirated carefully, and the cells were detached by gently resuspending 1-3 times with 1ml/6well E8 medium including 2µM Thiazovivin (TZV). After detaching and resuspending the desired number of cells was transferred to a Geltrex-coated 6-well plate containing 1.5ml E8/TZV medium. The TZV was removed with the next medium change.

3.1.4 Cryopreservation of hiPSC on Geltrex

In order to cryopreserve hiPSC, the cells were washed once with 1ml/6well Versene and incubated again in Versene for 3-5min (depending on iPSC line) at RT. Versene solution was aspirated carefully, the cells were detached by carefully resuspending with 1ml/6well E8 medium and transferred to a 15ml falcon tube. The cells were sedimented by centrifugation for 5min at 200xg. The medium was aspirated, the cells were resuspended in 1ml Bambanker freezing medium and transferred to a cryotube. The cells were frozen and stored at -80°C.

3.1.5 Thawing hiPSC on Geltrex

To thaw hiPSC the cells were thawed rapidly in a 37°C water bath and transferred quickly into a 15ml falcon containing 5ml E8 medium. Afterwards the cells were sedimented by centrifugation at 200xg for 5min. The supernatant was discarded, and the cells were resuspended in 2ml E8 medium containing 2µM Thiazovivin and transferred to a well of a 6-well plate.

3.1.6 Spontaneous *in vitro* differentiation of iPSC

In the process of pluripotency characterization of all iPSC lines the ability of the cells to spontaneously differentiate into cells of all three germ layers was tested. Therefore, cryopreserved mitotically inactivated MEFs were thawed in a 37°C water bath, transferred to 5ml DMEM, centrifuged at 200xg for 5min and resuspended in 1ml E8 medium. In parallel, iPSC of the desired line were detached using Versene and resuspended in 1ml/6well E8 medium as well. MEFs and iPSC were counted with the Thoma hemocytometer and 2.63 million MEFs and 5.25 million hiPSC were mixed and filled up with E8 to a total volume of 20ml. 200µl of this cell mixture were added to each well of a 96-well u-bottom plate. The plate was centrifuged briefly to allow EB formation at the bottom of the plates and the cells were incubated under standard conditions. The medium was changed on day 1, 3, 5 and 7 by carefully removing 100µl old medium and replacing it by 100µl Iscove differentiation medium (see Tab. 3). On day 8, eight EBs were pooled into a 1.5ml reaction tube, centrifuged, the supernatant discarded and the cells snap-frozen and stored at -80°C for later RNA isolation and PCR analysis. The remaining EBs were plated onto 12-well plates (8 EBs/well) with or without cover slips according to the scheme shown in Fig. 9.

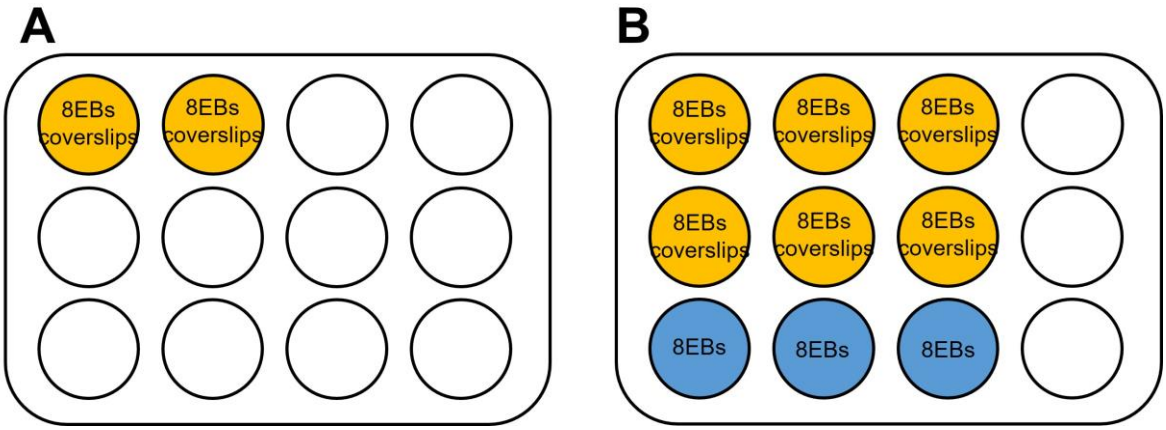

Fig. 9: Plating scheme for spontaneous *in vitro* differentiation day 8.

The cells were incubated further, and the medium was changed every 2-3 days with Iscove differentiation medium. On day 8+10 the cells plated onto plate A (Fig. 9) were fixed as described in 3.1.11 and the plates were stored at 4°C until later IF staining of α-feto protein (AFP). On day 8+25 cells on the six coverslips on plate B (Fig. 9) were fixed for later IF staining of αSMA and βIII-tubulin. The cells of the remaining three wells were collected as pellets, snap-frozen and stored at -80°C for later RNA isolation and PCR analysis.

3.1.7 Directed differentiation into iPSC-stromal cells

For directed differentiation into iPSC-stromal cells (StC) a previously published protocol (Iyer *et al.*, 2016) was modified. A schematic overview of the differentiation process can be found in Fig. 10.

To differentiate iPSC directly into iPSC-stromal cells 20,000 cells/well were plated onto Geltrex-coated 12-well plates. When reaching ~80-90% confluency after four days of cultivation (day 0) the differentiation process was started by once washing the cells with RPMI1640 and inducing differentiation into stromal cells by adding StC-IM medium for 48h. On day 2 the non-canonical Wnt signaling was inhibited by medium change to CDM to induce a differentiation into a mesodermal direction. On day 3 the cells were passaged with 150,000 cells/well onto Geltrex-coated 12-well plates using 0.25% trypsin/EDTA for 5min at 37°C. The cells were cultured in StC-SM medium for seven days with medium change every second day. Then the medium was changed to StC-EM+C to induce specification into the cardiac lineage and support fibroblast proliferation. The medium was changed every second day. On day 14 the cells were detached by Accutase treatment for 10-20min at RT, followed by additional Versene treatment for 5min at RT. 250,000 cells/well were plated onto Geltrex-coated 6-well plates and cultured in StC-EM medium. The medium was changed every second day. The cells were passaged again around day 22 again using Accutase/Versene treatment, to provide more space important for proper expansion of the cells. Afterwards, cells were passaged depending on cell density about once a week. Between passage five and 15 cells could be expanded to higher cell numbers and plated onto T25- or T75-flasks for analysis, like ECT casting, pellet collection or IF staining or cryopreservation.

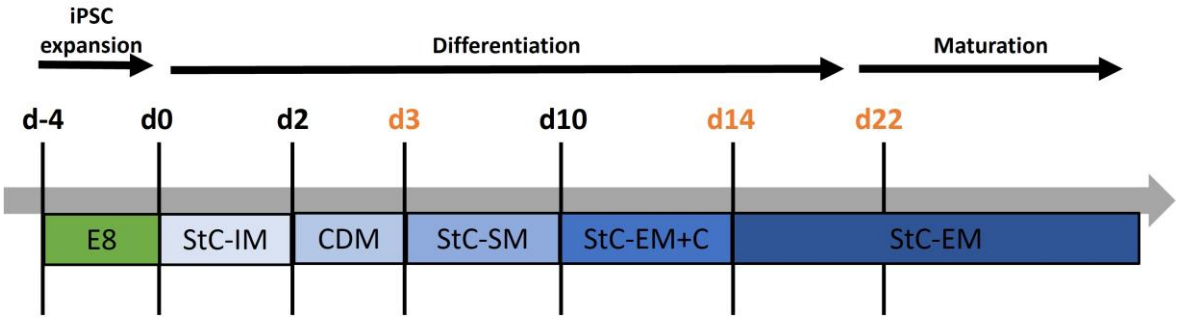

Fig. 10: Schematic overview of directed differentiation into stromal cells. The days marked in orange indicate days of passaging. Differentiation was started when iPSC reached ~80-90% confluency. E8= Essential 8 medium, StC-IM=Stromal cell induction medium, CDM=Cardiac differentiation medium, StC-SM=Stromal cell specification medium, StC-EM=Stromal cell expansion medium, C=CHIR99021.

3.1.8 Directed differentiation into ventricular iPSC-cardiomyocytes

For directed differentiation of iPSC into iPSC-cardiomyocytes, a protocol was used based on the modulation of canonical and non-canonical Wnt signaling pathways as previously described (Burridge and Zambidis, 2013; Lian *et al.*, 2013). A schematic overview of the differentiation process can be found in Fig. 11.

iPSC were seeded onto Geltrex-coated 12-well plates. When reaching 70-90% confluency (d0) the medium was exchanged by Cardio differentiation medium (2ml/well) which was

supplemented with 4µM of the GSK3-inhibitor CHIR99021 to activate Wnt signaling. After 48h (d2) the medium was changed to Cardio differentiation medium (2ml/well) supplemented with 5µM of the inhibitor of Wnt signaling, IWP2. Another 48h later (d4) the medium was replaced by Cardio differentiation medium (2ml/well) without further supplements. On day six the medium was changed to Cardio culture medium (2ml/well), which was changed every second day. The cells started functional beating between day seven to 14, which was when the cells were digested in lower cell density onto Geltrex-coated 6-well plates. For this, the cells were incubated in 0.5ml/well 0.25% Trypsin/EDTA for 5min at 37°C and resuspended in equal amounts of FCS. The cells were transferred to a 15ml falcon and centrifuged for 5min at 200xg. The supernatant was aspirated, and the pellet resuspended in Cardio digestion medium. The cells were counted with a Thoma hemocytometer, and 600,000 cells were plated into 2ml/well Cardio digestion medium onto 6-wells plates. After 48h the medium was changed to Cardio selection medium to metabolically select for pure iPSC-cardiomyocytes culture by depletion of glucose and supplementation of lactate. Depending on purity and well-being of the cells, the medium was changed to Cardio culture medium (2ml/well) after 4-6 days of selection. Cardio culture medium was changed every 3-4 days for long-term culture. The iPSC-cardiomyocytes were cultivated for 90 days before analysis if not stated otherwise.

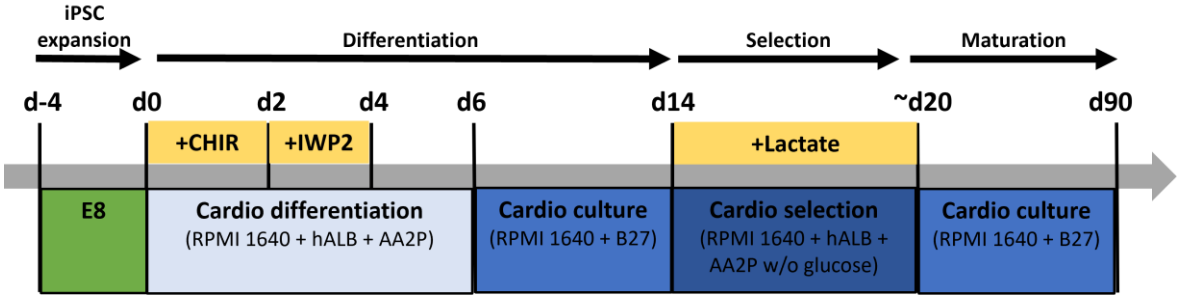

Fig. 11: Schematic overview of directed differentiation into ventricular iPSC-cardiomyocytes. The differentiation started with Wnt pathway activation for 48h via addition of CHIR99021, followed by Wnt pathway inhibition for 48h via addition of IWP2. The addition of lactate and depletion of glucose on day 16 allowed metabolic selection.

3.1.9 Digestion of iPSC-cardiomyocytes

For different analyses certain cell densities or cell numbers of iPSC-cardiomyocytes were required for proper conduction of experiments and comparison of results. For this, the iPSC-cardiomyocytes were replated from long-term culture 6-well dishes (initially 600,000 cells) in the required number onto suitable dishes. Densities and cell numbers for certain experiments are summarized in

Tab. ***16***. For digestion of iPSC-cardiomyocytes 1ml/well 0.25% Trypsin/EDTA were added for 3-5min at 37°C. The detached cells were resuspended in equal amounts of FCS and transferred to a 15/50ml falcon. The cells were centrifuged for 5min at 200xg, the supernatant was aspirated, and the pellet resuspended in Cardio digestion medium. If necessary, the cell number was evaluated by using the Thoma hemocytometer. Desired amounts of cells were plated onto Geltrex-coated plates or dishes into Cardio digestion

medium. After 48h the medium was changed to Cardio culture medium. Until analysis the medium was changed every 2-3 days.

Tab. 16: Number of iPSC-cardiomyocytes used for different read-outs.

Experiment	Dish/plate	Cell number	Density	Culture time after digestion until analysis
Sarcomere analysis of iPSC-cardiomyocytes	12-well with 20mm cover slip	2.5 x 10^4	Single cells/small colonies	5-7 days
IF of iPSC-cardiomyocytes	12-well with 20mm cover slip	2.5 x 10^4	Single cells/small colonies	5-7 days
Ca^{2+} with Fluo-4	6-well with 25mm cover slip	1.8-2.3 x 10^5	Confluent monolayer	7-8 days
Ca^{2+} with FURA-2	35mm FluoroDish	3.0 x 10^4	Single cells	7-8 days
Cell Size with CASY	12-well with 20mm cover slip	2.0 x 10^4	Single cells/small colonies	10 days
ROS (AmplexRed)	6-well	6.0 x 10^5	Confluent monolayer	7-14 days

3.1.10 Pellet collection of cells

For pellet collection, cells (fibroblasts, iPSC, iPSC-cardiomyocytes, iPSC-StC) were washed once with 1ml/well 1x DPBS. The cells then were mechanically detached in 1ml 1x DPBS with a cell scraper into a 1.5ml tube. The cells were centrifuged for 1min at 13,000xg. The supernatant was aspirated, and the pure cell pellet was snap-frozen in liquid nitrogen. The cell pellets then were stored at -80°C until further analysis.

3.1.11 Fixation of cells on coverslips

In order to fix cells on coverslips for immunostaining, the cells were washed once with 1ml/well 1x DPBS. 1ml/well Histofix was added, and the cells were incubated for 20min at RT. The Histofix was removed, and the cells were washed 2x with 1ml/well 1x DPBS. Afterwards 2ml/well 1% BSA/1x DPBS was added, the plates were sealed with parafilm and stored at 4°C until further analysis.

3.1.12 Cell size measurement using CASY

To analyze the cell size of iPSC-cardiomyocytes the CASY cell counter and analyzer was used. For this 25,000 cells/well were plated onto Geltrex-coated 12-well plates and cultivated for ten days. Three hours before measurements the Cardio culture medium was renewed. The cells were washed once with 1ml/well Versene and digested using 0.25% Trypsin/EDTA for 10min at 37°C. The cells were resuspended in equal volume of FCS and transferred to a 1.5ml tube. The cells were centrifuged for 10min at 100xg. The supernatant

was removed, and the cell pellet was resuspended in 250µl Cardio culture medium (without TZV). The cell solution was added to 10ml CASYton isotonic buffer. The CASY cell counter and analyzer then was used to analyze the iPSC-cardiomyocytes for mean and peak diameter. In brief, the sample is sucked up through a small capillary through an electric field. Each cell induces an electric stimulus, whose size is directly proportional to the cell volume of each cell. By setting the detection minimum manually to 14.99 µm, it was possible to exclude cell debris and dead cells and to include iPSC-cardiomyocytes only.

3.1.13 CRISPR/Cas9 genome editing

To analyze the role of the identified FLNC variant (c.6560G>C het, p.Arg2187Pro) within the DCM development, isogenic controls of the patients´ iPSC lines were generated by CRISPR/Cas9 genome editing. In these lines the specific FLNC variant was rescued to FLNC wildtype, whereas the rest of the patient`s genotype was remained (Fig. 12 A). Two different crRNAs were designed to target the Cas9 enzyme to the mutated FLNC locus in two separate experiments. The crRNAs were designed at CRISPOR.org (http://crispor.tefor.net/) (Tab. 5). Several possible crRNAs were suggested, the used crRNAs were chosen based on high specificity scores (i.e., low number of predicted off-target effects; MIT and CFD scores were used) and close proximity of the corresponding PAM sites to the targeted variant. Close proximity of the PAM to the target site allows DSB close to the site of intended editing, which should increase probability of nucleotide exchange/repair upon HDR. The following crRNAs were chosen and generated at IDT: 5`-TGATCTCCGTGCGCTCCGTG-3` (FLNC1, Fig. 12 B) and 5`- CTGATCTCCGTGCGCTCCGT-3` (FLNC2, Fig. 12 C). Both crRNAs were designed to target the reverse strand of *FLNC*. The crRNA FLNC1 had a MIT score of 93 and a CFD score of 97. The crRNA FLNC2 had a MIT score of 94 and a CFD score of 97. The PAM sites for both crRNA were spanning the targeted variant (Fig. 12 B, C). This additionally holds the advantage that upon correct HDR (repair of variant) the PAM site was destroyed, and re-cutting probability was reduced. The HDR template was generated at IDT as well: 5´-AGCGCCTGACACGCACCTTCACACGCAGCAGCCACACCTACACCC**G**CAC**C**GAGCGCACGGAGAT **A**AGCAAGACGCGGGGCGGGGAGACAAA-3` (Fig. 12 D). The HDR template harbored the wildtype FLNC variant at position c.6560G/p.Arg2187 (highlighted in red, Fig. 12D) and two artificially introduced, synonymous mutations at the PAM and crRNA binding sites (highlighted in red and green, Fig. 12 D). These synonymous mutations were introduced to prevent additional binding of the crRNAs and following DSB by the Cas9, after successful editing and hence improving editing efficiency. The Cas9 protein, crRNA, and the ssDNA HDR template were introduced into the iPSC by electroporation as described below.

1. **Generation of CRISPR-RNA mix**
   5µl crRNA (100µM) were mixed with 5µl tracrRNA (trans-activating-crRNA, 100µM) and incubated for 5min at 95°C. Following, the CRISPR-RNA mix was cooled down to RT for about 15min.
2. **Generation of CRISPR-RNP complex**
   The CRISPR-RNA mix (see 1.) was mixed properly and 6µl of it were added to 2µl Cas9 protein (10µg/ml). The mixture was incubated for 20min at RT and then was transferred to 37°C.

3. **Preparation of Nucleofector solution**
   82µl nucleofector solution and 18µl nucleofector supplement (both provided with the Human Stem Cell Nucleofector Kit 2) were mixed with 8µl of the CRISPR-RNP complex (see 2.), 1µl of electroporation enhancer and 3µl of the designed HDR template (100µM). The mix was incubated at 37°C.
4. **Preparation of iPSC**
   One hour prior to the start of the experiment the medium of 4/6 wells of iPSC (~70-80% confluency) was changed from E8 to 1ml/well StemFlex/TZV (2µM). The cells were washed twice with Versene and were detached as previously described. The cells were resuspended in StemFlex/TZV and counted with the Thoma hemocytometer. 2x106 cells were transferred to a 1.5ml tube and centrifuged for 5min at 200xg. The supernatant was aspirated, and the cell pellet was resuspended in the nucleofector solution (see 3.).
5. **Electroporation**
   The cell solution was transferred to a nucleofection cuvette and placed into the Amaxa Nucleofector II Device. For electroporation, the program B-016 was used. Afterwards, the cell suspension was transferred carefully to 800µl fresh StemFlex/TZV, without transferring the foam. The cell suspension was splitted (300µl/well) to four Geltrex-coated 6-wells into StemFlex/TZV/PenStrep. Two wells were treated with 6.67µl HDR enhancer (20µM), one well was treated with 3.34µl HDR enhancer (10µM) and one well remained untreated. The cells were incubated under standard conditions. The medium was changed 20h after the electroporation to fresh StemFlex/TZV/PenStrep.
6. **Singularization**
   48h after electroporation the cells were detached by using Versene and were counted with the CASY cell counter. For this 20µl of the cell suspension was added to 10ml CASY ton buffer. Different cell numbers (800, 1000, 1200, 1400, 1600, 1800 cells) were plated onto Geltrex-coated 6-well plates. StemFlex medium was changed every second day.

The cells were grown under standard conditions for 7-10 days. 36 colonies were picked, and each was transferred to a new well of a Geltrex-coated 6-well plate. The cells were grown until reaching 70-80% confluency. Then the cells were detached by using Versene for 10min. Half the cells were cryopreserved in Bambanker medium and stored at -80°C, the other half was pelleted and snap-frozen in liquid nitrogen for gDNA isolation and Sanger sequencing.

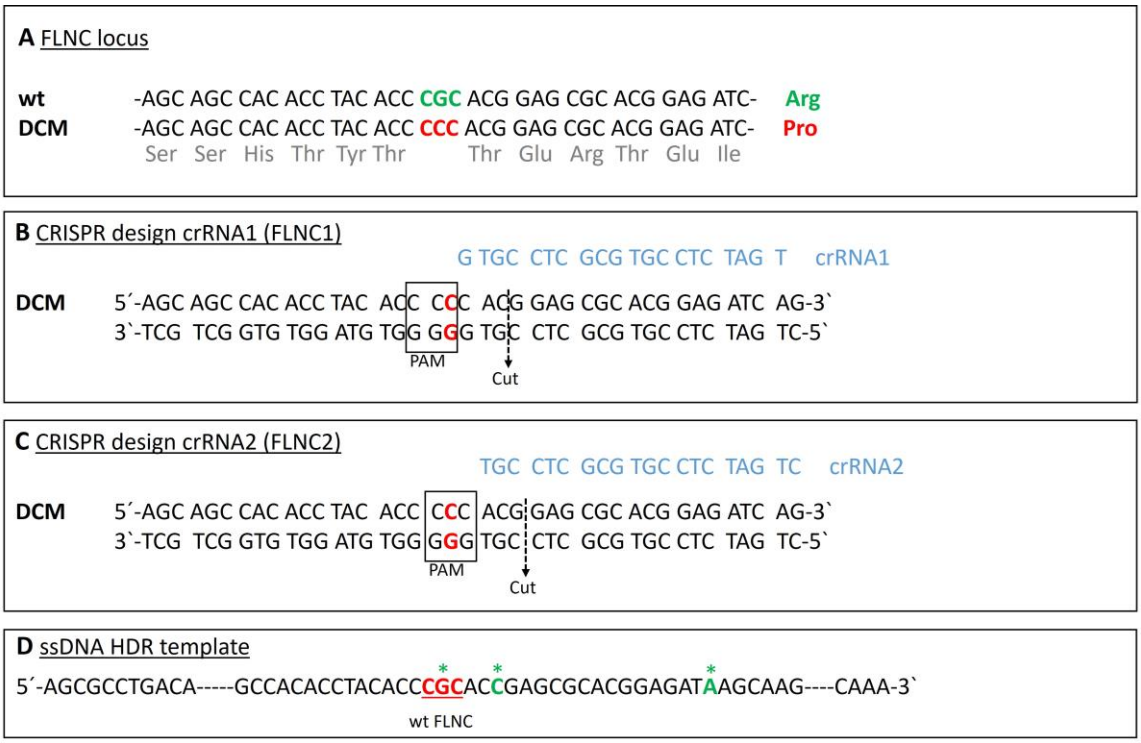

Fig. 12: CRISPR strategy to rescue *FLNC* variant in DCM iPSC patient lines. A The *FLNC* locus of wt and DCM patients with the respective nucleotide exchange. **B** CRISPR design for DCM using crRNA1 (FLNC1). **C** CRISPR design for DCM using crRNA2 (FLNC2). **D** HDR template used for both CRISPR approaches. * Synonymous mutations.

3.2 Molecular biology

3.2.1 Genomic DNA isolation

Genomic DNA (gDNA) was isolated from iPSC and iPSC-cardiomyocytes using the QIAmp DNA kit (Qiagen) according to manufacturer`s instructions following the protocol for "cultured cells." Concentration was determined by using a NanoPhotometer (Implen) and DNA was diluted to 100ng/µl in nuclease-free H_2O for further analysis.

3.2.2 RNA isolation

For expression analysis RNA needed to be isolated from snap-frozen cell pellets. For RNA isolation of iPSC, iPSC-StC and EBs the SV Total RNA-Isolation System kit (Promega) was used according to manufacturer`s instructions. For RNA isolation of iPSC-cardiomyocytes the Relia Prep RNA Tissue Miniprep System kit (Promega) was used according to manufacturer`s instructions. In both cases, the suggested DNA digestion step was omitted, as a separate DNase I treatment was performed prior to reverse transcription.

3.2.3 DNase I digestion

To purify the RNA by removing residual co-isolated DNA, a DNase I digestion step was performed for all RNA samples prior to reverse transcription. For this, the DNase I kit (Zymo Research) was used according to manufacturer`s instructions. Following, the RNA was purified to remove components of the DNase I digestion and to concentrate the RNA again. For this, the RNA Clean & Concentrator-5 Kit (Zymo Research) was used according to

manufacturer`s instructions. The resulting final RNA concentration was determined using a NanoPhotometer (Implen).

3.2.4 Reverse transcription of RNA

For expression analysis the isolated and purified RNA was transcribed into c(opy)DNA using the enzyme reverse transcriptase. The iScript cDNA Synthesis Kit (BioRad) was used according to manufacturer`s instructions. In brief, 200ng of each RNA sample in a volume of 15µl were mixed with 4µl 5x iScript™ Reaction Mix and 1µl iScript™ Reverse Transcriptase to a total volume of 20µl. For each reaction, a negative control (-RT sample) was prepared without adding the reverse transcriptase enzyme, to check for proper DNA removal in the Dnase I digestion step. All samples were incubated in a thermal cycler following the protocol shown in Tab. 17. After the reverse transcription 20µl nuclease-free ddH_2O were added to each sample to obtain a final concentration of 1µg/µl for further analysis.

Tab. 17: Reaction protocol for reverse transcription using the iScript cDNA Synthesis Kit (BioRad).

Step	Time (min)	Temperature
Priming	5	25°C
Reverse transcription	20	46°C
RT inactivation	1	95°C
Optional step	Hold	4°C

3.2.5 Semi-quantitative PCR

For semi-quantitative PCR, a master mix (Tab. 18) with a total volume of 24µl per sample was prepared for each genomic marker to be analyzed according to the number of samples. In addition to the analyzed samples, the -RT and a water sample were used as negative controls. 1µl (1µg/µl) sample was added per reaction. The samples were prepared on ice, placed, and run in a thermal cycler. A general protocol shown in Tab. 19 was used. The protocol needed to be adjusted based on the used primers in annealing temperature and number of cycles (see Tab. 13). The PCR product was evaluated by agarose gel electrophoresis.

Tab. 18: Master mix for semi-quantitative PCR. To each reaction of 24µl master mix, 1µl sample (1µg/µl) was added.

Components of master mix	Amount per sample
Nuclease-free water	15.3 µl
5x Green GoTaq reaction buffer	5 µl
10 mM dNTPs	1.6 µl
10 µM sense primer	1 µl
10 µM antisense primer	1 µl
GoTaq DNA polymerase	0.1 µl
Total	**24 µl**

Tab. 19: Reaction protocol for semi-quantitative PCR. Annealing temperature and cycle number (X) needed to be adjusted specifically for each primer pair. Respective conditions for each primer pair can be found in Tab. 13.

Step	Temperature (in °C)	Time (in min)	Cycles
Initial Denaturation	95	3:00	1
Denaturation	94	0:15	X
Annealing	X	0:15	
Elongation	72	0:30	
Final Elongation	72	10:00	1
Hold	4	∞	∞

3.2.6 Quantitative PCR

In order to quantify the amount of specific gene expression a quantitative real-time PCR (qPCR) was performed. For the qPCR, the BioRad CFX Connect Real-time PCR system was used. A master mix (Tab. 20) was prepared by calculating each sample and negative controls (-RT, water) as duplicates. 19µl/well of the master mix were pipetted into a well of a 96-well plate. The cDNA (1µl/well) was added, the plate was sealed and centrifuged shortly. The plate was applied to the BioRad CFX Connect Real-time PCR machine and the protocol shown in Tab. 21 was used. The machine calculates the threshold cycle (ct) value, which is defined as the PCR cycle at which enough PCR product was amplified to cross a certain background threshold. The lower the ct value, the higher the expression of a specific gene. Ct values >35 were considered negative. To calculate relative amounts of genes expressed, the ΔCt method was used, in which the ct value of specific genes was normalized to the ct value/expression of housekeeping genes, like *GAPDH, 18S* or *TUBB5*. Normalized data was then evaluated by the $2^{-\Delta\Delta Ct}$ method.

Tab. 20: Master mix for quantitative PCR. To each reaction of 19µl master mix, 1µl sample (1µg/µl) was added.

Components of master mix	Amount per sample
iQ SYBR Green Supermix	10µl
Nuclease-free water	7µl
10 µM sense primer	1µl
10 µM antisense primer	1µl
Total	**19µl**

Tab. 21: Reaction protocol for quantitative PCR.

Step	Temperature (in °C)	Time (in min)	Cycles
Initial Denaturation	95	3:00	1
Denaturation	94	0:10	40
Annealing	60	0:20	
Elongation	72	0:30	
	95	0:10	1
Melt curve	60-95	in 0.05°C steps	

3.2.7 Agarose gel electrophoresis

PCR product presence and size of semi-quantitative PCRs were evaluated by agarose gel electrophoresis. Depending on expected product size 1.5-2.0% agarose gels were prepared. For this, agarose powder was mixed with 1x TBE buffer and boiled in a microwave to dissolve completely. After cooling down to RT, Midori Green Advanced (in-gel DNA stain, 0.07µl/ml) was added. The agarose solution was cast into a gel tray, where it polymerized for 30min. When the gel was polymerized, it was transferred to a running chamber filled with 1x TBE buffer. The comb was removed. 10µl 100bp Gene ruler and 5-20µl PCR product were loaded. The PCR fragments were separated at 120V for 30-60min. The PCR products then were visualized using the ChemiDoc XRS+ imaging system and the Image Lab software.

3.2.8 Gel extraction

If necessary (e.g., for subsequent Sanger sequencing), PCR products could be extracted from the agarose gel again. For this, the PCR product band was cut precisely from the gel and was transferred to a 2.0ml tube. In this case, exposure to UV light was reduced to a minimum to prevent formation of pyrimidine dimers. Using the QIAquick Gel Extraction kit (Qiagen) according to manufacturer`s instructions, including recommended additional steps for more pure products for subsequent sequencing, the DNA could be extracted and concentrated. DNA concentration was determined by using a NanoPhotometer (Implen).

3.2.9 Sanger sequencing

For regular check of iPSC line identity and screening for edited clones after CRISPR/Cas9 Sanger sequencing was performed. Sanger sequencing was performed at Microsynth Seqlab, Göttingen. For this, cell pellets were collected, gDNA was isolated (3.2.1) and the desired gene sequence was amplified by semi-quantitative PCR (3.2.5). The PCR product was applied to an agarose gel (0) and extracted (3.2.8) again to enhance product purity and to reduce subsequent sequencing background. 1.5ng/µl per 100bp of PCR product were sent in a final volume of 12µl + 3µl of the respective primer (10µM) to Microsynth Seqlab, where Sanger sequencing was performed and analyzed. The resulting chromatograms were analyzed with the BioEdit software.

3.2.10 Alkaline phosphatase staining

Activity of the ALP is upregulated in stem cells and hence works as a general marker for pluripotency characterization of the iPSC lines used. For this purpose, staining of the ALP was performed on the iPSC using the ALP staining kit (Sigma-Aldrich). iPSC were plated onto Geltrex-coated 6-well plates. When reaching ~40% confluency and TZV being removed from the medium for minimum 24h the staining was performed. A fixing solution, containing formalin, acetone and citrate buffer, was prepared according to manufacturer`s instructions. The cells were washed twice with 1x DPBS and fixed for 30sec at RT. After washing the cells twice with $ddH_2O$ a staining solution prepared according to manufacturer`s instructions was added. The staining solution consisted of fast red-violet dye, sodium nitrate, ddH_2O, and naphthol, where all components were provided by the kit and needed to be mixed prior to the staining. The cells were incubated in staining solution

for 20-30min at 37°C. Afterwards, the cells were washed twice with ddH_2O and air-dried ON. Stained cells were stored at RT until images were taken.

3.2.11 Immunofluorescence (IF) staining of 2D cells

IF staining of different cells was used to demonstrate expression of specific proteins and their localization within these cells. For this, primary antibodies are used, directly binding the protein of interest at a certain epitope. The specific binding of this antibody, then can be visualized by additional adding a secondary, fluorochrome-labeled antibody, species-specific directed against the primary antibody. For IF staining the cells were plated onto Geltrex-coated 20mm round coverslips placed into a well of a 12-well plate. iPSC were plated to reach ~40% confluency after 48h. For iPSC-cardiomyocytes ~25-30x10^4 cells, for iPSC-StC ~50-80x10^4 cells were plated. After passaging the cells were cultivated for 7-10 days after digestion to allow recovery of the cells.

Cells were fixed as described in (3.1.11), washed twice with 1x DPBS and blocked in 1% BSA/1x DPBS for at least 2h at RT or ON at 4°C. After blocking the coverslip was removed from the 12-well plate and washed with non-sterile 1x DPBS. The coverslip was placed to a humidified chamber and 200µl of the primary antibody mixed with staining buffer (1% BSA/0.1% Triton X_{100}/1x DPBS) was added. The primary antibody was incubated ON at 4°C in a humidified chamber. On the next day, the coverslip was washed three times with non-sterile 1x DPBS, and 150µl of the respective secondary antibody mixed with staining solution was added and incubated for 1h at 37°C in the dark. After incubation of the secondary antibody, the coverslip was washed again three times in non-sterile 1x DPBS and were stained with DAPI (1:50,000 in 1% BSA) for 10min at RT in the dark, to visualize the cells nuclei. Following the DAPI staining, the coverslip was washed three times in non-sterile 1x DPBS and once in ddH_2O before being mounted on microscopy slides using the Fluoromount-G mounting medium. The coverslips were sealed with nail polish and stored at 4°C until imaging. All antibodies and respective conditions used for IF can be found in Tab. 22.

Tab. 22: Antibodies and respective conditions used for IF staining of iPSC-cardiomyocytes.

Primary antibody	Host species, isotype	Dilution	Secondary antibody	Dilution
Staining of iPSC				
LIN28	Goat, IgG	1:300	Alexa555 Donkey-anti-goat	1:1000
NANOG	Goat, IgG	1:200	Alexa555 Donkey-anti-goat	1:1000
OCT4	Goat, IgG	1:40	Alexa555 Donkey-anti-goat	1:1000
SOX2	Mouse, IgG_{2A}	1:200	Cy3 Goat-anti-mouse IgG+IgM	1:300
TRA-1-60	Mouse, IgM	1:200	Alexa488 Donkey-anti-mouse IgG+IgM	1:200
Staining of embryoid bodies				
αSMA	Mouse, IgG_{2A}	1:3000	Alexa488 Donkey-anti-mouse IgG	1:1000
AFP	Rabbit, IgG	1:500	Alexa555 Donkey-anti-rabbit	1:1000

TUBB3	Mouse, IgG_{2A}	1:2000	Alexa488 Donkey-anti-mouse IgG	1:1000
Staining of iPSC-cardiomyocytes				
α-actinin	Mouse, IgG	1:500	Alexa488 Donkey-anti-mouse IgG	1:1000
cTNT	Mouse, IgG	1:500	Alexa488 Donkey-anti-mouse IgG	1:1000
FLNC	Rabbit, IgG	1:100	Alexa555 Donkey-anti-rabbit	1:750
CX43	Rabbit, IgG	1:400	Alexa555 Donkey-anti-rabbit	1:1000
MLC-2V	Rabbit, IgG	1:200	Alexa555 Donkey-anti-rabbit	1:1000
TTN (M8/M9)	Rabbit, IgG	1:750	Alexa555 Donkey-anti-rabbit	1:750
Staining of iPSC-StC				
αSMA	Mouse, IgG_{2A}	1:3000	Alexa488 Donkey-anti-mouse IgG	1:1000
COL1A1	Mouse	1:2000	Alexa488 Donkey-anti-mouse IgG	1:1000

3.2.12 Immunofluorescence staining of paraffin-embedded tissue sections

To analyze the expression of certain cardiac markers in explanted heart tissue of the diseased father paraffin-embedded tissue sections were prepared and stained with fluorescently labeled antibodies. The tissue was embedded prior to the start of this thesis by technicians of the lab. All steps were performed in staining cuvettes. For this, first the paraffin was removed by a dewaxing process in which the sections were hydrated again as follows:

Tab. 23: Dewaxing protocol for paraffin-embedded tissue sections.

Reagent	**Time**
Roti Histol	2x 5min
100% Ethanol	2x 3min
95% Ethanol	3min
80% Ethanol	3min
70% Ethanol	3min
ddH_2O	2x 5min
1x PBS	5min

Following the dewaxing process, the antigens were unmasked with citrate buffer. For this, the citrate buffer was heated until boiling for about 5min at 600W. Then the slides were added to the boiling buffer and further incubated/boiled for 15min at 160W. The slides were cooled down within the citrate buffer for 20min at RT before being washed with 1x 1x DPBS for 5min. Afterwards the slides were blocked in 100µl/slide blocking solution (5% BSA/0.1% Triton-X_{100}/PBS) for 1h at RT, before 50µl/slide primary antibody in antibody solution (2% BSA/0.1% Triton-X_{100}/PBS) was added and incubated ON at 4°C protected from light. The used antibody dilutions can be found in Tab. 24. On the following day, the slides were washed twice with PBS for 5min. Then the slides were blocked again in 100µl/slide blocking solution for 30min at RT, before 50µl/slide secondary antibody in antibody

solution was added and incubated for 1h at RT protected from light. The used antibody dilutions can be found in Tab. 24. In a next step, the slides were washed again twice with PBS, followed by a DNA staining with 100µl/slide Hoechst 33342 (1µg/ml) for 10min at RT, protected from light. The slides were washed once with ddH_2O for 5min at RT and were mounted with Mowiol mounting medium and a coverslip and dried ON at 4°C protected from light.

Tab. 24: Antibodies used for IF staining of paraffin-embedded tissue sections.

Primary antibody	Host species, isotype	Dilution	Secondary antibody	Dilution
FLNC	Rabbit, IgG	1:50	Alexa594 goat-anti-rabbit	1:200
Titin M8/M9	Rabbit, IgG	1:50	Alexa594 goat-anti-rabbit	1:200

3.2.13 Analysis of sarcomeric regularity

To analyze the regularity of sarcomeric structure within iPSC-cardiomyocytes, 25,000 iPSC-cardiomyocytes were plated onto Geltrex-coated 20mm round coverslips placed into a well of a 12-well plate. Cells were cultivated for another 7 days to allow recovery prior to fixation (3.1.11). The iPSC-cardiomyocytes were immunofluorescently stained for α-actinin and titin, to visualize sarcomeric Z-disc and M-line, respectively, as described in 3.2.11. 20-30 images of individual iPSC-cardiomyocytes per coverslip were taken. Analyzing sarcomeric regularity, the frequency of M-line and Z-disc in each iPSC-cardiomyocytes was determined. For this, the images were analyzed with ImageJ/Fiji. First, an implemented macro, called *tubness*, was used to analyze tube-like structures, like Z-disc and M-line. By applying the Fast Fourier Transformation (FFT), the resulting spatial structures were converted into frequency information as sine and cosine waves (Fig. 13). Onto these data, the *radial profile plot* plugin (ImageJ) was applied, to quantify the radial profiles (Fig. 13). The more regular the radial profiles, the more sine and cosine waves added up to a first-order peak (Fig. 13). The height of this first-order peak represented the sarcomeric regularity and was analyzed by the LabChart software.

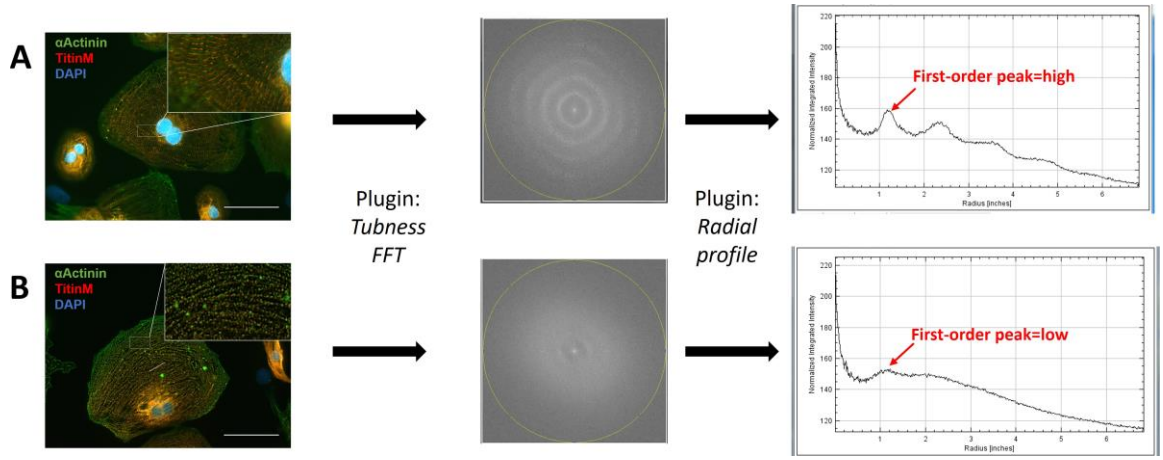

Fig. 13: Workflow for analysis of sarcomeric regularity using FFT. A Cells with a regular sarcomere structure displayed a distinct radial profile during analysis and the first-order peak is clearly identifiable and quantifiable. **B** Cells with an irregular sarcomere structure showed no radial profile and no identifiable first-order peak.

3.2.14 Detection of hydrogen peroxide activity

To analyze the level of oxidative stress within the iPSC-cardiomyocytes, the production of H_2O_2, a ROS, was analyzed exemplarily using the AmplexRed Hydrogen/Peroxide/Peroxidase Assay Kit (Thermo Fisher Scientific). The assay is based on the principle that in reaction with H_2O_2 the AmplexRed reagent is oxidated to the fluorescent resorufin, that can be detected spectrophotometrically. In preparation for the assay 600,000 iPSC-cardiomyocytes were plated onto a Geltrex-coated well of a 6-well plate. On the day of measurement, the assay was conducted following manufacturer`s instructions. First, a H_2O_2 standard ranging from 0-1µM were generated and pipetted as duplicates to a 96-well plate. The cells were washed once with 1x DPBS and 640µl/well Working Solution 1 was added and incubated for 30min at 37°C. In parallel, 50µl Working Solution 2 was added to the standards. Following incubation, 100µl/well cell culture supernatant was pipetted to the 96-well plate in triplicates. The luminescence was measured with a microplate reader (Berthold Technologies) with an excitation of 540nm and emission of 620nm at RT. A standard curve was generated and the H_2O_2 concentrations of the samples were calculated accordingly.

3.2.15 Treatment of cells with Angiotensin Receptor-Neprilysin Inhibitor (ARNi)

In collaboration with Novartis the ARNi Entresto should be tested on heart failure iPSC-cardiomyocytes. For this, 7-week-old iPSC-cardiomyocytes of the diseased father were digested and 600,000 cells were plated onto Geltrex-coated wells of a 6-well plate. The cells were allowed to settle for seven days with medium change of Cardio culture medium three times a week. From day seven onwards the cells were either not treated, treated with DMSO as vehicle control, treated with Entresto (13µM Valsartan + 40µM Sacubitril), treated with Valsartan (13µM) only or treated with Sacubitril (40µM) only. The treatments were done in 2ml/well Cardio culture medium supplemented with 1x Penicillin/Streptomycin. The medium was changed three times per week and the treatment was conducted for 14 days. On day 14 the hydrogen peroxide production was detected using the AmplexRed Hydrogen/Peroxide/Peroxidase Assay Kit as described in 3.2.14.

3.2.16 Western blot analysis

3.2.16.1 Protein isolation from iPSC-cardiomyocytes pellets

For protein isolation the frozen iPSC-cardiomyocytes pellet needed to be lysed. For this purpose, the iPSC-cardiomyocytes pellet was resuspended in 100-130µl protein lysis buffer (2.5) and was incubated for 30min on ice. Following, the lysate was centrifuged at 300xg and 4°C for 8min. The supernatant was transferred carefully to a fresh 1.5ml reaction tube. To determine protein concentration the Pierce bicinchoninic acid (BCA) protein assay kit was used according to manufacturer`s instructions. In brief, the lysate was diluted 1:20 in 1x DPBS, the working solution was prepared following the manufacturer`s protocol based on the number of samples. The assay was performed in triplicates in a 96-well format. The plate was incubated at 37°C for 30min. Following, the samples were measured at a wavelength of 562nm using the Mithras2 LB 943 microplate reader (Berthold Technologies). The protein lysates were stored at -80°C until further usage.

3.2.16.2 SDS-polyacrylamide electrophoresis

To analyze expression of certain proteins, the proteins within the lysate needed to be separated by size. First, they were denatured to destroy quaternary, tertiary, and secondary structure of the proteins, to be able to separate them by length only. For this, the samples (1µg/µl) were mixed with 1x DPBS and Laemmli buffer to a total volume of 17µl and incubated at 37°C for 30min. Afterwards, 15µl of denatured protein sample or 10µl of prestained protein ladder were loaded into one well of previously casted SDS-polyacrylamide gels. These were prepared prior to the start of the experiments, consisting of a 15% separation gel (~2/3 of the gel) at the bottom, followed by a 6% separation gel (~1/6 of the gel) and 4% stacking gel (~1/6 of the gel) at the top, containing a 15-well comb. The readily prepared SDS-polyacrylamide gels were loaded into an electrophoresis chamber, the chamber was filled with 1x running buffer, the comb was removed, and the samples could be loaded. The gel was run at constant 15-20mA/gel until the dye-front reached the end of the SDS-polyacrylamide gel.

3.2.16.3 Protein transfer and detection

After being separated by gel electrophoresis, the proteins were transferred onto a PVDF or nitrocellulose membrane, respectively, by a semi-dry transfer system. For this, either a nitrocellulose membrane (pore size 0.45µm) was used in combination with TB-buffer system or a methanol-activated (incubation for 1min) PVDF membrane (pore size 0.45µm) was used with anode and cathode buffer system (see Tab. 25). Additionally, six Whatman paper per membrane were prepared. For transfer onto nitrocellulose membrane Whatman paper, membrane and gel were equilibrated for 5min in 1x TB buffer. For transfer onto methanol-activated membrane, three Whatman paper, membrane and gel were equilibrated for 5min in cathode buffer and the remaining three Whatman paper were equilibrated for 5min in anode buffer. Afterwards, the blot sandwich was assembled avoiding formation of air bubbles in a transfer cassette (from bottom to top: three Whatman paper, membrane, gel, three Whatman paper). For the actual transfer, the Trans-Blot Turbo Transfer System from BioRad was used, which allows fast protein transfer. The transfer was performed at constant 25V and a maximum of 2.3A for a specific time, depending on the size of the protein that should be transferred (Tab. 25). After transfer, the blot sandwich was disassembled, and the membrane was washed 1x with ddH_2O and 1x with TBS-T. To check the quality of the transfer the membrane was incubated for 10min in Ponceau Red solution, followed by washing in ddH_2O until the protein bands became visible. Following, the membrane was washed 10min in TBS-T, blocked in 5% milk/TBS-T or BSA/TBS-T for 1h at RT under mild shaking and subsequently incubated in primary antibody diluted in 1% milk/TBS-T ON at 4°C. Certain antibodies required incubation for 48h at 4°C, see Tab. 25. After incubation, the membrane was washed 3x in TBS-T for 10min each, before incubation with the appropriate secondary antibody coupled to horseradish peroxidase (HRP) for 1h at RT. This was followed by washing the membrane again 3x with TBS-T for 10min. For imaging with the ChemiDoc XRS+ imaging system, first a “colorimetric” image was taken, to capture the protein ladder. Then the membrane was incubated with a chemiluminescent HRP substrate that could be converted by the HRP bound to the secondary antibody. For proteins which are expressed at higher levels, the membrane was

incubated for 5min with the Immobilon Western substrate. Whereas weakly expressed proteins were visualized immediately after adding the SuperSignal West Femto Maximum Sensitivity Substrate to the membrane. After adding the substrate solution, the membrane was imaged with the setting “Chemi High Resolution” with a “Signal accumulation mode” that captured an image every five seconds over a time course of five minutes. The best image was chosen, and the band intensity was quantified using the Image Lab software. The membrane again was washed 1x with TBS-T and incubated in Ponceau Red solution for 1h at RT to strip off the bound antibody. The Ponceau Red was removed by short washing steps with ddH_2O and TBS-T. Afterwards, the membrane was either blocked again to identify another protein with a different antibody or was stored at -20°C for later usage.

Tab. 25: Antibodies and respective conditions used for Western blots

Target Protein	Dilution	Size (kDa)	Transfer: Membrane/Time
CaMKIIδ ox, Rb IgG	1:1000 milk, 48h	58	PVDF/9min
CaMKIIδ, Rb IgG	1:1000 milk, 48h	58	PVDF/9min
Connexin43, Rb IgG	1:1000 milk	43	Nitrocellulose/9min
FLNC, Rb IgG	1:1000 milk	290	Nitrocellulose/9min
NCX, Mou IgG	1:500 milk, 48h	70/112/116	Nitrocellulose/9min
PLN, Mou IgG	1:5000 milk	5/25	PVDF/5min
PLN-Ser16p, Rb IgG	1:5000 milk	5/25	PVDF/5min
PLN-Thr17p, Rb IgG	1:5000 milk	5/25	PVDF/5min
RyR2, Rb IgG	1:5000 milk	560	Nitrocellulose/11min
RyR2-S2808p, Rb IgG	1:1000 milk	560	Nitrocellulose/11min
RyR2-S2814p, Rb IgG	1:4000 milk	560	Nitrocellulose/11min
CaMKIIδ ox, Rb IgG	1:1000 milk, 48h	58	PVDF/9min
SERCA2a, Mou IgG	1:20000 milk	110	Nitrocellulose/9min
Vinculin, Mou IgG	1:1000 milk	116	Nitrocellulose & PVDF/9min

3.2.17 Flow cytometry

To analyze the quality of iPSC-cardiomyocytes culture quantitatively flow cytometry was performed, evaluating the number of cTNT positive cells. For this, eight weeks old iPSC-cardiomyocytes (half a full six well) was digested using 0.25% Trypsin/EDTA for 10min at 37°C. The cells were resuspended in equal amounts of FCS and transferred to a round bottom polystyrene test tube. The cells were centrifuged for 5min at 200xg, the supernatant was discarded, and the cell pellet washed with 1x DPBS and following centrifugation. The cells were fixed by resuspending them in 4% Histofix and incubation for 20min at RT. The Histofix was removed by an additional centrifugation step and the cells were washed twice with 1x DPBS. Afterwards 1% BSA was added for blocking and the cells were stored at 4°C until further analysis. For staining, the cells were split into three samples: one blank sample, not treated with any antibody, one secondary antibody control, only treated with secondary but not with primary antibody and the actual sample, treated with primary and secondary antibody. Only cells of the actual sample were incubated ON with the cTNT antibody (1:500, Tab. 11) at 4°C, whereas the other two samples were stored in FACS buffer only. On the next day, the sample as well as the secondary antibody control cells were washed three times with FACS buffer and incubated with AlexaFluor488 donkey-anti-mouse (1:500, Tab. 12) secondary antibody for 1h at RT in the dark. After this step,

cells of all three samples were washed three times with 0.2% BSA and resuspended in 500µl 1x DPBS. The samples were measured at the flow cytometer (FACSCanto II Cell Analyzer; BD Biosciences, CA, USA). Here, 10,000 events were analyzed at forward scatter 228V, side scatter 440V and AlexaFluor488 390V. The detection gate was set based on the blank sample and the $cTNT^+$ [%] cells were corrected by subtraction of unspecific binding events determined by the secondary antibody control.

3.2.18 Quantitative fluorescent *in situ* hybridization to analyze telomere length

In order to investigate the length of the telomeres quantitatively via fluorescent in situ hybridization (qFISH) iPSC and iPSC-cardiomyocytes needed to be applied onto Superfrost microscope slides. For this, iPSC and iPSC-cardiomyocytes were detached using Versene or Trypsin/EDTA, respectively. The cells were counted with a Thoma hemocytometer, and two cell dilutions were prepared for each cell type – iPSC were diluted to 750,000 cell/ml and 500,000 cells/ml and iPSC-cardiomyocytes were diluted to 1,000,000 cells/ml and 750,000 cells/ml. 100µl of each dilution were spun onto the Superfrost microscope slides. For this white filter cards and a Cytospin 4 centrifuge at 800x rpm for 5min were used. Samples were air-dried and stored at 4°C until further usage. All qFISH analyses were performed by Dr. Shambhabi Chatterjee as collaboration with the group of Dr. Christian Bär (Medizinische Hochschule Hannover, MHH). The analyses were performed as previously published (Canela *et al.*, 2007). In brief, the cells were incubated in hybridization solution supplemented with a fluorophore-conjugated peptide nucleic acid probe directed against the telomeric repeats. Following hybridization, the samples were imaged with a fluorescence microscope. The fluorescence intensities were quantified to calculate the relative telomere length. The longer the telomere, the more probes will hybridize and the more intense the fluorescent signal will be.

3.2.19 Telomerase Repeated Amplification Protocol (TRAP) assay

In order to analyze the telomerase activity within the iPSC a TRAP assay was performed. For this iPSC pellets were collected, snap frozen and stored at -80°C until further usage. The actual TRAP assay was performed by Dr. Shambhabi Chatterjee as collaboration with the group of Dr. Christian Bär (Medizinische Hochschule Hannover, MHH). In general, the TRAP assay is based on a two-step PCR protocol. In a first step, the cell lysate (previously generated) is mixed with a telomere substrate (TS primer). In an incubation step, the telomerase present in the cell lysate will add hexameric telomere repeats to the telomere substrate. In case a sample does not possess a telomerase or if the telomerase has been inactivated (like in negative controls) no product is made. In a second step the telomerase products formed during the first step, are amplified in a PCR using a primer pair directed against the hexameric repeats. These PCR products are then finally run on an agarose gel and imaged. If a cell lysate contains telomerase enzyme it can add hexameric repeats to the telomere substrate. Thus, a cell lysate with high telomerase activity will have several products, where each product is 6bp longer than the other. This will generate the so-called TRAP ladder, where each band is 6bp longer than the previous one.

3.3 Functional analysis

3.3.1 Engineered Human Myocardium (EHM)

To analyze the role of iPSC-cardiomyocytes in a 3D environment, engineered human myocardium was generated with iPSC-cardiomyocytes of external controls, DCM patients and isogenic controls. All experiments concerning EHMs were done in collaboration with Dr. med. Malte Tiburcy (Institute of Pharmacology and Toxicology of the University Medical Center Göttingen). Tissue casting, maintenance and drug application was performed by Branimir Berecic, MSc. Ca^{2+} response measurements and analysis were performed by Dr. Malte Tiburcy.

3.3.1.1 Generation of EHM

Generation of EHMs was performed following an already published protocol (Tiburcy *et al.*, 2020). In brief, iPSC were directly differentiated into iPSC-cardiomyocytes as described in 3.1.8. For EHM generation they were used at four weeks old, directly after metabolic selection, without in-between cryopreservation. In addition to the iPSC-cardiomyocytes human foreskin fibroblasts (HFF, from ATCC) were thawed and expanded in cell culture. At the day of casting, the iPSC-cardiomyocytes and HFF were mixed in a 70%/30% ratio in a total of 0.5 million cells. The cell mix was stored on ice. A collagen hydrogel mix was prepared on ice as follows: 0.3mg/tissue bovine collagen type I was mixed with equal volume of 2x RPMI and the pH was neutralized by adding 0.1M NaOH dropwise until the phenol red changed its color from yellow to red. Afterwards, the prepared cell mixture ($0.5x10^6$cells/tissue) was added to the prepared collagen hydrogel mix. The total volume of the ready mix was 180µl/tissue. The cell-hydrogel mix was then pipetted into wells of a 48-well plate containing two interconnected flexible poles. The EHM hydrogel settled for 1h in an incubator before medium was added. The medium was changed daily until analysis. Daily optical analysis of pole deflection as well as Ca^{2+} -response measurements in a 37°C tempered, Tyrode`s solution containing organ bath were performed and analyzed by Branimir Berecic and Dr. Malte Tiburcy.

3.3.1.2 Optical imaging of EHM

As the tissues were casted around two flexible, fluorescently-labelled poles, pole deflection driven by contraction of the tissues could be measured. For this, a high-speed camera was used to record the tissues movements, using a multi-well recording device with an integrated UV-A light source (developed by Dr. Tim Meyer, Institute of Pharmacology and Toxicology, University Medical Center Göttingen). Tissue contraction induced pole deflection reducing the distance between the two poles. This allows determination of EHM beating frequency (number of full contractions over a certain time span), as well as maximum contraction (difference of pole distance in fully contracted tissues vs distance of poles in basal position) by each EHM recorded. Analyses were done by Branimir Berecic.

3.3.1.3 Analysis of EHM contractile function

For analysis of contractile function, the tissues were placed around two hooks in an organ bath with gassed (5% CO_2/95% O_2) and tempered (37°C) Tyrode`s solution. The hooks were

adjusted for each tissue individually to reach their maximum tension/pre-load (=resting force). EHMs were electrically paced at 1.5Hz in this position. To determine the force of contraction (FOC) of the EHMs, difference in maximum and minimum force induced by EHM twitching was calculated. FOC changes upon increasing extracellular Ca^{2+} concentrations or upon stimulation with isoprenaline at EC_{50} Ca^{2+} could be investigated. Analysis of EHM contractile function was performed and evaluated by Dr. Malte Tiburcy.

3.3.2 Engineered connective tissue

To analyze the role of CFB in the development and pathogenesis of DCM, primary CFB of the DCM1 patient (extracted from explanted heart tissue prior to the start of the thesis), primary skin fibroblasts (SFB) of the DCM1 patient (isolated from skin biopsy) and iPSC-derived stromal cells of patient and isogenic control iPSC lines were used to prepare ECT as described by Santos *et al.* (Santos *et al.*, 2021). These tissues were analyzed to investigate the functional role of the different cells. All experiments concerning ECT were done in collaboration with Prof. Dr. Susanne Lutz (Institute of Pharmacology and Toxicology of the University Medical Center Göttingen) and with excellent technical assistance by Bastian Bues and Dr. Gabriela Santos.

3.3.2.1 Generation of ECT

To prepare ECT the (cardiac) fibroblasts and iPSC-derived stromal cells were mixed with collagen to form 3D tissues. As optimal collagen fibrillogenesis and gelation is dependent on parameters like ionic strength, pH and temperature the following parameters were crucial within the casting process. First, all components needed to be ice-cold, to avoid early collagen gelation. Second, the casting process is extremely time sensitive, and all steps needed to be performed as fast as possible.

CFB and SFB were cultured in HFBM+b10 medium until passage 4-6. iPSC-derived stromal cells were differentiated and cultured until passage 5-10 as described in 3.1.7. When reaching ~80% confluency CFB and SFB were detached using 0.25% Trypsin/EDTA and iPSC-derived stromal cells were detached using accutase treatment. The cells immediately were stored on ice and cell number and viability were determined with the CASY cell counter. For this 20µl of the cell suspension was added to 10ml CASY ton buffer. The cells were centrifuged for 10min at 300xg and 4°C and were resuspended in an appropriate volume of fibroblast growth medium and kept on ice. A collagen hydrogel mix was prepared as follows: 0.3mg/tissue bovine collagen type I was mixed with equal volume of 2x DMEM and the pH was neutralized by adding 0.2M NaOH dropwise until the phenol red changed its color from yellow to red. Afterwards, the prepared cells ($0.5x10^6$cells/tissue) were added dropwise and with constant circular motion of the falcon to the prepared collagen hydrogel mix. The total volume of the ready mix was 180µl/tissue. The cell-hydrogel mix was then pipetted into moulds around two flexible poles in a 48-well plate. These flexible poles are elastically interconnected, and hence allow tissue contraction over time. After casting, the tissues solidified for ~45min in an incubator at 37°C, before 500µl/well fibroblast growth medium (FGM3) was added. The medium was changed every day until analysis at day 13 or das 21.

3.3.2.2 Contraction analysis of ECT

As the tissues were casted into moulds around two flexible, fluorescently-labelled poles, pole deflection driven by contraction of the tissues could be measured. For this, the tissues were imaged daily using a multi-well recording device with an integrated UV-A light source (developed by Dr. Tim Meyer, Institute of Pharmacology and Toxicology, University Medical Center Göttingen). Tissue contraction induced pole deflection reducing the distance between the two poles. Hence, tissue contraction was calculated as the inverted change in distance of the two poles in comparison to the initial distance at d0, directly after tissue casting. Analysis was done using the microDisplay 5.4.1.2 software and ImageJ program.

3.3.2.3 Determination of cross-sectional area (CSA) of ECT

Tissue compaction mainly is driven by matrix remodeling due to secretion of factors and cell-driven matrix compression. To analyze this, the CSA of the ECT were calculated. For this, on the day of measurement (day 13 or 21) images of top and side view of the ECT were taken with a Stereo Lumar.V12 stereomicroscope. Horizontal line scans at 10 or 20 different positions of side view and top view images, respectively, were performed and the mean diameters of top view (d_t) and side view (d_s) were calculated. Based on this, the CSA was calculated as follows: $CSA=\pi\times(d_t/2)\times(d_s/2)$.

3.3.2.4 Destructive tensile strength measurement and stress strain analysis

Destructive tensile strength measurements of the ECT were performed using an RSA-G2 rheometer. All measurements were performed by Bastian Bues. For the measurement, the tissues were loaded carefully onto two hooks in a 37°C 1x DBPS containing organ bath. When loaded, the tissues were stretched uniaxially at a constant linear rate of ~1% of their initial length per second until rupture. Therefore, the tissues were stretched at 0.03mm/s. For analysis, the obtained force values (mN) were divided by the CSA to determine stress values (kPa), which were plotted against the distance between the two hooks. Based on the resultant curve, the start of the toe region (initial length of the tissue immediately before the stretch) was determined manually as L_0. Following, the strain values could be calculated for every point measured by $(L_{total}-L_0)/L_0$, where L_{total} represents the total gap at the individual measuring points. For background subtraction, the stress value at L_0 was used. The resulting values were plotted in the final stress-strain curve (see Fig. 14).

Such a resulting stress-strain curve displays two regions, as schematically shown in Fig. 14: the elastic region and the plastic region. The elastic region, where the curve is linear, is defined as the stress/strain region in which the original dimensions of the tissue would completely recover when the applied load is removed. In the elastic region the strain is proportional to the applied stress. The ratio between stress and strain is determined as Young`s modulus, which can also be determined by linear regression from the curve corresponding to the slope of the linear part of the elastic region. The Young`s modulus is a mechanical property that represents the stiffness of the tissue. The higher the Young`s modulus the stiffer the tissue. The elastic region ends at the yield point. From this point on the elongation of the tissue is no longer proportional to the increase in stress, hence the curve is no longer linear, and the plastic region is reached. In this region the tissue will

remain deformed and cannot recover its actual dimensions even if the load is removed. Here, fiber microfracturing takes place and the stress will decrease. The plastic region ends at the so-called failure point. The failure point corresponds to the ultimate rupture of the tissue characterized by a sudden drop in stress that can be seen in the curve.

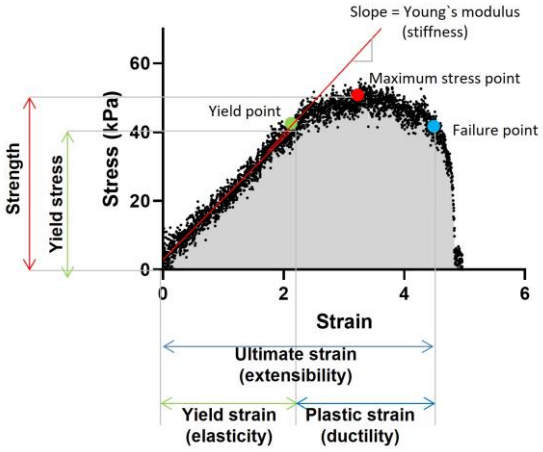

Fig. 14: Stress-strain curve of ECT after destructive tensile strength measurement showing the main measured parameters. The yield point corresponds to the limit of the elastic region, whereas the region between yield point and failure point corresponds to the plastic region (ductility). In the elastic region the strain is proportional to the applied stress. The slope of this linear phase represents the Young`s modulus corresponding to the stiffness of the tissue. The maximum stress point represents the maximum strength the tissue can endure, before microfracturing of the tissue induces a decrease in stress. Eventually the failure point is reached at the ultimate strain (extensibility), represented by a sudden drop in stress induced by tissue rupture.

3.3.3 FURA-2AM Ca^{2+} measurements

To analyze intracellular Ca^{2+} dynamics the iPSC-cardiomyocytes were stained with the ratiometric fluorescent dye FURA-2. FURA-2 can bind free Ca^{2+} ions (Grynkiewicz *et al.*, 1985). Its derivative FURA-2-acetoxymethyl ester (FURA-2AM) can cross cell membranes via passive diffusion. Within the cell cellular esterases remove the ester groups and regenerate the FURA-2. Upon binding of intracellular Ca^{2+}, FURA-2 can be excited at 340nm, whereas free FURA-2 is excitable at 380nm (He *et al.*, 2018). Due to the different excitation states a 340/380 ratio can be calculated allowing comparable Ca^{2+} measurements as it compensates dye loading differences among samples and the possibility to determine the diastolic Ca^{2+} content.

For FURA-2AM analysis ten weeks old iPSC-cardiomyocytes were digested using 0.25% Trypsin/EDTA and 30,000-40,000 cells were plated onto Geltrex-coated 35mm round Fluoro dishes with a glass bottom. The cells recovered for 7-9 days, and the medium was changed every 2-3 days. For analysis, the cells were incubated with 1ml 1x Tyrode`s solution supplemented with 5µl FURA-2AM (5µmol/l) and 1.3µl Pluoronic for 15min at RT. Everything was performed in a dark room. Following, the staining solution was discarded, and the cells were washed once with 1x Tyrode`s solution only for another 15min at RT to allow cellular rebalance and de-esterification of FURA-2AM. For measurement, the Tyrode`s solution was refreshed by discarding the old solution and adding 1.5ml new 1x Tyrode`s solution. The cells were stimulated with a MyoPacer Cell Stimulater (IonOptix) by

applying a constant field stimulation of 30V and 10ms and increasing frequencies of 0.25, 0.5 and 1Hz at RT. The steady-state Ca^{2+} transients of the FURA-2AM loaded cells were recorded by excitation at 340nm and 380nm and detection of emitted fluorescence at 510nm using an epifluorescence microscope (Olympus Motic AE31 microscope with an IonOptix epifluorescence acquisition system). 3-7 single cells were measured for each Fluoro dish, each at 0.25, 0.5 and 1Hz. The last cell was stimulated with caffeine (10µM) by applying one drop of caffeine solution (10mM stock diluted 1:1000 in 1x Tyrode`s solution) precisely to the measured cell. Caffeine triggers the opening of RYR2 and hence induces complete Ca^{2+} release from the SR.

For analysis, a F_{340nm}/F_{380nm} ratio was calculated to determine the intracellular Ca^{2+} levels. Following, the background ratio was subtracted and the average event ratio of ten signal events at 0.25Hz and 0.5Hz was calculated. With this, diastolic Ca^{2+} (ratio baseline), systolic Ca^{2+} (transient amplitude), time to peak, time to 50% relaxation, time to 80% relaxation, SR Ca^{2+} load (caffeine-induced transient amplitude), caffeine-induced time to 80% relaxation and fractional release were analyzed. Indirectly SERCA activity (k_{SERCA}) was calculated by subtracting the rate decay constant k_{caff}, from the systolic Ca^{2+} transient k_{sys}. All analyses were performed using the IonWizard software (IonOptix).

3.3.4 Fluo-4 Ca^{2+} measurements

To complement the Ca^{2+} measurements with the FURA-2AM system by analysis of Ca^{2+} sparks and support of kinetics data, cells were also stained with the cytosolic Ca^{2+} dye Fluo-4.

For Fluo-4 analysis ten weeks old iPSC-cardiomyocytes were digested using 0.25% Trypsin/EDTA and 180,000-280,000 cells were plated onto Geltrex-coated 25mm round coverslips in a well of a 6-well plate to form a monolayer. The cells recovered for 7-9 days, and the medium was changed every 2-3 days. For analysis, the cells were washed once with 1x Tyrode`s solution. The staining solution was prepared by mixing 3.8µl Fluo-4 (2.5µM) vigorously with 0.9µl Pluronic F-127 and adding 1.5ml 1x Tyrode`s solution. The cells were incubated with staining solution for 30min at 37°C in the dark. Afterwards, the staining solution was discarded, and the cells were washed twice with 1x Tyrode`s solution. The coverslip containing the stained cells was carefully placed into the measuring chamber and 900µl fresh Tyrode`s solution was added for measurement. The measurement was performed on a LSM 720 confocal microscope with a 63x magnification oil objective. The cells were paced at 0.25Hz with 18V/3ms with a MyoPacer Cell Stimulater (IonOptix). The ZEN 2009 software (Zeiss) was used, applying the following settings: excitation 488nm with 1.0-2.2%, a pinhole of 6AU with 700 gain and offset 0. Lines for measurement were drawn in the cytoplasmic region excluding the nucleus. A line scan was generated applying the following settings: 20,000 cycles, 12bit unidirectional, zoom factor 3, 512 pixels, no delay and maximum scan speed (945.5µs per line scan = 18.9s/total line scan recording). 18-20 cells were measured for each coverslip.

3.4 Statistical analysis

Statistical analysis was performed using GraphPad Prism version 8 and 9 (GraphPad Software, Inc., CA, USA). Data are presented as mean ± standard error of the mean (SEM) and statistical significance was accepted as $p < 0.05$. The unpaired two-tailed Student's t-test was used to check for statistically significant differences between the means of two groups. The significance was visualized as # = $p < 0.05$, ## = $p < 0.01$, ### = $p < 0.001$ and #### = $p < 0.0001$. One-way analysis of variance (ANONA) tested for statistically significant differences between the means of more than two groups. Two-way ANONA tested for statistically significant differences between the means of more than two groups dependent on two independent variables (e.g., Force/[Ca^{2+}]). Multiple comparisons of one-way and two-way ANONA additionally allowed the comparison of each mean with every other tested mean and was corrected according to Tukey. The significance was visualized in the graphs with * = $p < 0.05$, ** = $p < 0.01$, *** = $p < 0.001$ and **** = $p < 0.0001$.

4 Results

4.1 Recruitment of DCM index family

For this study of underlying genetic and molecular causes of DCM a four-member index family was recruited, including patients with severe DCM and healthy family members (Fig. 15). The family was recruited by the Institute for Cardiology and Pneumology, University Medical Center Göttingen and was willing to donate somatic material for this study. The study was approved by the ethical committee of the University Medical Center Göttingen (Az 21/1/11 and Az 31/9/00).

The family includes the father, denoted as DCM1, who suffered from sudden DCM at the age of 40 years with an EF of <20% and needed heart transplantation. The oldest daughter, DCM3, also suffered from severe DCM with an early sudden onset at 6-month-old and also received heart transplantation at the age of 1.5 years. The second daughter (DCM4), as well as the mother (DCM2) do not show any cardiac phenotype.

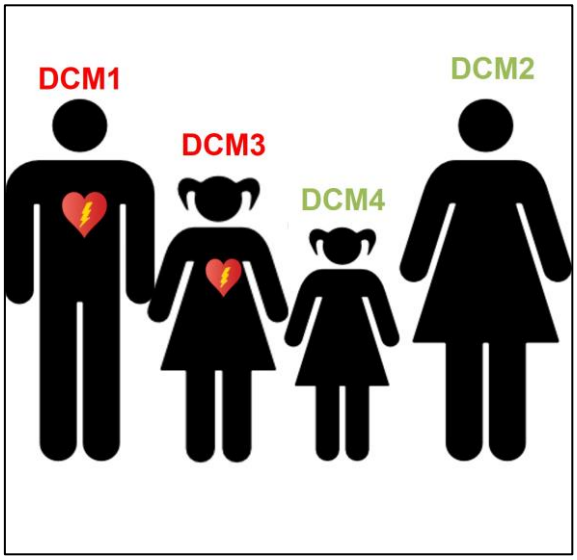

Fig. 15: Overview of DCM index family. All family members are shown. The father (DCM1) as well as the oldest daughter (DCM3) suffered from severe DCM. The mother (DCM2) and the younger daughter (DCM4) do not show any cardiac phenotype.

4.1.1 Pedigree analysis reveal *de novo* appearance of DCM in index family

As the presence of DCM in two consecutive generations with a sudden onset and severe phenotype hints towards a genetic, heritable predisposition it was interesting to check for previous DCM cases within this family. Therefore, the pedigree of the diseased father, including previous generations, was analyzed (Fig. 16). This showed a history of heart attacks within the male ancestors of the index patient DCM1, but no other cardiomyopathy (-like) phenotype. This indicates that the DCM only arose within the small index family. Hence, it might be based on a *de novo* mutation.

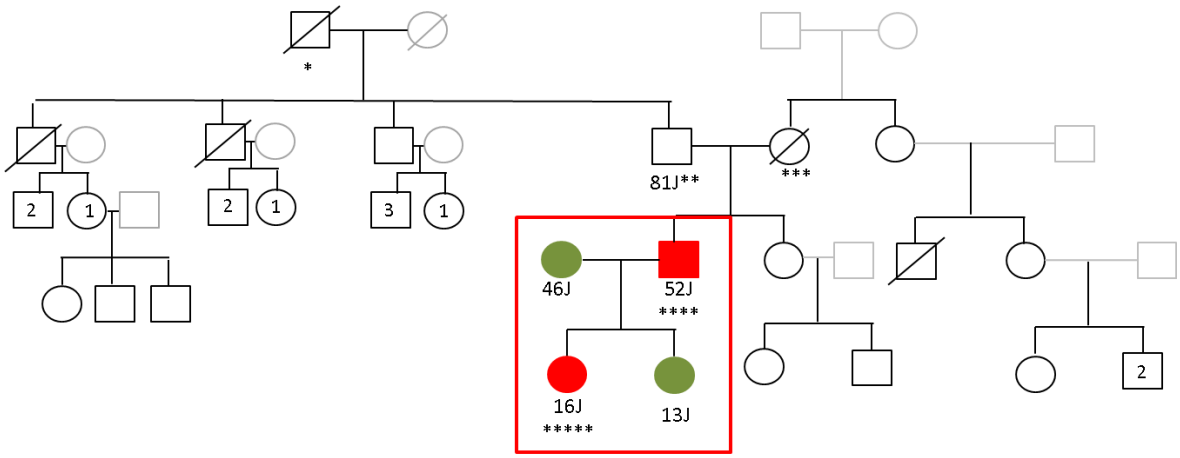

*	two heart attacks
**	mild heart attack with 71
***	died from neuronal disease
****	index patient (DCM1), severe DCM, HT with 40
*****	index patient (DCM3), severe DCM, HT with 1.5

Fig. 16: Family pedigree of index patient DCM1. The family pedigree of the diseased father is shown, including previous generations. Red-rimmed the DCM index family is marked. Red-filled diseased family members are marked. Green-filled healthy family members are shown. * indicate cases of (heart) disease. HT=heart transplantation

4.1.2 Identification of potentially predisposing new variants in FLNC and integrin-linked kinase within the DCM family

To analyze potential underlying predisposing genetics WES of somatic cells of all four family members was conducted at the NGS facility for Integrative Genomics (NIG) at the University Medical Center Göttingen (UMG). This was complemented by Panel sequencing of 192 cardiac genes of iPSC of the diseased family members by the Human Genetics Department at the University Medical Center Göttingen (UMG). The obtained data was analyzed for potentially pathogenic variants by Prof. Dr. Bernd Wollnik and Dr. Arne Zibat (Human Genetics, UMG). Most relevant variants are shown in Fig. 17 A. The two most pathogenic assumed variants were identified in the genes *FLNC* and integrin-linked kinase (*ILK*). A few other, already reported, and benign variants were depicted and used for cell line identification within cell culture by regular sanger sequencing. First, a variant in the myosin binding protein C3 (MYBPC3) was identified in cells of the diseased father and daughter but was absent in healthy mother and daughter (Fig. 17 A). MYBPC3 is a gene that often is associated with HCM (Cirino and Ho, 1993). However, the identified variant, a substitution of valine to methionine at amino acid position 158 (rs3729986) is classified as benign by ClinVar (https://www.ncbi.nlm.nih.gov/clinvar/) and HGMD (http://www.hgmd.cFB.ac.uk/ac/search.php) databases. Additionally, a variant in the cytochrome b-245 alpha-chain (CYBA, subunit of the NADPH oxidase) was identified in all family members (Fig. 17 A). However, this variant was identified in a homozygous state only in cells of the diseased father and healthy daughter and can be found in a heterozygous state in the cells of the diseased daughter and healthy mother. Again, the identified variant, a substitution of tyrosine to histidine at amino acid position 72 (rs4673) is classified as

benign by ClinVar and HGMD databases. Furthermore, a variant in the MYH7 (coding for βMHC) was identified in cells of the diseased father and both daughters in a heterozygous state (Fig. 17 A). Variants in MYH7 often are associated with a diverse set of cardiomyopathies as HCM and DCM. The identified variant, a substitution of glycine to serine at amino acid position 1101 (rs367546859) is classified as variant of uncertain significance by ClinVar and HGMD databases and hence might or might not be disease causing or might contribute to a diseased phenotype in addition to other variants. A variant in DSP was identified in cells of the diseased father (Fig. 17 A). DSP is expressed in desmosomes of cardiomyocytes and variants are often associated with several cardiomyopathies. However, the identified variant, a duplication of the first adenine (p. Met1fs, rs17133512), is classified as mostly benign by ClinVar and HGMD databases. As already mentioned, combination of these gene variants allows identification of the different family lines. Both diseased family member can be distinguished by CYBA (DCM1 homozygous, DCM heterozygous) and DSP (DCM1 fs, DCM3 wt) variants (Fig. 17 A). Healthy family members, on the other hand, can be distinguished by CYBA (DCM2 heterozygous, DCM4 homozygous) and MYH7 (DCM2 wt, DCM4 heterozygous missense variant) variants (Fig. 17 A). Presence/absence of all variants was confirmed by Sanger sequencing (Fig. 17 B).

In addition to these already described variants, two new variants in two different genes were identified by WES and panel sequencing in cells of diseased father and daughter but not in cells of healthy family members – namely variants in the *FLNC* (ENST00000325888) and *ILK* (ENST00000299421) gene. Both are missense variants – FLNC: c.6560G>C, heterozygous; p.Arg2187Pro and ILK: c.1274T>C, heterozygous; p.Met425Thr (Fig. 17 A). Both variants were identified by three different variant caller independently and mapping quality, coverage as well as ALT index are of high quality. The presence of both variants was confirmed by sanger sequencing in cells of diseased father and daughter as shown in Fig. 17 B. Both variants were analyzed in detail by Dr. Arne Zibat (Institute for Human Genetics, University Medical Center Göttingen). These analyses led to the conclusion that both variants are new and not described so far, as both could not be found in literature, nor in clinical databases as ClinVar and HGDM, nor in biological databases as ExAC (Exome Aggregation Consortium, https://ngdc.cncb.ac.cn/databasecommons/database/id/3774) and gnomAD (Genome Aggregation Database, https://gnomad.broadinstitute.org/). Six out of seven prediction tools classified both variants as “potentially damaging.” Based on the ACMG (American College of Medical Genetics) guidelines (Richards *et al.*, 2015) both variants are VUS (variants of unknown significance), with the addition of being “likely pathogenic” (evidence by the criteria PP1-S [co-segregation with disease in multiple affected family members], PM2 [absent in population databases], PP3 [Multiple lines of computational evidence support a deleterious effect on gene or gene product], PP2 [Missense variant in a gene that has a low rate of benign missense variation and where missense variants are a common mechanism of disease]). For both genes (*FLNC* and *ILK*) missense variants are reported which are associated with DCM (Begay *et al.*, 2016; Brodehl *et al.*, 2019b; Knoll *et al.*, 2007). For FLNC, reported variants are associated with a severe phenotype with a higher risk to develop arrhythmias or sudden cardiac death, compared to many other genetic-based cardiomyopathies (Begay *et al.*, 2016; Eden and Frey, 2021;

Ortiz-Genga *et al.*, 2016; Verdonschot *et al.*, 2020). Already reported FLNC missense variants cluster to the ROD2 domain, where the identified variant is located as well (Verdonschot *et al.*, 2020). Most FLNC missense variants are associated with HCM, but few FLNC missense variants (e.g. p.Gly2070Ser) are also associated with DCM and are located in the ROD2 domain as well (Ortiz-Genga *et al.*, 2016). For ILK, in contrast, significantly fewer reports are available associating DCM with ILK variants. Most associations are based on bioinformatical prediction tools, and hence, less is known about the clinical contribution (Bang *et al.*, 2022; Haas *et al.*, 2015). Additionally, ILK missense variants are more often associated with arrhythmogenic cardiomyopathy, than with DCM (Brodehl *et al.*, 2019b). However, some reports also associate ILK missense variants with severe DCM with greatly reduced EF (Knoll *et al.*, 2007; Meder *et al.*, 2011). Interestingly, those reported ILK missense variants (p.Ala262Val) are located in the kinase domain of ILK, like the variant identified within the DCM index family in this work (Knoll *et al.*, 2007).

A

Gene	sDCM1	sDCM2	sDCM3	sDCM4
MYBPC3	c.472 G>A het, p.Val158Met	wt	c.472 G>A het, p.Val158Met	wt
CYBA	c. 254 T>C homo, p.Tyr72His	c. 254 T>C het, p.Tyr72His	c. 254 T>C het, p.Tyr72His	c. 254 T>C homo, p.Tyr72His
MYH7	c.3406 G>A het, p.Gly1101Ser	wt	c.3406 G>A het, p.Gly1101Ser	c.3406 G>A het, p.Gly1101Ser
DSP	c.1dup p.Met1fs	wt	wt	wt
FLNC	c.6560G>C het, p.Arg2187Pro	wt	c.6560G>C het, p.Arg2187Pro	wt
ILK	c.1274T>C, het, p.Met425Thr	wt	c.1274T>C, het, p.Met425Thr	wt

B

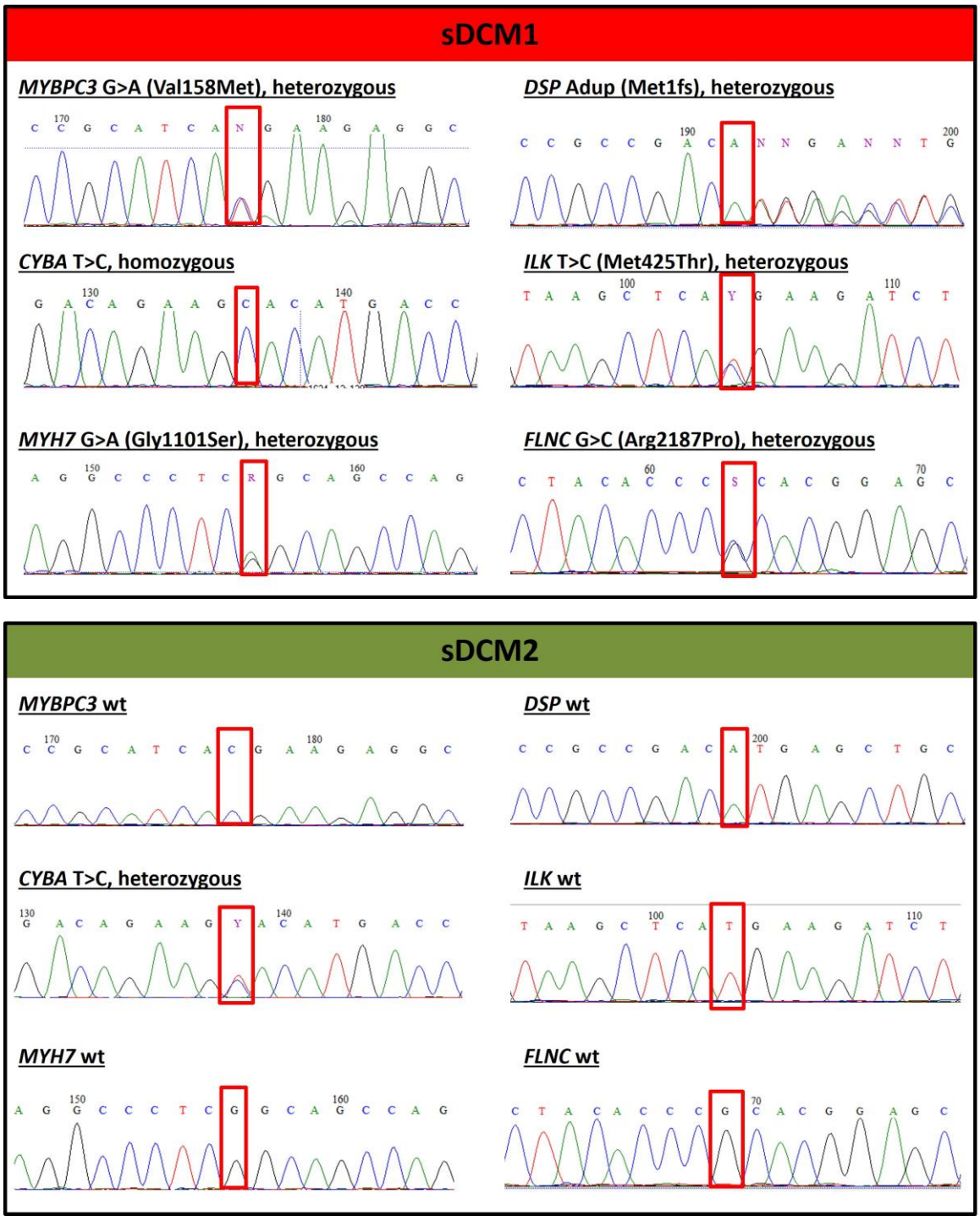
sDCM1
MYBPC3 G>A (Val158Met), heterozygous
DSP Adup (Met1fs), heterozygous
CYBA T>C, homozygous
ILK T>C (Met425Thr), heterozygous
MYH7 G>A (Gly1101Ser), heterozygous
FLNC G>C (Arg2187Pro), heterozygous
sDCM2
MYBPC3 wt
DSP wt
CYBA T>C, heterozygous
ILK wt
MYH7 wt
FLNC wt

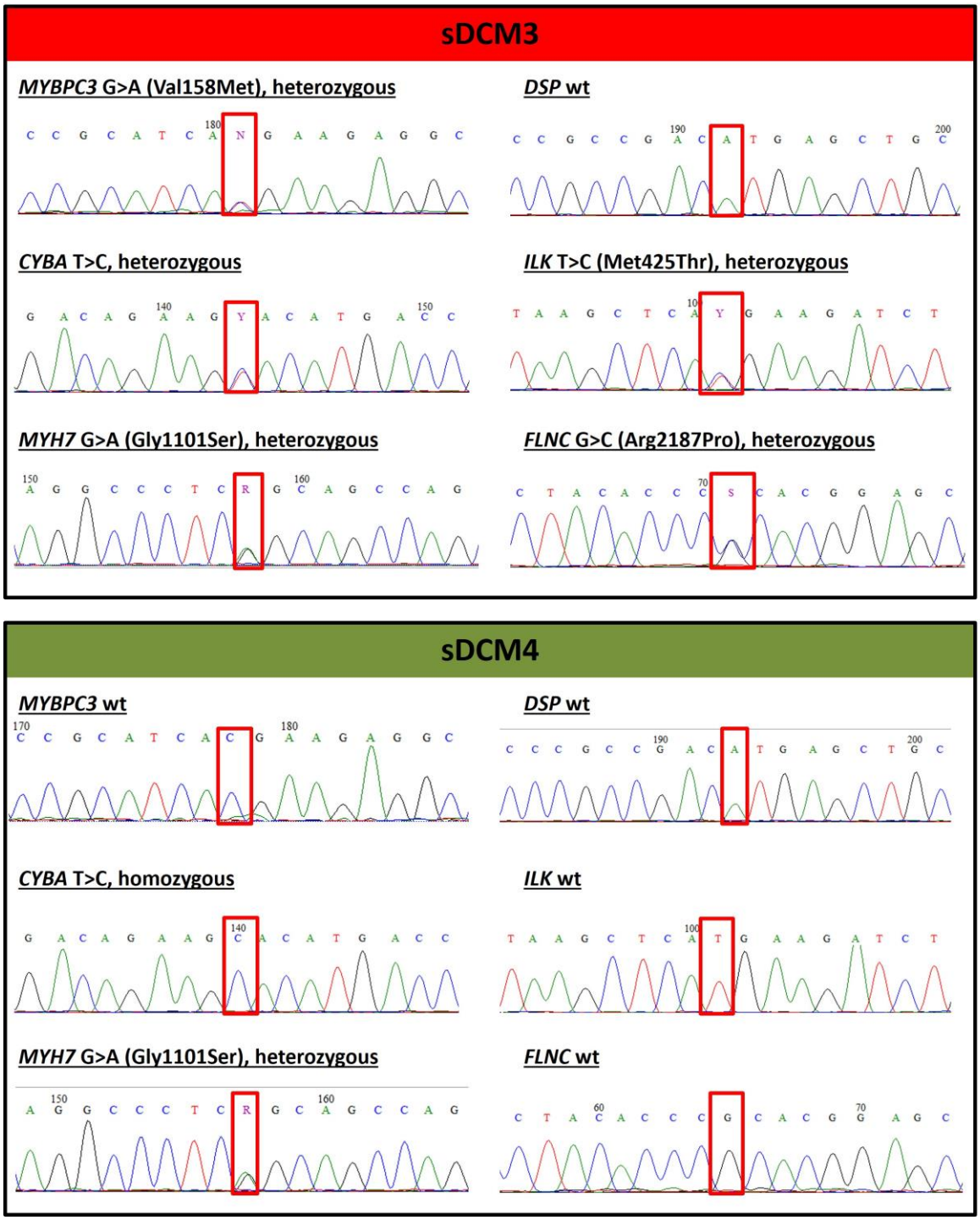

Fig. 17: Identification and verification of DCM-associated SNPs and variants within the DCM family. A Shown are the most relevant SNPs and variants identified by WES and panel sequencing within the DCM index family. **B** Shown are the chromatograms after sanger sequencing confirming presence of the identified variants in cells of all family members.

4.1.3 Generated patient-specific iPSC of all DCM family members display full pluripotency

As previously described (4.1.2), the newly identified FLNC missense variant is localized in a mutation hot spot, FLNC-associated DCM display a severe phenotype, and several reports demonstrate the significantly increasing role of FLNC variants within the DCM pathophysiology. Although the identified ILK variant is not reported so far and ILK-associated DCM cases are linked to severe phenotypes as well, current literature on ILK-associated DCM is low. Hence, this work will further focus on the role of the newly identified FLNC variant to the DCM pathophysiology within the index family. Therefor the model of patient-specific iPSC was chosen. For this purpose, all family members donated somatic material. A skin biopsy was taken from the father, from which SFB were isolated. All other family members donated a blood sample from which PBMCs were isolated. SFB and PBMCs were used for reprogramming prior to the start of this thesis. For reprogramming, the non-genome integrating sendai virus was used, encoding for the four classical minimal Yamanaka factors – OCT4, c-MYC, KLF-4 and SOX2 in a special stoichiometric ratio. Hence, the iPSC lines are called sDCM. Experimental data of diseased father and daughter (DCM1 and DCM3, respectively) are displayed in red color in every graph and figure, and data of healthy mother and daughter (DCM2 and DCM4, respectively) are displayed in green color in every graph and figure. For every family member, two iPSC clones were chosen for cultivation. Before starting all experiments, these lines were analyzed for their pluripotent character.

Pluripotency characterization was performed with passage 25 earliest and is exemplarily shown for one cell line of each family member in the following paragraph. All generated iPSC lines of all family members showed a classical stem cell morphology by growing in typical compacted well-defined colonies with small, uniform and round-shaped cells and little outgrowing arms in the periphery (Fig. 18 A). Additionally, all iPSC lines showed elevated activity of ALP as shown by appearance of a violet staining of all iPSC colonies (Fig. 18 B). Furthermore, the iPSC were analyzed for expression of pluripotency-associated markers on protein level by IF staining (Fig. 18 C). All iPSC lines showed high expression of the transcription factors SOX2, OCT4 and NANOG as specific nuclear staining of these markers was detected, which colocalized with nuclear DAPI staining (Fig. 18 C). Additionally, expression of the translational enhancer and RNA-binding protein LIN28 could be detected in the cytoplasm (Fig. 18 C). Finally, expression of the cell surface protein tumor rejection antigen 1-60 (TRA1-60) could be detected by specific staining of the cell membrane (Fig. 18 C).

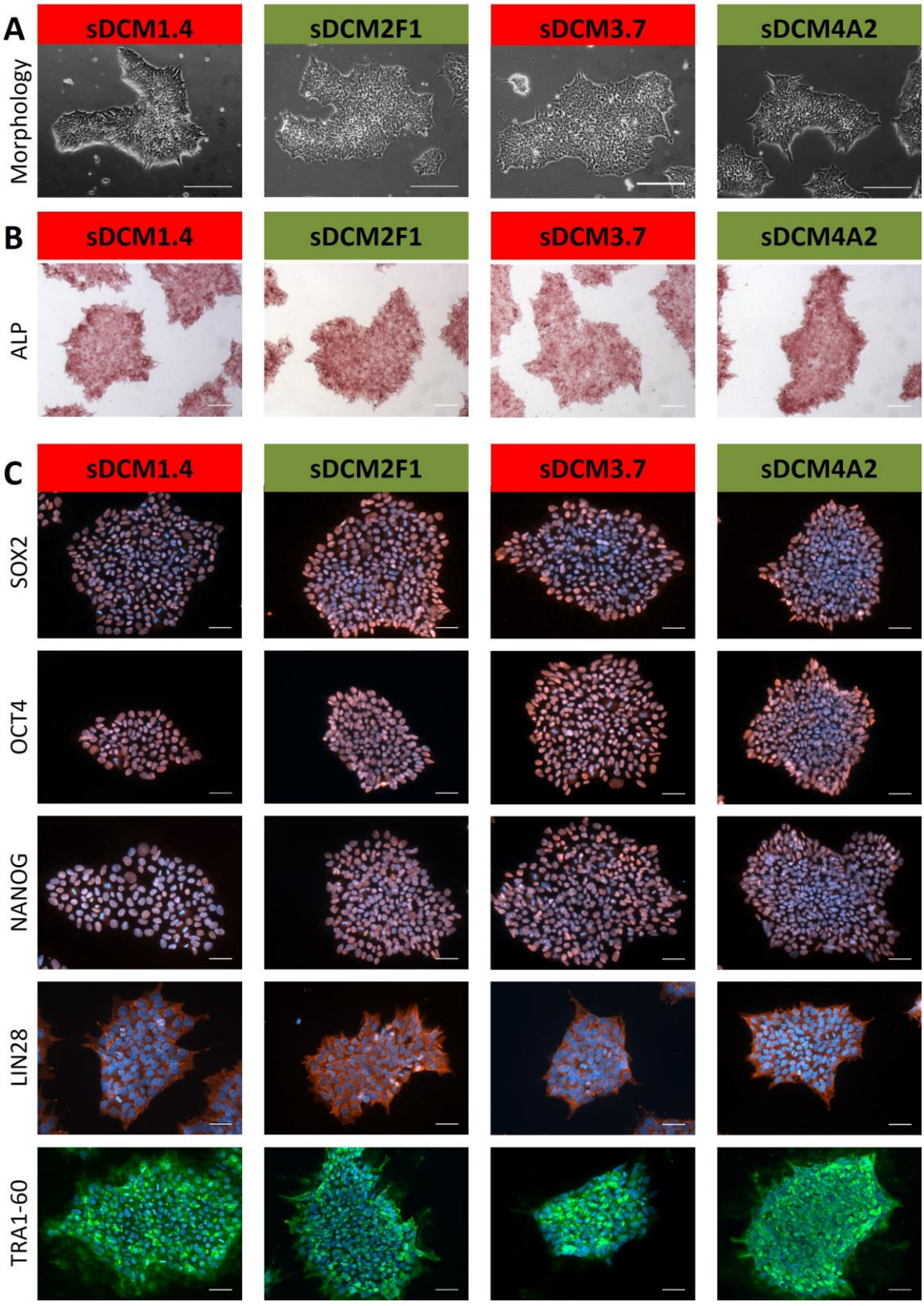

Fig. 18: Pluripotency characterization by cell morphology and specific protein expression. Shown are **A** brightfield and **B** ALP images of the generated iPSC lines of all family members. Images were taken with a Zeiss Axio Observer A1 inverted microscope. Scale bar=200µm. **C** Additionally, images of the pluripotency markers SOX2 (red), OCT4 (red), NANOG (red), LIN28 (red) and TRA1-60 (green) are shown as merged images with the nuclear DAPI (blue) staining. All images were taken with a Zeiss Axio Observer A1 inverted microscope. Scale bar=50µm.

In addition, the expression of pluripotency-associated markers was tested on mRNA level by qPCR analyses (Fig. 19). The expression levels of these different markers of the iPSC of all family members were compared to expression levels of the markers of an already characterized and published iPSC line as positive control and fibroblasts and PBMCs (from which the iPSC were reprogrammed) as negative controls. All patient-specific iPSC lines showed upregulation of typical pluripotency markers, like *SOX2* (Fig. 19 A), *OCT4* (Fig. 19 B), *NANOG* (Fig. 19 C), *LIN28* (Fig. 19 D) and growth differentiation factor-3 (*GDF3*) (Fig. 19 E) on mRNA level. The expression of all five markers was significantly higher in all iPSC lines compared to somatic fibroblasts and PBMCs (Fig. 19). Additionally, the expression of all five markers of all iPSC lines was mostly comparable to the expression of the positive control (Fig. 19).

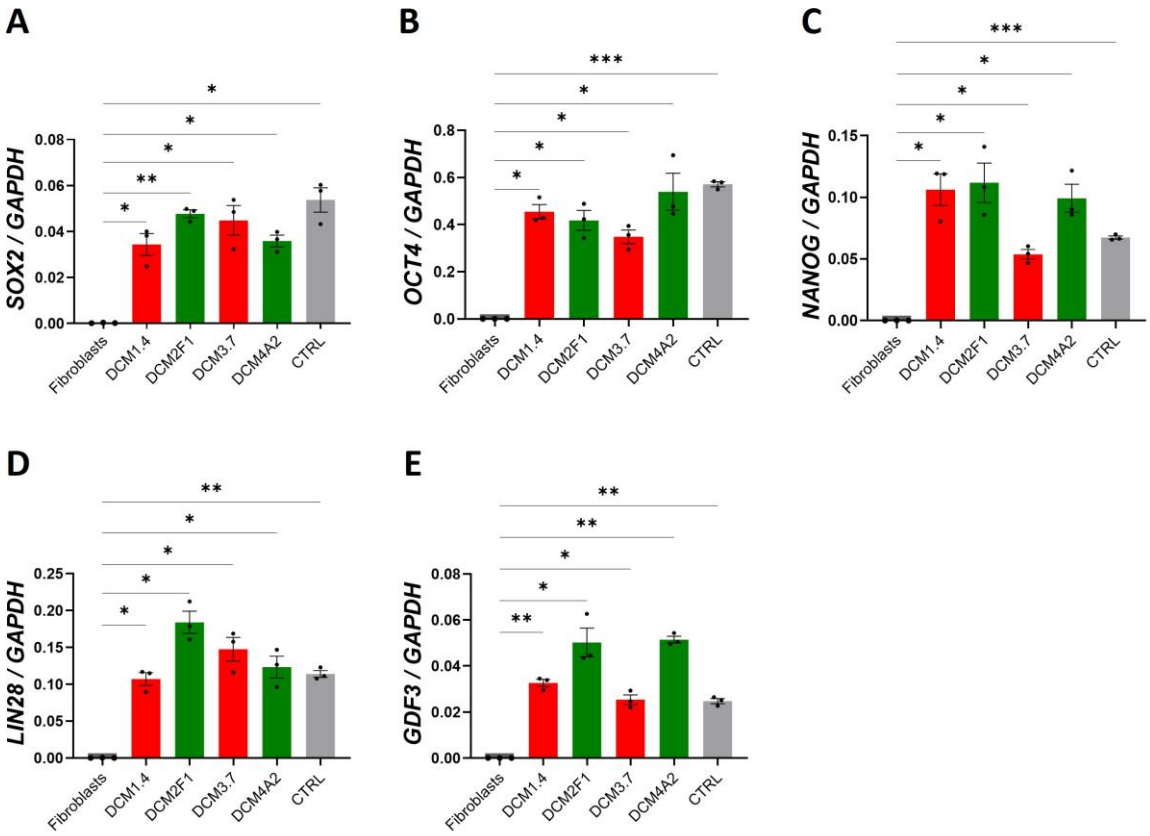

Fig. 19: Expression of endogenous pluripotency-associated markers on mRNA level. Quantitative PCR analyses of iPSC lines of all four family members, fibroblasts and PBMCs (for simplicity only labeled fibroblasts in the graphs) as negative control and already published control (CTRL) iPSC lines (all n=3 passages) to analyze the expression levels of different pluripotency-associated markers. Quantified expression of **A** *SOX2*, **B** *OCT4*, **C** *NANOG*, **D** *LIN28* and **E** *GDF3* is shown. Expression levels of all markers were normalized by corresponding expression of *GAPDH*, and analyses were done using the ΔCt method. Statistical analysis (one-way ANONA with Tukey`s correction) compared all groups with each other. Data are presented as mean ± SEM. * = $p < 0.05$, ** = $p < 0.01$ and *** = $p < 0.001$.

After demonstrating the general expression of classical pluripotency-associated markers, the iPSC were analyzed for the *in vitro* differentiation potential. Therefore, the iPSC were cultured with mitotically-inactivated MEF to form EB in which the iPSC differentiated spontaneously. The EB were cultivated for 33 days, and samples were taken on days 0, 8, 8+10 and 8+25 and analyzed for the expression of markers of all three germ layers on

protein and mRNA level. Protein expression of markers of all three germ layers was confirmed by IF staining (Fig. 20). Expression of the endodermal marker AFP was confirmed by a typical and specific staining of tight clusters of cells around the nucleus (Fig. 20). Expression of the mesodermal αSMA was verified by a positive staining displaying a typical lined pattern of actin filaments (Fig. 20). Finally, the expression of the ectodermal βIII-tubulin was proven by a specific staining of elongated cells with characteristic neuronal-like projections (Fig. 20).

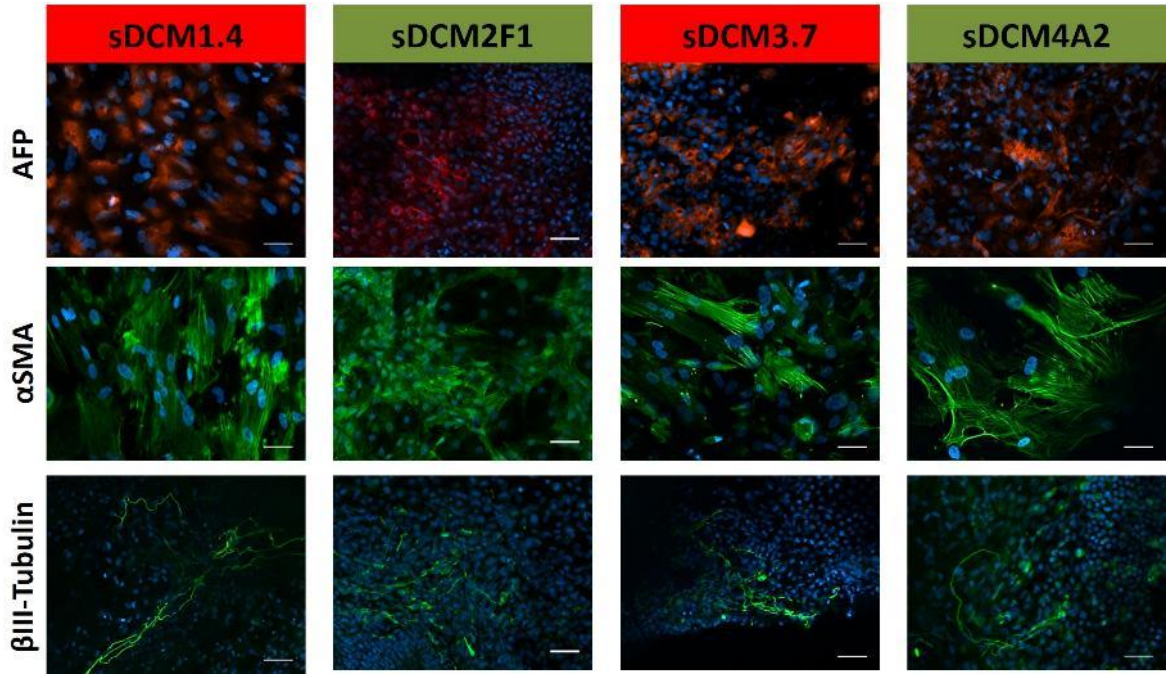

Fig. 20: Expression of germ layer-specific proteins after spontaneous *in vitro* differentiation of iPSC. Representative images of iPSC of all family members stained positive for AFP (endoderm, red), αSMA (mesoderm, green) and βIII-tubulin (ectoderm, green), all shown as merged images with the nuclear stain DAPI (blue). All images were taken with a Zeiss Axio Observer A1 inverted microscope. Scale bar=50µm.

Additionally, mRNA expression of markers of all three germ layers was analyzed by classical RT-PCR. As can be seen in Fig. 21, all samples showed steady-state expression of *GAPDH*, used as housekeeping gene. Additionally, all iPSC showed expression of the pluripotency-associated marker *OCT4* at d0, whose expression is decreasing over time, indicating the loss of a pluripotent state and the development to a more differentiated cell type (Fig. 21). In contrast, expression of endodermal markers, like *AFP* and serum albumin (*ALB*), as well as expression of mesodermal markers, like *αMHC* or *cTNT* is increasing over time. The same can be seen for the expression of ectodermal markers, like microtubule-associated protein 2 (*MAP2*) and paired box 3 (*PAX3)*. All these markers are absent or only expressed on low level in iPSC and cannot be detected in MEF, with which the iPSC were co-cultivated. This indicates the expression of markers of all three germ layers was dependent on the differentiation of the iPSC into cells of different lineages.

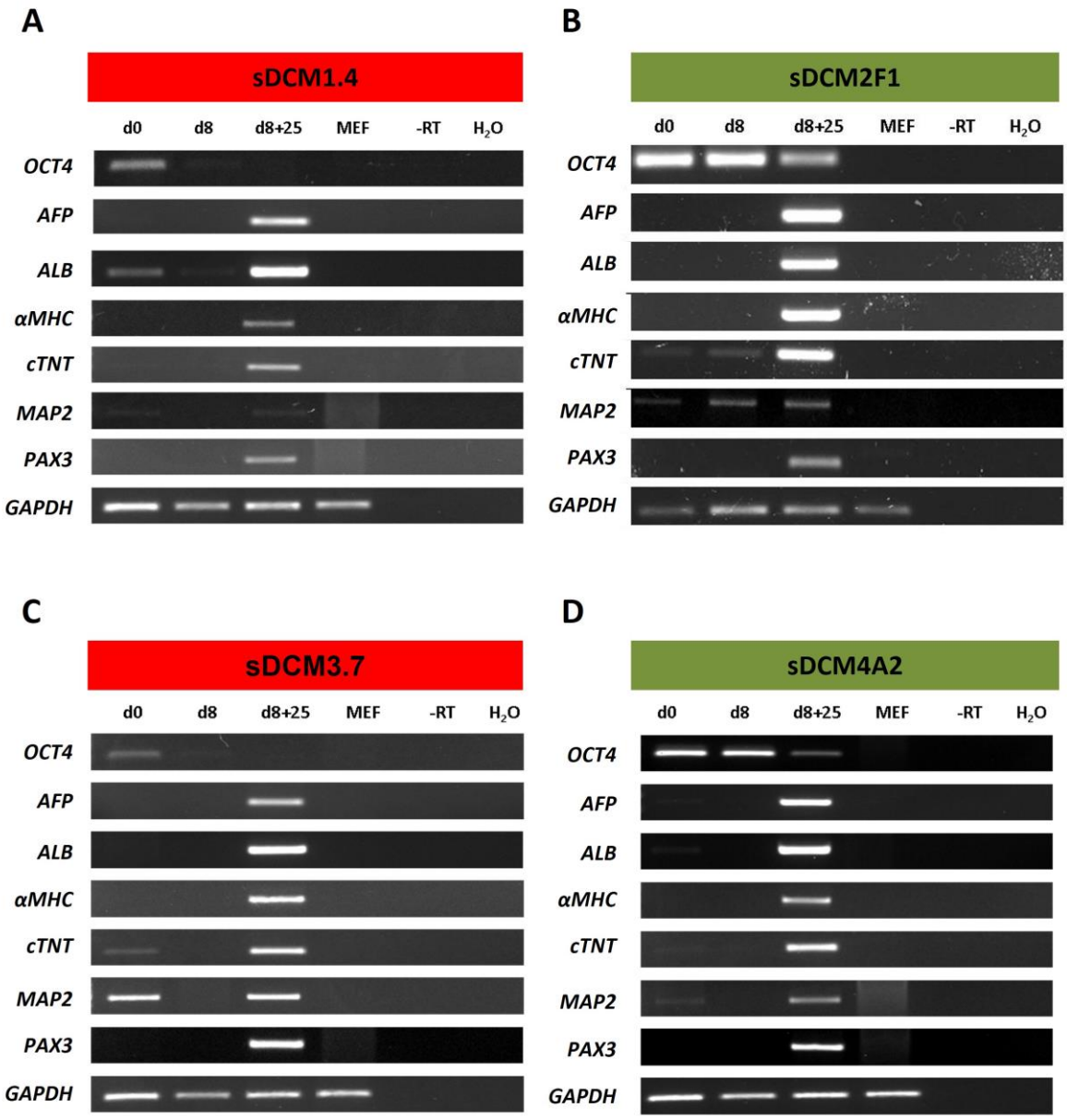

Fig. 21: Expression of germ layer-specific genes after spontaneous *in vitro* differentiation of iPSC. Results of semi-quantitative PCR of EB of all family members (**A** sDCM1.4, **B** sDCM2F1, **C** sDCM3.7, **D** sDCM4A2) at different time points (d0, d8, d8+25). The iPSC showed *OCT4* expression at day 0. Expression of markers of all germ layers, like *AFP* and *ALB* as endodermal, *αMHC* and *cTNT* as mesodermal and *MAP2* and *PAX3* as ectodermal markers was increasing. MEF, used as negative control, did not show expression of any of these specific markers. *GAPDH* was used as housekeeping gene.

4.1.4 Successful directed differentiation into patient-specific iPSC-cardiomyocytes

To study the role of the identified FLNC variant within the DCM pathophysiology, patient-specific iPSC were directly differentiated into functional beating, ventricular iPSC-cardiomyocytes. The used differentiation protocol was adapted from Lian *et al.* (Lian *et al.*, 2013) which uses manipulation of the Wnt signaling by addition of small molecules, CHIR99021 and IWP2, to resemble the *in vivo* development of cardiomyocytes. Although already quite efficient compared to spontaneous differentiation approaches, some non-cardiomyocyte cells arise during the differentiation process (Tohyama *et al.*, 2013). Hence,

a metabolic selection step was included in the following differentiation. Here, glucose was replaced by lactate, which the most cells cannot, but cardiomyocytes can use as carbon source. After differentiation and selection, the iPSC-cardiomyocytes were cultured for up to 90 days, which allows for longer maturation of the cells.

4.1.4.1 Quality control of generated iPSC-cardiomyocytes

Despite a precise directed differentiation protocol of iPSC into iPSC-cardiomyocytes and a subsequent metabolic selection step, the quality of the individual differentiation experiments may vary based on the cell system. To allow reliable comparison of subsequent analyses, the used iPSC-cardiomyocytes differentiation experiments were analyzed for purity, quality and sub-type specificity prior to cellular and functional analyses. Fig. 22 shows quality control results of exemplarily and representatively chosen differentiation experiments. All iPSC-cardiomyocytes used for further experiments showed comparable results of all parameters shown. For this, all iPSC-cardiomyocytes differentiation experiments were quantified for the purity of the culture by flow cytometry after staining for the cardiac marker cTNT (Fig. 22 A). Cells stained with the secondary antibody only were used as negative control (Fig. 22 A). Flow cytometry revealed an average purity of cardiac differentiation experiments of 85% ± 10% of all lines (Fig. 22 A). Differentiation experiments below 75% $cTNT^+$ cells were not used for further analyses. Additionally, the expression of classical cardiac markers, like cTNT, α-actinin and titin was analyzed on protein level by IF staining (Fig. 22 B). Cells stained positive for this marker by displaying a sarcomere structure (Fig. 22 B). For cardiac sub-type specification, the iPSC-cardiomyocytes were also stained for ventricular myosin light chain-2 (MLC2v), also demonstrating a sarcomere structure (Fig. 22 B). The results of MLC2v staining and cTNT flow cytometry were combined to quantify the number of ventricular cardiomyocytes amongst all cardiomyocytes on protein level (Fig. 22 C). This yielded an average amount of 70% ± 5% ventricular iPSC-cardiomyocytes per differentiation experiments (Fig. 22 C). To further check for the correct cardiac sub-type the iPSC-cardiomyocytes were analyzed for the expression of ventricular and atrial markers on mRNA level by qPCR (Fig. 22 D). These analyses revealed upregulated expression of the ventricular marker *MLC2v* of the generated iPSC-cardiomyocytes compared to atrial differentiated control iPSC-cardiomyocytes (Fig. 22 D). The level of *MLC2v* expression was comparable to ventricular differentiated control iPSC-cardiomyocytes (Fig. 22 D). In contrast to this, the expression of the atrial marker paired-like homeodomain transcription factor 2 (*PITX2*) was significantly downregulated in the generated iPSC-cardiomyocytes compared to atrial differentiated control iPSC-cardiomyocytes (Fig. 22 D). The level of *PITX2* expression in ventricular DCM1-4 iPSC-cardiomyocytes was low and comparable to ventricular differentiated control iPSC-cardiomyocytes (Fig. 22 D).

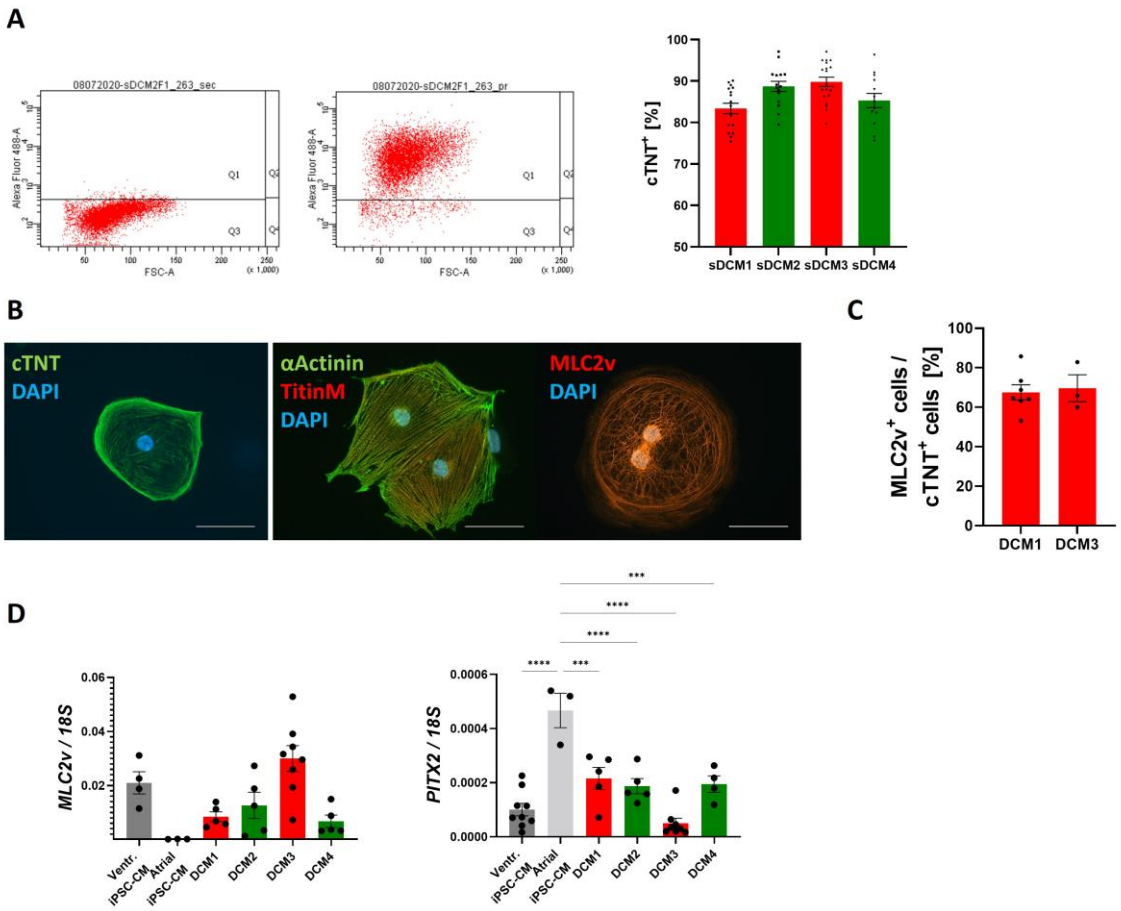

Fig. 22: Representative quality control analyses of iPSC-cardiomyocytes. A Representative flow cytometry analyses of iPSC-cardiomyocytes of all family members stained for cTNT (Alexa Fluor488-conjugated secondary antibody). cTNT-positive cells are shown in gate Q1. Cells only stained with secondary antibody were used as negative control. The gating is shown exemplarily for iPSC-cardiomyocytes of DCM2 (healthy mother). **B** Exemplarily chosen images of IF staining of iPSC-cardiomyocytes of DCM2 (healthy mother) of cTNT (green), α-actinin (green), titinM (red) and MLC2v (red), all displaying sarcomere structure. The nuclei were stained with DAPI (blue). Scale bar=50µm. **C** Relative quantification data of cardiac sub-type marker expression MLC2v amongst all cTNT$^+$ cells on protein level. **D** Quantitative PCR analyses of cardiac sub-type specific genes *MLC2v* (ventricular marker) and *PITX2* (atrial marker). Expression levels of both markers were normalized by corresponding expression of *18S*. Analyses were done using the ΔCt method. Each dot represents one ventricular differentiation experiment. Statistical analysis (one-way ANONA with Tukey`s correction) compared all groups with each other. Data are presented as mean ± SEM. *** = $p < 0.001$ and **** = $p < 0.0001$.

4.1.4.2 Decreased differentiation efficiency of DCM1 iPSC into iPSC-cardiomyocytes

In addition to the quality control analyses of the beating iPSC-cardiomyocytes, the number of successful differentiations amongst all started differentiation experiments was quantified. For this, the number of differentiation experiments started with a sufficient confluency of 70-80% at d0 was compared to differentiation experiments at least reaching the state of functional beating. Differentiation experiments which reached this state were counted as successful. Differentiation experiments which did not reach the state of functional beating were counted as failed. This includes differentiation experiments in which the cells detached at any point during the differentiation process, or where the cells changed morphology but did not start beating or did not start beating without changing

morphology. Out of all differentiation experiments started with iPSC of the diseased father (DCM1) only 47.46% differentiations yielded functional beating cardiomyocytes, 52.54% of all experiments failed (Fig. 23). This is the lowest differentiation efficiency rate amongst all iPSC lines of the family. Interestingly, a high proportion of these failed differentiation experiments consisted of cells with cardiomyocyte morphology, but these cells did not start beating. In comparison to this, differentiation experiments of iPSC of the healthy family members, the mother (DCM2) and the younger daughter (DCM4), were comparably successful with 62.07% and 68.97%, respectively (Fig. 23). In case of failure, the differentiation experiments of these iPSC lines mainly detached after addition of the small molecules CHIR99021 or IWP2. Differentiation experiments of iPSC of the diseased daughter (DCM3) showed the highest success rate with 90% differentiations with functional beating iPSC-cardiomyocytes (Fig. 23).

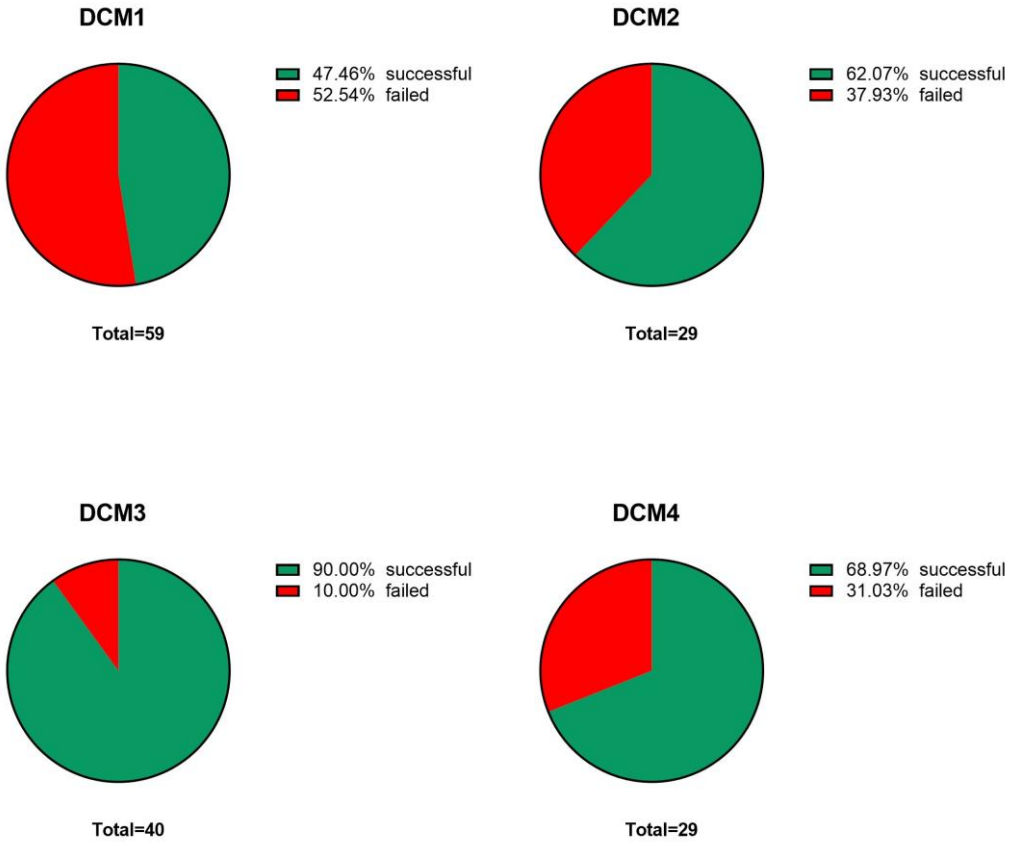

Fig. 23: Analysis of differentiation efficiency of iPSC into iPSC-cardiomyocytes. Quantification data showing the relative amount of successful versus failed differentiation experiments of iPSC into iPSC-cardiomyocytes of all family members. Successful experiments are characterized by reaching the state of functional beating. Failed experiments did not start beating.

4.2 Cellular analysis of DCM iPSC-cardiomyocytes

4.2.1 Dysregulated sarcomere structure in DCM iPSC-cardiomyocytes

A major characteristic of a DCM heart phenotype is the impairment of proper contraction of the heart. This is based on defects within the muscle fiber. The smallest contractile units which are important for force generation within a heart are the sarcomeres within the

individual cardiomyocytes. These sarcomeres form a highly regular structure important for proper contraction and force propagation. The assembly of several sarcomeres form myofibrils, which add up to form a muscle fiber. To form this highly regulated structures several specialized proteins are involved. One of these is FLNC, important for generation and maintenance of myofibrils. Among others, FLNC is important for crosslinking sarcomeric f-actin and formation of several stabilizing interactions. Hence, the identified FLNC variant might have effects on the sarcomere structure. Based on this, the sarcomeric regularity was analyzed by IF staining against α-actinin (to visualize the Z-disc) and titin M8/M9 (to visualize the M-line). Images were taken with a fluorescent microscope and analyzed by FFT (3.2.13). The IF staining displayed a highly regulated pattern of alternating α-actinin and titin bands within the sarcomeres of iPSC-cardiomyocytes of healthy mother and daughter (Fig. 24 A). In contrast to this, IF staining of iPSC-cardiomyocytes of diseased father and daughter demonstrate the complete absence of a regulated sarcomere organization (see Fig. 24 A). Quantification using FFT supports these visual observations (Fig. 24 B, C). The sarcomeric regularity of diseased iPSC-cardiomyocytes is significantly decreased in both structures – M-line and Z-disc (Fig. 24 B, C). Compared to external control iPSC-cardiomyocytes as well as iPSC-cardiomyocytes of healthy mother and daughter the M-line regularity is decreased by ~33% in iPSC-cardiomyocytes of diseased father and daughter (Fig. 24 B). The Z-disc regularity is decreased by ~58% in iPSC-cardiomyocytes of the diseased father and ~50% in iPSC-cardiomyocytes of the diseased daughter (Fig. 24 C).

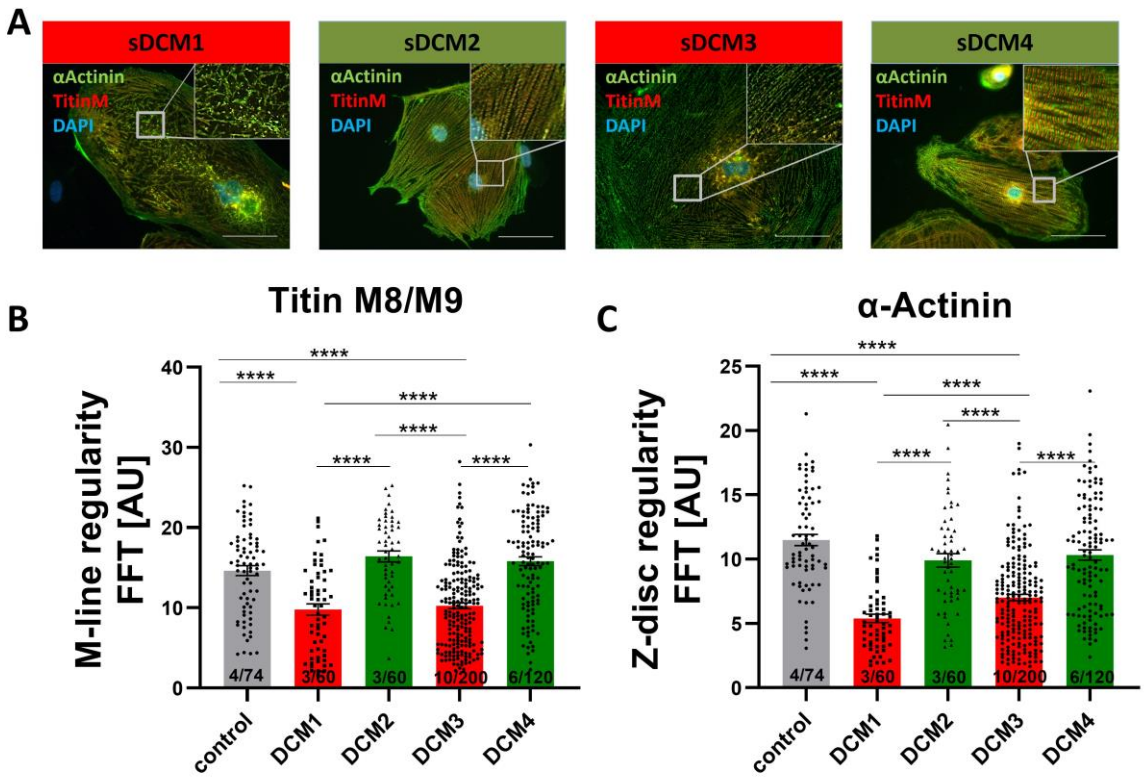

Fig. 24: Sarcomeric regularity is decreased in DCM iPSC-cardiomyocytes. A Representative IF staining against α-actinin (green) and titin M8/M9 (red) of iPSC-cardiomyocytes of all family members to analyze the sarcomere structure. The nuclei were stained with DAPI (blue). Scale bar=50µm. **B + C** Quantification data of **B** M-line (Titin M8/M9) and **C** Z-disc (α-actinin) regularity after applying FFT to the IF images. For every cell line multiple cells and differentiations were analyzed, as indicated at the bottom of each bar (number of

differentiations/number of analyzed cells). Four of the DCM3 differentiation experiments were analyzed by Eva-Maria Staufenberg (MSc student). The peak height of the first-order peak was analyzed for each cell and is represented within the graph. Data is represented as ± SEM. P-values were determined using one-way ANONA multiple comparisons with Tukey`s correction. **** = p < 0.0001.

4.2.2 Differences in cell size of DCM iPSC-cardiomyocytes

To unravel a potential hypertrophic phenotype of the diseased iPSC-cardiomyocytes the cells of all family members and external controls were analyzed with the CASY cell counter and analyzer to investigate the cell size of the individual iPSC-cardiomyocytes. Cells of several differentiation experiments were analyzed. The CASY measurements revealed significant differences in mean (Fig. 25 A) and peak (Fig. 25 B) diameter of DCM1, DCM2 and DCM3 iPSC-cardiomyocytes. iPSC-cardiomyocytes of the healthy daughter showed comparable mean (Fig. 25 A) and peak (Fig. 25 B) diameter to external control cells. Compared to external control iPSC-cardiomyocytes, as well as to DCM2, DCM3 and DCM4 iPSC-cardiomyocytes, the iPSC-cardiomyocytes of the diseased father (DCM1) showed significantly decreased mean (Fig. 25 A) and peak (Fig. 25 B) diameter. External control iPSC-cardiomyocytes had a mean diameter of 24.26±0.091µm and DCM1 iPSC-cardiomyocytes of 23.36±0.05µm (Fig. 25 A). Similar differences were found for the peak diameter (Fig. 25 B). External control iPSC-cardiomyocytes had a peak diameter of 22.88±0.16µm and DCM1 iPSC-cardiomyocytes of 21.79±0.098µm (Fig. 25 B). In contrast to this, iPSC-cardiomyocytes of the healthy mother (DCM2) and diseased daughter (DCM3) showed significantly increased mean (Fig. 25 A) and peak (Fig. 25 B) diameter, compared to external controls. These cells had a mean diameter of 26.19±0.15µm (DCM2) and 25.62±0.12µm (DCM3), respectively (Fig. 25 A). The peak diameter was 25.09±0.21µm (DCM2) and 24.89±0.18µm (DCM3), respectively (Fig. 25 B).

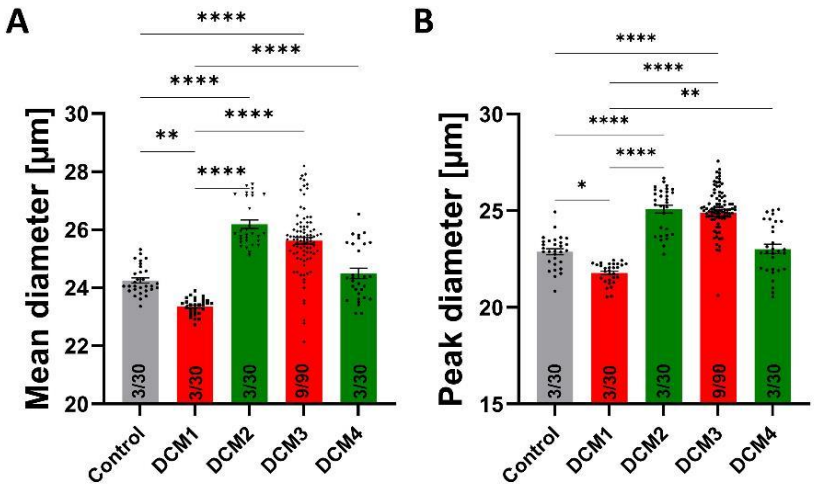

Fig. 25: Cell size of iPSC-cardiomyocytes differs among family members. Quantification data of measurements of iPSC-cardiomyocytes with the CASY cell counter and analyzer. Compared to external control iPSC-cardiomyocytes, the iPSC-cardiomyocytes of DCM1 showed decreased mean (**A**) and peak (**B**) diameter; the iPSC-cardiomyocytes of DCM2 and DCM3 showed increased mean (**A**) and peak (**B**) diameter; the iPSC-cardiomyocytes of DCM4 showed comparable mean (**A**) and peak (**B**) diameter. Numbers within the bars indicate the number of iPSC-cardiomyocytes differentiation experiments / number of analyzed cells. Three of the DCM3 differentiation experiments were measured by Eva-Maria Staufenberg (MSc student). Data is represented as ± SEM. P-values were determined using one-way ANONA multiple comparisons with Tukey`s correction. * = p < 0.05, ** = p < 0.01, *** = p < 0.001 and **** = p < 0.0001.

4.3 FLNC gene editing

4.3.1 Successful generation of isogenic control iPSC lines using CRISPR/Cas9

The previous described data demonstrated a diseased sarcomeric phenotype of iPSC-cardiomyocytes derived from patients with DCM (father and daughter), who display the identified FLNC variant, c.6560G>C (p.R2187P) and ILK variant, c.1274T>C (p.Met425Thr). To investigate whether the identified FLNC variant might be the causative mutation leading to the identified pathogenic phenotype, isogenic rescue-FLNC lines were generated using the CRISPR/Cas9 gene editing method. For this, first iPSC of the diseased father (DCM1) were chosen to revert the heterozygous missense mutation back to wildtype FLNC, expressing an arginine at aa position 2187 homozygously (Fig. 26 A). As the choice of crRNA is crucial for the gene editing outcome, two different crRNAs (FLNC1 and FLNC2, Fig. 12) guiding the Cas9 in close proximity to the SNP mutation, were tested in parallel experiments, both using the same HDR template (coding for wildtype FLNC, Fig. 12). 36 clones were picked for each experiment (FLNC1 and FLNC2) and were sequenced to evaluate the gene editing efficiency (Fig. 26 B). When using crRNA FLNC1 0% of the analyzed clones were edited to wildtype FLNC (Fig. 26 C). Instead, only frameshifts induced by insertions and deletions could be observed. In contrast to this, using crRNA FLNC2 37.5% (6/16 clones analyzed) successfully edited clones could be found (Fig. 26 C). When including mixed clones into this calculation the editing efficiency would even increase up to 81% (13/16 clones analyzed, Fig. 26 C). Mixed clones derived from picking iPSC colonies containing edited and non-edited cells. These clones in principle could be purified by subsequential singularization and are mainly a result of handling issues. Based on these results, only crRNA FLNC2 was used for editing of iPSC of the diseased daughter (DCM3). Here, gene editing yielded an efficiency of 50% (7/14 clones analyzed, Fig. 26 C). Again, when including mixed clones editing efficiency would even increase up to 78.6% (11/14 clones analyzed, Fig. 26 C). Sequencing of all edited clones showed that these contained one out of two synonymous mutations which were integrated into the HDR template to avoid recutting and hence increase efficiency (Fig. 26 B). The second synonymous mutation was encoded more upstream of the cut and the SNP was not found in the edited sequence (Fig. 26 B). Three clones of each isogenic FLNC-rescue line were chosen for further experiments, K1, K5, K9 for DCM1 and K19, K23, K24 for DCM3, respectively. These clones were characterized for pluripotency and cardiomyocyte differentiation and were tested for off-target effects, which might have occurred due to CRISPR/Cas9 gene editing. All clones were sequenced every 5-10 passages to test for constant *FLNC* rescue.

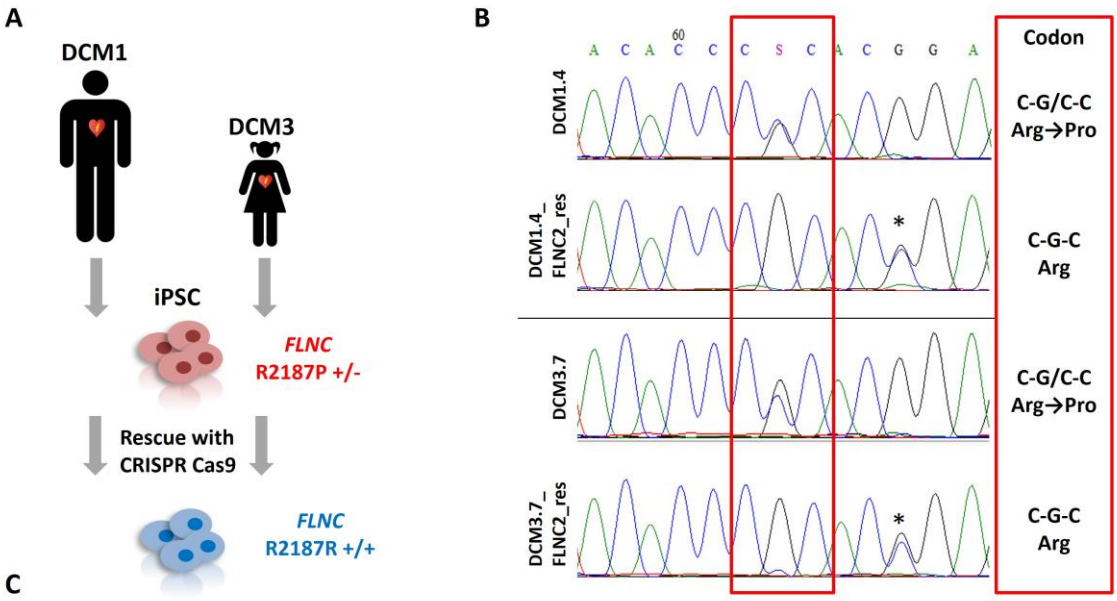

C

	gRNA FLNC1 on DCM1.4	gRNA FLNC2 on DCM1.4	gRNA FLNC2 on DCM3.7
Clones total	36	36	36
Clones analyzed	6	16	14
CRISPR efficiency	0%	37.5% - 81% (incl. mixed clones)	50% - 78.6% (incl. mixed clones)
Clones thawed	0	3 (K1, K5, K9)	3 (K19, K23, K24)

Fig. 26: Generation of isogenic *FLNC*-rescue iPSC. A Principle of generation of isogenic FLNC-rescue iPSC from DCM-iPSC. **B** Shown are Sanger sequencing results of the *FLNC* locus where the identified missense variant was found. This includes the position c. 6559-6561 coding for aa 2187 of the *FLNC* gene. Patient lines encode the C-C/G-C, coding heterozygously for proline/arginine at aa position 2187, whereas rescue lines encode the C-G-C, homozygously coding for arginine at aa position 2187. * marks the integrated synonymous mutation provided by the HDR template. **C** Shown is a table representing editing efficiency obtained for the different editing approaches using different crRNAs and target iPSC lines. Clones total represents the number of clones randomly picked for analysis after singularization of the edited iPSC. Clones analyzed represents the number of sequenced clones out of all clones picked.

4.3.2 Generated isogenic control iPSC display full pluripotency

To ensure CRISPR/Cas9 gene editing did not have any effect on the pluripotent character of the generated iPSC lines the cells were analyzed for expression of classical pluripotency markers and were applied to an *in vitro* spontaneous differentiation experiment like the patient iPSC-lines. Pluripotency characterization is exemplarily shown for one isogenic control line of each diseased family member in the following paragraph. Pluripotency characterization of the remaining clones can be found in the Suppl. Fig. 3, and Suppl. Fig. 4. Experimental data of FLNC-rescue lines will be displayed in blue color in every graph and figure. All generated isogenic control iPSC showed a classical stem cell morphology and activity of ALP (Fig. 27, Suppl. Fig. 3). Furthermore, the iPSC were analyzed for expression of pluripotency-associated markers on protein level by IF staining (Fig. 27, Suppl. Fig. 3). All isogenic iPSC showed high expression of the transcription factors SOX2, OCT4 and NANOG as a specific nuclear staining of these markers could be detected, which colocalized with nuclear DAPI staining (Fig. 27 A, Suppl. Fig. 3). Additionally, expression of the translational enhancer and RNA-binding protein LIN28 could be detected by a specific staining in the

cytoplasm and no staining of the nucleus (Fig. 27 A, Suppl. Fig. 3). Finally, expression of the cell surface protein TRA1-60 could be detected by specific staining of the cell membrane (Fig. 27 A, Suppl. Fig. 3). Expression of SOX2, OCT4, NANOG, LIN28 and GDF3 was confirmed on mRNA level as well (Fig. 27 B).

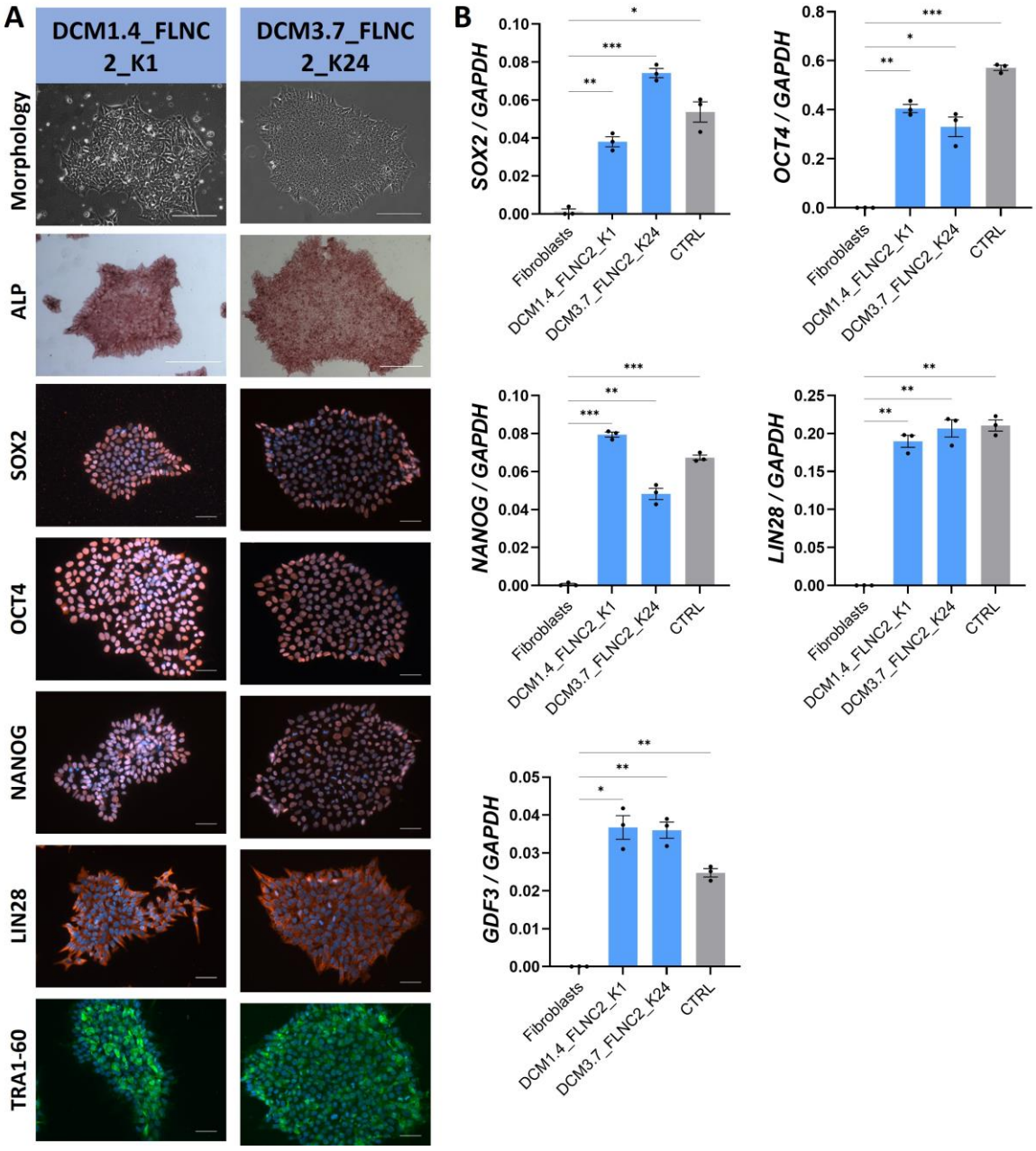

Fig. 27: Pluripotency characterization of *FLNC* gene edited iPSC clones. Pluripotency characterization results of the mainly used gene edited iPSC clones of DCM1 and DCM3 – K1 and K24, respectively. **A** Brightfield and ALP images of the generated gene edited iPSC lines. Images were taken with a Zeiss Axio Observer A1 inverted microscope. Sacle bar=200µm. Additionally, images of the pluripotency markers SOX2 (red), OCT4 (red), NANOG (red), LIN28 (red) and TRA1-60 (green) are shown as merged images with the nuclear DAPI (blue) staining. All images were taken with a Zeiss Axio Observer A1 inverted microscope. Scale bar=50µm. **B** Quantitative PCR analyses of iPSC clones K1 and K24, fibroblasts and PBMCs as negative control (only stated as fibroblasts in the graphs) and already published control (CTRL) iPSC lines (all n=3 passages) to analyze the expression levels of different pluripotency-associated markers. Shown are analyses of *SOX2, OCT4, NANOG, LIN28* and *GDF3*. Expression levels of all markers were normalized by corresponding expression of *GAPDH,* and analyses were done using the ΔCt method. Statistical analysis (one-way ANONA with Tukey`s correction)

compared all groups with each other. Data are presented as mean ± SEM. * = p < 0.05, ** = p < 0.01 and *** = p < 0.001.

Analysis of spontaneous *in vitro* differentiation experiments on protein level by IF staining confirmed expression of the endodermal AFP, the mesodermal αSMA and the ectodermal βIII-tubulin (Fig. 28, Suppl. Fig. 4). In addition to this, analysis on mRNA level by RT-PCR revealed decreasing expression of the pluripotency-associated marker *OCT4* over time, whereas expression of endodermal markers, like *AFP* and *ALB*, as well as expression of mesodermal markers, like *αMHC* or αSMA (*ACTA2*) was increasing over time. The same was shown for the expression of ectodermal markers, like *MAP2* and paired box 6 (*PAX6*). Like for patient iPSC lines, these markers were largely absent in iPSC and cannot be shown in MEFs.

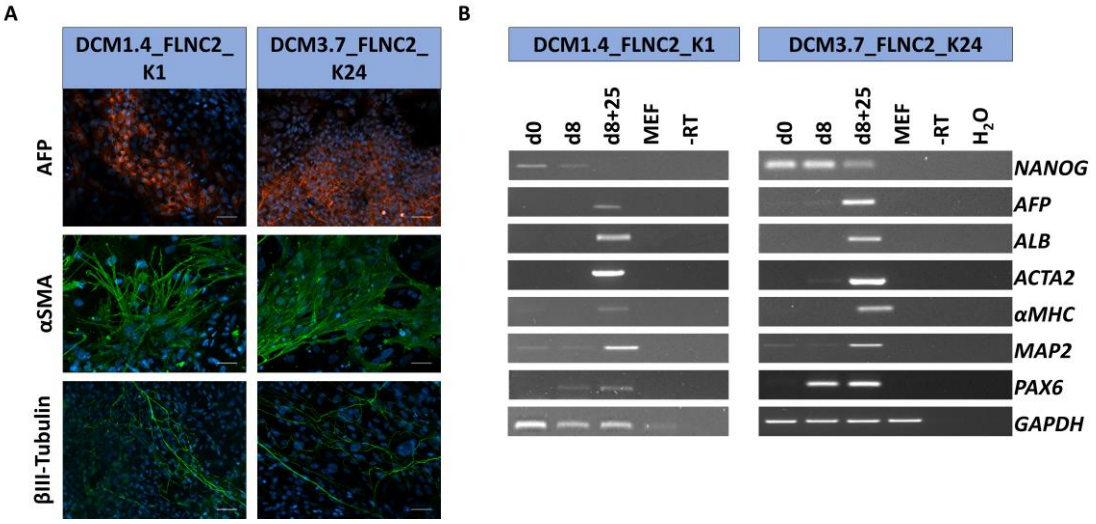

Fig. 28: Spontaneous *in vitro* differentiation of *FLNC* gene edited iPSC clones. Pluripotency characterization results of the mainly used gene edited iPSC clones of DCM1 and DCM3 – K1 and K24, respectively. **A** Representative images of iPSC stained positive for AFP (endoderm, red), αSMA (mesoderm, green) and βIII-tubulin (ectoderm, green), all shown as merged images with the nuclear stain DAPI (blue). All images were taken with a Zeiss Axio Observer A1 inverted microscope. Scale bar=50µm. **B** Results of semi-quantitative PCR of EB gene edited clones at different time points (d0, d8, d8+25). The iPSC showed *OCT4* expression at day 0. Over time, expression of markers of all germ layers, like *AFP* and *ALB* as endodermal, *ACTA2* and *αMHC* as mesodermal and *MAP2* and *PAX6* as ectodermal markers is increasing. MEFs, used as negative control, do not show expression of any of these markers. *GAPDH* was used as housekeeping gene.

4.3.3 Absence of off-target effects in CRISPR/Cas9 generated FLNC-rescue isogenic control iPSC

The CRISPR/Cas9 method was used to change the *FLNC* variant back to wildtype sequence within cells of the diseased family members father (DCM1) and daughter (DCM3). For this, a crRNA was used which encodes a complementary sequence that can bind to the desired gene locus and by this guides the Cas9 enzyme to the correct position to induce the cut. However, this crRNA often not only binds to the desired locus but also might be complementary to other sequences within the genome. Although complementary binding to so called off-target sequences is usually not 100% but rather is characterized by one or more mismatches, off-target cutting by the Cas9 enzyme cannot be excluded. Hence, it is important to analyze potential off-target sequences for sequence changes after

CRISPR/Cas9 gene editing. Off-target cutting might be most likely at sequences with lowest number of mismatches. Due to this, only the top 5 predicted off-target sequences were analyzed after FLNC gene editing by Sanger sequencing. These top 5 candidates were predicted using the Jefferson Off-Spotter website (https://cm.jefferson.edu/Off-Spotter/), which searches genome wide for complementary sequences of the crRNA. The Jefferson Off-Spotter identified one off-target with 3 mismatches compared to the crRNA. Despite the three mismatches, binding of the crRNA might be possible. This was located in an intergenic region of the leucine-rich repeat containing G protein-coupled receptor 4 (*LGR4*) gene. Additionally, three off-targets with 4 mismatches compared to the crRNA were identified. One in the first exon of the glutamine-fructose-6-phosphate transaminase-2 (*GFPT2*) gene, one in an intron of the immunoglobulin superfamily, member 11 (*IGSF11*) gene and one in an intron of the NLR family, pyrin domain containing 6 (*NLRP6*) gene. The last predicted off-target sequence with five mismatches compared to the crRNA was in an intron of the Janus kinase and microtubule interacting protein 3 (*JAKMIP3*) gene. Sanger sequencing of these predicted off-targets was performed of iPSC of the diseased family members – DCM1 and DCM3 – and the corresponding isogenic control lines – DCM1_res and DCM3_res – after CRISPR/Cas9 gene editing (Fig. 29). The primers were designed to flank the potential cutting locus, which is three nucleotides upstream of the PAM site. For simplicity, only a short sequence is shown in Fig. 29, always including the cutting site (PAM site highlighted in blue). Nevertheless, for analysis, the whole sequence was analyzed and no other difference between the edited and non-edited lines than stated below could be observed. Analysis of the resulting chromatograms show that no off-target in any of the analyzed genes or lines can be observed, as there are no differences when comparing the lines before and after CRISPR/Cas9 gene editing (Fig. 29). However, two random variants were identified. First, when analyzing the *GFPT2* off-target site for patient and isogenic control line of the diseased father DCM1 (DCM1.4 and DCM1.4_FLNC2_K1), showed a heterozygous deletion (delCCCACGGAG, het) within the predicted *GFPT2* off-target site (Fig. 30, deletion locus highlighted in red). The same deletion can be found in a homozygous manifestation (delCCCACGGAG, homo) in patient and isogenic control line of the diseased daughter (DCM3.7 and DCM3.7_FLNC2_K24; Fig. 30, deletion locus red-rimmed). An additional sequence comparison to wildtype sequence is shown in Fig. 30. As these deletions, regardless of heterozygous (DCM1) or homozygous (DCM3) appearance, are present in both – before and after CRISPR – it is not a result of any off-target effect. Additionally, when evaluating the sequences of the *JAKMIP3* off-target site for patient-derived line sDCM1.4 and the corresponding isogenic control line DCM1.4_FLNC2_K1 a heterozygous SNP (G>T) can be found. As this SNP appears in both lines – before and after CRISPR – it is not derived from any off-target effect and can be counted as secondary finding only. As this SNP is located in an intron of the *JAKMIP3* gene, it most likely does not have a severe effect.

LGR4

Off-target: ATGAGCTCCGTGAGCTCCGT GGG

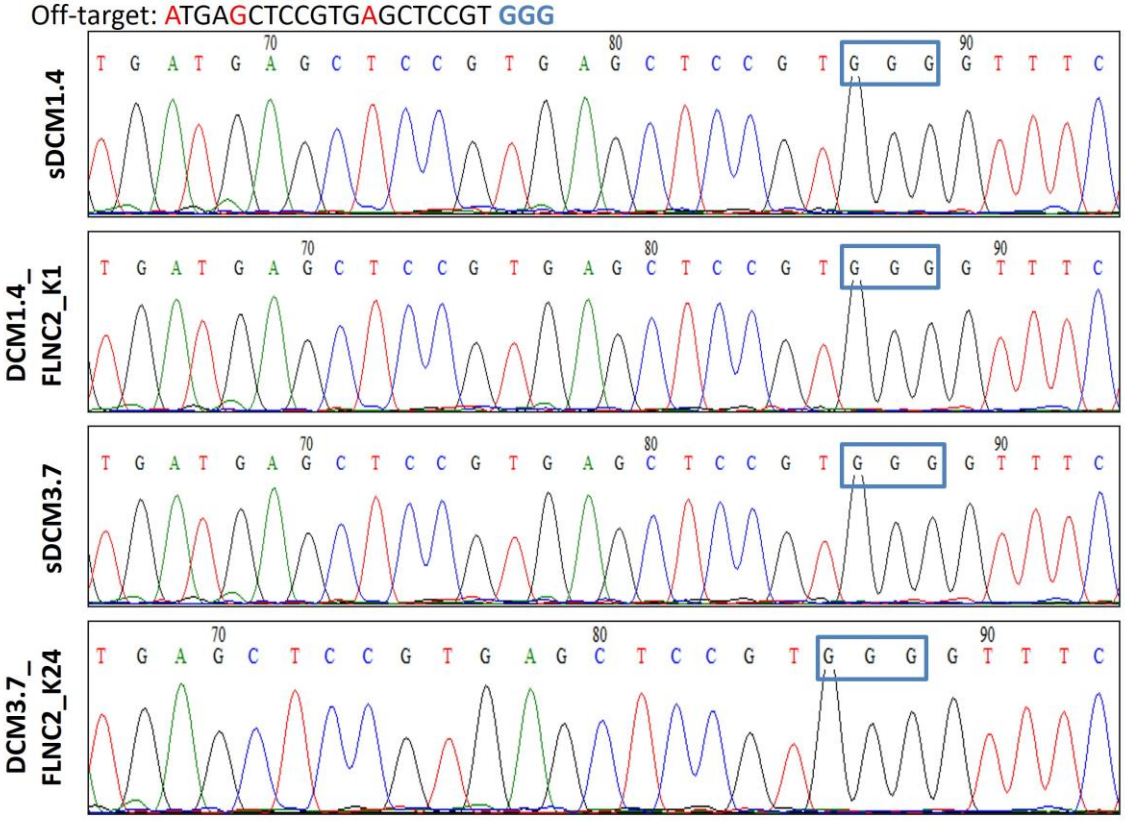

GFPT2

Off-target: GTGGGCTCCGTGGGCTCCGT GGG (Off-target on rev strand, shown fw strand)

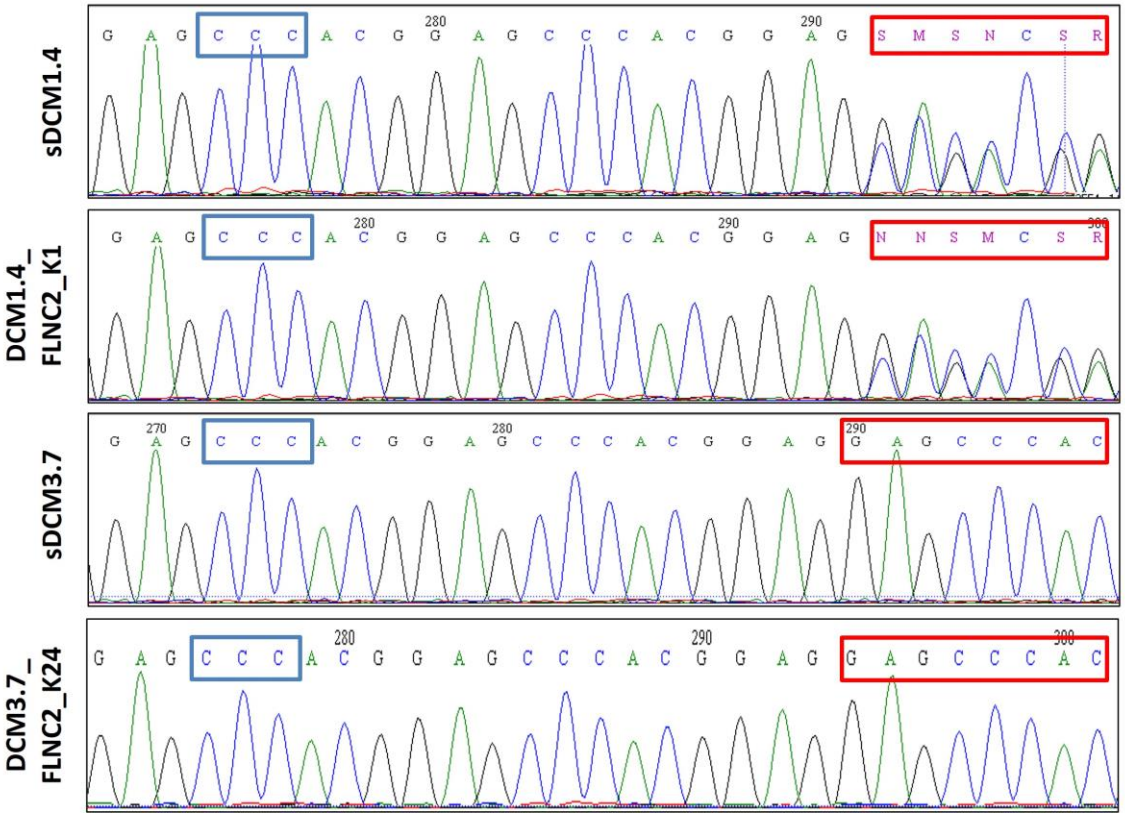

IGSF11

Off-target: CTGCTCTCCCTTCTCTCCGT **GGG**

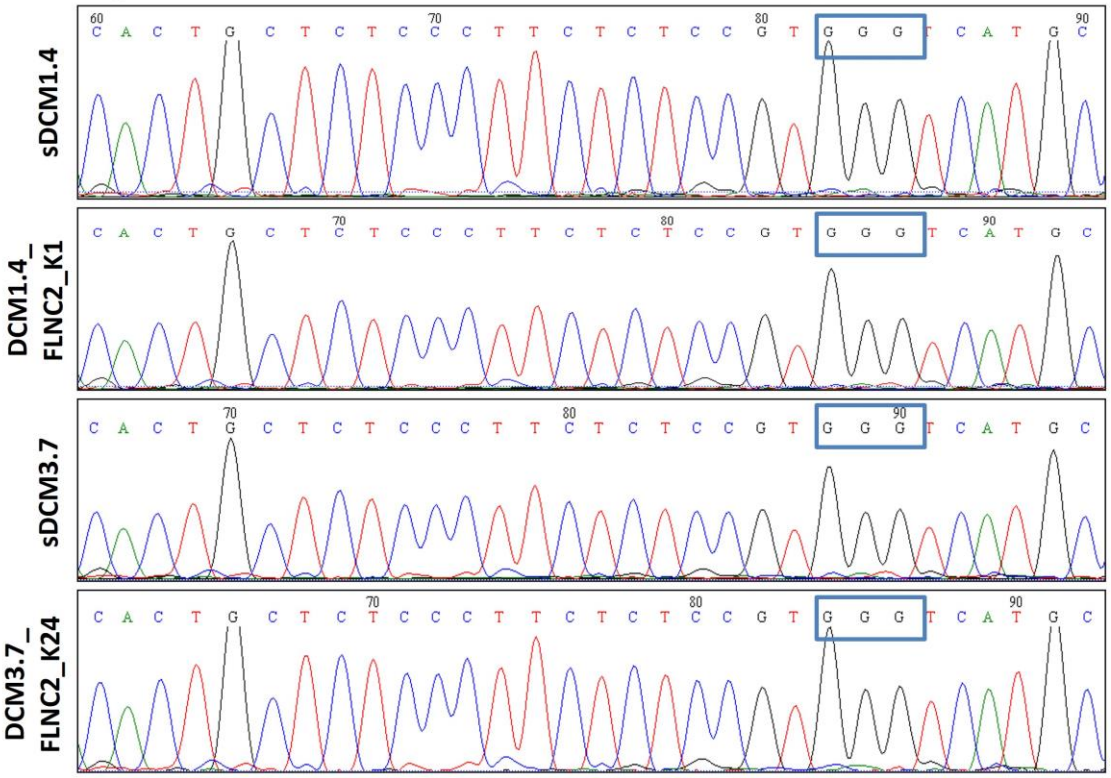

NLRP6

Off-target: CTGCTCTCAGCCCGCTCCGT **GGG** (Off-target on rev strand, shown fw strand)

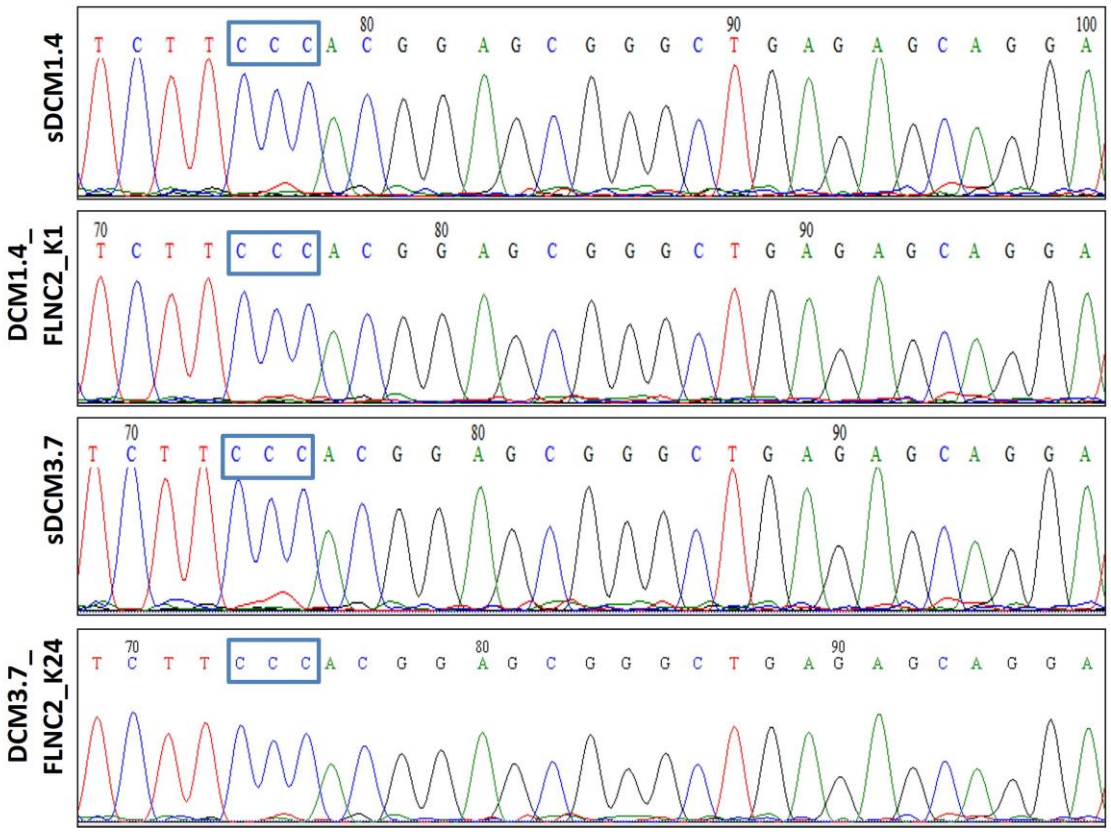

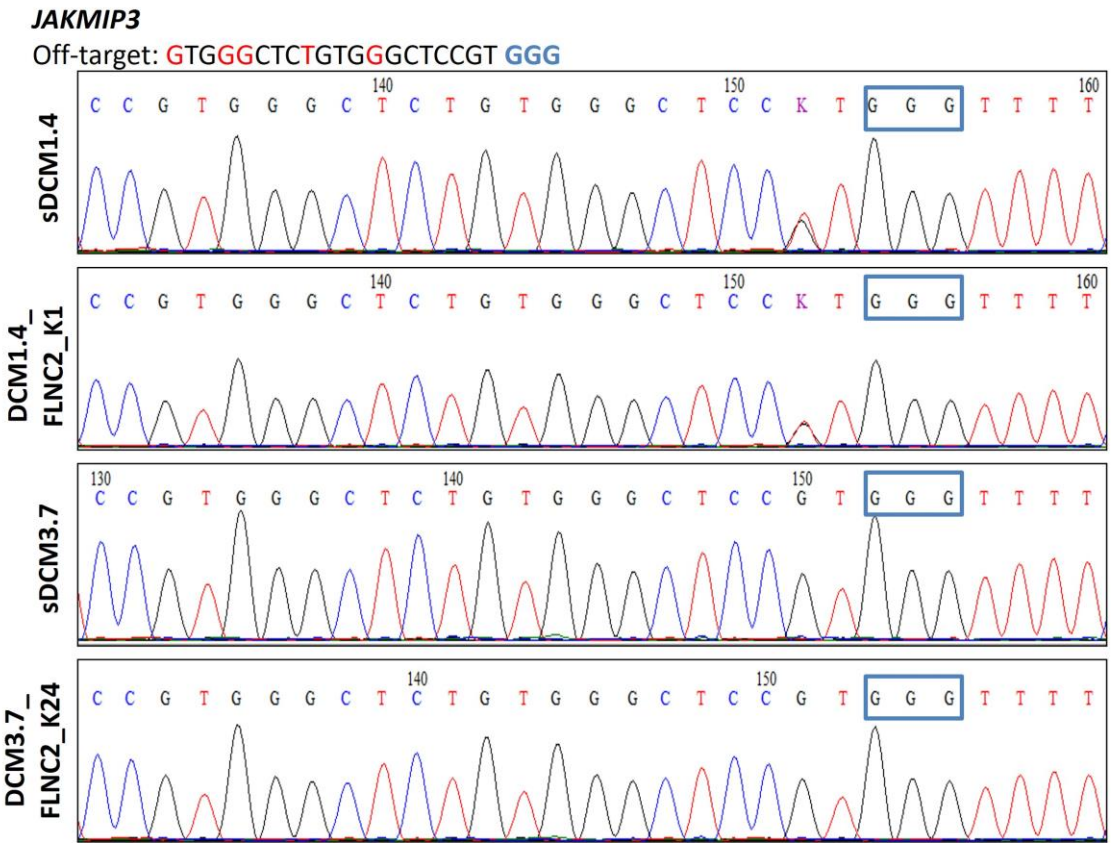

Fig. 29: Off target analysis of *FLNC* gene edited iPSC clones. Sanger sequencing chromatograms of the top 5 predicted off-target sites (Jefferson Off-Spotter) of patient-derived iPSC lines before and after CRISPR/Cas9 to rescue the *FLNC* variant. Chromatograms are shown for potentially targeted sequences of *LGR4, GFPT2, IGSF11, NLRP6* and *JAKMIP3* for iPSC lines DCM1.4, DCM1.4_FLNC2_K1, DCM3.7 and DCM3.7_FLNC2_K24. PAM sites are labelled in blue/blue boxes. Red boxes show deletions in GFPT2.

WT	CCGCGGAGCCCACGGAGCcCACGGAGccCAcGGAGGAGCCCACGGAGGAGCCCCAGCGTC
3.7	CCGCGGAGCCCACGGAGCCCACGGAGxxxxxxxxxxGAGCCCACGGAGGAGCCCCAGCGTC del:CCCACGGAG, homo
K24	CCGCGGAGCCCACGGAGCCCACGGAGxxxxxxxxxxGAGCCCACGGAGGAGCCCCAGCGTC del:CCCACGGAG, homo
1.4	CCGCGGAGCCCACGGAGCCCACGGAGSMSNCSRMGGAGNNSMCSSAGNANCCCAACGGNC del:CCCACGGAG, het
K1	CCGCGGAGCCCACGGAGCCCACGGAGNNSMCSRMGGAGNNSMCSSAGNANCCCAACGGNC del:CCCACGGAG, het

Fig. 30: Sequence comparison of wildtype, patient, and isogenic control lines of *GFPT2* off-target site. *GFPT2* off-target site sequences based on Sanger sequencing for wildtype (NM_005110.4), iPSC lines DCM1.4, DCM1.4_FLNC2_K1, DCM3.7 and DCM3.7_FLNC2_K24. Highlighted in grey the predicted off-target site (lower case letters mark the mismatches to the crRNA) is marked. Red the deleted sequence is shown.

4.3.4 Quality control of gene edited isogenic control iPSC-cardiomyocytes

Like quality control experiments of patient-derived iPSC-cardiomyocytes, FLNC gene edited iPSC-cardiomyocytes were analyzed for purity, quality, and sub-type specificity prior to cellular and functional analyses. Fig. 31 only shows quality control results of exemplarily and representatively chosen differentiation experiments. All iPSC-cardiomyocytes used for further experiments showed comparable results of all parameters shown. Flow cytometry revealed an average purity of cardiac differentiation experiments of 85% ± 10% of all lines (Fig. 31 A). Additionally, IF staining of classical cardiac markers, like cTNT, α-actinin and titin was positive as the cells showed a sarcomere structure of all markers (Fig. 31 B). For cardiac

sub-type specification, the iPSC-cardiomyocytes were also stained for MLC2v, also displaying a sarcomere structure (Fig. 31 B). An average amount of 70% ± 5% ventricular iPSC-cardiomyocytes per differentiation experiments was obtained (Fig. 31 C). To further confirm the correct cardiac sub-type the iPSC-cardiomyocytes were analyzed for the expression of ventricular and atrial markers on mRNA level by qPCR (Fig. 31 D). These analyses revealed upregulated expression of the ventricular marker *MLC2v* of the generated iPSC-cardiomyocytes compared to atrial differentiated control iPSC-cardiomyocytes (Fig. 31 D). The level of *MLC2v* expression was comparable to ventricular differentiated control iPSC-cardiomyocytes (Fig. 31 D). In contrast to this, the expression of the atrial marker *PITX2* was significantly downregulated in the generated iPSC-cardiomyocytes compared to atrial differentiated control iPSC-cardiomyocytes (Fig. 31 D). The level of *PITX2* expression in ventricular differentiated iPSC-cardiomyocytes of DCM1_res and DCM3_res was comparable low as seen in ventricular differentiated control iPSC-cardiomyocytes (Fig. 31 D).

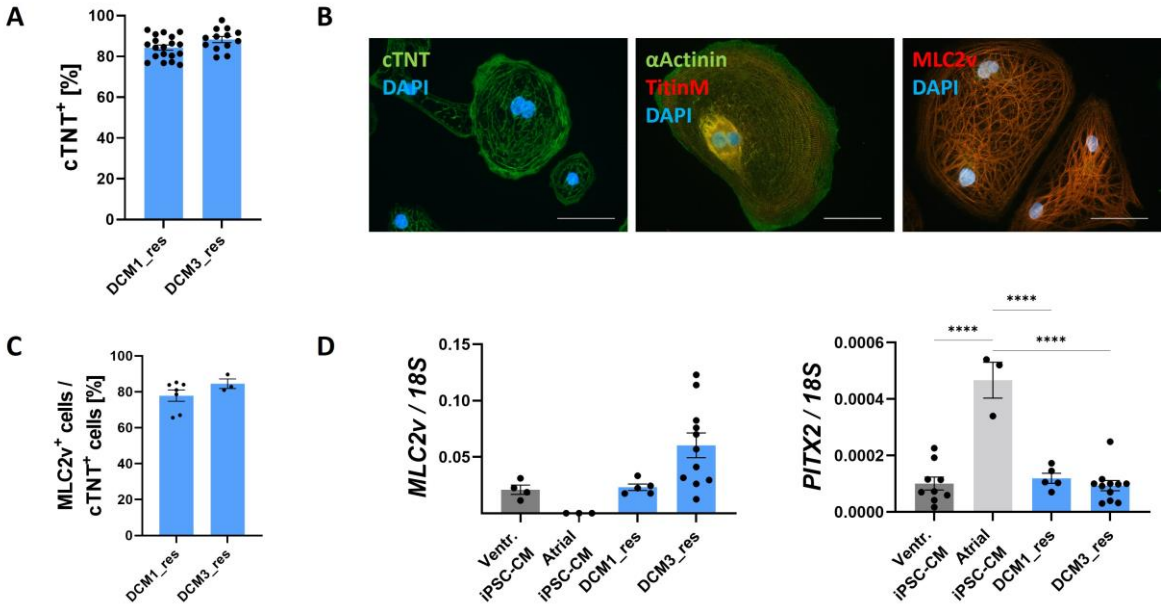

Fig. 31: Representative quality control analyses of gene edited iPSC-cardiomyocytes. A Representative flow cytometry analyses of gene edited iPSC-cardiomyocytes stained for cTNT (Alexa Fluor488-conjugated secondary antibody). **B** Exemplarily chosen IF staining of iPSC-cardiomyocytes of DCM1_res of cTNT (green), α-actinin (green), titin M8/M9 (red) and MLC2v (red), all displaying sarcomere structure. The nuclei were stained with DAPI (blue). Scale bar=50µm. **C** Relative quantification data of cardiac sub-type marker expression MLC2v amongst all cTNT$^+$ cells on protein level. **D** Quantitative PCR analyses of cardiac sub-type specific genes *MLC2v* (ventricular marker) and *PITX2* (atrial marker). Expression levels of both markers were normalized by corresponding expression of *18S,* and analyses were done using the ΔCt method. **A + C + D** Each dot represents one cardiac differentiation experiment. Statistical analysis (one-way ANONA with Tukey`s correction) compared all groups with each other. Data are presented as mean ± SEM. **** = $p < 0.0001$.

4.3.5 Differentiation efficiency of isogenic control DCM1_FLNC2 iPSC into iPSC-cardiomyocytes is improved compared to DCM1-iPSC

As differentiation efficiency was dramatically reduced for DCM iPSC-cardiomyocytes, differentiation efficiency of corresponding isogenic control DCM1_res iPSC-cardiomyocytes was analyzed, as described before (4.1.4.2). The iPSC derived from the diseased father

(DCM1) showed the lowest differentiation efficiency of <50%. In contrast, the isogenic FLNC-rescue DCM1 cells showed noteworthy improvement of differentiation efficiency to a success rate of 72.41% (Fig. 32). This success rate of ~70% is comparable to control iPSC of mother (DCM2) and healthy daughter (DCM4, Fig. 32). In patient-derived iPSC of the diseased father, differentiation efficiency was largely limited by the problem that the cells did change to cardiomyocyte morphology but did not start beating. In contrast to this, in FLNC-rescue isogenic control DCM1_res cells this phenotype could no longer be observed as predominant reason of differentiation failure. In these cells, the differentiation efficiency was mainly limited by detachment of the cells during the differentiation process, like it was the case for control cells.

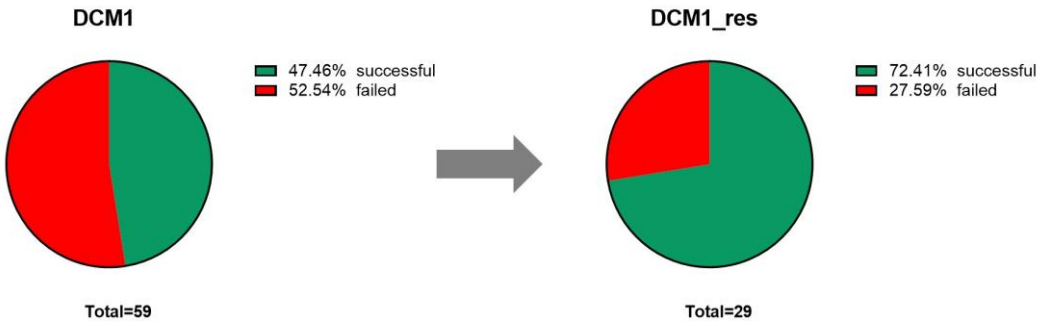

Fig. 32: Analysis of differentiation efficiency of isogenic control iPSC of DCM1 into iPSC-cardiomyocytes. Quantification data showing the amount of successful versus failed differentiation experiments of iPSC into iPSC-cardiomyocytes of DCM1 isogenic control lines. Successful experiments are characterized by reaching the state of functional beating. Failed experiments did not start beating.

4.3.6 Rescue of sarcomeric regularity in isogenic control iPSC-cardiomyocytes

The gene edited isogenic FLNC-rescue lines were differentiated into iPSC-cardiomyocytes and analyzed for sarcomeric regularity as described previously (3.2.13). IF staining of isogenic control iPSC-cardiomyocytes of father (DCM1_res) and daughter (DCM3_res) showed a highly regulated pattern of alternating α-actinin and titin bands within the sarcomeres, in contrast to iPSC-cardiomyocytes of diseased father and daughter, where a regulated sarcomere organization could not be observed (Fig. 33 A). Quantification using FFT supports these visual observations (Fig. 33 B, C). The sarcomeric regularity of isogenic control DCM3_res iPSC-cardiomyocytes is significantly increased in both – M-line and Z-disc – to a level comparable to control iPSC-cardiomyocytes (Fig. 33 B, C). The sarcomeric regularity of isogenic control DCM1_res iPSC-cardiomyocytes is significantly increased in both – M-line and Z-disc – as well (Fig. 33 B, C). However, whereas regularity of M-line is comparable to control iPSC-cardiomyocytes, regularity of Z-disc is also significantly improved, but not to a level of control regularity (Fig. 33 B, C). This data indicates that the FLNC variant most likely causes the sarcomeric disarray observed in patient-derived iPSC-cardiomyocytes.

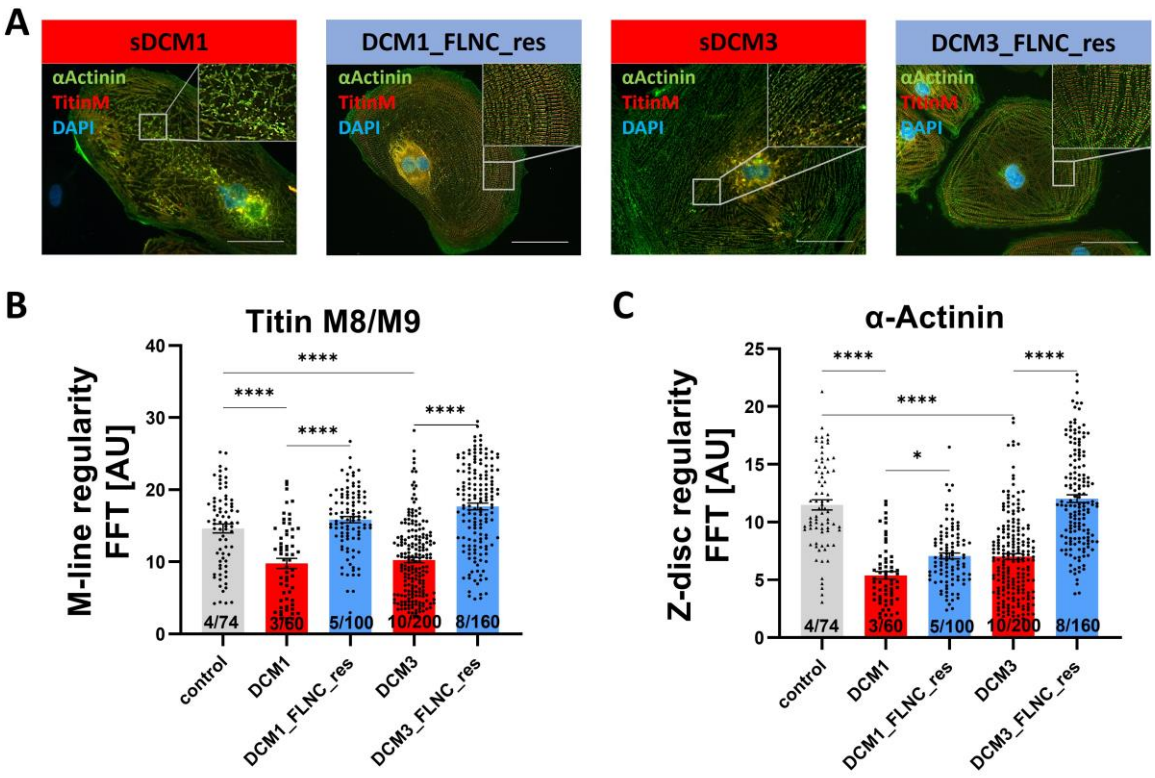

Fig. 33: Sarcomeric regularity is rescued in isogenic control iPSC-cardiomyocytes. A Representative IF staining against α-actinin (green) and titin M8/M9 (red) of iPSC-cardiomyocytes to analyze the sarcomere structure. The nuclei were stained with DAPI (blue). Scale bar=50µm. **B + C** Shown is quantification data of **B** M-line and **A** Z-disc regularity after applying FFT to the IF images. For every cell line multiple cells and differentiations were analyzed, as indicated at the bottom of each bar (number of differentiations/number of analyzed cells). For each cell, the peak height of the first-order peak was analyzed and is represented within the graph. Four of the DCM3 and 6 of the DCM3_res differentiation experiments were analyzed by Eva-Maria Staufenberg (MSc student). Data is represented as ± SEM. P-values were determined using one-way ANONA multiple comparisons with Tukey`s correction. * = $p < 0.05$, ** = $p < 0.01$, *** = $p < 0.001$ and **** = $p < 0.0001$.

4.3.7 Rescue of cell size of DCM1 iPSC-cardiomyocytes after FLNC gene editing

As cell size of iPSC-cardiomyocytes derived from DCM patients was significantly different compared to iPSC-cardiomyocytes derived from external controls it was analyzed if the FLNC rescue had an effect on cell size of iPSC-cardiomyocytes. Analyses with the CASY cell counter and analyzer indeed showed increased cell size of isogenic control DCM1_res iPSC-cardiomyocytes to a level of external control iPSC-cardiomyocytes (Fig. 34). The mean diameter of DCM1_res iPSC-cardiomyocytes of 24.13±0.065µm was comparable to this of external control iPSC-cardiomyocytes of 24.26±0.09µm and significantly larger than the mean diameter of the diseased DCM1 iPSC-cardiomyocytes of 23.36±0.05µm (Fig. 34 A). Comparable results were obtained analyzing the peak diameter as shown in Fig. 34 B. Here peak diameter of DCM1_res iPSC-cardiomyocytes of 22.75±0.1µm was comparable to this of external control iPSC-cardiomyocytes of 22.88±0.15µm and significantly larger than the mean diameter of the diseased DCM1 iPSC-cardiomyocytes of 21.79±0.097µm (Fig. 34 B). Whereas cell size of iPSC-cardiomyocytes of the diseased father (DCM1) seems to be rescued after FLNC gene editing, the enlarged cell size of iPSC-cardiomyocytes of the

diseased daughter (DCM3) even increased further after FLNC rescue (Fig. 34 A, B). The mean diameter of 26.76±0.8µm of the DCM3_res iPSC-cardiomyocytes significantly larger compared to iPSC-cardiomyocytes of DCM3 of 25.62±0.11µm (Fig. 34 A). The peak diameter of the DCM3_res iPSC-cardiomyocytes of 25.81±0.12µm also was significantly increased compared to iPSC-cardiomyocytes of DCM3 of 24.89±0.18µm (Fig. 34 B).

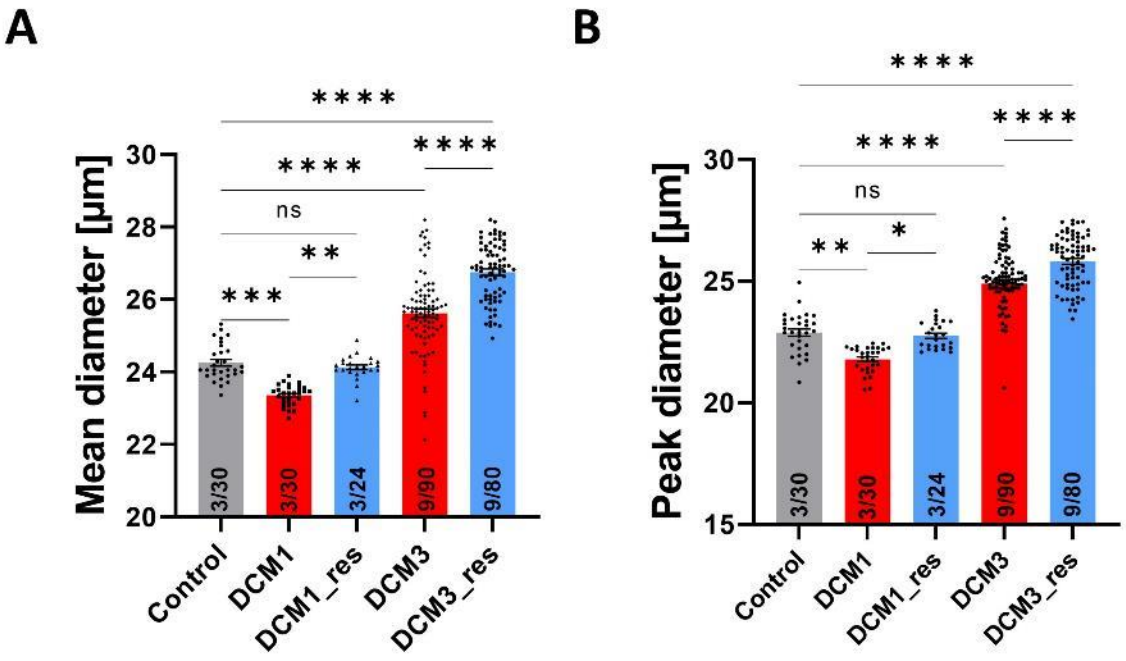

Fig. 34: Cell size of iPSC-cardiomyocytes changes after FLNC gene editing. Quantification data of measurements of iPSC-cardiomyocytes with the CASY cell counter and analyzer. **A** Mean diameter and **B** Peak diameter. Numbers within the bars indicate the number of iPSC-cardiomyocytes differentiation experiments / number of analyzed cells. Five of the DCM3/DCM3_res differentiation experiments were measured by Eva-Maria Staufenberg (MSc student). Data is represented as ± SEM. P-values were determined using one-way ANONA multiple comparisons with Tukey`s correction. * = $p < 0.05$, ** = $p < 0.01$, *** = $p < 0.001$ and **** = $p < 0.0001$.

4.4 Molecular analysis of DCM and isogenic control iPSC-cardiomyocytes

4.4.1 FLNC rescue enhances maturation state of iPSC-cardiomyocytes

During human heart development an isoform switch of the cardiac myosin heavy chain (MHC) protein can be observed (Guo and Pu, 2020; Reiser *et al.*, 2001). In early stages of the human heart development the α-MHC isoform, encoded by the *MYH6* gene, is predominantly expressed (Reiser *et al.*, 2001). With ongoing maturation of the heart, the relative amount of the β-MHC isoform, encoded by the *MYH7* gene, is increasing and becomes predominant (Reiser *et al.*, 2001). Although iPSC-derived cardiomyocytes rather resemble a neonatal phenotype, changes in MHC isoform usage can be observed between less and more matured cells (Eschenhagen and Carrier, 2019; Zhao *et al.*, 2020b). Hence, generated DCM and FLNC-rescued isogenic control iPSC-cardiomyocytes were analyzed for mRNA expression of the two MHC isoforms – α-MHC and β-MHC. Important to note, pellets of all iPSC-cardiomyocytes used for the analysis were taken at the same age of three-

months. Even though no statistically significant mean differences were observed, clear changes in isoform expression can be observed between diseased and healthy/isogenic control iPSC-cardiomyocytes (Fig. 35). In the diseased iPSC-cardiomyocytes – DCM1 and DCM3 – *MYH6* expression (DCM1: 0.1273 ±0.036, DCM3: 0.09054 ± 0.018) is increased and *MYH7* expression (DCM1: 0.395 ±0.079, DCM3: 0.9099 ± 0.21 to) is decreased compared to corresponding isogenic control iPSC-cardiomyocytes – DCM1_res (*MYH6*: 0.07625 ±0.016, *MYH7*: 0.6487 ±0.098) and DCM3_res (*MYH6*: 0.04687 ±0.013, *MYH7*: 1.241 ±0.1971), respectively (Fig. 35 A, B). Based on the expression analysis of the individual *MYH* isoforms, a *MYH7/MYH6* ratio was calculated, which can be used as a measure of maturation. The higher the *MYH7/MYH6* ratio, the higher the maturation state of the cells. The *MYH7/MYH6* ratio increased 2.26-fold from DCM1 to isogenic DCM1_res iPSC-cardiomyocytes (with DCM1 4.627 ±1.784 and DCM1_res 10.48 ±2.951, Fig. 35 C). A similar trend could be observed for DCM3 and isogenic DCM3_res, where the *MYH7/MYH6* ratio increased 2.77-fold (with DCM3 12.05 ±3.912 and DCM3_res 33.33 ±9.018, Fig. 35 C). In conclusion, the FLNC-rescued isogenic control iPSC-cardiomyocytes show a slightly higher maturation state compared to the corresponding diseased iPSC-cardiomyocytes, although not statistically significant.

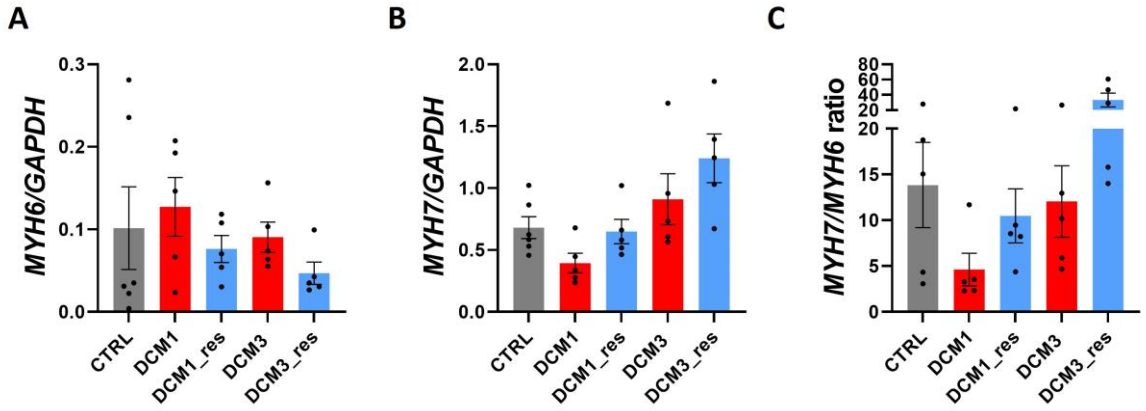

Fig. 35: Expression analysis of cardiomyocyte maturation markers *MYH6* and *MYH7* in DCM iPSC-cardiomyocytes. Quantitative PCR data of external control (CTRL), diseased DCM1 and DCM3 and isogenic control iPSC-cardiomyocytes is shown. **A** Expression of predominantly early-stage expressed *MYH6* is slightly upregulated in diseased iPSC-cardiomyocytes compared to external and isogenic controls. **B** Expression of predominantly later-stage expressed *MYH7* is slightly downregulated in diseased iPSC-cardiomyocytes compared to isogenic controls. **C** Ratio of *MYH7/MYH6* expression as a marker for maturation is lower in diseased iPSC-cardiomyocytes compared to isogenic control cells. **A + B + C** Expression levels of both markers were normalized by corresponding expression of *GAPDH,* and analyses were done using the ΔCt method. Data is represented as ± SEM. No significances were detected. Each dot represents one ventricular cardiac differentiation experiment.

4.4.2 Unaffected expression and localization of mutated FLNC

Previously described data pointed towards a sarcomeric phenotype being linked to the newly identified FLNC variant, c.6560G>C (p.R2187P), discovered in diseased father and daughter of the index family. To analyze the underlying molecular mechanisms leading to the identified phenotype and the overall DCM, first mRNA expression of *FLNC* was analyzed by qPCR (Fig. 36 A). *FLNC* expression within iPSC-cardiomyocytes of all family members and external control cells was normalized to *GAPDH* as housekeeping gene. As shown in Fig. 36

A, *FLNC* was expressed similarly in diseased and healthy iPSC-cardiomyocytes (Fig. 36 A). To analyze potential dysregulation of FLNC expression on protein level, Western blot experiments were performed for external control, diseased and isogenic control iPSC-cardiomyocytes (Fig. 36 B). These Western blot experiments did not show any differences in FLNC expression between healthy and diseased iPSC-cardiomyocytes (Fig. 36 B). Isogenic control iPSC-cardiomyocytes also did not show dysregulation of FLNC expression on protein level (Fig. 36 B).

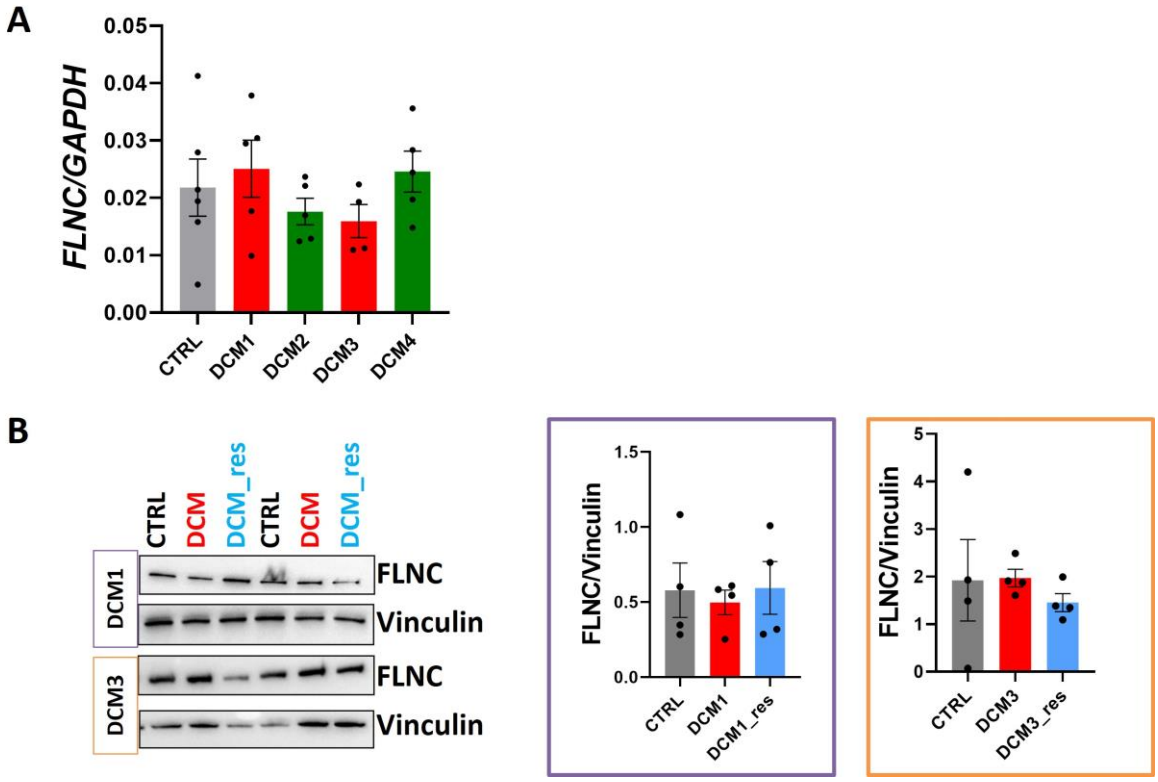

Fig. 36: Expression analysis of FLNC in DCM and isogenic control iPSC-cardiomyocytes. A Quantitative PCR data of *FLNC* expression in external control (CTRL), diseased DCM1 and DCM3, and healthy DCM2 and DCM4 iPSC-cardiomyocytes. Expression levels were normalized by corresponding expression of *GAPDH,* and analyses were done using the ΔCt method. No differential mRNA expression of *FLNC* could be shown**.** Each dot represents one ventricular cardiac differentiation experiment. **B** Shown is Western blot data of external control (CTRL), diseased DCM1 and isogenic control DCM1_res iPSC-cardiomyocytes, as well as external control (CTRL), diseased DCM3 and isogenic control DCM3_res iPSC-cardiomyocytes of FLNC normalized to vinculin expression. Compared to external control iPSC-cardiomyocytes, the diseased and isogenic control iPSC-cardiomyocytes did not show differential protein expression of FLNC. Each dot represents one ventricular cardiac differentiation experiment.

Besides investigating a potential dysregulation of FLNC expression, potential mislocalization of FLNC was analyzed by IF staining (Fig. 37 A, B). First, expression of titin and FLNC was analyzed in explanted, paraffin-embedded non-failing and DCM1 myocardium sections (Fig. 37 A). Importantly, non-failing tissue sections could be prepared as longitudinal sections displaying clear myofilaments. In contrast, the DCM1 tissue was embedded only allowing cross sectioning of the tissue and the respective muscle fibers. Hence, analyzing proper titin and FLNC localization was difficult in DCM1 tissue, since the needed structures (sarcomeres and/or ICD) were only visible in small areas by chance (Fig. 37 A). Nevertheless, antibody staining of non-failing tissue revealed a highly structured titin

pattern representing an organized sarcomere of several matured and connected myocytes (Fig. 37 A, yellow triangle). Similarly, an organized pattern of titin could be shown in DCM1 tissue in certain areas (Fig. 37 A, yellow triangle). However, due to the predominant cross-sectioning, this pattern was only visible for some cells and a clear structure of connected myocytes could not be shown. Due to the limited number of cells sliced in proper orientation, quantification of sarcomeric regularity comparable to analysis within iPSC-cardiomyocytes was not possible. IF staining directed against FLNC revealed slight staining of sarcomeric-like structures (yellow triangle) and stronger staining at areas connecting individual cardiomyocytes to larger myofibers, representing the ICD (green arrows) in both, non-failing and DCM1 tissue sections (Fig. 37 A). However, since the DCM1 tissue was sliced in cross-sectional direction the myofibers were not displayed as clear as in non-failing tissue. Nevertheless, the staining shown was similar to ICD staining of non-failing tissue (Fig. 37 A). The same antibody was used to identify expression of FLNC in iPSC-derived cardiomyocytes (Fig. 37 B). Interestingly, like primary tissue, FLNC staining visualized sarcomeric-like structures (yellow triangle) and accumulated at cell-cell interactions (green arrow) of iPSC-cardiomyocytes, like ICD, in control iPSC-cardiomyocytes (Fig. 37 B). Similar to the staining of control iPSC-cardiomyocytes, diseased DCM1 and DCM3, as well as of FLNC-rescued DCM1_res and DCM3_res iPSC-cardiomyocytes visualized sarcomeric-like structures (yellow triangle) and cardiomyocyte cell-cell contacts (green arrow) (Fig. 37 B). Based on this data, no differences in FLNC localization in diseased DCM1 and DCM3 could be identified. However, future quantification analysis will give more insights into the localization of FLNC in control and diseased cardiomyocytes.

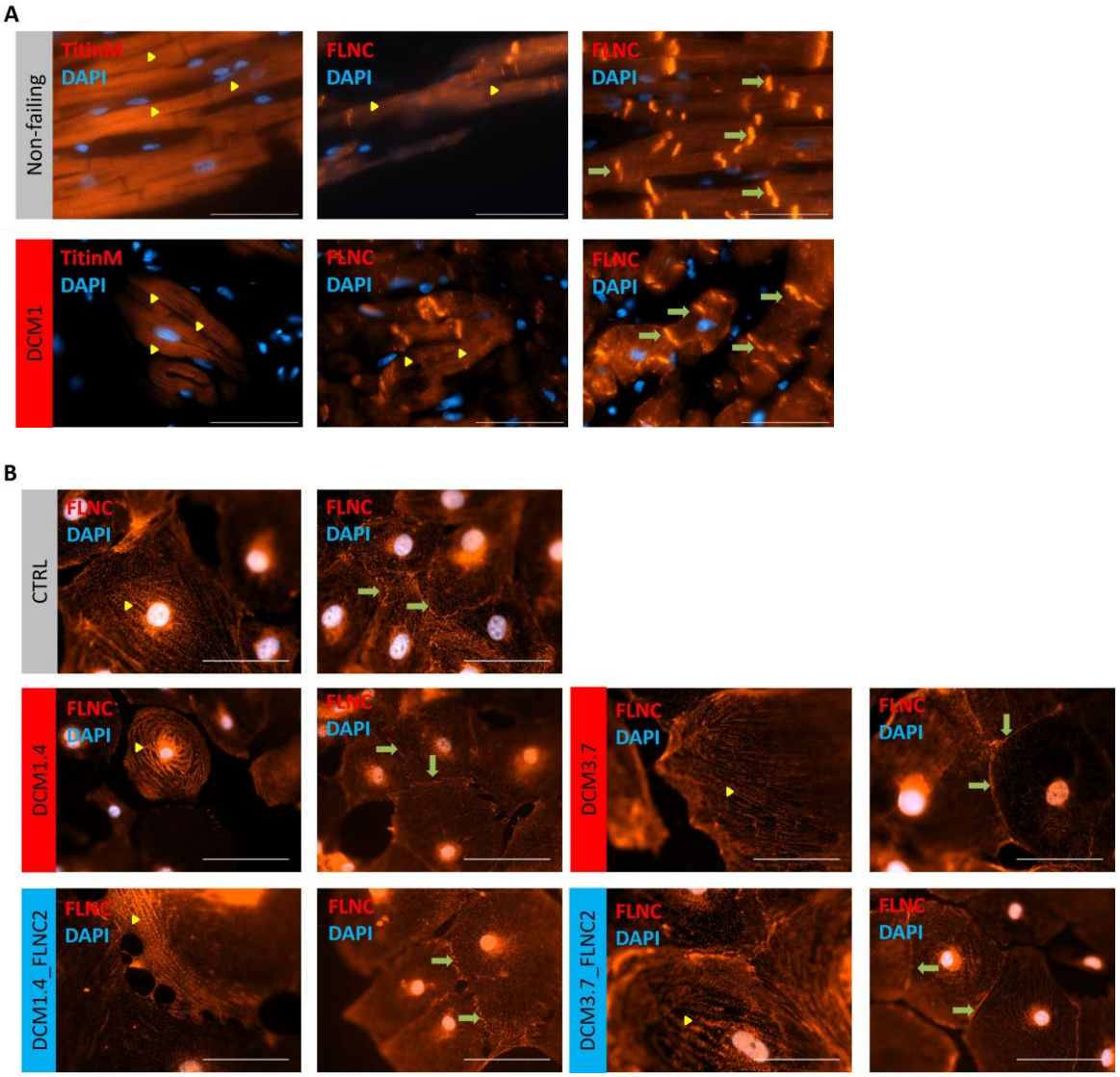

Fig. 37: Localization of FLNC in DCM and isogenic control (iPSC-) CM. A Titin M8/M9 (red) and FLNC (red) IF staining of primary, paraffin-embedded non-failing and DCM1 tissue, visualizing sarcomeric-like structures (yellow triangle) and ICD (green arrow). The nuclei were stained with DAPI (blue). Scale bar=50µm. **B** FLNC (red) IF staining of external control (CTRL), diseased DCM1 and DCM3, as well as isogenic control DCM1_res and DCM3_res iPSC-cardiomyocytes showing sarcomeric-like structures (yellow triangle) and accumulation at cardiomyocyte cell-cell contacts (green arrow) The nuclei were stained with DAPI (blue). Scale bar=50µm.

4.4.3 Unaffected expression of FLNC interaction partners

FLNC is interacting with many different proteins during Z-disc development, stabilization, and maintenance. A high number of these interactions are mediated via the second ROD domain, specifically via domain 20, where the identified variant is localized. Consequently, it might be possible that interactions to proteins binding FLNC at this position might be affected. In a first approach, mRNA expression of aciculin (*PGM5*), XIN (*XIN*), myotilin (*MYOT*) and myopodin (*SYNPO2*) was analyzed, all of which are proteins, which were reported to directly interact with FLNC within the unique 82aa insertion, where the identified variant is localized. Expression of all was analyzed by qPCR in external control iPSC-cardiomyocytes and iPSC-cardiomyocytes of all family members by qPCR. Expression was normalized to *GAPDH*. Aciculin, a protein colocalizing with FLNC at ICD and mature Z-

disc has a very high affinity for FLNC binding and interacts with FLNC domain 18-21, where the variant harboring 82aa insertion of domain 20 seems to be crucial for the binding (Molt *et al.*, 2014). The mRNA expression of *PGM5,* the aciculin encoding gene*,* was not altered in diseased iPSC-cardiomyocytes – DCM1 and DCM3 – compared to healthy iPSC-cardiomyocytes (Fig. 38 A). XIN, also a multi-adaptor protein, colocalizes with FLNC at ICD and non-straited muscle fibers and binds FLNC domain 20, where the variant is localized (van der Ven *et al.*, 2006). Expression of *XIN* in diseased iPSC-cardiomyocytes – DCM1 and DCM3 – was comparable to *XIN* expression in healthy iPSC-cardiomyocytes (Fig. 38 B). Myotilin, an α-actinin binding protein directly interacts with the 82aa insertion of FLNC and indirectly anchors FLNC to α-actinin (van der Ven *et al.*, 2000). As shown in Fig. 38 C, DCM1 and DCM3 iPSC-cardiomyocytes did not show dysregulated expression of *MYOT* compared to healthy iPSC-cardiomyocytes. Myopdin, also a multi-adaptor protein of the sarcomeric Z-disc, interacts with FLNC domains 20-21 (Linnemann *et al.*, 2010). Although, there was no significant dysregulation of *SYNPO2,* the myopodin encoding gene*,* in diseased iPSC-cardiomyocytes visible, there seemed to be a slight upregulation of *SYNPO2* in DCM1 and DCM3 iPSC-cardiomyocytes compared to healthy iPSC-cardiomyocytes (Fig. 38 D).

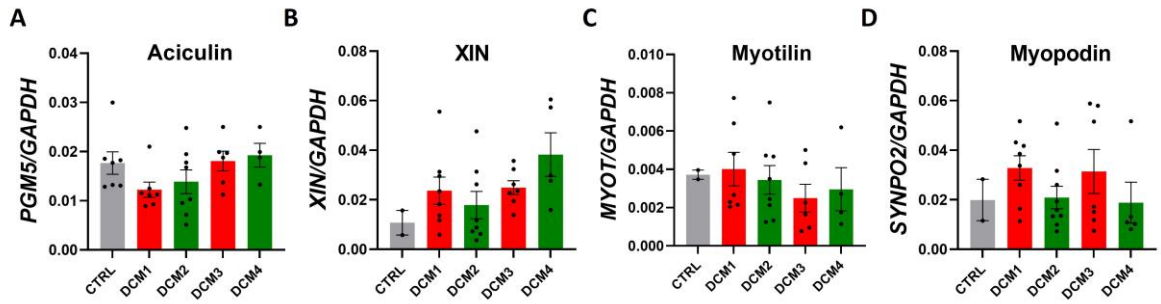

Fig. 38: Expression analysis of FLNC interaction partners in iPSC-cardiomyocytes. Quantitative PCR data of external control (CTRL), diseased DCM1 and DCM3 and healthy DCM2 and DCM4 iPSC-cardiomyocytes. Compared to external and family control iPSC-cardiomyocytes, the iPSC-cardiomyocytes of DCM1 and DCM3 did not show differential expression of FLNC interaction partners (**A**) *PGM5* (**B**) *XIN* (**C**) *MYOT* (**C**) *SYNPO2*. **A, B, C** Expression levels were normalized by corresponding expression of *GAPDH,* and analyses were done using the ΔCt method. Each dot represents one ventricular cardiac differentiation experiment.

4.4.4 Downregulation of Connexin43 protein expression in DCM iPSC-cardiomyocytes

GJ, made of connexin-composed channels, are important for propagation of the cardiac electrical stimulus from cell to cell (Kostin *et al.*, 2003). GJ remodeling often is observed in the human failing heart (Dupont *et al.*, 2001; Kostin *et al.*, 2003; Severs *et al.*, 2004). This remodeling often includes molecular downregulation of connexin43 (CX43) and changes of its distribution throughout the cell (Dupont *et al.*, 2001; Kostin *et al.*, 2003; Severs *et al.*, 2004). To investigate, whether a GJ remodeling phenotype is present in DCM iPSC-cardiomyocytes, CX43 expression and localization was analyzed. Analysis of CX43 protein expression by Western blot experiments revealed a downregulation of CX43 expression in DCM1 and DCM3 and corresponding isogenic control iPSC-cardiomyocytes (Fig. 39 A). However, this downregulation was only significant for DCM3_res iPSC-cardiomyocytes. IF staining of CX43 in combination with α-actinin, for better localization, showed expression

of CX43 in the plasma membrane and an accumulation at cell-cell contacts (Fig. 39 B). There was no obvious difference in amount or localization detectable between the different iPSC-cardiomyocytes analyzed (Fig. 39 B). However, as iPSC-cardiomyocytes do not form highly structured muscle fibers, and only form cell-cell contacts by chance, clear disturbance of CX43 localization would be difficult to detect. Finally, analysis of mRNA expression by qPCR did not show any statistical mean difference of CX43 (encoded by *GJA1*) expression in neither the DCM nor the isogenic control iPSC-cardiomyocytes compared to external control iPSC-cardiomyocytes (Fig. 39 C).

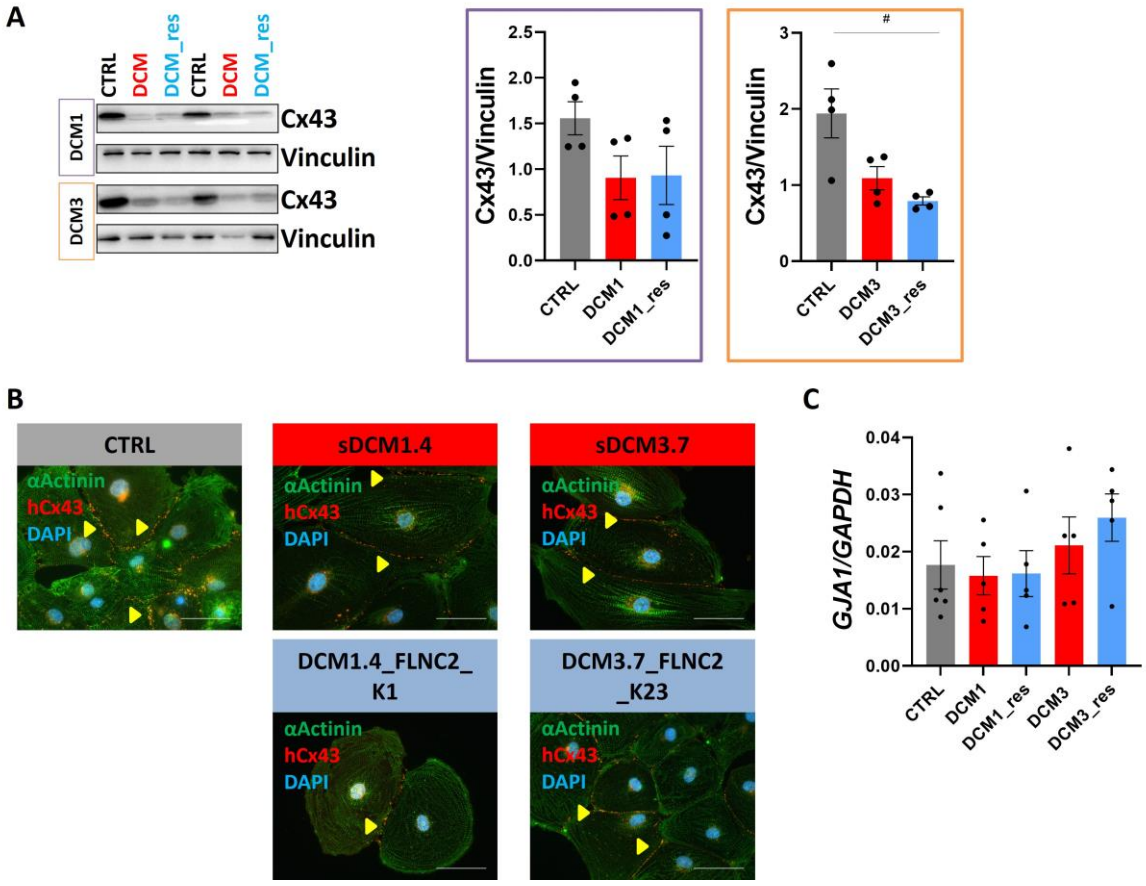

Fig. 39: Expression of CX43 in DCM and isogenic control iPSC-cardiomyocytes. A Western blot data of CX43 for external control (CTRL), diseased DCM1 and isogenic control DCM1_res iPSC-cardiomyocytes and external control, diseased DCM3 and isogenic control DCM3_res iPSC-cardiomyocytes, normalized to vinculin. Compared to external control iPSC-cardiomyocytes, the diseased and isogenic control iPSC-cardiomyocytes show downregulated CX43 expression on protein level. **B** Exemplarily chosen IF staining against α-actinin (green) and CX43 (red) of iPSC-cardiomyocytes. The nuclei were stained with DAPI (blue). Scale bar=50µm. CX43 is expressed in the plasma membrane and accumulates at cell-cell contacts (yellow triangle). **C** qPCR data of external control, DCM, and isogenic control iPSC-cardiomyocytes to assess the expression of CX43 (*GJA1*) on mRNA level. Expression was normalized to *GAPDH* expression. Comparable expression of CX43 can be observed in all analyzed lines. **A + C** Each dot represents one ventricular cardiac differentiation experiment. Data is represented as ± SEM. P-values were determined using Student`s t-test (#). # = $p < 0.05$.

4.4.5 DCM1 and DCM3 iPSC-cardiomyocytes show different regulation of genes and proteins important for Ca^{2+} handling

Ca^{2+} cycling is the driving force for cardiomyocyte contraction as it translates the electrical stimulus into myocyte contraction (1.1.1.1.1). For this, a tightly regulated network of Ca^{2+}

handling proteins within the cardiomyocytes is required for proper function (1.1.1.1.1). Irregularities within the Ca^{2+} homeostasis often have been associated with cardiac diseases, like DCM. Hence, expression of important Ca^{2+} handling proteins was investigated by Western blot analysis of external control, DCM and isogenic control iPSC-cardiomyocytes of diseased father (Fig. 40) and daughter (Fig. 41). Expression of all markers analyzed was normalized to expression of vinculin stained on the same membrane as each marker. First, expression of the RYR2 and its phosphorylation status at two distinct sites was analyzed. Active RYR2 is important for Ca^{2+} release from the SR upon stimulus. Phosphorylation of RYR2 leads to activation and can be mediated by protein kinase A (PKA, phosphorylation at position RYR-S2808) or CaMKIIδ (phosphorylation at position RYR-S2814). As can be seen in Fig. 40 and Fig. 41, no statistically significant mean difference in RYR2 expression can be observed neither between diseased and isogenic control iPSC-cardiomyocytes, nor compared to external control iPSC-cardiomyocytes. Phosphorylation of the PKA target site RYR-S2808 was comparable between external control, DCM and isogenic control iPSC-cardiomyocytes for both – DCM1 (Fig. 40) and DCM3 (Fig. 41) patient. However, phosphorylation of the CaMKIIδ target site RYR-S2814 was significantly upregulated in DCM1 iPSC-cardiomyocytes in comparison to external control cells (Fig. 40). Although not significant, phosphorylation of RYR-S2814 was also increased in isogenic control DCM1_res iPSC-cardiomyocytes compared to external control cells (Fig. 40). For DCM3 and isogenic DCM3_res iPSC-cardiomyocytes phosphorylation of RYR-S2814 is comparable to external control iPSC-cardiomyocytes (Fig. 41). Next, expression of the NCX was evaluated. NCX, together with SERCA2a and the MCU, is important to remove cytoplasmic Ca^{2+} after the systolic phase. There was no difference of NCX expression in iPSC-cardiomyocytes of DCM1 and isogenic control DCM1_res compared to external control iPSC-cardiomyocytes (Fig. 40). Yet, there was a significant downregulation of NCX expression in DCM3 iPSC-cardiomyocytes when comparing to external control cells. (Fig. 41). This downregulation seemed to be partially rescued in isogenic control DCM3_res iPSC-cardiomyocytes (Fig. 41). Additionally, expression of SERCA2a was analyzed. Again, no difference could be observed between DCM1, isogenic control DCM1_res and external control iPSC-cardiomyocytes (Fig. 40). But SERCA2a was significantly upregulated in DCM3 iPSC-cardiomyocytes compared to isogenic control DCM3_res iPSC-cardiomyocytes (Fig. 41). Additionally, SERCA2a tended to be upregulated in DCM3 iPSC-cardiomyocytes compared to external controls (Fig. 41). Furthermore, expression of the CaMKIIδ was analyzed, due to its key role in regulating different Ca^{2+} handling proteins by phosphorylation for example. As CaMKIIδ activity itself, is predominantly regulated by oxidation rather than phosphorylation or expression, the oxidization state of CaMKIIδ was analyzed as well. There were no significant changes in expression or oxidization detectable for DCM1 compared to DCM1_res or external control iPSC-cardiomyocytes (Fig. 40). In DCM3 iPSC-cardiomyocytes CaMKIIδ expression tended to be upregulated compared to isogenic and external control iPSC-cardiomyocytes (Fig. 41). The oxidization of CaMKIIδ in DCM3, however, was comparable to DCM3_res and external controls (Fig. 41). Finally, expression and activity of PLN was investigated. PLN acts as an inhibitor of SERCA activity and hence regulates Ca^{2+} kinetics. Upon phosphorylation of PLN, this inhibitor function is switched off. Similar to RYR2, PLN has two phosphorylation sites, either mediated by PKA (phosphorylation at position PLN-S16) or CaMKIIδ

(phosphorylation at position PLN-T17). Phosphorylation at both sites was analyzed by Western blot analysis. There was no statistically significant mean difference in PLN expression itself in diseased iPSC-cardiomyocytes compared to isogenic and external control iPSC-cardiomyocytes (Fig. 40, Fig. 41). However, PLN tended to be lower expressed in DCM1 and DCM1_res iPSC-cardiomyocytes compared to external control cells (Fig. 40). Interestingly, CaMKIIδ-mediated phosphorylation at position PLN-T17 was significantly increased in DCM1 and DCM1_res iPSC-cardiomyocytes (Fig. 40). For technical reasons, PLN-T17p could not be analyzed in DCM3 and DCM3_res iPSC-cardiomyocytes. There was no significant difference in PKA-mediated phosphorylation at position PLN-S16 of diseased iPSC-cardiomyocytes compared to healthy and isogenic control iPSC-cardiomyocytes (Fig. 41). Nevertheless, PLN-S16 phosphorylation tended to be decreased in DCM1, compared to healthy and isogenic controls, and tended to be increased in DCM3, compared to healthy and isogenic controls (Fig. 41). In summary, DCM1 iPSC-cardiomyocytes show increased CaMKIIδ-mediated phosphorylation of RYR-S2814 and PLN-T17, that cannot be rescued in isogenic control DCM1_res cells. In contrast to this, DCM3 iPSC-cardiomyocytes show decreased NCX and significantly increased SERCA expression, where both tended to be rescued in isogenic control iPSC-cardiomyocytes.

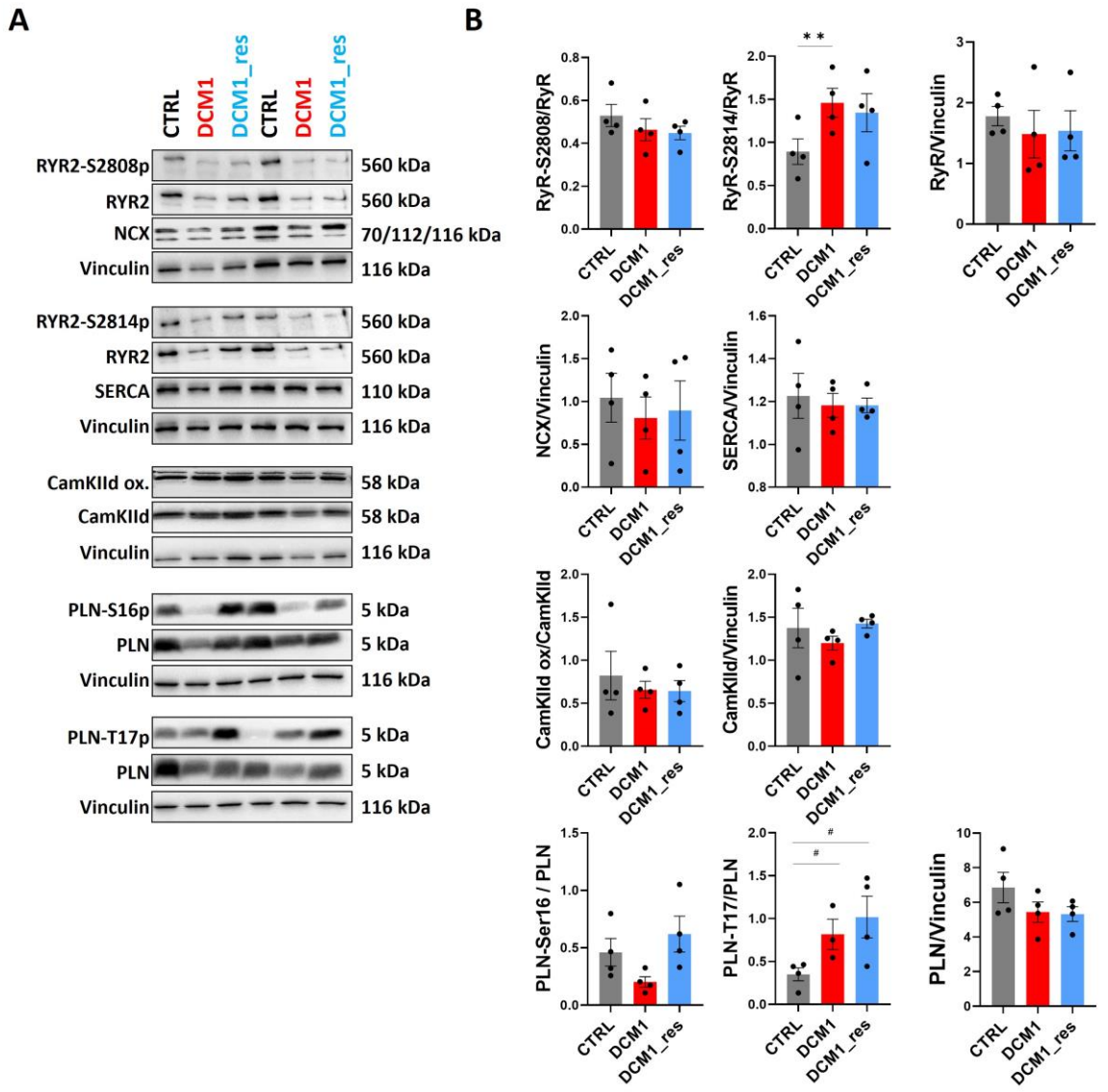

Fig. 40: Expression of important Ca^{2+} handling proteins in DCM1 and isogenic control iPSC-cardiomyocytes. **A** Western blot membranes of external control (CTRL), diseased DCM1 and isogenic control DCM1_res iPSC-cardiomyocytes for important Ca^{2+} handling proteins. All protein expressions were set in relation to the protein levels of vinculin. Vinculin staining was performed for each membrane individually. The size of the respective proteins is given in kDa. **B** Quantification data of the Western blot membranes for external control (grey), DCM1 (red) and isogenic control DCM1_res (blue) for all Ca^{2+} handling proteins analyzed. Data is represented as ± SEM. P-values were determined using one-way ANONA multiple comparisons with Tukey`s correction (*) or Student`s t-test (#). * = $p < 0.05$, ** = $p < 0.01$, # = $p < 0.05$. Each dot represents one ventricular cardiac differentiation experiment.

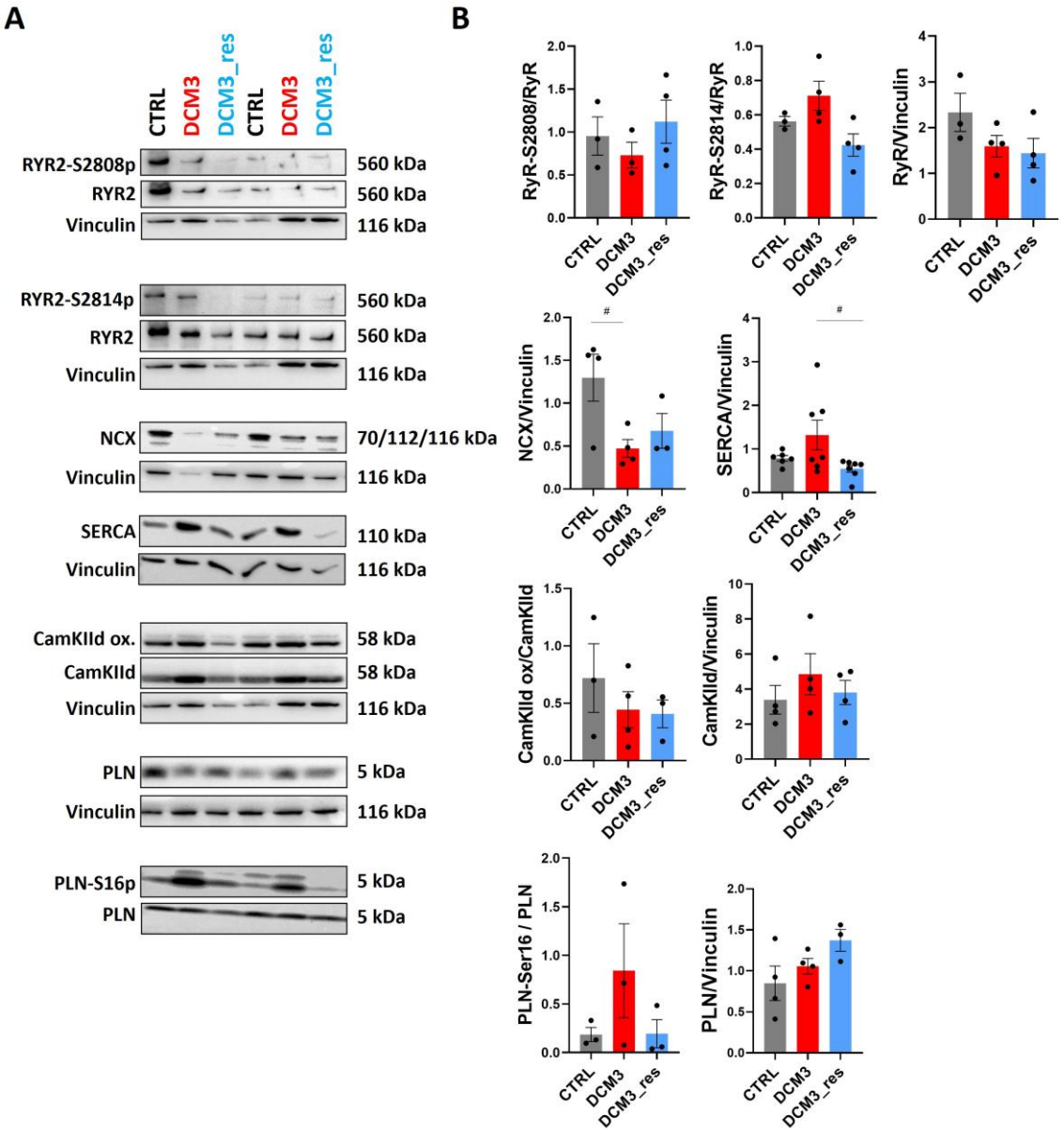

Fig. 41: Expression of important Ca^{2+} handling proteins in DCM3 and isogenic control iPSC-cardiomyocytes. **A** Western blot membranes of external control (CTRL), diseased DCM3 and isogenic control DCM_res iPSC-cardiomyocytes for important Ca^{2+} handling proteins. All protein expressions were set in relation to the protein levels of vinculin. Vinculin staining was done for each membrane individually. The size of the respective proteins is given in kDa. Western Blots of PLN and phosphorylated PLN_S16p were conducted by Eva-Maria Staufenberg (MSc) during a master thesis. **B** Quantification data of the Western blot membranes for external control (grey), DCM3 (red) and isogenic control DCM3_res (blue) for all Ca^{2+} handling proteins analyzed. Data is represented as ± SEM. P-values were determined using Student`s t-test. # = $p < 0.05$. Each dot represents one ventricular cardiac differentiation experiment.

In addition to expression analysis on protein level by Western blot experiments, the mRNA expression of selected corresponding genes was evaluated by qPCR (Fig. 42). Similar to protein data, SERCA is also upregulated on mRNA level in DCM3 iPSC-cardiomyocytes compared to external and isogenic control cells (Fig. 42 A). SERCA expression of DCM1 and corresponding isogenic control DCM1_res is comparable to external controls (Fig. 42 A). In contrast to protein data, where NCX was significantly downregulated in DCM3 iPSC-cardiomyocytes NCX expression on mRNA level of DCM3 and DCM3_res cells was

comparable to external controls (Fig. 42 B). However, NCX expression on mRNA level was significantly decreased in DCM1 and DCM1_res iPSC-cardiomyocytes compared to external controls (Fig. 42 B). Additionally, mRNA expression of PLN was analyzed and as shown in Fig. 42 C, DCM1 and DCM1_res showed significantly decreased PLN expression compared to external control iPSC-cardiomyocytes. PLN expression of DCM3 and DCM3_res iPSC-cardiomyocytes was comparable to control iPSC-cardiomyocytes (Fig. 42 C). Last, CaMKIIδ mRNA expression was significantly increased in DCM3 iPSC-cardiomyocytes compared to isogenic control DCM3_res cells (Fig. 42 D). CaMKIIδ expression of DCM1, DCM1_res and DCM3_res iPSC-cardiomyocytes was comparable to external controls (Fig. 42 D).

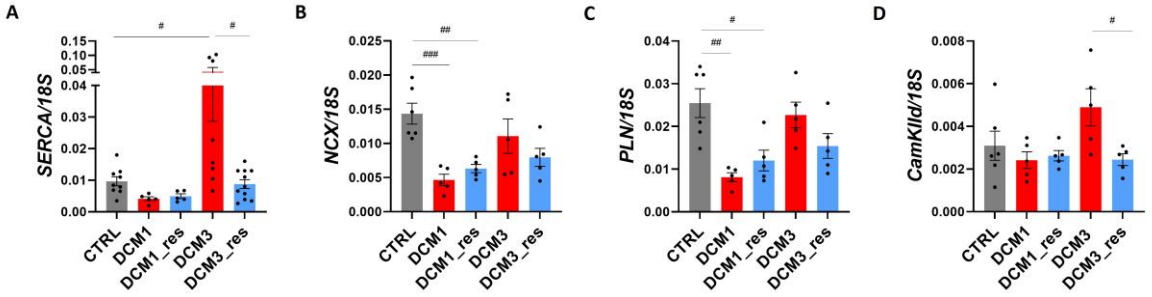

Fig. 42: Expression of important Ca^{2+} handling genes in DCM and isogenic control iPSC-cardiomyocytes. Quantitative PCR data of external control, diseased DCM1 and DCM3 and isogenic control iPSC-cardiomyocytes for Ca^{2+} handling genes **A** *SERCA*, **B** *NCX*, **C** *PLN* and **D** *CaMKIIδ*. Expression of all was normalized to *18S* expression. **A + B + C + D** Data is represented as ± SEM. P-values were determined using Student`s t-test. # = $p < 0.05$, ## = $p < 0.01$. Each dot represents one ventricular cardiac differentiation experiment.

4.5 Functional analysis of DCM and FLNC-rescue iPSC-cardiomyocytes

4.5.1 Aberrant Ca^{2+} handling in DCM iPSC-cardiomyocytes

Ca^{2+} cycling is the driving force for cardiomyocyte contraction as it translates the electrical stimulus into myocyte contraction (Eisner *et al.*, 2013; Eisner *et al.*, 2017). For this, a tightly regulated network of Ca^{2+} handling proteins within the cardiomyocytes is required for proper function. Irregularities within the Ca^{2+} homeostasis have often been associated with cardiac diseases, like DCM (Beuckelmann *et al.*, 1992; Lou *et al.*, 2012; Piacentino *et al.*, 2003). To investigate the pathophysiology within this DCM family in more detail, the Ca^{2+} homeostasis of external control, diseased, and isogenic control iPSC-cardiomyocytes was analyzed on a functional level by FURA-2 and Fluo-4 measurements.

4.5.1.1 Classical heart failure phenotype and slower Ca^{2+} kinetics of DCM iPSC-cardiomyocytes

To analyze Ca^{2+} homeostasis of DCM iPSC-cardiomyocytes the cells were stained with the FURA-2 probe, which is a ratiometric Ca^{2+} dye that changes its emission from 380nm to 340nm upon Ca^{2+} binding. This allows robust investigation of systolic Ca^{2+} transient amplitude and SR Ca^{2+} load as it eliminates the problem of different probe loading between different samples, by depicting all parameters as a 340/380nm ratio (Fig. 43 A).

Additionally, rise (time to peak) and decay (relaxation time) time can be analyzed (Fig. 43 A). Single cells were paced at 0.25Hz and following at 0.5Hz. All basal parameters were recorded at both frequencies.

Ca^{2+} transient amplitude was downregulated in both – DCM1 and DCM3 – diseased iPSC-cardiomyocytes compared to healthy iPSC-cardiomyocytes (Fig. 43 B). However, downregulation in DCM1 iPSC-cardiomyocytes was not significant (Fig. 43 B). Nevertheless, when analyzing the isogenic control DCM1_res iPSC-cardiomyocytes the Ca^{2+} transient amplitude in tendency seemed to be rescued towards control level (Fig. 43 B). In contrast to this, Ca^{2+} transient amplitude was significantly downregulated in DCM3 iPSC-cardiomyocytes and was not rescued in DCM3_res iPSC-cardiomyocytes (Fig. 43 B). Ca^{2+} transient amplitude often is used as a parameter for a heart failure phenotype, as less systolic Ca^{2+} is associated with reduced contraction (Roe *et al.*, 2015). Hence, this data points towards a general diseased phenotype of the diseased iPSC-cardiomyocytes. This effect is stronger in iPSC-cardiomyocytes of the daughter and FLNC rescue only improves this in iPSC-cardiomyocytes of the father, where the effect itself is smaller.

FURA-2 measurements, additionally, point towards slower Ca^{2+} kinetics in DCM iPSC-cardiomyocytes as shown by increased time to peak 50% (Fig. 43 C) and increased relaxation time 50% (Fig. 43 D). DCM3 iPSC-cardiomyocytes display slower Ca^{2+} kinetics, represented by increased relaxation time 80%, as well (Fig. 43 E). Although not significant, Ca^{2+} kinetics in tendency seem to be restored in DCM1_res iPSC-cardiomyocytes (Fig. 43 C, D). For DCM3 and DCM3_res iPSC-cardiomyocytes time to peak 50% kinetics also seem to be restored in tendency (Fig. 43 C), however relaxation time 50% (Fig. 43 D) and 80% (Fig. 43 E) are rather further increasing.

Fluo-4, like FURA-2 is a cytoplasmic Ca^{2+} probe. However, as it only emits light upon Ca^{2+} binding the individual measurement is faster, allowing to investigate changes in Ca^{2+} kinetics more precisely. Hence, rise and decay time were evaluated (Fig. 44 A). First, Ca^{2+} decay time was quantified (Fig. 44 B). Like shown with FURA-2 measurements, the decay time of DCM iPSC-cardiomyocytes – DCM1 and DCM3 – was slowed in comparison to external controls (Fig. 44 B). Additionally, in isogenic control iPSC-cardiomyocytes increased decay time in tendency was downregulated towards a level of external control iPSC-cardiomyocytes (Fig. 44 B). Rise time (time to peak) of DCM1 was comparable to control iPSC-cardiomyocytes, but significantly increased compared to isogenic DCM1_res iPSC-cardiomyocytes (Fig. 44 C). DCM3 and DCM3_res show significantly slowed rise time compared to external control iPSC-cardiomyocytes (Fig. 44 C).

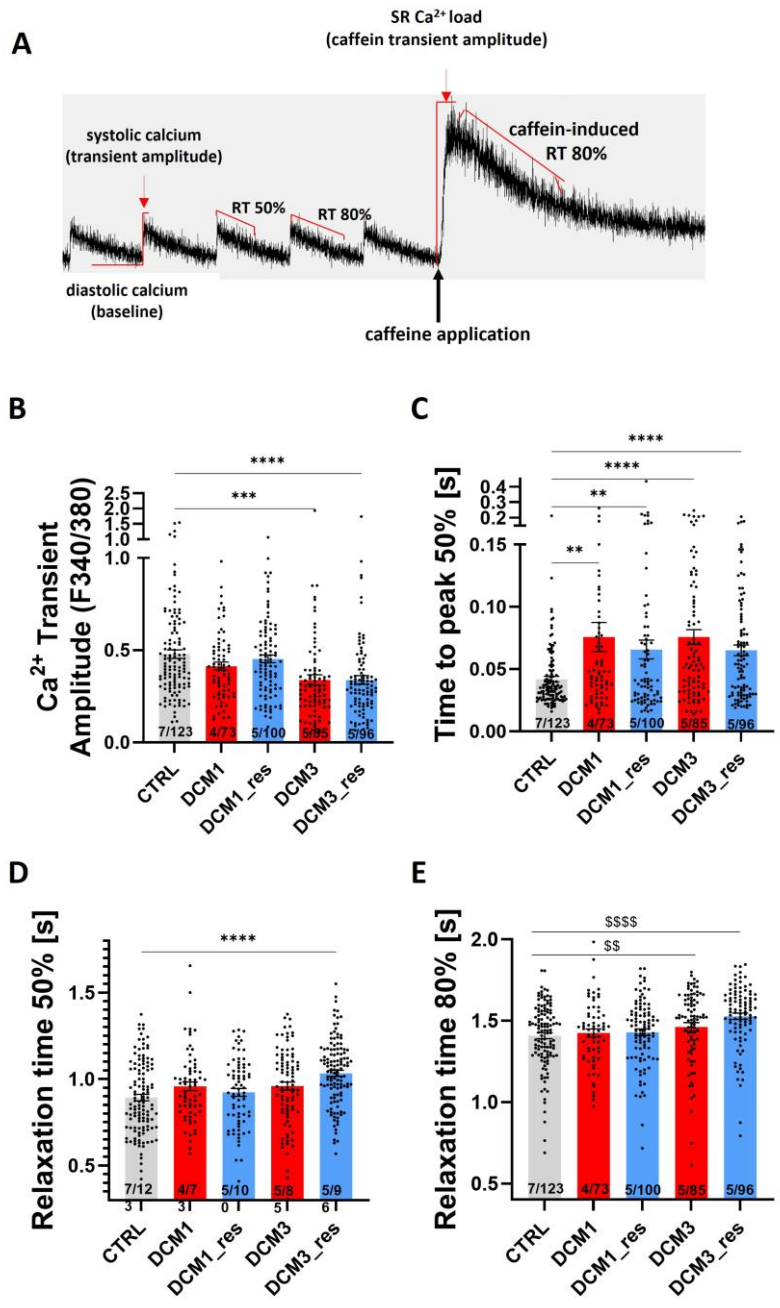

Fig. 43: FURA-2AM measurements to evaluate Ca^{2+} handling of diseased and FLNC rescued iPSC-cardiomyocytes. A Exemplary FURA-2AM single-cell Ca^{2+} trace obtained for each measurement to explain the different parameters. All parameters were based on the ratio of both FURA-2AM excitation wavelengths (340/380 nm). **B, C, D, E** FURA-2AM measurements of external control (CTRL), diseased DCM1 und DCM3 and DCM _res iPSC-cardiomyocytes. Quantitative data of **B** Ca^{2+} transient amplitude, **C** time to peak 50%, **D** relaxation time 50% and **E** relaxation time 80% all obtained after pacing the cells at 0.5Hz. The numbers within each bar indicate the number of iPSC-cardiomyocytes differentiation experiments / number of analyzed cells. Data is represented as ± SEM. P-values were determined using one-way ANONA multiple comparisons with Tukey`s correction (*) or Mann-Whitney Test ($). * = p < 0.05, ** = p < 0.01, *** = p < 0.001 and **** = p < 0.0001. $ = p < 0.05, §§ = p < 0.01, $$$ = p < 0.001 and $$$$ = p < 0. 0001.Each dot represents one ventricular cardiac differentiation experiment.

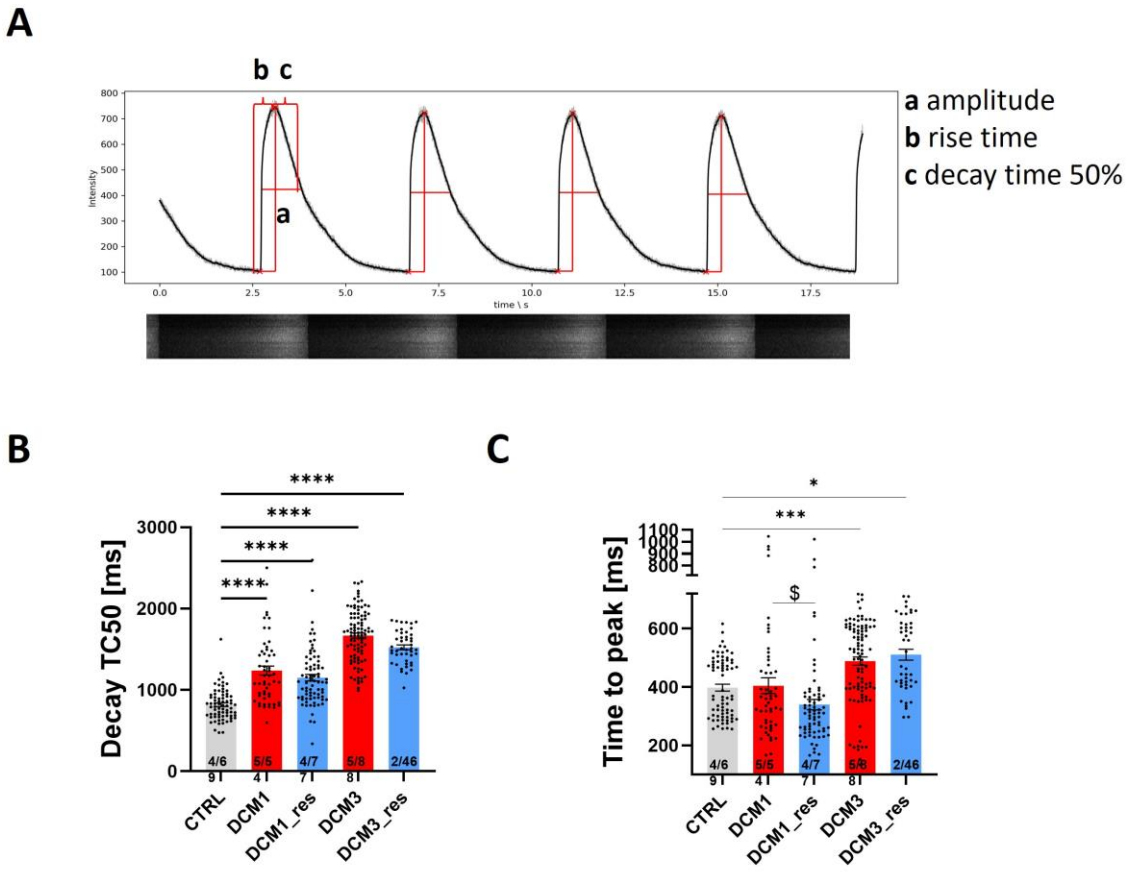

Fig. 44: Fluo-4 measurements to evaluate Ca^{2+} handling of diseased and FLNC rescued iPSC-cardiomyocytes. **A** Exemplary Fluo-4 single cell Ca^{2+} trace and line scan obtained after every measurement. **B, C** Fluo-4 measurements of external control (CTRL), diseased DCM1 und DCM3 and DCM_res iPSC-cardiomyocytes. Quantitative data of **B** decay time 50%, **C** time to peak 50%. The numbers within each bar indicate the number of iPSC-cardiomyocytes differentiation experiments / number of analyzed cells. Data is represented as ± SEM. P-values were determined using student`s t-test. P-values were determined using one-way ANONA multiple comparisons with Tukey`s correction (*) or Mann-Whitney Test ($). * = $p < 0.05$, ** = $p < 0.01$, *** = $p < 0.001$ and **** = $p < 0.0001$. $=$p < 0.05$. Each dot represents one ventricular cardiac differentiation experiment.

4.5.1.2 FLNC-dependent increased SERCA activity in DCM3 iPSC-cardiomyocytes

Caffeine application during FURA-2 measurements, leads to opening of the RYR2 in the SR and the fast release of Ca^{2+} stored in the SR. This allows evaluation of SR Ca^{2+} load and caffeine-induced relaxation time. Additionally, based on the difference of calculated constants of the decay time before and after caffeine application the SERCA activity can be theoretically calculated. Upon caffeine application the resulting caffeine transient amplitude, representing the SR Ca^{2+} load, was comparable between external control, DCM and isogenic control iPSC-cardiomyocytes (Fig. 45 A). The caffeine-induced relaxation time was increased in DCM3 and DCM3_res iPSC-cardiomyocytes, but no difference was observed in DCM1 (Fig. 45 B). No difference in SERCA activity could be observed for DCM1 iPSC-cardiomyocytes compared to external healthy or isogenic control cells (Fig. 45 C). Interestingly, SERCA activity of DCM3 was significantly enhanced compared to isogenic DCM3_res cells (Fig. 45 C). Although there is no difference in SERCA activity, when comparing DCM3 and external control iPSC-cardiomyocytes, the difference in SERCA

activity between diseased and isogenic control cells should not be neglected, especially because the comparison of these two lines is more direct and the observed effect is supported by Western blot (Fig. 41) an qPCR expression data for SERCA (Fig. 42).

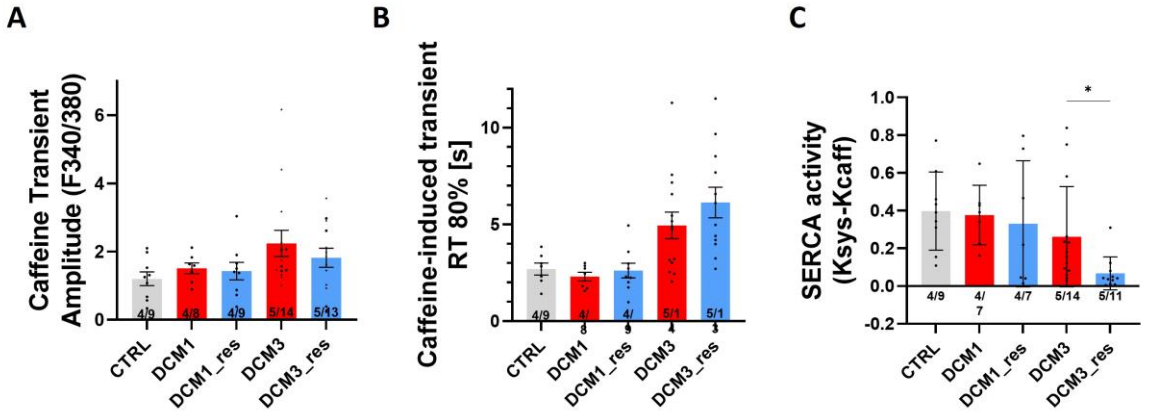

Fig. 45: FURA-2AM measurements to evaluate Ca^{2+} handling of diseased and FLNC rescued iPSC-cardiomyocytes. A + B Represented are FURA-2AM measurements of external control (CTRL), diseased DCM1 und DCM3 and DCM_res iPSC-cardiomyocytes after caffeine (10µM) treatment. **A** Caffeine transient amplitude and **B** Caffeine-induced RT 80% after pacing the cells at 0.25Hz. **C** Theoretically calculated SERCA activity. P-values were determined using one-way ANONA multiple comparisons with Tukey`s correction (*). * = $p < 0.05$. Each dot represents one ventricular cardiac differentiation experiment.

4.5.1.3 Pro-arrhythmic potential in DCM1 iPSC-cardiomyocytes

Fluo-4 measurements additionally allow to assess Ca^{2+} sparks. Ca^{2+} sparks appear due to spontaneous opening of RYR2 in the SR membrane during the diastolic phase and represent a parameter for a pro-arrhythmic potential. The Ca^{2+} spark frequency (CASPF) was slightly, but not significantly, increased in DCM1 iPSC-cardiomyocytes compared to external control iPSC-cardiomyocytes (Fig. 46), pointing towards an increased tendency for pro-arrhythmic events. This effect seemed to be restored in DCM1_res iPSC-cardiomyocytes (Fig. 46). DCM3 and DCM3_res in contrast, showed significantly reduced Ca^{2+} spark frequency compared to external controls (Fig. 46).

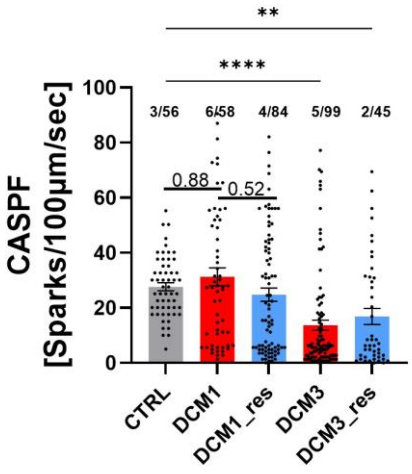

Fig. 46: Fluo-4 measurements to evaluate Ca^{2+} sparks of diseased and FLNC rescued iPSC-cardiomyocytes. Depicted are Ca^{2+} spark frequency (CASPF) measurements obtained with the Fluo-4 dye after pacing the cells at 0.25Hz. Quantitative data of external control (CTRL), diseased DCM1 und DCM3 and DCM_res iPSC-cardiomyocytes. The numbers within each bar indicate the number of iPSC-cardiomyocytes differentiation experiments / number of analyzed cells. Data is represented as ± SEM. P-values were determined using one-way ANONA multiple comparisons with Tukey`s correction (*). * = p < 0.05, ** = p < 0.01, *** = p < 0.001 and **** = p < 0.0001. Each dot represents one ventricular cardiac differentiation experiment.

4.5.2 Increased reactive oxygen species in DCM1 iPSC-cardiomyocytes can be reduced by ARNi treatment

Cardiomyopathies, like DCM, can be accompanied by increased cardiac oxidative stress as a consequence of cardiac remodeling and contractile dysfunction, which among others can be caused by mutations in sarcomere proteins. As the DCM patients of the index family have a missense mutation in the sarcomere protein FLNC the amount of H_2O_2, as most prominent indicator of oxidative stress, was assessed by the AmplexRed Hydrogen Peroxide Assay kit. The produced H_2O_2 amount of external control, DCM1 and DCM3 iPSC-cardiomyocytes was measured at basal conditions. H_2O_2 production of DCM3 and DCM3_res iPSC-cardiomyocytes was not changed compared to iPSC-cardiomyocytes of external controls (Fig. 47 A). In contrast to this, H_2O_2 production in DCM1 iPSC-cardiomyocytes was significantly increased (Fig. 47 A). The H_2O_2 amount was not restored upon FLNC-rescue in DCM1_res iPSC-cardiomyocytes but was comparably high like in DCM1 iPSC-cardiomyocytes (Fig. 47 A).

In collaboration with Novartis the ARNi Entresto was tested on heart failure iPSC-cardiomyocytes of the diseased father (DCM1, 3.2.15). Following a two-weeks treatment with Entresto and subsequent AmplexRed measurements the produced H_2O_2 amount of DCM1 iPSC-cardiomyocytes significantly decreased in comparison to DCM1 iPSC-cardiomyocytes under basal conditions (Fig. 47 B). When treating DCM1 iPSC-cardiomyocytes of the same passages with the two components – Valsartan and Sacubitril – of Entresto individually, the produced H_2O_2 amount of DCM1 iPSC-cardiomyocytes in tendency also decreased compared to DCM1 iPSC-cardiomyocytes with a higher effect seen for sacubitril (Fig. 47 B). However, this decrease was not significant (Fig. 47 B).

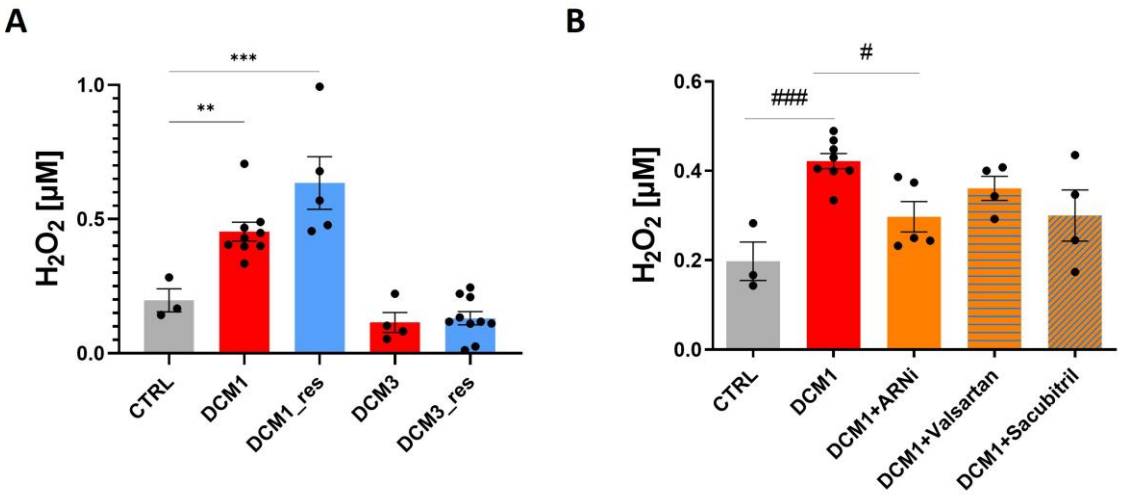

Fig. 47: Analysis of oxidative stress of DCM iPSC-cardiomyocytes. A Shown are AmplexRed measurements representing the produced H_2O_2 amount of external control (CTRL), DCM and DCM_res iPSC-cardiomyocytes under basal conditions. **B** Shown are AmplexRed measurements of external control and DCM1 iPSC-cardiomyocytes under basal conditions and DCM1 iPSC-cardiomyocytes after two-weeks treatment with the ARNi Entresto or with the two Entresto components – Valsartan and Sacubitril – alone. Data is represented as ± SEM. P-values were determined using one-way ANONA multiple comparisons with Tukey`s correction (*), or paired student`s t-test (#). * = p < 0.05, ** = p < 0.01, *** = p < 0.001 and **** = p < 0.0001. # = p < 0.05, ## = p < 0.01 and ### = p < 0.001. Each dot represents one ventricular cardiac differentiation experiment.

4.5.3 Increased tissue stiffness and decreased contractile function in DCM EHM can partially be restored upon *FLNC* rescue

Previously described data was only based on 2D cultures of iPSC-cardiomyocytes, however within the heart cardiomyocytes are incorporated into a complex 3D network of different cells and ECM components, acting together to fulfill the hearts vital functions. Hence, only analyzing 2D iPSC-cardiomyocytes on stiff surfaces cannot recapitulate the complete functional scope. Generation of EHM offers an approach to analyze cardiomyocyte function within a 3D environment composed of collagen and fibroblast. Still not fully recapitulating the heart tissue, this adds a certain level of complexity and enables analyzing cardiomyocyte function in a more translatable fashion. EHM generation, data acquisition and analysis were kindly performed by Branimir Berecic and Dr. Malte Tiburcy (Institute of Pharmacology and Toxicology of the University Medical Center Göttingen). In brief, 4-weeks old iPSC-cardiomyocytes were mixed with fibroblasts and a collagen hydrogel and casted into wells of a 48-well plate around two interconnected flexible poles 3.3.1.1). The tips of the flexible poles were labelled fluorescently which enabled optical analyses of pole deflection on a daily basis using a high-speed camera recording movements of the poles in every well. These movements were analyzed by an imaging software (made by Dr. Tim Meyer, Institute of Pharmacology and Toxicology Göttingen). Optical analyses were evaluated for EHM generated from iPSC-cardiomyocytes of two differentiation experiments for each line. Data is shown for day 28 after tissue casting. First, the optical analysis allowed to determine the strength (contraction in pixels) of the EHM by comparing distance between the poles when EHM were fully contracted (poles closest to each other) with the distance when poles were in basal position. This analysis showed significantly decreased contraction of diseased DCM1 and DCM3 EHM compared to EHM of healthy family members (Fig. 48 A). Lowest contraction was shown for DCM3 EHM (Fig. 48 A). Contraction of FLNC-rescued DCM1_res was not increased in comparison to DCM1 EHM (Fig. 48 A). Contraction of FLNC-rescued DCM3_res was significantly increased compared to diseased DCM3 EHM, but still lower than the EHM of healthy family members (Fig. 48 A). Additionally, optical analysis allowed determination of beating frequency by calculating number of full contractions in each amount of time. This showed comparable beating frequency for diseased DCM1, DCM3, isogenic control DCM1_res and healthy family member EHM of ~0.3Hz (DCM1: 0.2693Hz±0.014Hz, DCM1_res: 0.2779Hz±0.02Hz, DCM3: 031Hz±0.026Hz, and healthy family members: 0.304Hz±0.016Hz) (Fig. 48 B). Of note, beating frequency of FLNC-rescue DCM3_res EHM was significantly increased (0.4543Hz±0.035Hz) compared to diseased DCM3 EHM (Fig. 48 B). At the end of EHM culture (day 42), Ca^{2+}-response measurements were performed in a 37°C tempered,

Tyrode`s solution containing organ bath. Since one batch of EHM did not reach day 42, organ bath measurements were only performed for EHM from iPSC-cardiomyocytes of one differentiation experiment per line. For this, the tissues were placed around two hooks and stretched uniaxially by increasing the gap between the hooks. The tissues initially were stretched to maximum pre-load, where further stretching did not increase generated force anymore. The tissues remained in the position of maximum pre-load when increasing Ca^{2+} concentrations were added extracellularly to the Tyrode`s solution, and the force was determined. The force generated at the maximum pre-load position represents the resting force, which is a measure for inherent EHM stiffness. In general, resting force remained largely unchanged with increasing Ca^{2+} concentrations for all EHM analyzed. In more detail, DCM1 EHM showed the highest resting force, being significantly higher compared to healthy DCM2 EHM ($p<0.0001$). FLNC-rescue DCM1_res EHM decreased the resting force significantly ($p<0.05$), but was still significantly higher compared to healthy DCM2 EHM ($p<0.001$) (Fig. 48 C). Resting force of diseased DCM3 EHM was significantly higher compared to DCM2 EHM and was rescued to control level in isogenic control DCM3_res EHM (Fig. 48 C). When stretched to maximum pre-load the tissues were paced at 1.5Hz. Tissue contraction at different Ca^{2+} concentration was measured by changes in force induced by tissue twitching and the difference in maximum force and minimum force was determined as force of contraction (FOC). FOC of healthy DCM2 EHM was constantly increasing with increasing Ca^{2+} concentrations (Fig. 48 D), whereas diseased DCM1 and DCM3 as well as isogenic control DCM1_res and DCM3_res EHM reached a plateau of FOC at ~1.6mM Ca^{2+} (Fig. 48 D). In more detail, FOC of healthy DCM2 EHM was significantly higher compared to diseased DCM1 and DCM3 as well as isogenic control DCM1_res and DCM3_res EHM (Fig. 48 D). Like determined total contraction based on optical measurements, FOC of DCM3 EHM was lowest (Fig. 48 A). FOC of DCM1 and respective isogenic control DM1_res EHM was shown to be almost identical (Fig. 48 D). In trend, FOC of isogenic control DCM3_res EHM was increased compared to diseased DCM3 EHM but remained significantly lower compared to healthy DCM2 EHM (Fig. 48 D). Based on resting force (minimum force) and FOC (difference of max and min force) an active/passive force ratio could be calculated as ((max-min)/min). This ratio is a measure of overall tissue health. This showed a significantly reduced ratio for diseased DCM1 and DCM3, as well as isogenic control DCM1_res EHM compared to healthy DCM2 EHM (Fig. 48 E). Still not reaching DCM2 EHM ratio, the active/passive force ratio of DCM1_res EHM was significantly increased compared to corresponding diseased DCM1 EHM (Fig. 48 E). Similarly, active/passive force ratio of isogenic control DCM3_res EHM was significantly increased, compared to diseased DCM3 EHM and was not statistically different compared to healthy DCM2 EHM (Fig. 48 E).

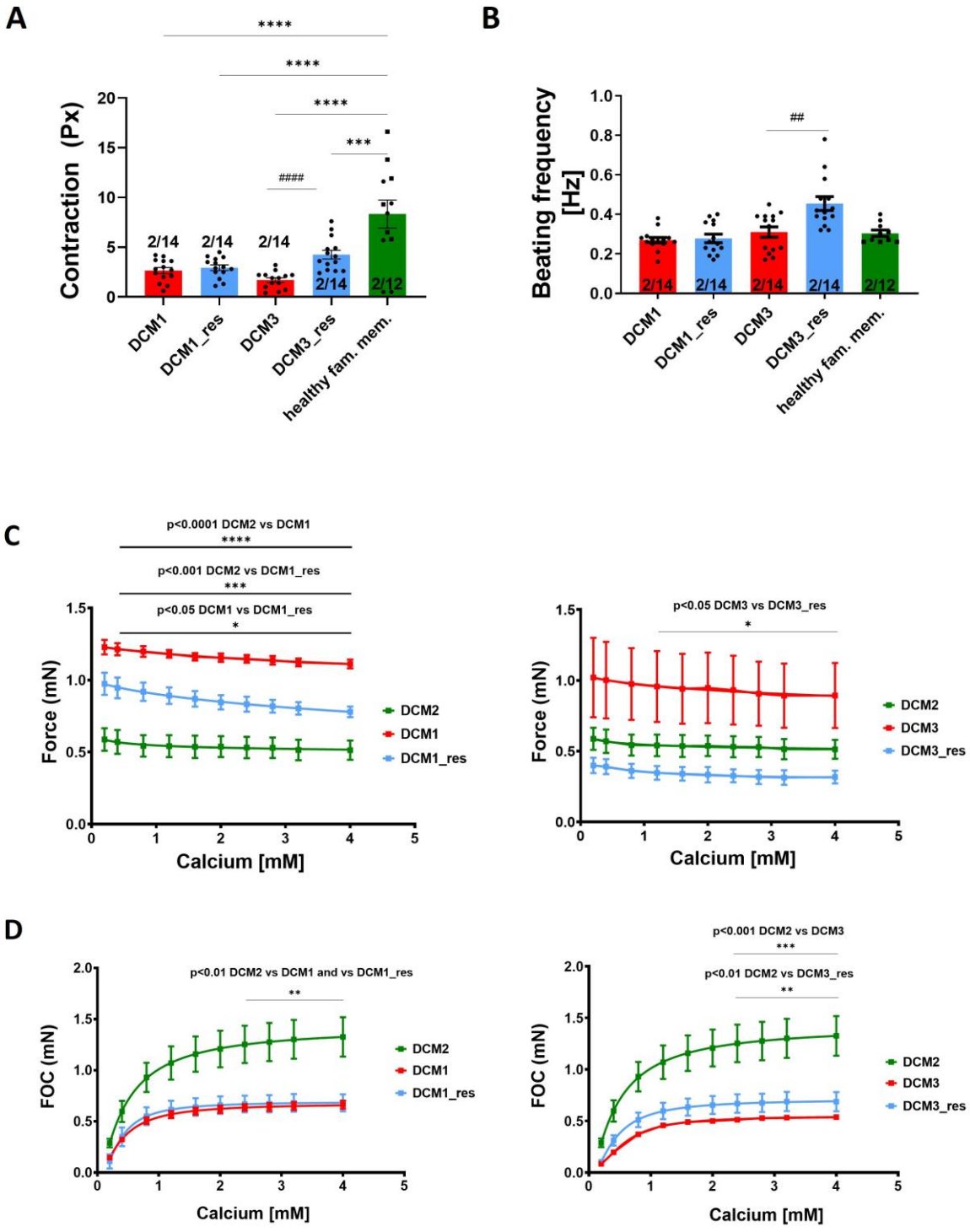
A
****
****
****
***
####
Contraction (Px)
20
15
10
5
0
2/14
2/14
2/14
2/14
2/12
DCM1
DCM1_res
DCM3
DCM3_res
healthy fam. mem.
B
##
Beating frequency [Hz]
1.0
0.8
0.6
0.4
0.2
0.0
2/14
2/14
2/14
2/14
2/12
DCM1
DCM1_res
DCM3
DCM3_res
healthy fam. mem.
C
p<0.0001 DCM2 vs DCM1
****
p<0.001 DCM2 vs DCM1_res
***
p<0.05 DCM1 vs DCM1_res
*
Force (mN)
Calcium [mM]
DCM2
DCM1
DCM1_res
p<0.05 DCM3 vs DCM3_res
*
Force (mN)
Calcium [mM]
DCM2
DCM3
DCM3_res
D
p<0.01 DCM2 vs DCM1 and vs DCM1_res
**
FOC (mN)
Calcium [mM]
DCM2
DCM1
DCM1_res
p<0.001 DCM2 vs DCM3
***
p<0.01 DCM2 vs DCM3_res
**
FOC (mN)
Calcium [mM]
DCM2
DCM3
DCM3_res

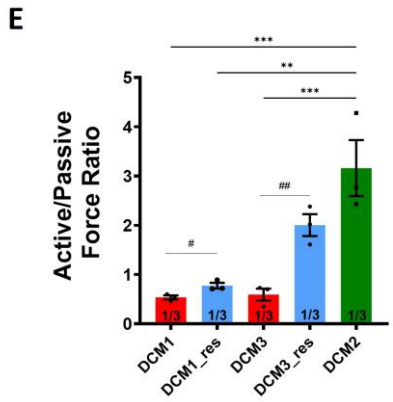

Fig. 48: Analysis of diseased, isogenic and control EHM. Shown is quantified data of DCM1, DCM1_res, DCM3, DCM3_res, and healthy DCM2 EHM. Data is represented as ± SEM. **A** Shown is contraction (in pixels) of 28-days old EHM determined by optical analysis of changes in pole deflection from basal to fully contracted position. **B** Shown is beating frequency of 28-days old EHM determined by optical analysis of number of pole deflections from basal to fully contracted position. n=12-14 EHM from two iPSC-cardiomyocytes differentiations for each line. **C** Shown in the resting force of 42-days old EHM after stretching the tissues to maximum pre-load determined under increasing Ca^{2+} concentrations (mM) and pacing at 1.5Hz measured in organ bath. n=3 EHM from one iPSC-cardiomyocytes differentiation for each line. **D** Shown is force of contraction (FOC) of 42-days old EHM determined under increasing Ca^{2+} concentrations (mM) and pacing at 1.5Hz measured in the organ bath. n=3 EHM from one iPSC-cardiomyocytes differentiation for each line. **E** Shown is the active/passive force ratio of 42-days old EHM based on organ bath measurements. **A, B, E** The numbers within each bar indicate the number of iPSC-cardiomyocytes differentiation experiments / number of analyzed EHM. P-values were determined using one-way ANONA multiple comparisons with Tukey`s correction (*), or student`s t-test (#). **C, D** P-values were determined using two-way ANONA multiple comparisons with Tukey`s correction (*). * = $p < 0.05$, ** = $p < 0.01$, *** = $p < 0.001$ and **** = $p < 0.0001$. # = $p < 0.05$, ## = $p < 0.01$, ### = $p < 0.001$ and #### = $p < 0.0001$.

4.6 Role of CFB in DCM development and pathophysiology

The heart comprises several different cell types, all contributing to its overall biological function. Although, the relative amount of certain cell types differs especially between ventricular and atrial tissue, the cellular composition in general includes cardiomyocytes, fibroblasts, mural cells (vascular smooth muscle cells and pericytes), EC and immune cells. All these cell types potentially might contribute to pathophysiological processes. However, cardiomyocytes and fibroblasts are the two most abundant cardiac cell types (Pinto *et al.*, 2016; Zhou and Pu, 2016). Therefore, in addition to the contribution of cardiomyocytes (as described previously), the role of CFB within the DCM pathophysiology of the index family should be analyzed in more detail.

This is also of special interest, as previous studies within the group demonstrated significantly increased fibrotic area within cardiac tissue of the explanted heart of the DCM1 patient after Masson's trichrome staining in comparison to cardiac tissue of external controls (Köhne, 2020).

4.6.1 Isolated CFB express several specific CFB marker

CFB were isolated from human cardiac tissue from DCM1 patient within the lab previously to the start of this project. Additionally, SFB were isolated from skin biopsy from DCM1 patient, also previously to the start of the thesis. As different fibroblast lineages are difficult

to distinguish, mRNA expression analysis was conducted to discriminate between the different lineages and by this characterize the specific fibroblast cell type. For better characterization normal human CFB (PromoCell) were used as positive control. Furthermore, expression of (cardiac) fibroblast specific markers within the fibroblasts, was compared to expression of these markers in iPSC-cardiomyocytes (DCM1) and in explanted LV myocardium. To distinguish fibroblasts from non-fibroblasts populations, the expression of collagen 1 (*COL1A1*) was analyzed, as a standard marker to identify any fibroblast population. As shown in Fig. 49 A, *COL1A1* expression was upregulated in diseased and normal CFB as well as in SFB, compared to iPSC-cardiomyocytes and tissue of the LV. Additionally, the expression of *FSP1* was upregulated in DCM1 CFB and SFB (Fig. 49 A). In contrast to this, *FSP1* expression in normal CFB was lower, and comparable to *FSP1* expression in iPSC-cardiomyocytes and explanted tissue (Fig. 49 A). Although *FSP1* was thought to be fibroblast-specific it is found in tissue during remodeling e.g., due to disease or injury. This might explain the presence of expression in DCM CFB and SFB and the absence in normal CFB. After discriminating fibroblast from non-fibroblast populations by *COL1A1* and *FSP1* expression, different fibroblast population were characterized. For this, expression of *TCF21*, a transcription factor essential for differentiation into CFB, was analyzed as marker specific for CFB. As expected, *TCF21* was only upregulated in DCM1 and normal CFB, but not in SFB (Fig. 49 A). It was also upregulated in explanted tissue of the LV (Fig. 49 A), which should be composed of CFB as well.

Additionally, markers of fibroblast activation were tested. However, this is still difficult as 2D culturing of fibroblast on stiff surfaces of classical cell culture plates induces a strong mechanical stress often leading to activation of these cells. Additionally, no precise markers are available, hence several markers need to be combined. First, expression of C*TGF*, a marker induced by TGFβ signaling triggering cellular processes of fibrosis was significantly upregulated in diseased and normal CFB but very low in SFB (Fig. 49 A). This might hint towards an activation of these cells – probably driven by 2D cultivation. Furthermore, expression of *POSTN* was analyzed. POSTN is an ECM protein that is highly upregulated after injuries and is often used as a distinguishing marker for activated fibroblasts. This marker was mostly upregulated in normal CFB, but not in diseased CFB (Fig. 49 A). Finally, expression of αSMA (*ACTA2*) was evaluated, as it often is upregulated in activated CFB as well. However, expression of *ACTA2* was extremely low in the analyzed fibroblast cells and was only upregulated in iPSC-cardiomyocytes as expected (Fig. 49 A). In addition to this, preliminary next generation sequencing (NGS) data confirmed the previous qPCR data and showed upregulation of all six markers in DCM1 CFB compared to whole myocardium (Fig. 49 B). In conclusion, the isolated fibroblast population can be characterized as activated cardiac (myo-) fibroblasts.

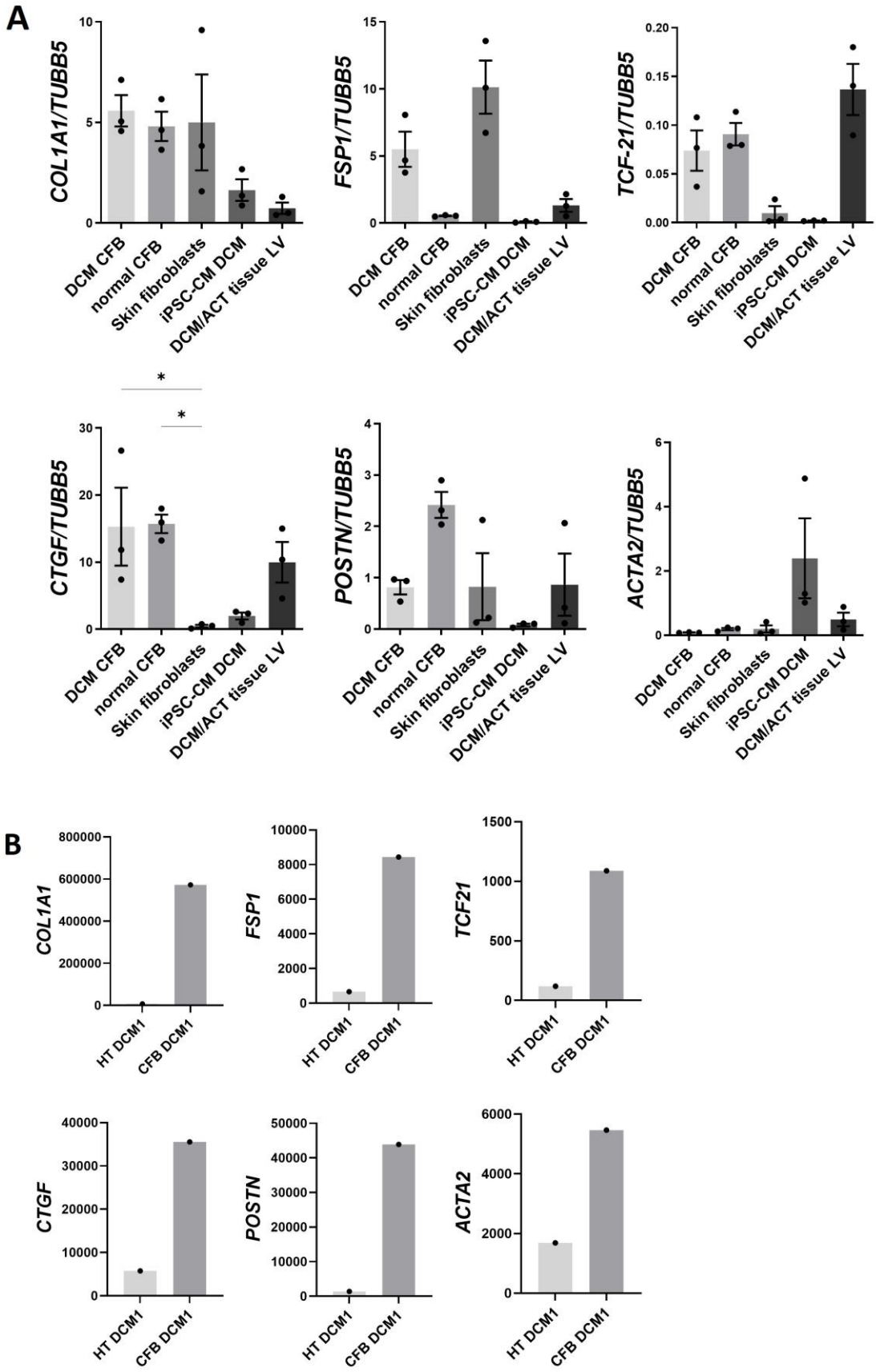

Fig. 49: Characterization of different fibroblast lineages by mRNA marker expression. A Shown are qPCR analyses of DCM1 CFB, normal CFB, skin fibroblasts, DCM1 iPSC-cardiomyocytes and explanted myocardium of the left ventricle of different DCM patients (all n=3 passages) to analyze the expression levels of different

(cardiac) fibroblast-associated markers. Shown are analyses of *COL1A1, FSP1, TCF21, CTGF, POSTN* and *ACTA2*. Expression levels of all markers were normalized by corresponding expression of *TUBB5,* and analyses were done using the ΔCt method. Statistical analysis (one-way ANONA with Tukey`s correction) compared all groups with each other. * = $p < 0.05$. Data are presented as mean ± SEM. **B** Shown are preliminary NGS results of DCM1 CFB and explanted myocardium of the left ventricle of DCM1 of different (cardiac) fibroblast-associated markers (*COL1A1, FSP1, TCF21, CTGF, POSTN* and *ACTA2*). Each dot represents one passage of the analyzed cell line.

4.6.2 Establishment of protocol for directed differentiation into iPSC-Stromal cells (StC)

The isolated cardiac and SFB from tissue obtained from the diseased father (DCM1) already held a lot of opportunities to analyze the role of the FLNC variant within CFB and their contribution to the DCM pathophysiology. However, to investigate the role of CFB and the contribution of the identified FLNC variant within these cells in more detail, isogenic control lines would be the best choice. Hence, within this project a protocol for directed differentiation of iPSC into iPSC-StC was established based on a previously published protocol (Iyer *et al.*, 2016). The differentiated cells will be termed iPSC-StC and not iPSC-CFB, since a CFB identity was not finally validated. With this protocol, all iPSC lines of all family members and the generated isogenic control lines could be differentiated into iPSC-StC.

The differentiation process directed the iPSC into a mesodermal direction to form stromal cells in a first step. For this, the medium was supplemented with CHIR99021, activin-A, BMP4 and FGF2. The cells started differentiating during the first days as seen in Fig. 50. Passaging and changing the medium to the StC-SM medium, differentiation towards epicardial cells was induced (Fig. 50 A). Indeed, an epicardial-like morphology was observed, characterized by distinct edged, cobblestone-like shape (Fig. 50 B, d6-d8). Medium switch to the StC-EM medium, should induce fibroblast differentiation from epicardial cells. In line with this, the cells developed towards early fibroblast-like cells with elongated morphology (Fig. 50 B, d21). Passaging the cells onto larger space led to expansion of the individual cells with an elongated, flat morphology with cell protrusions extending from the cell body to the periphery (Fig. 50 B, d30). However, during the establishment of the differentiation protocol, proliferation of the cells after passage two to three was extremely slow or rather stopped at all. This problem could not be overcome by passaging higher cell numbers to achieve a higher cell density after passaging, which usually is a critical point for iPSC handling. Only when replacing the used knock-out serum replacement by standard FCS, the cells continued to proliferate further than passage 3. Nevertheless, overall proliferation was slower compared to primary fibroblasts or iPSC. In general, a proper and constant morphology and proliferation was achieved from passage five until passage ten, when FCS was used.

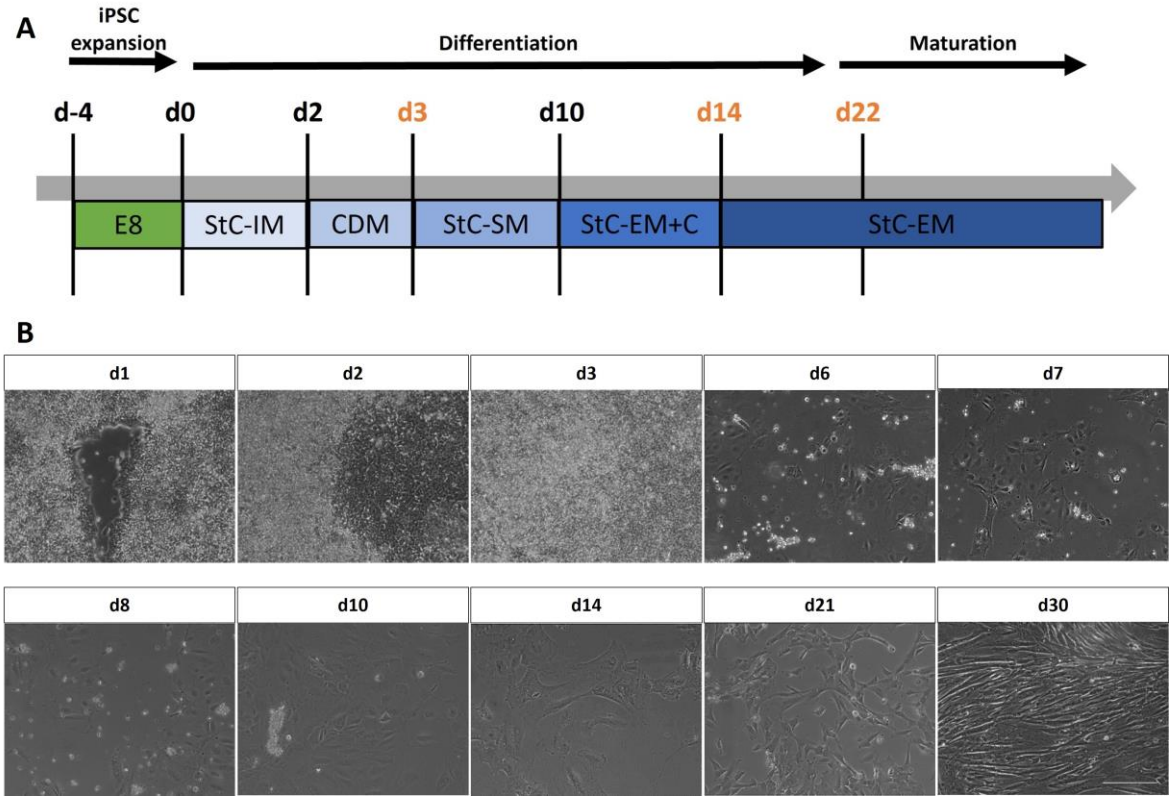

Fig. 50: Directed differentiation of iPSC into iPSC-StC. **A** Schematic overview of the directed differentiation protocol. The days marked in orange indicate days of passaging. Differentiation was started when iPSC reach ~80-90% confluency. E8=Essential 8 medium, StC-IM=Stromal cell induction medium, CDM=Cardiac differentiation medium, StC-SM=Stromal cell specification medium, StC-EM=Stromal cell expansion medium, C=CHIR99021. **B** Representative morphology images to follow the morphological progression from iPSC into iPSC-StC during directed differentiation. Starting with colony-forming iPSC on day 0. The first passaging revealed epicardial-like cells. The second passaging led to elongated cells, like fibroblasts. Over time the cells expanded further and showed elongated, flat morphology with cell protrusions extending from the cell body to the periphery. Images were taken with a Zeiss Axio Observer A1 inverted microscope and the AxioVision software. Scale bar= 200µm, d=day.

Although morphological appearance of the cells hinted towards a fibroblast population after the differentiation process, successful differentiation into the desired CFB cell type was assessed by qPCR analysis testing for the same markers already used to characterize the cell type of primary CFB. iPSC, which were used for differentiation were used as negative controls, and isolated primary CFB of the explanted heart of DCM1 served as positive control.

Even though *COL1A1* was expressed on lower level, compared to primary CFB, it was significantly upregulated compared to iPSC (Fig. 51). Interestingly, neither the fibroblast-specific marker *FSP1*, nor the CFB-specific marker *TCF21* were upregulated but rather showed similar expression levels like iPSC (Fig. 51). However, as shown before expression of both – *FSP1* and *TCF21* – was upregulated in primary CFB of DCM1 (Fig. 51). Expression of the pro-fibrotic *CTGF* was upregulated to a level comparable to primary CFB (Fig. 51). *POSTN* was even expressed higher in iPSC-StC compared to primary CFB (Fig. 51). Expression of *ACTA2* was upregulated compared to iPSC as well (Fig. 51). Based on this data, the differentiated cells do represent a fibroblast-like cell population with expression of *COL1A1* and seem to be in an activated state of (myo-) fibroblasts, indicated by the expression of *CTGF, POSTN* and *ACTA2*. However, the absence of *TCF21* expression needs

to be pointed out. However, expression of pro-fibrotic marker *CTGF, POSTN* and *ACTA2* is spreading between the different iPSC-StC differentiations analyzed. Since CFB activation is strongly mediated by culture on stiff 2D cell culture surfaces, differences in these parameters might be based on varying influence of 2D culture.

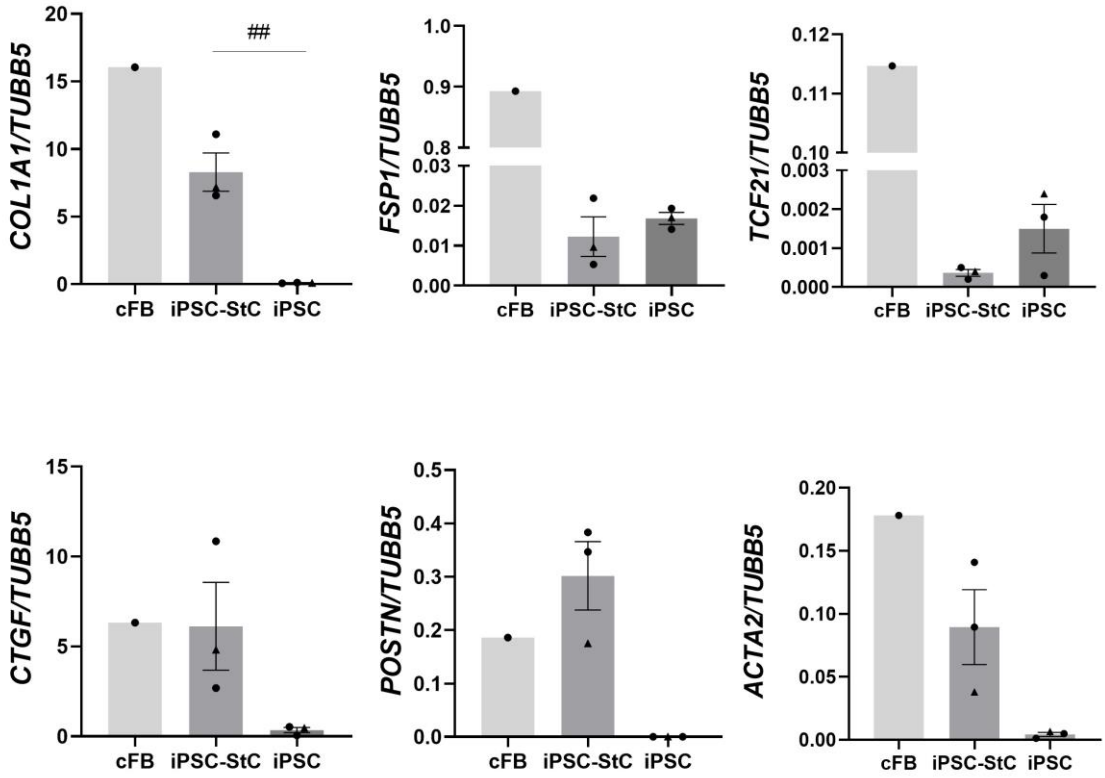

Fig. 51: Characterization of iPSC-derived StC by mRNA marker expression. Shown are qPCR analyses of DCM1 CFB, iPSC-derived StC (DCM1.4 p6+p7 [circle] and DCM3.7 p7 [triangle]) and iPSC (DCM1 [circle] and DCM3 [triangle]) to analyze the expression levels of different (cardiac) fibroblast-associated markers. Shown are analyses of *COL1A1, FSP1, TCF21, CTGF, POSTN* and *ACTA2*. Expression levels of all markers were normalized by corresponding expression of *TUBB5,* and analyses were done using the ΔCt method. Statistical analysis (unpaired Student`s t-test) compared iPSC and iPSC-CFB. Data are presented as mean ± SEM. # = $p < 0.05$, ## = $p < 0.01$. Each dot represents one iPSC-StC differentiation experiment or one iPSC passage of a primary CFB cell line.

In addition to analysis of (cardiac) fibroblast-specific marker expression on mRNA level IF staining were performed to test for fibroblast-specific marker expression on protein level. Fig. 52 shows exemplary staining of DCM1 iPSC-StC for collagen (COL1A1) as fibroblast-specific marker and αSMA to test for activation of (myo-) fibroblasts. The iPSC-StC stained positive for collagen shown by cytoplasmic, but no nuclear staining of all cells analyzed (Fig. 52 A). Very few cells stained positive for αSMA, as shown by cytoplasmic staining displaying a typical parallel fiber network (Fig. 52 B). Most of the cells only showed nuclear DAPI staining with the absence of αSMA staining, pointing towards a low activation state, which could be induced by 2D cell culture.

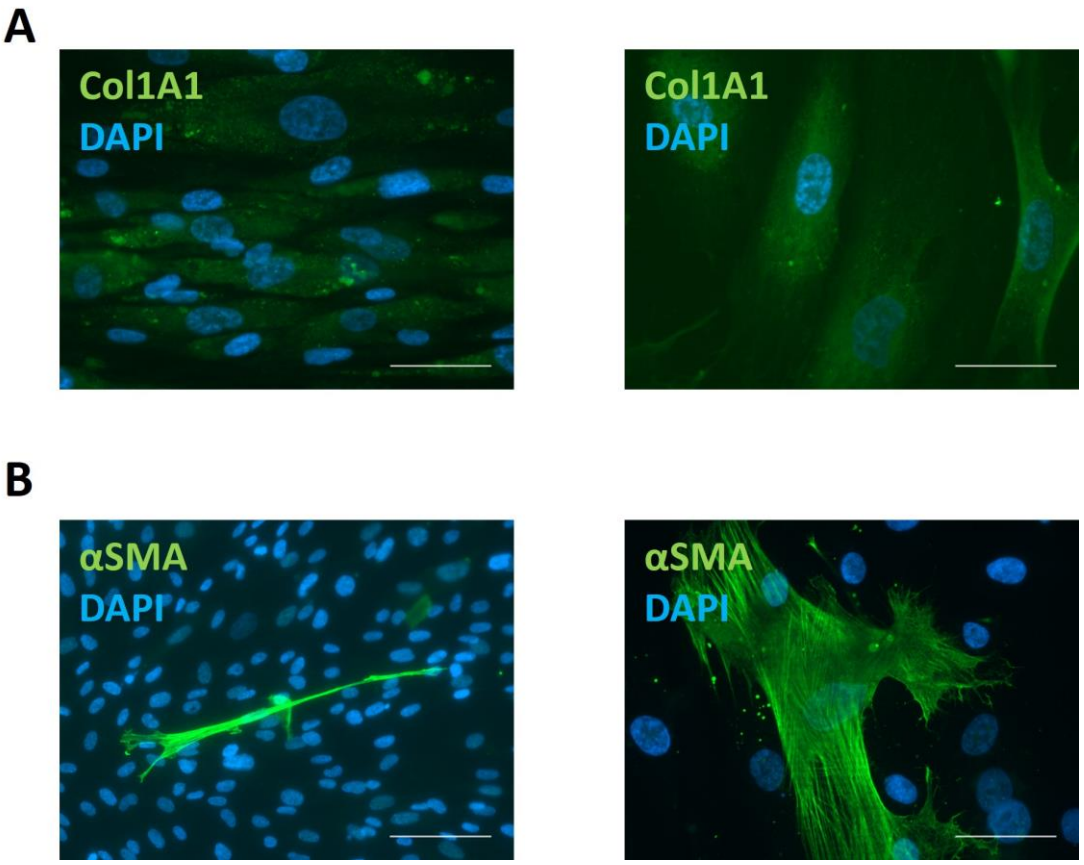

Fig. 52: IF staining of iPSC-StC. IF staining of iPSC-StC for **A** COL1A1 (green) and **B** αSMA (green). The nuclei were stained with DAPI (blue). All images were captured with a Zeiss Axio Observer Z1 inverted microscope and analyses were done with the AxioVision software. Scale bar= 200µm (**B**, left side) and 100µm (all others).

4.6.3 Analysis of 3D ECT

To analyze the functional role of CFB within the DCM pathophysiology primary and iPSC-derived fibroblast (-like) cells were casted together with collagen to form 3D ECT. The ECT were cultured for up to 13 or 20 days and were analyzed for different functional properties, including contraction, compaction, stiffness, and elasticity.

4.6.3.1 Reduced contraction in DCM1 ECT is restored upon FLNC rescue

The ECT were casted into moulds around two flexible poles. The tips of these poles were fluorescently-labelled. This could be used to determine ECT contraction over time, since ECT contraction induces pole deflection reducing the distance between the two poles. For this, the ECT were imaged one hour after casting for the first time, marking the initial distance of the poles at d0. Following, ECT were imaged daily over a period of 20 days. Based on this data, ECT contraction was calculated as the inverted change in distance of the two poles in comparison to the initial distance at d0. For all ECT, contraction appeared in a biphasic way with reaching a plateau at low level on day 3, followed by a second stronger contraction phase from day 5 on (Fig. 53 A, B). The second plateau is reached between day 16 and 20 (Fig. 53 A, B). The comparison of the pole deflection revealed that the diseased CFB and iPSC-StC showed a less pronounced contraction than the respective controls (Fig. 53 A, B). The rescued iPSC-StC line, in contrast, displayed a similar contractile

ability as the control iPSC-StC line (Fig. 53 B). DCM1 CFB showed lowest contraction at day 20 of 12.5%±8.8%, in contrast to a significantly stronger total contraction of normal CFB ECT with 35.2%±13.44% (Fig. 53 A). This was comparably shown for iPSC-derived ECT with lowest total contraction of 24.6%±18.3% for DCM1 iPSC-StC ECT, in contrast to significantly stronger total contraction of 34%±13.4% of control iPSC-StC ECT (Fig. 53 B). However, the contraction deficit was less pronounced in the iPSC-StC-derived ECT (Fig. 53 A, B). Interestingly, DCM1_res iPSC-StC ECT reached a total contraction of 39%±10.5%, which is comparable to normal ECT (primary and iPSC-derived) (Fig. 53 B).

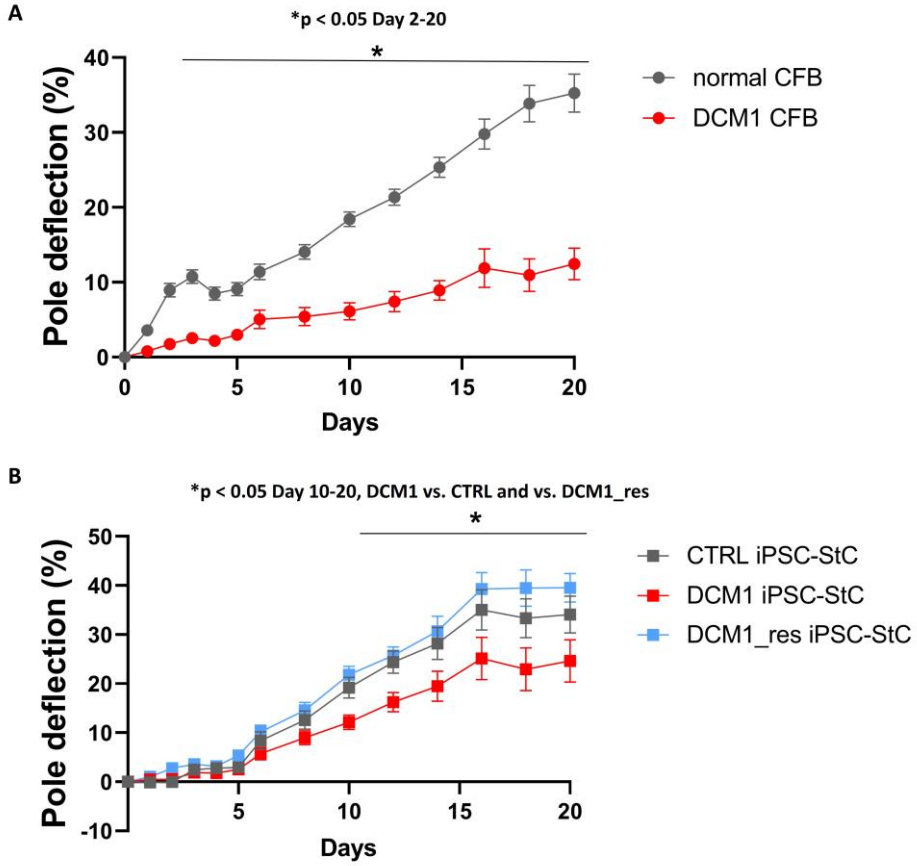

Fig. 53: Contraction analysis of ECT. ECT contraction data which was calculated based on pole deflection over a period of 20 days for **A** primary normal CFB and DCM1 CFB and **B** iPSC-derived control (CTRL), DCM1 and DCM1_res StC. Normal CF n=43, DCM1 CFB n=39, DCM1 iPSC-StC n=52, DCM1_res iPSC-StC n=46, control (CTRL) iPSC-StC n=33. Data are presented as mean ± SEM. Differences were analyzed using 2-way ANONA multiple comparisons with Tukey`s correction. * = p < 0.05.

4.6.3.2 Increased CSA in DCM1 ECT is restored upon FLNC rescue

On the day of measurement macroscopic images were taken as side and top view of each ECT analyzed. Line scans were prepared using ImageJ (Fig. 54 A). Based on the line scans, the mean diameter was calculated, and the CSA was determined as $CSA = \pi \times (\frac{ds}{2}) \times (\frac{dt}{2})$. CSA is a measure for ECT compaction. Analysis demonstrated a significant compaction deficit, as indicted by a higher CSA of primary CFB ECT of the diseased father (DCM1) compared to normal CFB ECT at both – day 13 (Fig. 54 C) and day 21 (Fig. 54 D). Additionally, CSA of iPSC-derived StC of the diseased father (DCM1) was significantly increased

compared to isogenic and normal control iPSC-StC at both – day 13 (Fig. 54 C) and day 21 (Fig. 54 D).

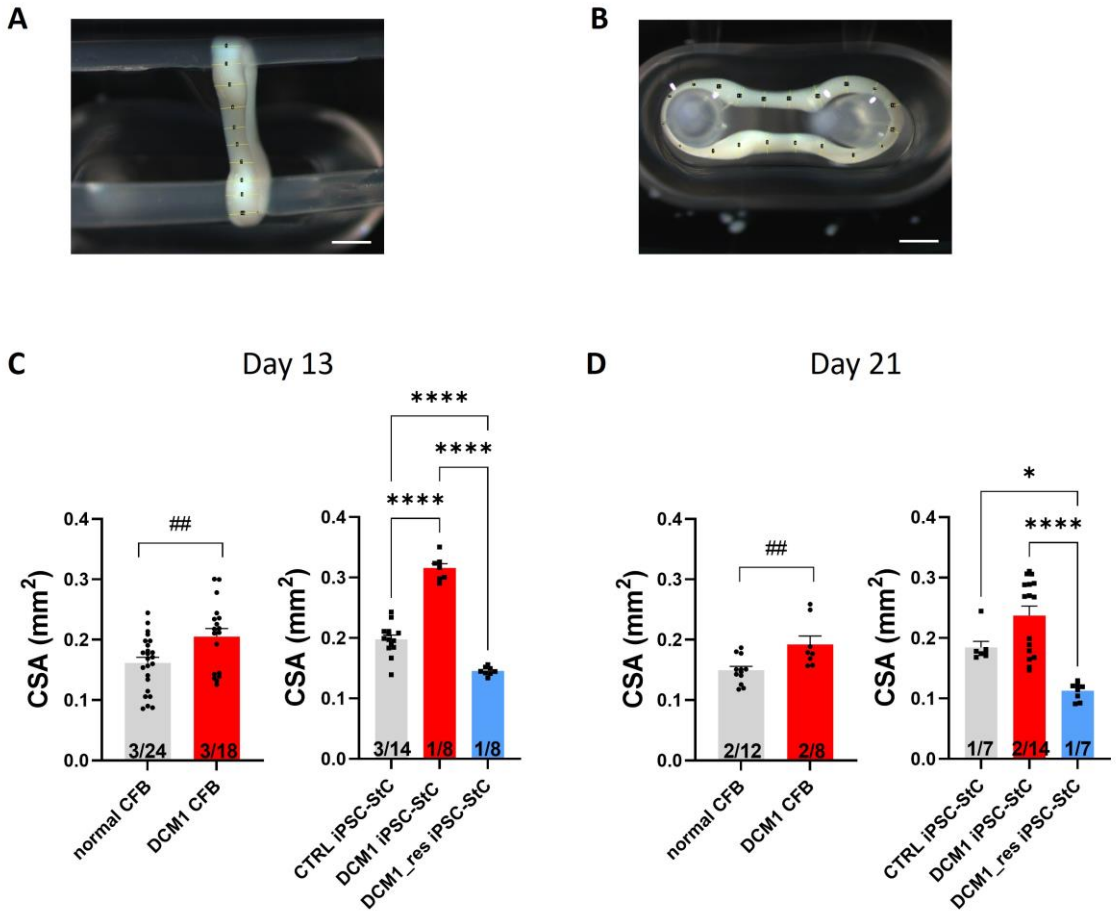

Fig. 54: CSA analysis of ECT. Shown are macroscopic images (Stereo Lumar V1.2, Zeiss) of **A** side and **B** top view on a representative ECT with line scans of the corresponding diameters determined using ImageJ software. Scale bar=1mm. CSA was determined based on the calculated diameters as $CSA = \pi \times (\frac{ds}{2}) \times (\frac{dt}{2})$. CSA was calculated for all analyzed ECT at **C** day 13 and **D** day 21. The values indicated in the bars represent numbers of casting experiments/number of analyzed ECT. Data are presented as mean ± SEM. Differences were analyzed using student`s t-test (#) to compare primary normal and diseased ECT or One-way ANONA multiple comparisons with Tukey`s correction (*) to compare iPSC-derived ECT. * = p < 0.05, ** = p < 0.01, *** = p < 0.001 and **** = p < 0.0001. # = p < 0.05, and ## = p < 0.01. Each dot represents one passage of primary cells or one differentiation experiment of iPSC-derived cells.

4.6.3.3 Increased tissue stiffness and decreased elasticity in ECT of primary DCM CFB

Destructive tensile strength measurements of the ECT were conducted of all lines at day 13 and day 21. The ECT were removed from the flexible poles and loaded onto two hooks in a tempered organ bath. Uniaxial tissue stretching occurred with 0.03 mm/s. To determine the stress values (kPA), the obtained force values (mN) were divided by the CSA. The obtained stress values were plotted against the relative change in the distance between the two hooks, to obtain the final stress-strain curves, from which important viscoelastic parameters, like Young`s modulus (stiffness), elasticity (strain at yield point), and extensibility (strain at failure point) could be determined. Fig. 55 A and B show

representative stress-strain curves of normal CFB and DCM1 CFB, respectively. When quantifying these parameters, the Young`s modulus was significantly increased in DCM CFB ECT compared to normal CFB at day 13 (Fig. 55 C) and day 21 (Fig. 55 D). Where the Young`s modulus remained comparably unchanged for all other ECT at day 13 (Fig. 55 C), there was a significantly decrease in DCM1 iPSC-StC compared to DCM1_res iPSC-StC at day 21 (Fig. 55 D). Elasticity and extensibility were decreased in DCM1 CFB compared to normal CFB at day 13 (Fig. 55 C) and day 21 (Fig. 55 D). Elasticity and extensibility remained unchanged in all other ECT (Fig. 55 C, D). Interestingly, all parameters analyzed showed comparable levels for primary and iPSC-derived StC (Fig. 55 C, D). Notably, the shown data is derived from only one casting experiment.

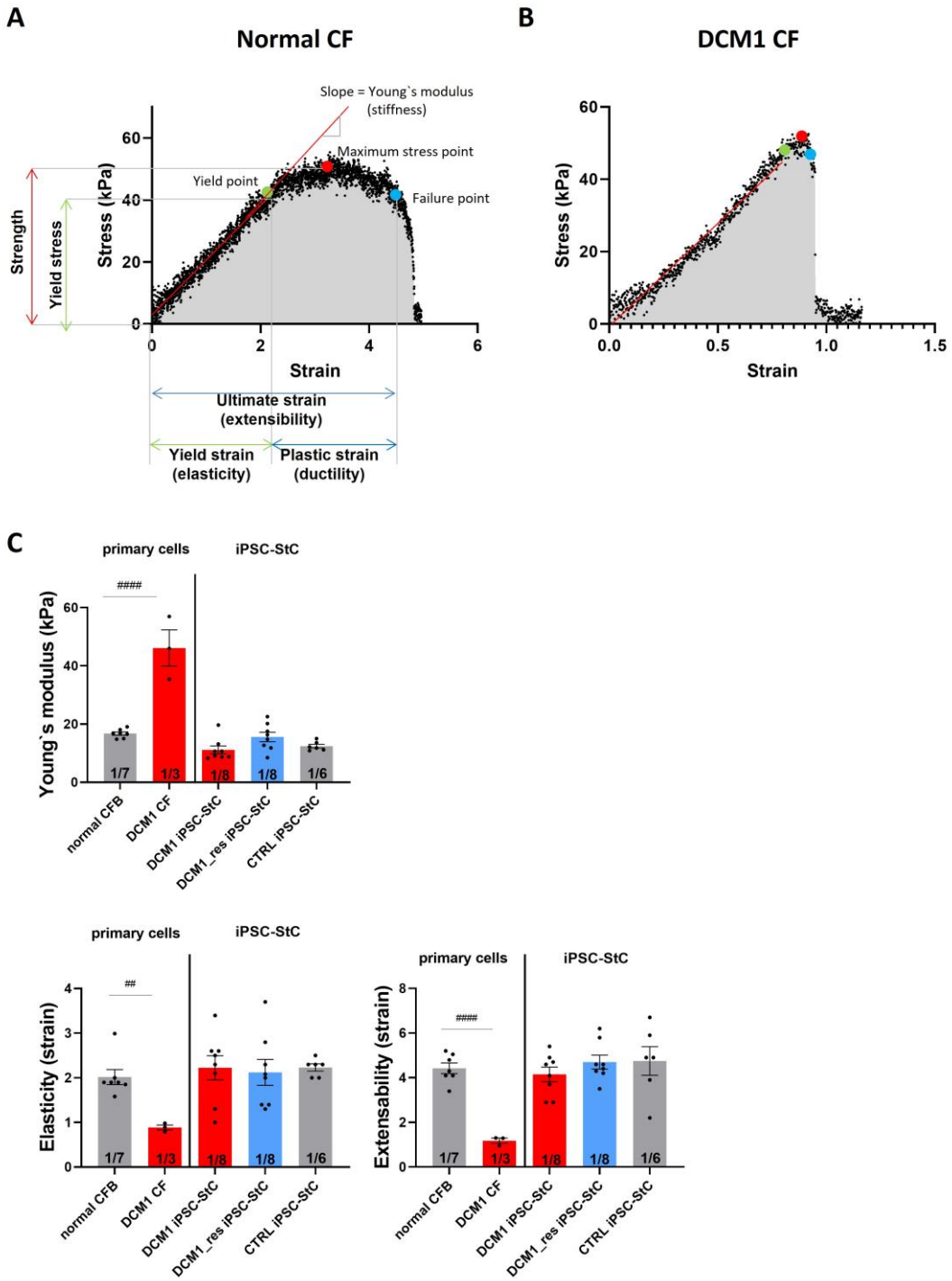

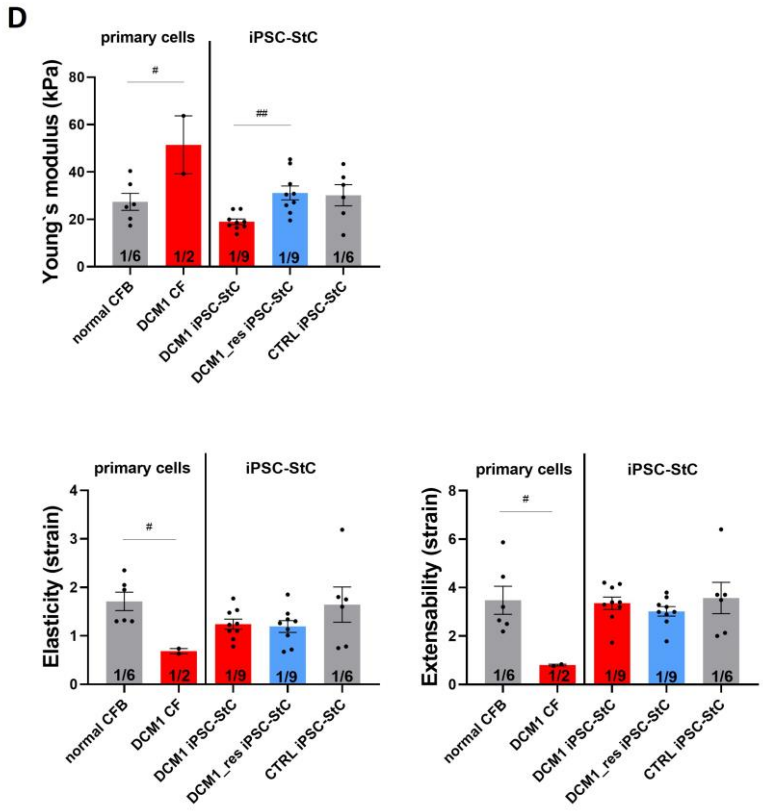

Fig. 55: Stress-strain analysis of ECT. Representable stress-strain diagrams of **A** normal CFB and **B** DCM1 CFB after destructive tensile strength measurement at day 13 using an RSA-G2 rheometer. For analysis, the obtained force values (mN) were divided by the CSA to determine stress values (kPa), which were plotted against the distance between the two hooks. **A** summarizes the main parameters analyzed. Young`s modulus as a marker for ECT stiffness, elasticity, and extensibility were analyzed for all ECT measured at **C** day 13 or **D** day 21. The values indicated in the bars represent number of analyzed ECT from one casting experiment. Data are presented as mean ± SEM. Differences were analyzed using student`s t-test. # = $p < 0.05$, ## = $p < 0.01$ ### = $p < 0.001$ and #### = $p < 0.0001$.

4.7 Role of telomere length in development and pathophysiology of DCM

During the past years several studies reported cardiomyocyte-specific telomere shortening in patients with cardiac diseases (Chang *et al.*, 2016; Chang and Blau, 2018; Chang *et al.*, 2018; Saliques *et al.*, 2010). Initially, this was only linked to age-related cardiac diseases, but subsequent studies also reported cardiomyocyte-specific telomere shortening in younger patients with genetically inherited DMD (Chang *et al.*, 2016; Saliques *et al.*, 2010). Further studies demonstrated cardiomyocyte-specific telomere shortening in patients with genetically inherited, HCM and DCM associated with mutations in proteins important for contractile function (Chang and Blau, 2018; Chang *et al.*, 2018). Additionally, a very recent study hypothesizes a link of cardiomyocyte-specific telomere shortening in DMD patients with classical molecular symptoms of DCM (Chang *et al.*, 2021). This includes a decrease in contractile force generation based on fibrosis as well as the loss of key structural proteins (among others leading to disruption of sarcomere organization), aberrant Ca^{2+} handling (decreased transient amplitudes and increased decay time) and increased ROS under basal

conditions (Chang *et al.*, 2021). Furthermore, this study provides evidence that in iPSC-derived cardiomyocytes of DMD patients a telomere shortening occurs proliferation-independent and similar effect cannot be observed in normal control iPSC-cardiomyocytes (Chang *et al.*, 2021). Based on these reports and the previously described findings within this project – loss of sarcomere organization, aberrant Ca^{2+} handling, increased fibrosis, decrease in contractile force generation and increased levels of ROS – the role of telomere length in the pathophysiology of DCM within this family should be investigated.

4.7.1 Increased telomere shortening in DCM iPSC-cardiomyocytes

To investigate whether telomere shortening might be of importance within the DCM pathophysiology in this index family, telomere length of iPSC and iPSC-cardiomyocytes was determined by qFISH analysis. For this purpose, iPSC samples of three passages of each family member and iPSC-cardiomyocytes samples of three different differentiation experiments of each family member were collected and subsequentially analyzed by qFISH experiments by Dr. Shambhabi Chatterjee at the Medizinische Hochschule Hannover in the group of Dr. Christian Bär. Detailed analyzes of the obtained data was carried out by the PhD candidate.

These data showed variances of telomere length in iPSC of the different family members (Fig. 56 A). This might be based on natural occurring biological variances. However, iPSC telomere length of all family members was in a similar range of 100 to 120 (Fig. 56 A). Similar variances can be observed in telomere length of iPSC-cardiomyocytes (Fig. 56 B). Overall iPSC-cardiomyocytes telomere length ranged between 80 to 100 (Fig. 56 B). In conclusion, these data showed a telomere shortening from iPSC to iPSC-cardiomyocytes of all four family members (Fig. 56 C). However, telomere shortening from iPSC to iPSC-cardiomyocytes is strongest in cells of diseased family members with a shortening of 14.5% and 24.82% for DCM1 and DCM3, respectively (Fig. 56 C). In comparison, telomere shortening in healthy family members DCM2 and DCM4 of 12% and 4.6%, respectively, is lower (Fig. 56 C). The iPSC to iPSC-cardiomyocytes telomere shortening is strongest in iPSC-cardiomyocytes of the diseased daughter (DCM3). In total the cells of the diseased daughter do not only show the strongest shortening of telomeres from iPSC to iPSC-cardiomyocytes, but also the shortest iPSC-cardiomyocytes telomeres in general (Fig. 56 B).

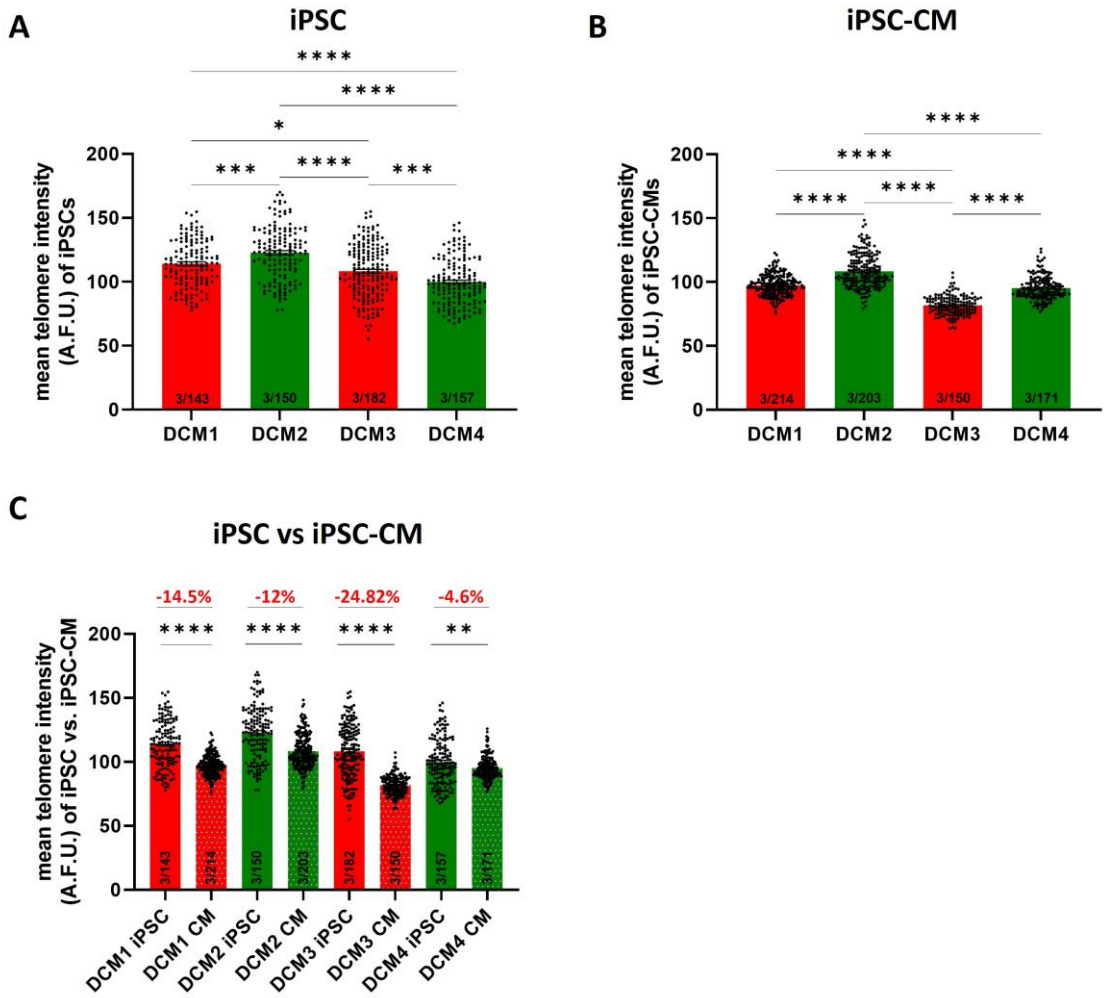

Fig. 56: qFISH analysis of telomere length of iPSC and iPSC-cardiomyocytes. A Quantified data of qFISH analysis of telomere length of iPSC of all family members. **B** Quantified data of qFISH analysis of telomere length of iPSC-cardiomyocytes of all family members. **C** Comparative qFISH results of telomere length of iPSC versus corresponding iPSC-cardiomyocytes of all family members. Percentages (red) indicate relative telomere shortening from iPSC to iPSC-cardiomyocytes. Numbers within the bars indicate the number of iPSC passages or iPSC-cardiomyocytes differentiation experiments / number of analyzed cells. Data is represented as ± SEM. P-values were determined using one-way ANONA multiple comparisons with Tukey`s correction. * = $p < 0.05$, ** = $p < 0.01$, *** = $p < 0.001$ and **** = $p < 0.0001$.

4.7.2 Unaffected telomerase activity

In order to analyze if the differences in telomere length of cells of the different family members might be based on variations of telomerase activity a TRAP assay was performed. The TRAP assay follows a three-step protocol of: 1. extension of an artificial telomerase substrate by addition of telomeric repeats by the endogenous telomerase of the analyzed cell lysate, 2. amplification of the extension product by PCR and 3. visualization of the amplified product by gel electrophoresis. The electrophoretically separated fragments form a so-called TRAP ladder with larger fragments running at the top and smaller fragments displayed at the bottom. By this the telomerase activity can be assessed – the more active the telomerase, the more telomeric repeats can be added during the extension step. Longer products correlate with higher telomerase activity. As positive control HEK cells were used, forming a TRAP ladder. As negative control a heat inactivated sample as

well as HUVEC cells were used, both not forming a TRAP ladder. As shown in Fig. 57, the TRAP ladder of all analyzed iPSC is longer than the TRAP ladder of HEK cells, as expected. Due to higher division rate, iPSC have an intrinsically higher telomerase activity compared to differentiated somatic cells. In total, there are no macroscopic differences in telomerase activity of the individual cell lines, as the TRAP ladder are of comparable length (Fig. 57). The TRAP ladder of DCM3.7_311 is of higher intensity (Fig. 57). However, TRAP ladder length is not significantly larger (Fig. 57). DCM1.4_528 and DCM3.7_310 have slightly smaller TRAP ladder (Fig. 57). As samples of two other passages of both lines showed TRAP ladder comparable to the other iPSC (Fig. 57), this observation might be based on technical issues or biological variations.

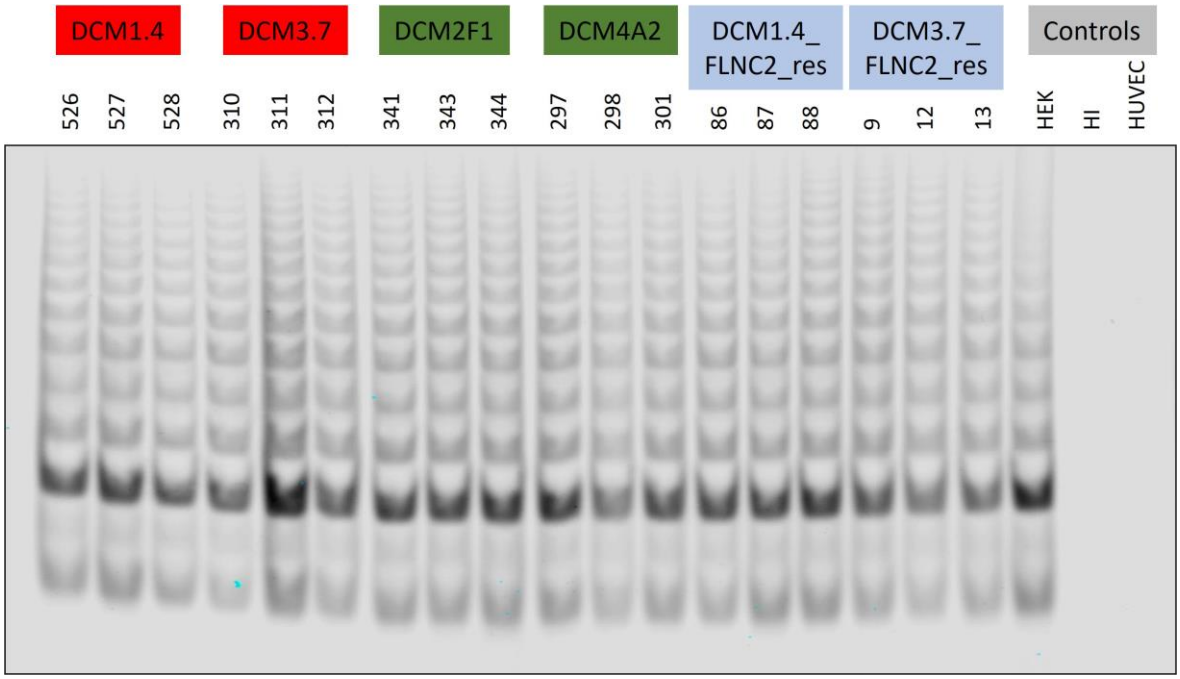

Fig. 57: TRAP assay to analyze telomerase activity of DCM iPSC. Shown is a gel electrophoreses picture displaying individual TRAP ladders representing the amount of telomerase activity of iPSC of all family members and isogenic FLNC_res iPSC after TRAP analysis. HEK cells were used as positive control and display a shorter TRAP ladder as they have lower telomerase activity compared to all iPSC. HI (heat inactivated) and HUVEC cells were used as negative controls and display no TRAP ladder. Numbers indicate lab internal consecutive numbers as individual identifiers.

5 Discussion

Cardiovascular diseases still are, despite rapid scientific and medical progress, a major threat to human health worldwide (Benjamin *et al.*, 2017). Among these, cardiomyopathies are one of the leading causes of heart failure (Benjamin *et al.*, 2017; Maron *et al.*, 2006). DCM is characterized by dilation of the left ventricle and systolic dysfunction but no left ventricular wall thickening, represents one of the most common causes of heart failure and the most frequent reason for heart transplantation worldwide (Hershberger and Siegfried, 2011; Michels *et al.*, 1992; Weintraub *et al.*, 2017). With an estimated prevalence of 40 DCM cases per 100.000 individuals, patient outcomes can range from a reduced quality of life, over heart failure and necessary heart transplantation to sudden cardiac death (Hershberger and Siegfried, 2011; Michels *et al.*, 1992; Weintraub *et al.*, 2017). The molecular basis of most DCM cases remains unknown; however, it seems to be evident that DCM can have genetic as well as acquired causes (Hershberger and Siegfried, 2011; Michels *et al.*, 1992; Weintraub *et al.*, 2017). Due to the high prevalence and severe outcome of DCM it is important to unravel the exact underlying molecular mechanisms which contribute to DCM development.

In this project the model of patient-derived iPSC-cardiomyocytes was used to establish a human *in vitro* DCM model and investigate the underlying molecular causes and functional consequences of DCM. For this purpose, a four-member index family was recruited containing patients with severe DCM and healthy controls. In the first part of this work, two new, potentially disease-causing missense variants in the *ILK* and *FLNC* genes were identified by WES and panel-sequencing of 192 cardiac genes. Previously generated iPSC-lines of all family members were characterized in this work for their pluripotency and differentiated into functional beating, ventricular iPSC-cardiomyocytes. DCM patient-derived iPSC-cardiomyocytes displayed a dysregulated sarcomeric structure compared to healthy family members. Based on this finding, the role of the newly identified FLNC variant, encoding an important sarcomeric protein, was investigated in more detail by generating isogenic control iPSC using the CRISPR/Cas9 gene editing system. The sarcomeric regularity of the isogenic control iPSC-cardiomyocytes of both patients was restored, giving first evidence for the crucial role of the FLNC variant within the DCM pathophysiology. In the second part of this project, the role of the FLNC variant was further analyzed on molecular and functional levels. Special attention was drawn on Ca^{2+} signaling, and the iPSC-cardiomyocytes ultimately were analyzed in a 3D model. In a third part of the present project, the role of CFB in addition to cardiomyocytes was investigated. The last part of this project, focused on potential cardiac-specific telomere shortening.

5.1 Identified FLNC missense variant is in a mutation and interaction hotspot of FLNC, the ROD2 domain

Up to 35% of all DCM cases have a family history and are associated with variants in more than 50 gene loci mainly encoding the cytoskeleton, sarcomere, splicing factors, nuclear envelope and mitochondrial proteins (Maron *et al.*, 2006; Michels *et al.*, 1992; Weintraub *et al.*, 2017). The DCM form analyzed within the recruited index family most likely is of heritable origin, as both – the father and one daughter – are diseased and already needed heart transplantation. However, the underlying genetic cause was not known so far. Pedigree analysis hinted towards a *de novo* occurrence of an unknown mutation, as the DCM first occurred within the DCM index family and displayed a high penetrance. WES and panel sequencing identified two new variants in two genes – *FLNC* (Arg2187Pro) and *ILK* (Met425Thr) – only recently associated with cardiomyopathies as potentially disease-causing (i.e. "likely pathogenic") (in collaboration with Prof. Dr. med. Bernd Wollnik, Human Genetics UMG, Fig. 17). Both variants were not described so far in the literature and could not be found in several clinical and biological databases. For both genes – *ILK* (Brodehl *et al.*, 2019b; Hannigan *et al.*, 2007; Traister *et al.*, 2014) and *FLNC* (Ader *et al.*, 2019; Agarwal *et al.*, 2021; Reinstein *et al.*, 2016; Verdonschot *et al.*, 2020) – missense variants are reported which are associated with cardiomyopathies. Several reports demonstrate the significantly increasing role of FLNC variants within the DCM pathophysiology (Begay *et al.*, 2016; Eden and Frey, 2021; Ortiz-Genga *et al.*, 2016; Verdonschot *et al.*, 2020). In contrast to this, current literature on ILK-associated DCM is low (Haas *et al.*, 2015; Knoll *et al.*, 2007; Meder *et al.*, 2011). Therefore, the identified FLNC variant was chosen as top candidate and was further investigated within this project. FLNC is a multi-adaptor protein, mainly expressed in skeletal and cardiac muscle, playing a role in muscle differentiation and maintenance of elongated muscle fiber structure (Popowicz *et al.*, 2006; van der Flier and Sonnenberg, 2001; Zhou *et al.*, 2010a). Its primary function is the cross-linking of sarcomeric f-actin (Popowicz *et al.*, 2006). Additionally, FLNC binds several other proteins and thus plays a role in Z-disc formation and in signaling processes between the sarcolemma and the myofibrillar Z-disc (van der Flier and Sonnenberg, 2001; Zhou *et al.*, 2010a). In more detail, the identified variant is localized within a highly conserved unique 82aa insertion of domain 20 of FLNC (Fig. 4). This insertion is characterized as an intrinsically disordered domain and is not found in otherwise highly homologous family members FLNA and FLNB. Additionally, this insertion seems to be sufficient for targeting to developing and mature Z-discs (Popowicz *et al.*, 2006; van der Flier and Sonnenberg, 2001; Zhou *et al.*, 2010a) and is crucial for binding to a plethora of interacting proteins, like xin (van der Ven *et al.*, 2006), myotilin (van der Ven *et al.*, 2000), myopodin (Linnemann *et al.*, 2010) and aciculin (Molt *et al.*, 2014). Hence, functional impairment of FLNC caused by the newly identified missense variant in the unique 82aa insertion of domain 20 might affect proper formation and function of this complex network, leading to the DCM phenotype.

Interestingly, most of the FLNC variants associated with cardiomyopathies (HCM, DCM, ACM) are found in the *ROD2* domain, where the newly identified variant is localized as well and which is essential for FLNC dimerization and Z-disc interaction (Mao and Nakamura, 2020). Thus, it seems as if aa changes within this region are crucial for the development of

cardiomyopathies. Furthermore, the exchange from an arginine to a proline seems quite severe, especially when considering that the arginine at this position is highly conserved across mammals and a potential phosphorylation site (Fu *et al.*, 2020). However, since the 82aa insertion is characterized as being intrinsically disordered, the aa change from arginine to proline rather does not affect protein 2D and 3D structure, since intrinsically disordered regions lack the ability to form stable 3D structures (Latysheva *et al.*, 2015). But site-specific phosphorylation of FLNC was hypothesized and partially demonstrated to regulate FLNC interaction, dynamics and function in mouse and human *in vitro* (Mao and Nakamura, 2020; Reimann *et al.*, 2020; Reimann *et al.*, 2017). Hence, the change from an arginine, as a putative phospho-site (Fu *et al.*, 2020) to a proline, might have direct effects onto the FLNC phosphorylation state. Additionally, several studies identified two phosphorylation hot spots within the FLNC protein – the hinge 2 region (Raynaud *et al.*, 2006; Reimann *et al.*, 2017), and domain 20, with special relevance of the unique 82aa insertion, where the newly identified variant is localized as well (Jay *et al.*, 2000; Murray *et al.*, 2004; Reimann *et al.*, 2020). PKCα-dependent phosphorylation of the hinge 2 region at Ser2623/Ser2624 in human (Raynaud *et al.*, 2006) and Ser2621/Ser2625 in mice (Reimann *et al.*, 2017) was shown to reduce the susceptibility to calpain-1 cleavage at position Thr2625. Calpain-1 cleavage would remove the dimerization domain and hence phosphorylation of the reported sites might regulate Z-disc disassembly (Mao and Nakamura, 2020). Phosphorylation of FLNC d20 was reported to be PKA- (Ser2152, (Jay *et al.*, 2000)), PKB/Akt- (Ser2213 (Murray *et al.*, 2004), Ser2233 (Reimann *et al.*, 2020)) and PKCα-dependent (Ser2236, (Reimann *et al.*, 2020)). Dual-site phosphorylation of Ser2233/Ser2236 (within the 82aa insertion) was reported to have protective effects against FILIP1-degradation and allows fast dynamics of FLNC, important for its signaling adaptor function (Reimann *et al.*, 2020). Although not unraveled so far, due to accumulation of phosphorylation sites in d20 and the unique 82aa insertion, which is crucial for Z-disc targeting and interaction to several proteins, all these studies suggest an effect onto these functions mediated by phosphorylation (Jay *et al.*, 2000; Murray *et al.*, 2004; Reimann *et al.*, 2020). Hence, although FLNC phosphorylation was mainly reported for serine-sites, the arginine occurring in the wildtype FLNC within the 82aa insertion might hold the potential for phosphorylation or other post-translational modifications (PTM), maybe regulating certain signaling or interaction functions of FLNC. The substitution of this arginine to a proline then would result in a loss of the PTM site, thereby affecting potential interactions.

Interestingly, FLNC-associated DCM cases generally display a more severe phenotype than other heritable DCM and worse prognosis with significant LV dilation and systolic dysfunction, but also with high levels of myocardial fibrosis and conduction abnormalities (Begay *et al.*, 2016; Eden and Frey, 2021; Ortiz-Genga *et al.*, 2016). The severity of FLNC mutations was also highlighted in the mouse model (Zhou *et al.*, 2020). Here homozygous cardiomyocyte-specific FLNC loss in embryos led to perinatal lethality and cardiomyocyte-specific induced FLNC knock-out in adult mice resulted in rapid DCM development (Zhou *et al.*, 2020). This is in line, with the severe DCM phenotype within the index family, characterized by drastically reduced EF (<20%), necessary heart transplantation, and increased levels of fibrosis. However, so far, most FLNC-associated DCM cases are linked to

truncating, rather than missense variants. Such truncating variants cluster all over the FLNC protein and are localized within the ABD (p.Tyr7Thrfs*51), the ROD1 domain (p.Tyr928*), the ROD2 domain (p.Gln2303*), as well as the dimerization domain (p.Asp2703Thrfs*61) (Ader *et al.*, 2019). Diverse distribution of truncation variants indicates limited position impact of these variants on the disease. Truncating variants are thus largely explained by induction of NMD of the FLNC mRNA leading to haploinsufficiency. Haploinsufficiency results in a decreased amount of normal FLNC protein, which was hypothesized as cause of Z-disc disarray and weakened binding of the Z-disc to the membrane, as well as impaired cell-cell adhesion. Consequently, truncating variants result in an impaired mechanotransduction and these patients often develop arrhythmia and fibrosis (Ader *et al.*, 2019; Eden and Frey, 2021; Verdonschot *et al.*, 2020). However, reduced FLNC mRNA or protein levels could not be observed in iPSC-cardiomyocytes harboring the newly identified FLNC variant in this project (Fig. 36), indicating that reduced amounts of FLNC are not the underlying cause of the DCM.

Missense variants in contrast, rather cluster to the ROD2 domain (Fig. 4). The ROD2 domain is highly important for targeting FLNC to the Z-disc and is required for interaction with many, especially Z-disc, proteins but rather associate with HCM cases (Ader *et al.*, 2019; Eden and Frey, 2021). The newly identified FLNC missense variant is associated with DCM and located in the ROD2 domain. Previously described missense variants, include variants in d20, in close proximity to the identified variant, like p.Gly2151Ser or p.Arg2133His (Valdes-Mas *et al.*, 2014). Such missense variants are associated with sarcomeric abnormalities, Z-disc irregularities, formation of insoluble FLNC protein aggregates, and increased activation of protein clearance mechanisms, like proteasome or autophagy pathways (Agarwal *et al.*, 2021; Eden and Frey, 2021; Valdes-Mas *et al.*, 2014). This is largely explained by the presence of misfolded proteins based on the missense mutations (Ader *et al.*, 2019; Gomez *et al.*, 2017; Valdes-Mas *et al.*, 2014). Interestingly, iPSC-cardiomyocytes harboring the newly identified FLNC variant also display severe sarcomere abnormalities (Fig. 24), especially impairing the Z-disc regularity, as described for other missense variants in this domain. Although not studied in detail, FLNC protein aggregate formation in the cytoplasm could not be observed by standard IF staining in diseased iPSC-cardiomyocytes in this project. Activation of protein clearance pathways was not analyzed so far. However, since the identified variant is in the intrinsically disordered 82aa insertion, it per se should not have severe effects onto protein structure. Hence, formation of protein aggregates would not necessarily be expected and also is not reported for FLNC-dependent DCM cases (Agarwal *et al.*, 2021; Begay *et al.*, 2018; Verdonschot *et al.*, 2020). It would be more feasible to hypothesize impaired interactions to important Z-disc/sarcomere binding partners, as described before (Ader *et al.*, 2019; Ortiz-Genga *et al.*, 2016), as cause for sarcomere abnormalities.

Interestingly, an *in vitro* study using different CRISPR/Cas9 gene edited human iPSC-cardiomyocytes showed that iPSC-cardiomyocytes with different FLNC variants do recapitulate the different disease mechanisms of truncating and missense FLNC variants as described in primary diseased tissue. Targeting the FLNC domain 15, they generated homozygous truncated FLNC, heterozygous truncated FLNC (leading to haploinsufficiency),

and a heterozygous in-frame deletion at position p.Gly1674 of FLNC in iPSC-cardiomyocytes (Agarwal *et al.*, 2021). Agarwal *et al.* demonstrated total ablation and haploinsufficiency reducing FLNC mRNA and protein levels, similar as reported for DCM-associated truncating FLNC variants. The reduced protein amounts might be associated with NMD in this *in vitro* study as well. The complete loss of FLNC was also associated with impaired sarcomere structure and function affecting overall contractility of iPSC-cardiomyocytes. This was explained by absence of actin cross-linking function and, surprisingly, with impaired expression of a diverse set of sarcomeric genes. Hence, total ablation of FLNC highlighted the role of FLNC in sarcomere assembly and stability. However, neither haploinsufficient, nor in-frame deletion variants did show impaired sarcomere content, organization, or function, as we found in our study for FLNC-R2187P. Nevertheless, by targeting domain 15 within ROD1 and not ROD2 domain or the ABD, which are mainly important for interactions to sarcomere proteins or actin cross-linking, respectively, absence of a sarcomeric phenotype is not surprising. Additionally, the tested variant was classified as benign at the end of the study, which might be a reason for a less severe phenotype. Nevertheless, like reported for pathogenic missense variants, the in-frame deletion variant was associated with insoluble cytoplasmic aggregate formation of FLNC and its binding partners. Interestingly, both – haploinsufficient and in-frame deletion variants – led to proteotoxic effects, shown by increased lysosome content and autophagy (Agarwal *et al.*, 2021). This study highlights, that the iPSC-cardiomyocytes model can recapitulate *in vivo* described pathogenic mechanisms of distinct FLNC variants.

Despite accumulating evidence of diverse FLNC variants being causative for isolated cardiomyopathy phenotypes and general mechanisms being attributed to truncating and missense variants, little is known about exact underlying molecular mechanisms. Although several studies postulate impaired interactions to FLNC binding partners, especially due to ROD2 domain located missense variants, no study could unravel such impaired interactions in detail so far. Consequently, the exact role of the newly identified FLNC variant within this project can only be speculated. The new variant is located in the ROD2 domain, within the unique 82aa insertion. This is a hot spot for previously reported missense mutations and phosphorylation sites. iPSC-cardiomyocytes harboring the newly identified variant display a sarcomeric, contraction and stiffness phenotype, as described for other missense variants. However, formation of protein aggregation, which is reported for many FLNC missense variants, could not be observed, but was not analyzed in detail. Nevertheless, this might be due to the location within the intrinsically disordered 82aa insertion, where aa changes are not expected to induce protein misfolding. Additionally, the substitution from the highly-conserved arginine to proline, removes a potential phosphorylation or PTM site, within a phospho-site hot spot region. Consequently, the identified variant might induce an impairment of interaction to certain binding partners, maybe driven by absence of a necessary PTM site or other factors, resulting in sarcomeric disarray. However, this requires further detailed analysis. This on the one hand, requires investigation of the resulting cellular and functional phenotype to unravel the pathomechanism. This is discussed in the following paragraphs in more detail. On the other hand, potentially affected interactions need to be identified, which should be investigated in the future. This would also include more detailed analysis of the impaired mechanisms within the sarcomere.

5.2 iPSC of all family members show full pluripotency

First shown by Yamanaka and Takahashi (Takahashi *et al.*, 2007; Takahashi and Yamanaka, 2006) somatic cells like patient-derived fibroblasts or PBMCs can be reprogrammed to iPSC. Prior to the start of this project, SFB of DCM1 patient and PBMCs of all other family members were isolated and reprogrammed by transient expression of OCT4, KLF4, SOX2 and C-MYC using the non-integrating Sendai virus. In a first part of this project, these iPSC lines were characterized for full pluripotency before differentiating them into specific cell types and using them for subsequent analysis. This is crucial, as improper reprogramming might result in difficulties of differentiation (Koyanagi-Aoi *et al.*, 2013; Takahashi and Yamanaka, 2016). The iPSC lines used for this work showed a classical iPSC morphology and high activity of ALP (Fig. 18). Additionally, expression of pluripotency-specific genes (Fig. 19) and proteins could be confirmed. The expression of these markers supports the pluripotent state and represents activation of endogenous pluripotency, as pluripotency markers like NANOG, LIN28, GDF3 and TRA1-60 are upregulated as well, although not being part of the vectors used for reprogramming. Furthermore, spontaneous *in vitro* differentiation experiments demonstrated the pluripotent potential of the iPSC by differentiation into cell types of all three germ layers (Fig. 20, Fig. 21). Some germ layer-specific markers were already expressed in some cell lines at the start of the differentiation protocol (Fig. 21). This might be explained by spontaneous differentiation of the iPSC during cell culture, where they usually should continue to be undifferentiated. This might occur when iPSC reach high confluency, which could induce spontaneous differentiation in some cells and should be avoided.

Taken together, this data demonstrates that all analyzed iPSC lines show full pluripotency without any differences. Making all lines suitable for (cardiac) differentiation.

5.3 Differentiated iPSC-cardiomyocytes show high purity and ventricular subtype-specificity but decreased differentiation efficiency of DCM1 iPSC

To use the iPSC to unravel the underlying molecular mechanisms of DCM within this index family, they were differentiated into iPSC-cardiomyocytes for subsequent analyses. In order to obtain a large quantity of highly pure iPSC-cardiomyocytes a direct differentiation protocol (Borchert *et al.*, 2017) was used, which combines previously reported protocols (Burridge *et al.*, 2014; Burridge and Zambidis, 2013; Lian *et al.*, 2012; Lian *et al.*, 2013). To ensure comparability of all iPSC-cardiomyocytes analyzed a chemically defined protocol was used, based on manipulation of Wnt signaling by subsequent addition of small molecules (3.1.8). To increase iPSC-cardiomyocytes purity and reduce number of non-cardiomyocyte cells, a metabolic selection step was performed based on glucose depletion and lactate supplementation (Tohyama *et al.*, 2013). This is possible as cardiomyocytes can metabolize lactate as carbon source, whereas most other cell types are dependent on glucose as carbon source and hence will not survive (Tohyama *et al.*, 2013). The combination of directed differentiation and metabolic selection achieved an

iPSC-cardiomyocytes purity of 85% ± 10% for all lines, assessed by flow cytometry for $cTNT^+$ cells (Fig. 22). Although at the lower limits, this yield is in line with other studies using similar monolayer-dependent, chemically defined iPSC-cardiomyocytes differentiation protocols, yielding ~90% $cTNT^+$ cells (Cyganek *et al.*, 2018; Zhao *et al.*, 2019).

In the present project, the underlying molecular mechanisms of a DCM should be investigated. Since DCM mostly affects the left ventricle, we focused on the differentiation of iPSC into ventricular iPSC-cardiomyocytes. Although a direct differentiation protocol was used already aiming for generating ventricular iPSC-cardiomyocytes, it was important to check for differentiation efficiency into the correct subtype and to exclude possible contamination with other, especially atrial, cardiomyocyte subtypes. For this, first IF staining of the ventricular myosin light chain-2 were conducted and quantified in comparison to $cTNT^+$ cells (Fig. 22). In average 70% ±5% of generated $cTNT^+$ cells were ventricular iPSC-cardiomyocytes (Fig. 22). Although this amount seems to be quite low, it is in line with several studies reporting a heterozygous cell population obtained from directed ventricular iPSC-cardiomyocytes differentiation (He *et al.*, 2003; Ma *et al.*, 2011; Zhang *et al.*, 2009; Zhao *et al.*, 2020a). These studies report outcome of monolayer differentiation ranging from 60-70% ventricular cardiomyocytes (Zhang *et al.*, 2009; Zhao *et al.*, 2020a). The remaining cells are largely comprised of atrial and nodal cells, as well as undifferentiated cells (He *et al.*, 2003; Ma *et al.*, 2011; Zhang *et al.*, 2009). Exact composition of non-ventricular iPSC-cardiomyocytes within this project was not analyzed. However, additionally, upregulated *MLC2v* expression as ventricular marker (Fig. 22), and downregulated *PITX2* expression as atrial marker (Hill *et al.*, 2019) (Fig. 22), further supported the predominant presence of ventricular iPSC-cardiomyocytes.

Within the process of iPSC-cardiomyocytes quality control, the differentiation efficiency from iPSC to functional beating iPSC-cardiomyocytes was assessed quantitatively. For this, all differentiation experiments of each cell line started with a sufficient confluency of 70-80% at d0 were compared to those differentiation experiments finally reaching functional beating (4.1.4.2). This analysis revealed the lowest differentiation efficiency for iPSC of the diseased father (DCM1) of only 47.46% (Fig. 23). Interestingly, a high proportion of these failed differentiation experiments showed cells with cardiomyocyte morphology, but these cells did not start beating. The cardiomyocyte identity of these cells was proven by IF staining of cTNT (data not shown). This was a special observation for the DCM1 cell line. Failed experiments of other cell lines were mainly based on detachment, regularly occurring and based on confluency variations. When analyzing differentiation efficiency of isogenic control DCM1_res iPSC, it was improved to 72.41%, comparable to a success rate of iPSC of healthy family members (Fig. 32). For DCM1 isogenic control iPSC-cardiomyocytes differentiation experiments failure was mainly based on detachment of the cells, whereas differentiation towards cardiomyocyte morphology without initiation of functional beating could not be observed anymore. This observation might be based on the dysregulated sarcomeric structure in DCM1 iPSC-cardiomyocytes (Fig. 24). Functional sarcomeres translate electrical stimuli into mechanical beating of the cells. Destroyed sarcomeres may be impaired in initiating contractile function. This might be associated with an altered Ca^{2+} sensitivity of the diseased iPSC-cardiomyocytes. A decreased Ca^{2+} sensitivity

often is reported for DCM myofilaments (Chung *et al.*, 2016; Groen *et al.*, 2020; Robinson *et al.*, 2007). Decreased Ca^{2+} sensitivity could be explained by the dysregulated sarcomere, impairing the formation of thin and thick filament interaction, as shown for other DCM mutations (Robinson *et al.*, 2007). This would lower the number of cross-bridging cycles within the sarcomeres and decrease overall contraction. Increasing Ca^{2+} concentrations would be required to use the low numbers of established thin/thick filament interactions efficiently to induce contraction (i.e., decreased Ca^{2+} sensitivity). However, increased relaxation time, shown by FURA-2 and Fluo-4 measurements (4.5.1.1), rather is contradictory to a decreased Ca^{2+} sensitivity of the diseased iPSC-cardiomyocytes. Furthermore, the identified increased resting force in DCM1 and DCM3 in the 3D EHM experiments, a measure of stiffness, point to an increased Ca^{2+} sensitivity, which was recently shown for the DCM-associated cardiac variant cTNT-R173W (Jung *et al.*, 2022). If an altered Ca^{2+} sensitivity plays a role in impaired contractility of these diseased iPSC-cardiomyocytes needs to be investigated in the future. Regardless of the exact molecular impairment induced by the dysregulated sarcomere, those differentiation experiments showing cardiomyocyte morphology but lacking functional beating, would represent successfully differentiated cells. Consequently, absence of beating, could be classified as a disease phenotype. This is supported by the observation, which restored sarcomeric regularity and increased differentiation efficiency co-segregate in isogenic control DCM1_res iPSC-cardiomyocytes. However, although iPSC-cardiomyocytes of the diseased daughter (DCM3) display similar loss of sarcomeric integrity as DCM1 iPSC-cardiomyocytes, these cells show high (90.00%, Fig. 23) differentiation efficiency, and morphologically differentiated cells lacking functional beating cannot be observed. These different findings might be influenced by further factors potentially differing between the different cell lines. These differences could be based on individual genetic backgrounds or on differences based on the cell system. This again highlights the importance of isogenic control lines. Nevertheless, the exact underlying cause for significantly reduced differentiation efficiency, which is enhanced upon FLNC rescue, remains elusive.

In summary, directed cardiac differentiation yielded iPSC-cardiomyocytes with high purity and predominantly ventricular subtype. However, DCM1 iPSC display a differentiation phenotype, often generating iPSC-cardiomyocytes without functional beating. This seems to be FLNC-dependent and might be based on the dysregulated sarcomere.

5.4 FLNC rescue genome editing

iPSC-cardiomyocytes research faces the challenge that despite myriads of quality control steps (reprogramming efficiency, pluripotency and iPSC-cardiomyocytes purity, maturity and subtype-specificity) during the generation process of iPSC-cardiomyocytes the individual differentiation experiments – of different lines and even among the same line – often show high variances when being analyzed (Williams *et al.*, 2020). Therefore, often several differentiation experiments are required to elucidate certain biological effects when comparing healthy and diseased iPSC-derived cardiomyocyte lines. Additionally, especially when studying disease conditions based on certain genetic variants, the variability of the genetic background among different individuals could influence the

experimental conclusion. Hence, when studying the role of a defined gene mutation with the iPSC-cardiomyocytes cell system, the use of isogenic control lines is inevitable. Isogenic control lines are generated from the actual diseased (or healthy) iPSC line, thus differences in e.g., reprogramming efficiency can be neglected, and the genetic background remains unchanged. In short, the diseased/healthy and corresponding isogenic control lines start at the same base and only differ in this specific genetic position. Isogenic control cells display the closest and most unbiased control group.

To study the role of the newly identified FLNC variant of the DCM patients within this family, iPSC lines of the diseased father and daughter were used to generate FLNC-rescue isogenic control lines using the CRISPR/Cas9 gene editing technology. The CRISPR/Cas9 gene editing technology has been shown as an efficient tool to initiate insertions, deletions, and nucleotide substitutions in several model organisms (Pickar-Oliver and Gersbach, 2019). To edit a single nucleotide, as needed for this project, a crRNA and HDR template need to be designed. The design of both is crucial for the gene editing outcome. First, the HDR template was designed as a ssDNA template of 91bp length, where the desired SNP (wildtype version) was in the center, flanked by 45bp at each site (Fig. 12). To enhance gene editing efficiency, two synonymous mutations were introduced into crRNA binding site of the HDR template, additionally the SNP repair destroyed the PAM site – both were introduced to inhibit re-cutting by the Cas9 after successful editing, as the binding of the crRNA was less efficient (Fig. 12) (Paquet *et al.*, 2016). Presence of the synonymous mutations after several passages additionally can be used as sequence control over time, to ensure identity of the correct lines. Secondly, the crRNA was designed to complementary bind near the targeted sequence in order to guide the Cas9 to the mutation where the enzyme should introduce a double-strand break as close as possible to the SNP. Additionally, crRNA should be chosen regarding potential off-target binding sites within the whole genome. These were bioinformatically predicted by using the CRISPOR crRNA design tool and the Jefferson Off-Spotter. A crRNA should have as less off-target binding sites as possible, and the crRNA should bind to these off-target sites rather inefficiently. The latter can be achieved, when the crRNA only is complementary to the off-target sites when tolerating mismatches. For this gene editing approach, only crRNAs were chosen having off-target sites with at least 3 mismatches and the off-target sites were not interfering with protein coding regions. Several studies have shown that electroporation of the crRNA and the Cas9 enzyme as a RNP complex is less toxic and more efficient compared to the usage of plasmids (Liang *et al.*, 2015; Zuris *et al.*, 2015). Therefore, electroporation of a previously formed RNP complex was conducted. As it has been shown that the choice of crRNA is crucial for gene editing efficiency (Xu *et al.*, 2018; Zheng *et al.*, 2017), two different crRNA, only shifted by one nucleotide, were tested experimentally for the DCM1 iPSC line, both with the same HDR template (Fig. 12). Interestingly, the approach with the FLNC1 crRNA yielded 0% (6 analyzed clones) successfully edited but only frameshifted clones, whereas the FLNC2 crRNA yielded 37.5% (16 analyzed clones) successfully edited clones (Fig. 26). This highlights the impact of crRNA on CRISPR outcome and is in line with previously reported studies demonstrating a variable editing efficiency of 1-42% for CRISPR/Cas gene editing approaches (Paquet *et al.*, 2016; Xu *et al.*, 2018). Notably, the FLNC2 crRNA PAM site was complementary to the variant harboring triplet, which was exchanged from *GGG*

to *GCG* after HDR using the HDR template. In contrast, the FLNC1 crRNA PAM site was complementary to a sequence shifted by only one nucleotide (Fig. 12), which was changed from *GGG* to *GGC* after HDR repair. Maybe mismatches of the *NGG* PAM site at the middle position (*N**G**G*) are more crucial for PAM site/crRNA binding, than mismatches at the last position (*NG**G***). Hence, this might have prevented re-binding of the FLNC2 crRNA and subsequent re-cutting of the Cas9 more efficiently, than for FLNC1 crRNA. Recurrent binding of FLNC1 crRNA and subsequent cutting, would have increased the risk of frameshifts in this case. This is supported by findings of Zhang *et al.* (Zhang *et al.*, 2014) showing that a NGC sequence (FLNC1) is a more potent non-canonical PAM site, compared to NCG sequences (FLNC2). Based on this observation, only FLNC2 crRNA was used for gene editing of DCM3 iPSC and an editing efficiency of 50% (14 analyzed clones) was yielded (Fig. 26). In both cases, the synonymous mutation closest to the Cas9-mediated cut was introduced into the sequence and was remained even after several passages of the chosen clones (Fig. 26). We hypothesize the reason for absence of the second synonymous mutation most likely lies within the fact, that the HDR template was only used very close to the cut site.

In addition to editing efficiency, the successfully edited clones needed to be analyzed for unintended off-target effects that might have occurred due to unspecific binding of the crRNA and subsequent cutting by the Cas9 (Li *et al.*, 2019). The most comprehensive approach would be whole genome sequencing of the gene edited DCM1_res and DCM3_res clones, to identify any possible off-target effect. For off-target site prediction the Jefferson Off-Spotter website (https://cm.jefferson.edu/Off-Spotter/) was used, which searches genome wide for complementary sequences of the crRNA adjacent to a PAM site. The top 5 predicted off-targets with lowest mismatch number to the crRNA were chosen for analysis of undesired cutting (4.3.3). For off-target analysis, iPSC lines before and after CRISPR/Cas9 gene editing were analyzed by Sanger sequencing using primers designed flanking the top five predicted off-target sites (Fig. 29). The top five off-target sites showed three (*LGR4*), four (*GFPT2*, *IGSF11* and *NLRP6*) or five (*JAKMIP3*) mismatches compared to the FLNC2 crRNA. There were more off-target sites with five mismatches predicted, however, only the first suggested, *JAKMIP3*, was analyzed. Comparison of sequencing results of diseased and isogenic control iPSC lines did not reveal any off-target effect at the analyzed genomic positions (Fig. 29). Interestingly, a homozygous (DCM3 and DCM3_res) or heterozygous (DCM1 and DCM1_res) deletion, respectively, was identified in the analyzed sequence of the *GFPT2* gene, which equals the 5´UTR of the gene (Fig. 30). However, as the exact same deletions were found in corresponding iPSC lines before and after gene-editing this observation cannot be based on off-target effects. Additionally, as the deletion was homozygous in DCM3/DCM3_res and heterozygous in DCM1/DCM1_res, it can also be excluded that the result occurred due to sequencing errors of this GC-rich and highly repetitive sequence. Nevertheless, GFPT2 is an important enzyme in the glutamate metabolism and the rate-limiting enzyme in hexosamine biosynthesis pathway (Nabeebaccus *et al.*, 2021; Wang *et al.*, 2022a). GFPT2 was shown to be enriched in CFB and was associated with regulation of CFB activation and regulation of the actin cytoskeleton (Wang *et al.*, 2022a). Additionally, it was generally shown to have protective effects against oxidative stress by counteracting H_2O_2 (Wang *et al.*, 2022b; Zitzler *et al.*,

2004). Hence, the finding should not be underestimated. The identified deletion within the GFPT2 5´UTR might affect translation efficiency and hence could have direct effects onto the mentioned function in CFB and oxidative stress response. Based on this information and the finding of FLNC-independent elevated levels of ROS within the DCM1 patient it is advisable to investigate the role of this deletion within the patients' cardiomyocytes and CFB in more detail. Moreover, a heterozygous SNP (G>T) can be found in the predicted *JAKMIP3* off-target sequence for DCM1 and DCM1_res (Fig. 29). Again, as this SNP is found in iPSC before and after gene editing it is not based on any off-target effect. Additionally, as this SNP is located in an intron of *JAKMIP3* it most likely does not have any severe effect.

Three clones of the successfully edited DCM1_res and DCM3_res CRISPR approaches were randomly chosen for further analysis, respectively. To exclude, that the gene editing had any effect on pluripotency, all FLNC rescue lines were characterized for their pluripotency again. All isogenic control lines showed full pluripotency shown by expression of important markers (Fig. 27) and *in vitro* spontaneous differentiation (Fig. 28). Finally, similar to patient iPSC-cardiomyocytes, the differentiated isogenic control iPSC-cardiomyocytes cultures showed high purity (85% ± 10%), and were shown to be predominately ventricular cardiomyocytes (Fig. 31).

In summary, isogenic FLNC rescue lines of DCM1 and DCM3 could be generated successfully, showing the FLNC wildtype sequence c.6560G (p.Arg2187Arg) as demonstrated by Sanger sequencing. The gene editing approach did not introduce any off-target effects at the top five predicted off-target sites and the isogenic control iPSC remained full pluripotency. Additionally, all cell lines can be differentiated into iPSC-cardiomyocytes of high purity and correct cardiac subtype. Hence, the isogenic control cells could be used to investigate the underlying molecular cause of the DCM of the index family in more detail.

5.5 FLNC-dependent dysregulated sarcomeric structure in DCM iPSC-cardiomyocytes

The basic contractile unit of (cardio-) myocytes is the sarcomere, constructed of a highly organized, complex interaction network of several structural and regulatory proteins and being precisely connected to the sarcolemma at ICD to allow force propagation to neighboring cells (Crocini and Gotthardt, 2021; Henderson *et al.*, 2017). Hence, sarcomeres are crucial for proper cardiac contraction. Disruption of this tightly regulated multiprotein assembly often is a major phenotypic symptom of genetically inherited cardiomyopathies, like DCM and HCM (Frazier *et al.*, 2011; Hassoun *et al.*, 2021) and was even identified as a distinguishable phenotype in diseased iPSC-derived cardiomyocytes (Eschenhagen and Carrier, 2019). To assess sarcomeric regularity within iPSC-cardiomyocytes of diseased and healthy family members, IF staining of Z-disc located α-actinin and the M-line localized proportion of titin were generated and quantified using FFT and radial profiling. These analyses revealed a significantly decreased sarcomeric regularity in iPSC-cardiomyocytes of the diseased father (DCM1) and daughter (DCM3) in comparison to healthy family members, external controls, and isogenic controls in both – Z-disc (α-actinin) and M-line

(titin M) (Fig. 24). This suggests, a FLNC-dependent cause for the identified sarcomeric disarray detected in the diseased iPSC-cardiomyocytes. However, the exact molecular mechanism affected by the FLNC variant inducing the sarcomeric disarray remains to be elucidated. These results are in line with several studies reporting associations of FLNC-dependent cardiomyopathies and sarcomeric disarrays as major molecular symptom (Eden and Frey, 2021; Mao and Nakamura, 2020; Verdonschot *et al.*, 2020). Thus, a sarcomeric disarray, typically described for DCM, can be technically visualized with the applied iPSC-cardiomyocytes system. The identified FLNC variant is located in a unique 82aa insertion of domain 20, which on the one hand is crucial for targeting FLNC to the Z-disc and on the other hand is necessary for the interaction of FLNC with several sarcomeric proteins. Accordingly, the loss of sarcomeric integrity found in iPSC-cardiomyocytes of the diseased family members may be based on misexpression/mislocalization of the FLNC protein itself or on particular disturbed interaction of FLNC to one or several sarcomeric proteins due to the amino acid substitution from arginine to proline. To analyze these possibilities, expression and localization of FLNC was analyzed (Fig. 36, Fig. 37). These analyses show no dysregulated expression of FLNC in diseased iPSC-cardiomyocytes compared to external controls, healthy family members or isogenic controls neither on mRNA nor on protein level (Fig. 36). Additionally, IF staining of FLNC show FLNC localization to sarcomeric-like structures as well as an accumulation at ICD in primary NF myocardium or cell-cell contacts in control iPSC-cardiomyocytes (Fig. 37), as described in the literature (Mao and Nakamura, 2020). Moreover, a similar expression pattern could be observed in primary DCM1 myocardium and diseased DCM1 and DCM3 and isogenic control DCM1_res and DCM3_res iPSC-cardiomyocytes (Fig. 37). These findings highlight two things: (1) FLNC indeed is expressed in iPSC-cardiomyocytes and localizes similarly within the iPSC-cardiomyocytes as shown in primary, adult cardiomyocytes, hinting to a more mature iPSC-cardiomyocytes phenotype than described in the literature. (2) Since no obvious FLNC mislocalization can be observed neither in primary nor in iPSC-derived DCM cardiomyocytes compared to non-failing/(isogenic) control (iPSC-) cardiomyocytes, the identified variant does not influence FLNC expression and localization. Hence, the dysregulated sarcomeric structure is not driven by altered expression or mislocalization of FLNC itself, making it more likely, that certain interactions to specific binding partners could be impaired. Interactions dependent on binding to domain 20 and its 82aa insertion include proteins like xin (van der Ven *et al.*, 2006), aciculin (Molt *et al.*, 2014), myotilin (van der Ven *et al.*, 2000) and myopodin (Linnemann *et al.*, 2010) (Fig. 5). However, mRNA expression of FLNC interaction partners xin, aciculin, myotilin or myopodin was not significantly changed compared to controls (Fig. 38 A-C). Still, a clear prove for an affected protein-protein interaction based on the identified FLNC variant is missing. Potentially impaired interactions need to be assessed in future experiments. This first would include Western blot analysis of DCM1 myocardium, like for the iPSC-cardiomyocytes, to support or oppose the iPSC-cardiomyocyte data that no interaction partner show differential expression. Furthermore, *in silico* binding prediction analysis could identify potentially affected interactions in more detail. Additionally, quantitative mass spectrometry approaches to identify changes in protein-protein interactions mediated by the FLNC variant on a global scale (Urban, 2016) could be conducted. These data could be supplemented by pull down

assays to analyze potential effects onto specific interactions with proteins, like xin, aciculin, myotilin or myopodin.

Taken together, using the iPSC-cardiomyocytes model a significant FLNC-dependent sarcomeric disarray could be identified as major phenotypical result of the FLNC-associated DCM within the index family. This characterizes the generated iPSC-cardiomyocytes as a suitable disease model. However, neither expression nor localization of FLNC itself is impaired. Hence, most likely the dysregulated sarcomeric structure is based on impaired interaction to important binding partners due to the identified variant.

5.5.1 Restored sarcomeric regularity enhances iPSC-cardiomyocyte maturation

It is known that iPSC-derived cardiomyocytes usually only represent an immature phenotype and do not resemble adult cardiomyocytes (Koivumaki *et al.*, 2018; Kolanowski *et al.*, 2017; Yoshida and Yamanaka, 2017). Although cardiomyocytes maturation was not a focus within this project, iPSC-cardiomyocytes were always cultured for ~90 days prior to analysis to increase their maturation state, since long-term culture was shown to enhance maturation of iPSC-cardiomyocytes (Lewandowski *et al.*, 2018).

After long-term culture, obtained iPSC-cardiomyocytes displayed a rather circular cell shape, which is resembling a cell shape of neonatal cardiomyocytes rather than a uniformly oblongness shape of mature/adult cardiomyocytes (Skorska *et al.*, 2022). Additionally, during prolonged culture iPSC-cardiomyocytes show reduction of their proliferation potential and 90-days cultured cells often are multinucleated. The proliferation potential of *in vivo* cardiomyocytes decreases with increasing maturation state, resulting in a final exit from the cell cycle in adult cardiomyocytes. Since mature cardiomyocytes do not undergo cell division after DNA replication, polyploid cells are generated. *In vivo*, polyploidy can only be observed from early neonatal states on (Bishop *et al.*, 2022; Wang *et al.*, 2022c). Hence, our generated multinucleated iPSC-cardiomyocytes at least demonstrate a rather neonatal, than the often-postulated fetal maturation state. Furthermore, upon differentiation, functional beating iPSC-cardiomyocytes were generated. These were capable of Ca^{2+} excitation-contraction coupling, as shown by FURA-2 and Fluo-4 measurements (4.5.1), displaying a certain level of maturation. However, these iPSC-cardiomyocytes did show spontaneous beating, which is absent in adult cardiomyocytes (Wang *et al.*, 2022c). During cardiomyocyte maturation, especially maturation of myofibrils is a major hallmark, important for life-long efficient heart contraction. This includes maturation of the sarcomeres, characterized by robust alignment of the different players within an individual sarcomere, expansion of the myofibril network and proper alignment of several sarcomeres to each other (Guo and Pu, 2020). Generated control iPSC-cardiomyocytes display a distinct sarcomere structure including highly repeatedly appearing Z-disc and M-line structures, as shown by IF staining of α-actinin or titin (Fig. 22). For diseased iPSC-cardiomyocytes, however, a FLNC-dependent sarcomeric disarray was identified, as previously described. Furthermore, the sarcomere protein FLNC was shown to be expressed at the Z-disc and was accumulating at cell-cell interactions, mimicking ICD, and hence was expressed similarly as reported for adult cardiomyocytes (Mao and

Nakamura, 2020; Pruna and Ehler, 2020) (Fig. 37). Although a clear sarcomere structure is displayed in prolonged-cultured iPSC-cardiomyocytes within this project, an evenly vertical alignment, like in mature cardiomyocytes could not be achieved, as shown by IF analysis of α-actinin or titin (Fig. 22).

During the process of sarcomere maturation an isoform switch of several sarcomere players from a fetal to an adult isoform can be observed. One of this is the isoform switch from the predominant expression of α-MHC (encoded by *MYH6*) in the fetal heart to the predominant expression of βMHC (encoded by *MYH7*) in the adult heart (Guo and Pu, 2020; Reiser *et al.*, 2001; Zhao *et al.*, 2020b). A *MYH6-to-MYH7* isoform switch in iPSC-cardiomyocytes upon prolonged 2D culture was demonstrated as well (Eschenhagen and Carrier, 2019; Zhao *et al.*, 2020b), which can be used as a measure of (iPSC-) cardiomyocyte maturation state. Therefore, in this work, the expression levels of *MYH6* and *MYH7* in diseased and external and isogenic control iPSC-cardiomyocytes were analyzed and a *MYH7/MYH6* ratio was calculated. *MYH6* expression was slightly upregulated in both – DCM1 and DCM3 iPSC-cardiomyocytes – compared to corresponding isogenic control iPSC-cardiomyocytes (Fig. 35). Additionally, *MYH7* expression was decreased in diseased iPSC-cardiomyocytes – DCM1 and DCM3 – compared to corresponding isogenic control cells (Fig. 35). Both relative expression levels resulted in a decreased *MYH7/MYH6* ratio of diseased iPSC-cardiomyocytes – DCM1 and DCM3 – representing a lower maturation state (Fig. 35). This is in line with other studies, reporting a decreased *MYH7/MYH6* ratio in iPSC-cardiomyocytes of DCM patients (Eschenhagen and Carrier, 2019). As the *MYH7/MYH6* ratio increases upon FLNC rescue, it can be concluded that the enhancement of iPSC-cardiomyocytes maturation is FLNC-dependent. The reduced *MYH7/MYH6* ratio of the diseased iPSC-cardiomyocytes, on the other hand, could be accounted as a disease phenotype. Distinction of a maturation defect, or a specific disease phenotype remains difficult with the iPSC-cardiomyocytes system and needs to be investigated in the future. As mentioned, the *MYH6-to-MYH7* isoform switch occurs during the sarcomere maturation, which includes generation of a robust sarcomere structure. The diseased iPSC-cardiomyocytes are characterized by loss of sarcomeric integrity, which is rescued in a FLNC-dependent manner in isogenic control cells. Hence, the FLNC-dependent sarcomeric disarray seems to influence the iPSC-cardiomyocytes maturation state and could be an additional disease marker.

In summary, the iPSC-cardiomyocytes generated within this project display several characteristics rather pointing towards a neonatal maturation state, than resembling the often-postulated fetal maturation state. Hence, prolonged culture of iPSC-cardiomyocytes does enhance the iPSC-cardiomyocytes maturation state. However, the *MYH7/MYH6* ratio, a measure for cardiomyocyte maturation and disease, is decreased in diseased iPSC-cardiomyocytes but can be enhanced upon FLNC rescue. Diseased iPSC-cardiomyocytes display a severe sarcomeric disarray, which can be restored by FLNC rescue. Combining both, it can be concluded, that the effect of the FLNC variant on the sarcomeric structure also influences the maturation state of the iPSC-cardiomyocytes.

5.5.2 FLNC-dependent reduction in cell size of DCM1 iPSC-cardiomyocytes as a consequence of sarcomeric disarray

In rare cases DCM can occur in mixed forms with HCM (Blagova *et al.*, 2020). Both cardiomyopathy types often present with similar symptoms like leg swelling or shortness of breath, based on inefficient blood pumping of the heart. However, this impairment of proper heart function is based on different structural changes of the heart. Where the DCM heart is characterized by dilation of the left ventricle due to thinner ventricular walls and elongated muscle fibers, HCM, in contrast, is characterized by reduction of the left ventricular chamber size due to asymmetric thickening of the septum and ventricular walls (Ciarambino *et al.*, 2021; Cirino and Ho, 1993; Hershberger and Jordan, 1993). To achieve this wall thickening, cardiomyocytes increase in size, due to the absence of proper cell proliferation in the adult heart. Hence, cardiomyocyte size can be used as a distinguishable factor for DCM and HCM on a cellular level, including iPSC-cardiomyocytes (Eschenhagen and Carrier, 2019). Hence, cell size of iPSC-cardiomyocytes of all family members was analyzed to test for hypertrophic phenotypes. This was of special interest as in addition to the potentially disease-causing variants in *ILK* and *FLNC* genes, SNPs in *MYBPC3* and *MYH7* were identified (4.1.2). Variants in *MYBPC3* and *MYH7* more often are associated with HCM than DCM. However, the identified *MYBPC3* and *MYH7* variants within this project, were classified as benign and should not have a severe impact on the disease phenotype. To ensure comparability, same cell densities were plated and cultured for exactly 10 days to allow the cells having enough space to spread to full cell size. Additionally, cell size was analyzed in 3D using the CASY cell counter and analyzer, since it was postulated to be more informative compared to pure 2D analysis (Eschenhagen and Carrier, 2019). In general, these analyses revealed huge differences in cell size (peak and mean diameter) of the analyzed iPSC-cardiomyocytes (Fig. 25). First, iPSC-cardiomyocytes of the healthy daughter (DCM4) displayed comparable cell size to external controls (Fig. 25). Cells of the diseased father (DCM1) showed significantly smaller cells compared to external controls (Fig. 25). In contrast to this, iPSC-cardiomyocytes of healthy mother (DCM2) and diseased daughter (DCM3) displayed significantly increased cell size (Fig. 25). Additionally, when comparing cell size of DCM and corresponding isogenic control iPSC-cardiomyocytes, the observed reduced cell size of DCM1, can significantly be restored to a size of external controls in FLNC-rescue isogenic control DCM1_res (Fig. 34). Particularly, as a significant rescue of cell size can be observed upon FLNC-rescue in isogenic control DCM1_res iPSC-cardiomyocytes, the decrease in cell size of DCM1 iPSC-cardiomyocytes might be based on the FLNC-dependent sarcomeric disarray (4.2.1; 4.3.6; 5.5). Due to FLNC-rescue the sarcomere can assemble properly again which gives structure and stability to the individual cardiomyocyte, maybe ultimately leading to expansion of cell size. In contrast to this, significantly increased cell size of DCM3 iPSC-cardiomyocytes is not changed upon FLNC-rescue (Fig. 34). Additionally, a similar increase in cell size can be observed in iPSC-cardiomyocytes of the healthy mother (Fig. 34). Most likely, some endogenous mechanism, probably inherited from maternal origin, is actively increasing the cardiomyocyte size of DCM3. If this in fact leads towards a pathological hypertrophic phenotype, remains arguable, since the healthy mother does not show any cardiac phenotype, but displays similar increased cardiomyocyte size. Increased cell size might be in the scope of naturally

occurring variances. Nevertheless, it might be a potential co-driver in disease progression of the diseased daughter, since the DCM and accompanied heart transplantation occurred with incredibly young age, making it likely that the DCM was driven by additional factors in comparison to the diseased father. Some studies postulate an association of increased cardiomyocyte cell size with defects in signal conduction between cells (Spach *et al.*, 2004). Hence, investigating conduction defects in iPSC-cardiomyocytes of healthy mother and daughter, could unravel if increased cardiomyocyte size has a pathological effect. The microelectrode array (MEA) system could be used to analyze for such changes in conduction kinetics in iPSC-cardiomyocytes. Furthermore, it cannot be ruled out entirely that the observed differences in cell size might be based on drawbacks using the iPSC-cardiomyocytes cell system or by differences in reprogramming. DCM1 iPSC were reprogrammed from fibroblasts, whereas iPSC from mother and daughters were reprogrammed from PBMC. This could only be excluded by comparative analysis of cell size of cardiomyocytes of primary tissue – which is, for obvious reasons, not available.

In summary, different cell size phenotypes in the two DCM patients – DCM1 and DCM3 – can be observed. DCM1 iPSC-cardiomyocytes show significantly reduced cell size compared to external controls, which can be rescued in a FLNC-dependent manner in isogenic control cells. This might be driven by a restored sarcomeric regularity upon *FLNC*-rescue. In contrast to this, DCM3 shows significantly enlarged iPSC-cardiomyocytes, which cannot be reduced by *FLNC*-rescue. This could be a first hint, towards the explanation why the DCM occurred at tremendous different age of father and daughter.

5.6 Downregulation of CX43 as a marker for heart failure

GJ, localized in the cell membrane of cardiomyocytes, are crucial for electrical coupling, since they connect the cytoplasm of neighboring cells (Rodriguez-Sinovas *et al.*, 2021). GJ are made of several connexons (or hemichannels), which in turn are formed by six connexins each (Rodriguez-Sinovas *et al.*, 2021). The most important connexin of the left ventricle is CX43 (Kostin *et al.*, 2003; Rodriguez-Sinovas *et al.*, 2021). GJ remodeling often is observed in the failing human heart (Dupont *et al.*, 2001; Kostin *et al.*, 2003; Severs *et al.*, 2004). To investigate, whether a GJ remodeling phenotype can be observed in analyzed DCM iPSC-cardiomyocytes CX43 expression and localization was analyzed. Western blots showed a downregulation of CX43 on protein level in diseased iPSC-cardiomyocytes compared to external controls (Fig. 39). This effect could not be restored in isogenic controls (Fig. 39). Nevertheless, downregulation of CX43 in DCM1 and DCM3 iPSC-cardiomyocytes on protein level is in line with previously published data (Dupont *et al.*, 2001; Kostin *et al.*, 2003; Severs *et al.*, 2004). Additionally, in DCM hearts this downregulation is associated with an abnormal distribution of CX43 in myocytes which are close to areas of fibrosis or display a sarcomeric disarray (Kostin *et al.*, 2003). In these areas, CX43 localization to the ICD within the myocytes was highly disrupted and localized towards lateral regions of the myocytes. This was associated with increased arrhythmogenicity and contractile dysfunction. Nevertheless, IF staining of iPSC-cardiomyocytes an accumulation of CX43 at cell-cell contacts (Fig. 39) and there was no obvious difference in localization detectable between the different iPSC-cardiomyocytes analyzed (Fig. 39). This is more

comparable, with healthy cardiomyocytes, where GJ are mainly localized to the cellular poles, accumulating in the ICD (Rodriguez-Sinovas *et al.*, 2021). However, since iPSC-cardiomyocytes are rather round shaped than elongated, classification of polarly ICD and lateral membrane regions is difficult. Hence, IF staining of NF and DCM1 explanted myocardium, similar to titin and FLNC staining, should be conducted in the future. This could more clearly identify potential mislocalization of CX43 away from the polarly ICD. In general, IF staining only allows to identify differences in protein localization, subtle differences in protein expression on a cellular level cannot be analyzed with this method. Hence, it cannot be excluded that the observed reduced protein expression shown, would also be reflected within the iPSC-cardiomyocytes on cellular level. This would require methods with high-resolution (STED) and subsequent high-sensitive quantification and should be investigated in the future. Interestingly, downregulation of CX43 in heart failure conditions and cardiomyopathies was shown to be induced by elevated levels of mitochondrial oxidative stress (Liu *et al.*, 2022a; Sovari *et al.*, 2013; Yang *et al.*, 2014b). In more detail, these studies show, that upon chronic activation of the renin-angiotensin-aldosterone system and increasing levels of AngII, often shown in heart diseases, mitochondrial ROS production increases. Increased mitochondrial ROS will activate the tyrosine kinase Src (c-Src), which in turn will reduce CX43 at the ICD. This will increase the risk for arrhythmias due to impaired electrical propagation between the cells (Liu *et al.*, 2022a; Sovari *et al.*, 2013; Yang *et al.*, 2014b). This described mechanism would be in line with the finding of increased ROS production in DCM1 iPSC-cardiomyocytes (Fig. 47), that can be treated with Entresto. Entresto contains valsartan, which acts as an angiotensin type I (AT1) receptor antagonists and thus inhibits downstream AngII signaling, that was reported to increase levels of mitochondrial ROS. Additionally, downregulation of CX43, within this project was shown on protein level only, and could not be recapitulated on mRNA level. This would be in line, with a c-Src-dependent posttranslational reduction of CX43 (Liu *et al.*, 2022a; Sovari *et al.*, 2013). Furthermore, DCM1 iPSC-cardiomyocytes also show slightly increased CASPF, as an indicator for a pro-arrhythmogenic potential. Based on these findings, it would be advisable to analyze mitochondrial ROS production in more detail. Additionally, an arrhythmogenic potential of diseased iPSC-cardiomyocytes could be further investigated using the MEA system in future experiments. All analysis should be performed under basal conditions as well as after Entresto or valsartan treatment, to analyze for direct effects of the renin-angiotensin-aldosterone system. Expression analysis of CX43 on protein level after Entresto/Valsartan treatment, could unravel a direct link between elevated mitochondrial ROS and arrhythmia in the diseased iPSC-cardiomyocytes.

In summary, the downregulation on protein level might reveal a role of CX43 remodeling within the pathophysiology of this DCM, which is not directly FLNC-dependent. Most likely, as reported in the literature (Kostin *et al.*, 2003; Spach *et al.*, 2004), this would be an effect on signal conduction between the cells, probably increasing an arrhythmogenic potential, like shown for DCM1 iPSC-cardiomyocytes. Based on literature (Sovari *et al.*, 2013), as well as on findings of increased ROS production in DCM1 iPSC-cardiomyocytes within this project, CX43 downregulation might be induced by mitochondrial ROS.

5.7 Aberrant Ca^{2+} handling in DCM iPSC-cardiomyocytes

The conversion of electrical stimuli into mechanical contraction of individual cells, muscle fibers and finally the whole heart, marks the central mechanism of heart function. Besides the need for proper sarcomeric structure to conduct mechanical contraction, upstream processes to initiate this mechanical contraction are necessary. The overall process is known as excitation-contraction coupling (Eisner *et al.*, 2017). It is driven by changing concentrations of the second messenger molecule Ca^{2+} within the cardiomyocytes during systolic and diastolic phases (Eisner *et al.*, 2013; Eisner *et al.*, 2017; Eisner *et al.*, 1998). To allow proper function a highly regulated network of different proteins and signaling molecules needs to be orchestrated in spatial and functional means (Eisner *et al.*, 2017; Eisner *et al.*, 2020; Eisner *et al.*, 1998). In accordance with this, heart failure conditions, usually characterized by contractile dysfunction, often are accompanied by dysregulated Ca^{2+} handling (Lou *et al.*, 2012; Roe *et al.*, 2015). To investigate the DCM phenotype of the index family further, Ca^{2+} homeostasis and kinetics were analyzed for diseased and isogenic control iPSC-cardiomyocytes on a functional level by Fluo-4 and FURA-2 measurements. These functional measurements were complemented by molecular analysis on mRNA and protein level.

5.7.1 Reduced transient Ca^{2+} amplitude and slower Ca^{2+} kinetics as a hallmark of DCM phenotype improve upon FLNC rescue

In general, FURA-2 measurements revealed decreased systolic Ca^{2+} (represented by Ca^{2+} transient amplitude, Fig. 43 B) in diseased iPSC-cardiomyocytes of DCM1 and DCM3 patients, which is in line with reported observations in other studies of myocytes and tissue explanted from patients with heart failure or DCM (Lou *et al.*, 2012; Sen *et al.*, 2000). This effect is less prominent in DCM1 iPSC-cardiomyocytes (Fig. 43 B) but in tendency is reversed upon FLNC rescue. In DCM3 iPSC-cardiomyocytes the systolic Ca^{2+} is significantly reduced, however it is not restored by FLNC rescue (Fig. 43 B). In addition to decreased systolic Ca^{2+} content in diseased iPSC-cardiomyocytes, FURA-2 and Fluo-4 analysis revealed slowed Ca^{2+} kinetics in diseased iPSC-cardiomyocytes in general. This phenotype is supported as being relevant by data demonstrating reduced Ca^{2+} kinetics in cells and tissue explanted from heart failure/DCM patients (Beuckelmann *et al.*, 1992; Piacentino *et al.*, 2003; Sen *et al.*, 2000). Rise time of the Ca^{2+} amplitude (represented as time to peak) is increased (slowed) in both – FURA-2 and Fluo-4 – analysis for diseased iPSC-cardiomyocytes (Fig. 43, Fig. 44). When comparing rise time of the corresponding isogenic control lines, FURA-2 showed a decrease in rise time for both, DCM1_res and DCM3_res, respectively (Fig. 43). Fluo-4 analysis only revealed a significant rescue of rise time in DCM1_res isogenic control iPSC-cardiomyocytes compared to DCM1 (Fig. 44).

The reduced systolic Ca^{2+} in general is based on a reduction of Ca^{2+} release from the SR or from the extracellular space (Roe *et al.*, 2015). This might be caused by decreased SR Ca^{2+} content. In addition to decreased SR Ca^{2+} content, impaired release of the Ca^{2+} from the SR could be causative for reduced systolic Ca^{2+} and increased rise time as well. This for example could include decreased activity of RYR2 or LTCC (Eisner *et al.*, 1998; Roe *et al.*, 2015). SR calcium content was analyzed by addition of caffeine, releasing all Ca^{2+} from the SR by

opening all RYR2. However, it was not decreased in diseased iPSC-cardiomyocytes compared to external or isogenic controls (Fig. 43 F). RYR2 was evaluated on protein level, and neither downregulation of basal RYR2, nor downregulation of activating RYR2 phosphorylation could be observed (Fig. 41). However, it should be noted that due to the high molecular weight, detection, and quantification of RYR2 and its phosphorylation states by Western blotting is difficult at basal conditions. More technical replicates should be performed to validate the findings. LTCC expression was not analyzed within this project and needs to be analyzed in future experiments. However, not only the expression of RYR2 and LTCC are important for fast and strong SR Ca^{2+} release, but also their spatial organization. In human myocardium t-tubules are formed close to the Z-disc. This allows close contact of t-tubule membrane, with integrated LTCC and the SR harboring the RYR2. This structure is called the cardiac dyad, bringing clusters of LTCC in proximity with clusters of RYR2 (Eisner *et al.*, 2017; Roe *et al.*, 2015). Disruption of t-tubule organization in heart failure, hence, is described to be causative for reduced systolic Ca^{2+} content and increased rise time (Roe *et al.*, 2015). Yet, a mature t-tubule organization is described to be lacking in iPSC-cardiomyocytes and cannot be disrupted (Cadet and Kamp, 2017). Smaller size of iPSC-cardiomyocytes compared to adult cardiomyocytes can compensate for t-tubule absence in healthy iPSC-cardiomyocytes. However, not only the t-tubule system is crucial for spatial organization within the cardiomyocytes, but at least similar important is the highly regulated sarcomeric structure which orchestrates the localization of many (Ca^{2+}) proteins within the cardiomyocytes (Crocini and Gotthardt, 2021; Gautel and Djinovic-Carugo, 2016). Diseased iPSC-cardiomyocytes of DCM1 and DCM3 patients display highly dysregulated, if not total absence of sarcomeric structure. Maybe this spatial disorganization accounts for decreased systolic Ca^{2+} content and increased rise time in a similar way as disruption of t-tubule organization. At least it is conceivable, that due to the absence of decent sarcomere structure, several proteins important for Ca^{2+} handling, including RYR2 usually closely localized to the Z-disc, are inadequately located within the cardiomyocytes, hampering efficient Ca^{2+} signaling. FLNC rescue restores the sarcomeric regularity, suggesting that proteins can align properly and Ca^{2+} signaling is restored, including increase in systolic Ca^{2+} content and faster rise time.

In addition to rise time, decay time (represented as relaxation time in FURA-2 measurements), was increased (slowed) as well in diseased iPSC-cardiomyocytes in both analyses. Decay time is largely determined by SERCA and NCX activity (Roe *et al.*, 2015). SERCA expression and activity was shown to be significantly upregulated in DCM3 iPSC-cardiomyocytes on mRNA, protein and functional level (Fig. 41, Fig. 42, Fig. 45). However, upregulation of SERCA activity is contradictory to increased decay time and will be discussed later (5.7.3). No changes of SERCA expression and activity were observed in DCM1 iPSC-cardiomyocytes (Fig. 41, Fig. 42, Fig. 45). NCX was significantly downregulated on protein level in DCM3 iPSC-cardiomyocytes compared to control iPSC-cardiomyocytes. In isogenic control DCM3_res iPSC-cardiomyocytes NCX expression was slightly increased, compared to DCM3 cells. Hence, NCX could be a contributor for slowed decay time. However, similar to slowed rise time, slowed decay time might also be driven by destroyed sarcomeric structure based on the FLNC variant. The resulting mislocalization of important

proteins, might also slow down the removal of Ca^{2+} from the cytoplasm in the diastolic phase.

In summary, analysis of Ca^{2+} handling and kinetics revealed a reduced systolic Ca^{2+} and slowed Ca^{2+} kinetics (rise and decay) in diseased iPSC-cardiomyocytes of DCM1 and DCM3, which is in accordance with previously reported effects for DCM. Isogenic controls show partially restored systolic Ca^{2+} and Ca^{2+} kinetics. The major structural phenotype of diseased iPSC-cardiomyocytes, which is rescued in isogenic controls, the sarcomeric disarray, might be a critical factor for dysregulated Ca^{2+} handling.

5.7.2 CaMKIIδ-dependent phosphorylation of RYR2 and PLN in DCM1 iPSC-cardiomyocytes to compensate for slower Ca^{2+} kinetics

Intracellular Ca^{2+} handling is regulated by phosphorylation and/or dephosphorylation of several important proteins (Eisner *et al.*, 2013). This includes regulation of RYR2 via phosphorylation. Phosphorylation at position RYR2-S2808 is mediated by PKA, whereas phosphorylation at position RYR2-S2814 is mediated by CaMKIIδ (Danila and Hamilton, 2004). Increase in RYR2 phosphorylation is associated with higher RYR2 open probability and often is seen in heart failure (Roe *et al.*, 2015). Western blots revealed increased CaMKIIδ-dependent phosphorylation at RYR2-S2814 in DCM1 iPSC-cardiomyocytes, which was partially rescued in isogenic control cells (Fig. 40). Interestingly, Fluo-4 analysis showed slightly increased CASPF in DCM1 iPSC-cardiomyocytes, which was reduced in isogenic control iPSC-cardiomyocytes (Fig. 46). Ca^{2+} sparks in turn are promoted by CaMKIIδ-dependent RYR-S2814 phosphorylation, which is in line with our results (Ai *et al.*, 2005; Guo *et al.*, 2006). In addition to RYR2, PLN activity is regulated by phosphorylation. PLN is an inhibitor of SERCA function. Phosphorylation will inactivate this inhibitor function and increase SERCA activity. Similar to RYR2, phosphorylation of PLN can be either mediated by PKA (PLN-S16) or CaMKIIδ (PLN-T17) (Mattiazzi *et al.*, 2005). Western blots showed an increased CaMKIIδ-dependent PLN phosphorylation at position PLN-T17 of DCM1 iPSC-cardiomyocytes, which was slightly rescued in isogenic control DCM1_res (Fig. 40). Additionally, qPCR analysis showed statistically significant downregulation of basal PLN in DCM1 and DCM1_res (Fig. 42). A similar trend can be seen on protein level (Fig. 40). Taken together, increased CaMKIIδ-dependent phosphorylation of RYR2 (direct activation of RYR2) and PLN (indirect activation of SERCA) as well as downregulation of total PLN will promote fastened Ca^{2+} kinetics. However, this is contradictory to functional analysis of Ca^{2+} handling, which revealed slower Ca^{2+} kinetics. Hence, upregulated phosphorylation of both might be a compensatory effect to counteract slower Ca^{2+} kinetics and maintain a minimal proper Ca^{2+} handling. This is at least supported by partial rescue of RYR2-S2814 and PLN-T17 phosphorylation in isogenic control cells. As in both cases, RYR2 and PLN, a CaMKII-dependent upregulation of phosphorylation could be observed, it is reasonable that CaMKIIδ activity must be upregulated. However, CaMKIIδ expression is not upregulated on protein level for DCM1 iPSC-cardiomyocytes (Fig. 42) but demonstrated to be regulated by posttranslational modifications as oxidation and phosphorylations. Since ROS was elevated in DCM1, we hypothesized an increase in oxidation of CaMKIIδ, which was not confirmed by Western blot analysis (Fig. 40). If CaMKIIδ activity might be regulated by phosphorylation

needs to be elucidated in future studies and could not be completed in this study because of technical issues.

5.7.3 Increased SERCA activity in DCM3 affects alterations in Ca^{2+} handling

Analyzing Ca^{2+} handling of iPSC-cardiomyocytes of the diseased daughter (DCM3) revealed a significant upregulation of SERCA expression on mRNA and protein level (Fig. 41, Fig. 42). Additionally, SERCA activity was shown to be increased compared to isogenic control iPSC-cardiomyocytes by FURA-2 measurements (Fig. 43). Both, expression and activity, were rescued in isogenic control iPSC-cardiomyocytes (Fig. 41, Fig. 42, Fig. 43). SERCA (more precisely SERCA2a, the cardiac specific isoform) is located in the SR membrane and is important for Ca^{2+} recycling from the cytoplasm back to the SR to induce myocardial relaxation (Park and Oh, 2013). SERCA2a interacts with several different proteins, which influence the SERCA2a activity state (Kranias and Hajjar, 2012; Park and Oh, 2013). A major regulator of SERCA2a activity is PLN. SERCA2a and PLN form a tight interaction complex, and in its unphosphorylated state PLN has an inhibitory function on SERCA2a activity (Kranias and Hajjar, 2012). However, no increase in PLN phosphorylation or a downregulation of total PLN in DCM3 iPSC-cardiomyocytes could be observed in this study. Hence, increased SERCA2a activity as seen in DCM3 iPSC-cardiomyocytes, could not be explained by PLN phosphorylation or a downregulation of total PLN (Fig. 42). Additionally, despite a significant increase in SERCA2a expression and activity, Ca^{2+} kinetics are slowed down. In this study, slower Ca^{2+} kinetics may be explained predominantly as a result of dysregulated sarcomere organization as described above (5.7.1). Upregulated SERCA2a can also affect Ca^{2+} handling, as we observed a faster relaxation time in DCM3 compared to isogenic lines as well as slightly increased SR Ca^{2+} content (Fig. 43, Fig. 44). Molecular analysis demonstrated decreased NCX expression and decreased PLN-T17 phosphorylation in DCM3 iPSC-cardiomyocytes compared to external controls with partial rescue in isogenic control iPSC-cardiomyocytes (Fig. 41). Hence, these two mechanisms (decreased NCX expression and decreased PLN-T17 phosphorylation) might be compensatory effects to counteract the extremely upregulated SERCA2a activity. In general, increased SERCA2a expression and activity in DCM3 iPSC-cardiomyocytes seems to have an (compensatory) effect on slowed Ca^{2+} kinetics but is not the cause for observed aberrant Ca^{2+} handling. But it is still unclear what comes first.

So far, most studies reported unchanged or even decreased expression and activity of SERCA2a in patients with DCM (Meyer *et al.*, 1995; Schwinger *et al.*, 1995). Thus, the finding of observed increased SERCA2a on expression and activity level is contradictory to previous findings. It might be a simple secondary, compensatory effect, to counteract the slower Ca^{2+} kinetics. However, upregulated SERCA2a expression is restored in FLNC-rescue isogenic control iPSC-cardiomyocytes back to control level on mRNA and protein level, whereas Ca^{2+} handling remains partially impaired. Hence, there also might be an FLNC-dependent regulation of SERCA2a activity in DCM3 iPSC-cardiomyocytes.

To add an additional level of complexity, the DCM patients within this family not only harbor the described FLNC variant, but also an ILK variant, which was classified as “likely-pathogenic” as well (4.1.2). Hence, an FLNC-dependent regulation of SERCA2a activity

might be supported by recent findings, where patients with FLNC-dependent arrhythmogenic cardiomyopathy showed dysregulation of ILK signaling pathways (Hall *et al.*, 2020). ILK is a multifunctional protein, with roles in signal transduction and protein scaffolding by diverse protein interactions (Gorska and Mazur, 2022). On the one hand, FLNC-dependent altered ILK signaling negatively impacts cell adhesion and actin cytoskeleton organization (Hall *et al.*, 2020). On the other hand, further studies discovered that ILK forms a scaffolding complex with SERCA2a and PLN at the Z-disc and there might be regulation of SERCA2a expression by ILK (Traister *et al.*, 2014). Based on these general findings, there might be two levels of FLNC-dependent ILK regulation leading to upregulated SERCA2a. Either, the FLNC variant affects ILK signaling in an unknown way, resulting in upregulation of SERCA2a expression. Or, and more relatable, the FLNC-dependent sarcomeric dysregulation disrupts the ILK-SERCA2a-PLN scaffolding complex, which in an unknown way would lead to upregulation of SERCA2a expression/activity. This might be due to a loss of a regulatory/inhibitory effect of ILK on SERCA2a. Due to FLNC-rescue, the sarcomere structure would be restored, the ILK-SERCA2a-PLN complex would be formed again, and SERCA2a expression would be restored. So far, it is unclear if the ILK variant contributes to the DCM phenotype and how or if ILK and FLNC variants influence each other. However, there are studies reporting ILK/FLNC overlaps and ILK/SERCA2a interactions. Hence, it would be worth, analyzing this in more detail to unravel the complete underlying DCM pathophysiology within this family.

In summary, the identified upregulation of SERCA2a in iPSC-cardiomyocytes of the diseased daughter does influence Ca^{2+} kinetics but is not the underlying cause for altered Ca^{2+} handling. The SERCA2a upregulation seems to be FLNC-dependent, however, how the FLNC variant leads to SERCA2a upregulation remains unclear. This upregulated SERCA2a activity in iPSC-cardiomyocytes of the diseased daughter highlights an additional difference compared to the diseased father and may provide a potential cause for early disease onset.

5.8 FLNC-independent elevated levels of ROS in DCM1 iPSC-cardiomyocytes can be treated with the Angiotensin Receptor-Neprilysin Inhibitor Entresto

ROS display a group of oxygen containing, highly reactive chemical species. This includes O_2^-, OH^- and H_2O_2. Low levels of ROS occur under physiological conditions and have important roles to maintain different levels of cell homeostasis (D'Oria *et al.*, 2020; Munzel *et al.*, 2015). However, due to dysregulation of the balance of production of ROS and the removal by the antioxidant defense machinery, high levels of ROS can occur, which is called oxidative stress (D'Oria *et al.*, 2020). Cardiomyopathies, like DCM, can be accompanied by increased levels of oxidative stress (Munzel *et al.*, 2015; Sam *et al.*, 2005). This often is a consequence of cardiac remodeling and contractile dysfunction, which can be caused by mutations in sarcomere proteins (Lynch *et al.*, 2015). To evaluate if the FLNC missense mutation in DCM1 and DCM3 impacts the generation of oxidative stress in these patients, the amount of H_2O_2, as most prominent indicator of oxidative stress, was assessed by the AmplexRed Hydrogen Peroxide Assay kit. The AmplexRed analysis revealed a significantly

increased H_2O_2 production in DCM1 iPSC-cardiomyocytes (Fig. 47 A). This was not restored in isogenic control DCM1_res iPSC-cardiomyocytes (Fig. 47 A). In contrast to this, the produced H_2O_2 amount of DCM3 and DCM3_res iPSC-cardiomyocytes remained comparable to iPSC-cardiomyocytes of external controls (Fig. 47 A). Since the upregulation of ROS production in DCM1 iPSC-cardiomyocytes is not restored in corresponding isogenic control cells, this observation is not FLNC-dependent. This is further supported by the observation of unchanged H_2O_2 levels in DCM3 and DCM3_res cells compared to external controls. This highlights the importance of isogenic control lines, to analyze the role of certain gene mutations. Therefore, it can be concluded that elevated H_2O_2 levels are specific to DCM1 patient. Absence of increased H_2O_2 production in DCM3 is probably based on a different genetic background of the different patients. The exact underlying cause for increased H_2O_2 amounts requires further investigation and cannot be determined by AmplexRed measurements only.

In collaboration with Novartis the ARNi Entresto was tested on DCM1 iPSC-cardiomyocytes (4.5.2). ARNi is a supramolecular complex of sacubitril and valsartan. ARNi was recommended to be applied to heart failure patients instead of ACE inhibitors as it was shown to be relatively safe while improving left ventricular function and remodeling (Badreldin *et al.*, 2022; Liu *et al.*, 2022b). Sacubitril leads to inhibition of natriuretic peptide degradation by inhibiting the crucial enzyme neprilysin. As a consequence, natriuretic peptides ANP and BNP are increasing. Elevated ANP and BNP levels induce diuresis and vasodilation (Badreldin *et al.*, 2022; Liu *et al.*, 2022b). However, it will also increase AngII-dependent aldosterol secretion, which will have vasoconstrictive effects (Badreldin *et al.*, 2022; Liu *et al.*, 2022b). To counteract the latter one, valsartan is administered in combination. Valsartan acts as an AT1 receptor antagonists and thus inhibits AngII-dependent aldosterone release (Badreldin *et al.*, 2022; Liu *et al.*, 2022b). This will have positive effects on heart failure development by reducing myocardial oxygen consumption and sympathic nerve excitability. Among other assays, AmplexRed measurements were performed following a two weeks treatment with Entresto to assess the levels of H_2O_2 production. This showed significantly decreased H_2O_2 levels in treated DCM1 iPSC-cardiomyocytes in comparison to DCM1 iPSC-cardiomyocytes under basal conditions (Fig. 47 B). This shows that Entresto has positive effects on heart failure iPSC-cardiomyocytes with regard to lowering elevated H_2O_2 levels. To investigate the underlying molecular mode of action, the two Entresto components – valsartan and sacubitril – were tested individually on DCM1 iPSC-cardiomyocytes. This was of special interest as sacubitril rather acts on cell systems or organs than having effects on individual cells, suggesting valsartan being the major player in regulation of ROS production in heart failure iPSC-cardiomyocytes. It could be hypothesized, that valsartan`s action on G-protein coupled AT1 receptors inhibits downstream G-protein coupled signaling cascades having an effect on ROS production (Iborra-Egea *et al.*, 2017; Zhang *et al.*, 2016). However, when treating DCM1 iPSC-cardiomyocytes only with valsartan or sacubitril alone, the produced H_2O_2 amount did not decrease significantly compared to untreated DCM1 iPSC-cardiomyocytes as it was seen for treatment with Entresto combining both compounds (Fig. 47 B). Nevertheless, in tendency produced ROS was decreased when treated either with valsartan or sacubitril, respectively, compared to untreated DCM1 cells (Fig. 47 B). This effect was stronger upon treatment

with sacubitril. This suggests an synergistic effect of both compounds on intracellular ROS production of heart failure iPSC-cardiomyocytes as it was reported for effects on cell death and matrix remodeling in patients (Iborra-Egea *et al.*, 2017). However, sacubitril might be more important. Although underlying molecular mechanisms need to be unraveled, Entresto provides a pharmacological approach to improve patients` health with regard to lowering oxidative stress. To analyze the underlying mechanisms further, NGS of untreated and treated samples could be conducted to reveal regulated signaling pathways associated with ROS production.

5.9 Mechanical impairment in DCM EHM is partially restored by FLNC rescue

DCM is largely characterized by systolic/contractile dysfunction (Elliott *et al.*, 2008; Weintraub *et al.*, 2017). This is based on a complex set of remodeling processes affecting different cell types like cardiomyocytes and CFB as well as the ECM. Furthermore, a divers set of signaling processes is initiated. A major player within these remodeling and signaling processes are the cardiomyocytes. Hence, within this work a DCM iPSC-cardiomyocytes family model was generated to unravel the underlying pathomechanisms. These 2D analysis revealed dysregulated sarcomeres (5.5) affecting cardiomyocyte maturation (5.5.1) and Ca^{2+} homeostasis (5.7). It was shown that these effects were based on a newly identified FLNC variant (5.1). However, to investigate the effect of these impairments on the overall heart function it is important to analyze the mechanical functionality of diseased and isogenic control iPSC-cardiomyocytes in a 3D environment. For this, state-of-the-art EHM generation enables analyzing cardiomyocyte (mechanical) function by modeling the human myocardium, considering a 3D environment, presence of ECM and fibroblasts as potential interacting cell types. In this project, EHM from DCM and FLNC-rescue isogenic controls as well as control iPSC-cardiomyocytes were generated to analyze potential mechanical impairment in DCM EHM and to investigate the role of the FLNC variant onto mechanical properties. The shown results are largely preliminary since they are based on only one differentiation experiment of the used iPSC-cardiomyocytes and on only one casting process – two crucial points easily affecting EHM mechanics. Hence, the obtained results need to be interpreted carefully and further replicates are needed to support observed results. In general, EHM contraction, representing EHM strength, is significantly lower in diseased and FLNC-rescued isogenic control EHM of father and daughter compared to control EHM (Fig. 48 A). Only in FLNC-rescued DCM3_res EHM contraction is significantly improved compared to diseased DCM3 EHM, however not reaching contraction strength of control EHM (Fig. 48 A). Similarly, FOC of diseased and isogenic control EHM is significantly lower compared to control EHM and only DCM3_res EHM showed improved FOC compared to diseased DCM3 EHM (Fig. 48 D). This demonstrates that diseased EHM indeed show impaired contractile function as expected for DCM-derived (iPSC-) cardiomyocytes. Highlighting the suitability of this system to model a DCM disease state. However, upon FLNC-rescue contractile function is not rescued to control level. Nevertheless, there is a slight improvement in FOC and a significant improve in optical data of contraction of DCM3_res EHM compared to diseased EHM, indicating that the FLNC

variant actually does affect mechanical function. Yet, due to the rescue of the sarcomeric regularity in isogenic control iPSC-cardiomyocytes upon FLNC rescue, a more prominent improvement of contractile function would have been expected. Interestingly, resting force of diseased EHM of father and daughter was significantly increased compared to healthy tissues (Fig. 48 C) and could be rescued in isogenic control EHM towards a level of control EHM (Fig. 48 C). Sidenote, isogenic control EHM of the daughter (DCM3_res) improved their resting force to the level of control tissues, whereas isogenic control EHM of the father (DCM1_res) show significantly lowered resting force compared to corresponding diseased DCM1 EHM, but did not reach a level of control tissues (Fig. 48 C). The resting force can be used as a measure for inherent tissue stiffness since higher stiffness of the tissue would increase the applied force to reach maximum tissue pre-load. Meaning, the higher the resting force, the higher the tissue stiffness. Hence, the observed high resting force in diseased DCM1 and DCM3 EHM hints towards a diseased/stiff phenotype. This higher tissue stiffness might be based on the dysregulated sarcomere observed in these iPSC-cardiomyocytes (Fig. 24). This is supported by the fact, that the resting force (i.e. stiffness) decreases upon FLNC-rescue in isogenic control EHM (Fig. 48 C) and the major phenotype based on the FLNC-variant is the dysregulated sarcomere as shown in 2D analyses (Fig. 33). Nevertheless, increased tissue stiffness could also be a result or at least be worsen of/by lower iPSC-cardiomyocytes number or regulation of the ECM/fibrotic-like processes. Since cardiomyocyte loss is a major phenotype in DCM based on mechanical stress and remodeling processes (D'Oria *et al.*, 2020; Hong *et al.*, 2000; Kajstura *et al.*, 1995) IF staining of the EHM could be conducted to evaluate the iPSC-cardiomyocytes content in the different tissues. Different cardiomyocyte content could be a result of casting problems, but also could represent the DCM phenotype of cardiomyocyte loss due to apoptosis. Consequently, if differences in cardiomyocyte content could be observed, apoptotic processes could be analyzed in future experiments in 2D and 3D iPSC-cardiomyocytes culture. Additionally, it might be possible that interactions between diseased iPSC-cardiomyocytes and the used fibroblast might induce any remodeling processes leading to fibrotic-like processes. As increased fibrosis was observed in explanted heart tissue of the diseased father (Köhne, 2020) and isolated CFB from this tissue generate significantly stiffer ECT (4.6.3) such an interaction might be reasonable. Additionally, preliminary EHMs conducted prior to this project, analyzed combinations of diseased iPSC-cardiomyocytes and primary CFB of the DCM1 together with healthy iPSC-cardiomyocytes and CF (data not shown). These analyses demonstrated a significantly reduced FOC of EHM composed of healthy iPSC-cardiomyocytes and diseased CFB, clearly highlighting a role of the CFB on EHM contraction. To analyze this further, IF staining or single cell sequencing and subsequent gene ontology (GO) analysis of the generated diseased and isogenic tissues could be performed to check for upregulation of fibrotic processes. If this should be the case, the exact underlying interaction mechanisms between (iPSC-) cardiomyocytes and fibroblasts (e.g., CFB) and the role of the FLNC variant should be analyzed in more detail. Based on FOC and resting force results an active/passive force ratio was calculated as a measure for tissue health (Fig. 48 E). This revealed, that diseased DCM1 and DCM3 tissues showed lowest ratio, indicating most diseased tissues (Fig. 48 E). Upon FLNC rescue, DCM1_res and DCM3_res showed significantly increased active/passive force ratio,

compared to corresponding DCM1 and DCM3 tissues. Interestingly, DCM3_res even display a ratio comparable to control tissues (Fig. 48 E). This indicates, that the FLNC variant indeed affects tissue health in both DCM1 and DCM3 EHM. This improvement is largely based on decreased resting force. Nevertheless, two major questions arise due to these analyses – (1) Why do the isogenic control tissues only show slight improvement in general? And (2) Why do isogenic control EHM of the father (DCM1_res) show lower improvement compared to DCM1 EHM than DCM3_res compared to DCM3 EHM. Hypothesizing that the dysregulated sarcomere is the major player affecting cardiomyocyte contractile function, upon FLNC rescue and subsequent recovery of the sarcomere, contraction/FOC as well as resting force should be improved towards healthy EHM as well. Not reaching this, might be a problem due to small number of analyzed EHM and analysis of EHM only based on one differentiation and casting process. Hence, further repetitions of EHM generation and analysis should be performed with iPSC-cardiomyocytes from several differentiation experiments, to analyze, if the minor effects shown here can be confirmed or worked out more clearly. Only then, it can be concluded properly, if the FLNC variant is the major cause for impaired mechanical EHM function. Additionally, the absence/weakness of improvement in DCM1_res EHM compared to diseased DCM1 EHM could be based on a rather suboptimal differentiation of DCM1_res iPSC-cardiomyocytes or problems during the casting or EHM culture as well. However, it is suspicious that in all measurements DCM1_res EHM perform worse compared to DCM3_res EHM. Interestingly, upon FLNC-rescue DCM3_res iPSC-cardiomyocytes show restored sarcomeric regularity to control level in both – M-line and Z-disc (Fig. 33). In contrast to this, DCM1_res iPSC-cardiomyocytes show a restored M-line regularity, but only improved Z-disc regularity not reaching the control level (Fig. 33). The exact cause for this remains unknown. However, this might indicate that the sarcomeric disarray is not completely rescued in the DCM1_res iPSC-cardiomyocytes, which could explain a lower improvement of tissue stiffness and absence of improvement of FOC/contraction. Additionally, FLNC-independent increased oxidative stress was shown for DCM1 and DCM1_res iPSC-cardiomyocytes (Fig. 47), which might have effects on EHM mechanical function and could be an explanation for the low improvement of mechanical function in FLNC-rescued DCM1_res EHM. However, the exact underlying cause for these differences remains elusive and requires detailed analysis, starting with more EHM experiments, to draw reliable conclusions. This could include pharmacological treatment with Omecamtiv (myosin-activator) or Mevacamten (myosin-inhibitor), since, as already discussed (5.3), altered Ca^{2+} sensitivity might play a role in impaired contractility of these diseased iPSC-cardiomyocytes and resulting EHM.

In general, the EHM model system showed impaired mechanical function – decreased contraction and increased stiffness – of diseased tissues, comparable to a general DCM phenotype of the human myocardium. Especially tissue stiffness is significantly improved upon FLNC-rescue, highlighting the role of the FLNC variant to the mechanical function of a 3D tissue. However, contractile function was only improved in DCM3_res EHM, and not changed in DCM1_res EHM compared to corresponding diseased EHM.

5.10 Role of CFB in DCM pathophysiology

The heart is a multicellular organ, composed of different cell types acting together to fulfill the important functions of the heart within the organism. In addition to cardiomyocytes, whose role in DCM pathophysiology was investigated above, many other cell types, like EC, fibroblasts, vascular smooth muscle cells, pericytes or immune cells can be found in the heart (Pinto *et al.*, 2016; Zhou and Pu, 2016). Besides EC, cardiomyocytes and fibroblasts are the two most abundant cardiac cell types (Zhou and Pu, 2016). In the healthy heart CFB fulfill a plethora of important functions. Amongst these, controlling homeostasis of the ECM by secretion and degradation of several components, like collagen and MMP, is the most prominent function of CFB (Souders *et al.*, 2009). ECM provides a basement membrane for all other cardiac cells. And proper ECM homeostasis additionally is important for efficient propagation of mechanical stimuli throughout the heart. In addition to this, CFB secrete cytokines and growth factors, are involved in angiogenesis and have several cell signaling functions (Souders *et al.*, 2009; Zeisberg and Kalluri, 2010). Moreover, CFB directly interact with various cell types by cell-cell interactions. This includes direct interactions with cardiomyocytes and EC via CX43, allowing electrical coupling between these cells (Banerjee *et al.*, 2006; Louault *et al.*, 2008; Souders *et al.*, 2009). Considering its various functions in the heart, it is not surprising that pathophysiological changes of the heart are accompanied by crucial changes in CFB function. Failing hearts often are associated with increasing fibrosis (Zeisberg and Kalluri, 2010), which is also a major symptom in DCM (Cojan-Minzat *et al.*, 2021). Fibrosis is mainly based on an imbalance of ECM homeostasis resulting in an increased ECM synthesis and simultaneous decrease in ECM degradation. This overall increase in ECM leads to mechanical stiffness of the heart and will impair diastolic functions (Zeisberg and Kalluri, 2010). Additionally, an increase in ECM may also impair electrical coupling between cardiomyocytes, leading to contraction defects (Spach and Boineau, 1997). This remodeling of the heart leading to fibrosis mainly is driven by fibroblasts. More precisely by fibroblast activation to myofibroblasts and proliferation (Cojan-Minzat *et al.*, 2021; Zent and Guo, 2018).

Since previous studies within the group demonstrated significantly increased fibrotic area of myocardium of the explanted heart of the DCM1 patient (Köhne, 2020), analyzing the role of CFB to DCM pathophysiology was of special interest.

5.10.1 Characterization of primary CFB and their activation state

Although tremendous research was done to unravel CFB function in healthy and disease heart, leading to uncontroversial results of the important role of CFB, little is known about the molecular origin of resident and activated CFB (Eschenhagen, 2018; Zeisberg and Kalluri, 2010). This is mainly due to the absence of unique markers to identify CFB populations (Aujla and Kassiri, 2021; Hall *et al.*, 2021). The difficulty in clearly identifying CFB and different CFB subpopulations is also based on a highly dynamic switch in the functional state of quiescent and activated CFB (Eschenhagen, 2018). Additionally, CFB are of heterogenous origin. Resident CFB mainly derive from $TCF21^{+}$, epicardial-derived cells by EMT (Krenning *et al.*, 2010). A smaller proportion was reported to originate from the embryonic endocardium via EndMT (Krenning *et al.*, 2010). However, the origin of activated

or myofibroblasts is largely controversial (Aujla and Kassiri, 2021). Nevertheless, consensus was made that the majority of activated or myofibroblasts derive from resident fibroblasts upon activation and proliferation (Kanisicak *et al.*, 2016; Zeisberg and Kalluri, 2010). Nonetheless, several studies showed that activated or myofibroblasts can also derive from secondary sources like EC (Widyantoro *et al.*, 2010), pericytes (Kramann *et al.*, 2015) or blood born cells (Mollmann *et al.*, 2006). The reason and consequences for this is not unraveled yet. Still, the diverse sources of CFB also contribute to difficulties in clearly identifying CFB populations. Hence, the best way to identify fibroblast populations is by the combination of different markers.

Hence, to characterize primary CFB and SFB isolated from explanted heart and skin biopsy of patient DCM1, respectively, they were analyzed by qPCR for expression of a combination of fibroblast specific markers in comparison to commercially available, normal CFB, iPSC-derived cardiomyocytes of patient DCM1 and heart tissue of the left ventricle of DCM patients. These analyses revealed a clear upregulation of the general fibroblast marker collagen 1 (*COL1A1*) in all fibroblast samples (Fig. 49 A). In contrast to this, *FSP1* was upregulated in DCM1 CFB and SFB, compared to control CFB with low expression (Fig. 49 A). This is in line with previously published data: Although, FSP1 was used as specific marker for CFB for a long time, recent studies demonstrated that it is only expressed by a small subpopulation of primarily perivascular CFB (Ivey and Tallquist, 2016; Kong *et al.*, 2013; Tallquist and Molkentin, 2017). As the majority of $FSP1^+$ cells was identified as $CD45^+$ hematopoietic cells, $FSP1^+$ CFB may represent blood-derived fibroblasts (Kong *et al.*, 2013; Ruiz-Villalba *et al.*, 2015). Additionally, it was reported that FSP1 is mainly found in tissue during remodeling e.g., due to disease or injury (Tallquist and Molkentin, 2017). This might explain the presence of *FSP1* expression in DCM CFB and the absence in normal CFB. This again highlights the difficulties in CFB characterization.

To differentiate between CFB and SFB the expression of *TCF21* was analyzed since the majority of resident CFB derive from $TCF21^+$ (pro-) epicardial cells. As expected, *TCF21* was only upregulated in DCM1 and normal CFB, but not in SFB (Fig. 49 A). This also demonstrates that these cells mainly derived from an epicardial origin during development. Additionally, *TCF21* was upregulated in explanted heart failure tissue (Fig. 49 A). This *TCF21* upregulation can be explained by proliferation and activation of resident CFB to myofibroblasts in heart failure associated with fibrosis as demonstrated in this myocardium (Aujla and Kassiri, 2021). Additionally, markers of fibroblast activation were tested, which remains difficult because of two reasons: (1) the changes between activation states are rather continuously (Aujla and Kassiri, 2021; Eschenhagen, 2018) and (2) 2D culture of fibroblasts on stiff surfaces of classical cell culture plates induces mechanical stress and CFB activation (Aujla and Kassiri, 2021; Hall *et al.*, 2021). Hence, identified activation of fibroblasts not necessarily represents pathological changes. Additionally, markers for fibroblast activation are often not only expressed by activated fibroblasts but also by other cell types. Nevertheless, *CTGF,* a marker induced by TGFβ signaling and associated with fibroblast-to-myofibroblast transdifferentiation (Koitabashi *et al.*, 2008)*,* was upregulated in DCM1 and normal CFB (Fig. 49 A), hinting towards a myofibroblast phenotype. In contrast, expression of *POSTN* was mostly upregulated in normal CFB but only low in DCM1

CFB (Fig. 49 A). POSTN is an ECM protein expressed in embryonic CFB and myofibroblasts deriving from TCF21$^+$ resident CFB, but not in adult fibroblasts (Kanisicak *et al.*, 2016). This in general hints towards an activation of a myofibroblast phenotype of both – DCM1 and normal CFB. The differences in expression might be explained by more prominent activation of normal CFB by 2D culture. Alternatively, it could be hypothesized that activated CFB arise from distinct CFB subpopulations of these two samples. In this theory, activated normal CFB would more prominently arise from TCF21$^+$ resident CFB of epicardial origin, than activated DCM1 CFB. Expression of αSMA (*ACTA2*) was low in DCM1 and normal CFB but was increased in iPSC-cardiomyocytes. In theory, αSMA expression is described to be induced upon CFB transdifferentiation into myofibroblasts in a transient manner (Eschenhagen, 2018; Zeisberg and Kalluri, 2010) and decreases with time, especially in chronic cardiac fibrosis (Fu *et al.*, 2018). However, αSMA is not myofibroblast specific, as it is also expressed by other cell types, like cardiomyocytes as shown in our and other studies (Arnoldi *et al.*, 2012; Eschenhagen, 2018). At least for DCM1 CFB the reported decrease of αSMA in myofibroblasts of patients with chronic cardiac fibrosis (Fu *et al.*, 2018) might explain the low αSMA here, despite the fact the DCM1 patient showed increased fibrosis which is associated with high levels of myofibroblasts. Nevertheless, preliminary NGS data showed upregulation of all six markers in isolated CFB of DCM1 patients compared of myocardium (Fig. 49 B).

Taken together, these results supported the expression of *COL1A1, TCF21*, and *FSP1* in DCM1 CFB and therefore the CFB origin of these primary isolated cells. Conclusion on the activation state is more difficult to make, however, there seems to be activation shown by upregulation of *CTGF*. Only low levels of αSMA might be explained by a chronic cardiac fibrosis state in which αSMA gets time-dependently downregulated.

5.10.2 Directed differentiation of CFB-like cells from iPSC

In addition to the primary CFB of the diseased father isolated from explanted left ventricular myocardium, iPSC-derived CFB should be generated, which would allow a direct comparison of diseased CFB and isogenic control CFB, analyzing a putative role of the FLNC variant in CFB. For this, a differentiation protocol was established to generate stromal cells from iPSC using an frequently described approach that is based on the most prominent embryonic origin of CFB – the epicardial cells (Tallquist and Molkentin, 2017). Hence, this differentiation protocol starts with generating iPSC-derived epicardial cells, which are subsequently treated with FGF2 to induce CFB differentiation (Bao *et al.*, 2016; Giacomelli *et al.*, 2020; Iyer *et al.*, 2016; Zhang *et al.*, 2019; Zhao *et al.*, 2017). The established protocol used in this study was generally based on the protocol described by Iyer *et al.* (Iyer *et al.*, 2016) but was modified at several points. The protocol can be divided into five steps including early mesoderm induction, cardiac progenitor induction, epicardial cell fate specification, CFB differentiation and CFB expansion (Fig. 7, Fig. 50). As described in many protocols (Giacomelli *et al.*, 2020; Guadix *et al.*, 2017), differentiation into epicardial cells was started with supplementation of 1µM CHIR99021, 5ng/ml Activin A and 9ng/ml BMP4 (differently to Iyer *et al.* who used 10ng/ml BMP4 and 10µM Ly294002, an inhibitor of PI3 kinase) to induce an early mesodermal fate. In addition FGF2 was added in this early step of differentiation as well as suggested by Iyer *et al.* (Iyer *et al.*, 2016). To induce cardiac

differentiation canonical WNT signaling was inhibited by addition of IWP-2, which inhibits the membrane-bound acetyltransferase porcupine that palmitoylates WNT proteins, activating its signaling capability (Chen *et al.*, 2009). Subsequently differentiation into epicardial-like cells was initiated by addition of BMP4, RA and CHIR99021, which were shown to act synergistically to efficiently induce epicardial differentiation (Guadix *et al.*, 2017; Iyer *et al.*, 2016). Indeed, morphological changes towards an epicardial-like morphology of edged, cobblestone-like cells could be observed (Fig. 50 B). These obtained epicardial-like cells were further differentiated to fibroblasts by addition of FGF and VEGF for long term culture as described by Iyer *et al.* (Iyer *et al.*, 2016). During this time, the morphology of the cells developed towards early fibroblast-like cells with elongated morphology (Fig. 50 B), which is in line with already published protocols (Giacomelli *et al.*, 2020; Zhang *et al.*, 2019; Zhao *et al.*, 2017). mRNA expression analysis of the markers used for characterization of primary CFB confirmed CFB differentiation. This demonstrated expression of *COL1A1, CTGF, POSTN* and *ACTA2* in iPSC-StC (Fig. 51). COLA1A and ACTA2 expression additionally could be confirmed on protein level by IF staining (Fig. 52). More detailed, *COL1A1* mRNA expression was significantly upregulated compared to iPSC but lower compared to primary DCM1 CFB (Fig. 51). *CTGF* and *ACTA2* were expressed at similar levels like in primary CFB and *POSTN* expression was even slightly increased compared to primary CFB (Fig. 51). These findings suggest that indeed fibroblast-like cells were generated which do rather resemble activated than quiescent fibroblasts. Notably, expression of *FSP1* and *TCF21* was not upregulated and remained on a level comparable to iPSC (Fig. 51). Lack of *FSP1* expression might not change the overall assumption of having generated CFB since this marker is not expressed in every CFB subpopulation as described before. However, absence of *TCF21* expression is contradictory. This is because epicardial-derived CFB express TCF21, which is indispensable for EMT from epicardial-derived cells into CFB (Acharya *et al.*, 2012; Hu *et al.*, 2020; Moore-Morris *et al.*, 2016). $TCF21^{low}$ epicardial-derived cells rather differentiate into VSMC upon EMT (Acharya *et al.*, 2012; Hu *et al.*, 2020; Moore-Morris *et al.*, 2016). Additionally, in general epicardial-derived cells are the predominant origin of CFB (Pinto *et al.*, 2016; Zhou *et al.*, 2010b) and within this project a differentiation protocol was used recapitulating the *in vivo* differentiation of CFB via the epicardial lineage. Furthermore, other protocols using a similar way of iPSC-CFB differentiation via epicardial progenitor cells usually show a TCF21 expression (Bao *et al.*, 2016; Zhang *et al.*, 2019). However, Iyer *et al.* do show expression of TCF21 in iPSC-derived epicardial-like cells, but do not comment on TCF21 expression in later stage iPSC-derived CFB (Iyer *et al.*, 2016). Notably, other groups also report absence of TCF21 in iPSC-derived CFB (personal communication). Interestingly, Zhang *et al.* report downregulation of TCF21 upon TGFβ-stimulated myofibroblast transdifferentiation in iPSC-CFB and primary CFB and suggest TGFβ inhibition to keep quiescent, TCF21-expressing CFB (Zhang *et al.*, 2019). Consequently, absence of *TCF21* expression in iPSC-StC within this project might be associated with generation of activated myofibroblasts rather than quiescent fibroblasts. Analysis of TCF21 expression of cells at earlier timepoints during the differentiation process, especially the epicardial-like cells, should be performed in the future to analyze for TCF21 expression at these stages, like reported in the literature (Iyer *et al.*, 2016; Zhang *et al.*, 2019). Additionally, NGS and subsequent GO analysis of cells of all intermediate

differentiation steps and IF staining for TCF21 expression could add more information to answer this question.

In summary, all analyzed cell lines expressed *COL1A1*$^{+}$, *POSTN*$^{+}$, *CTGF*$^{+}$, *ACTA2*$^{+}$ and displayed classical fibroblast morphology, suggesting a successful differentiation of iPSC to iPSC-derived CFB-like cells. Hence, these cells could be used for functional analysis in 3D model. However, the absence of *TCF21* expression needs further investigation and should be kept in mind for functional analysis.

5.10.3 Analysis of 3D ECT

With having tissue-derived primary CFB of the diseased father (DCM1) and corresponding iPSC-derived DCM1 and DCM1_res (FLNC repair) stromal cells at hand, analysis of their function should shed more light onto the general contribution of CFB to the DCM pathophysiology and additionally should analyze if the FLNC variant has effects in CFB function, maybe also driving DCM disease. To investigate the function of CFB and the fibrotic process the 3D model of ECT was applied, in which the CFB were embedded within a collagen matrix (Santos *et al.*, 2021). Notably, casting and culturing ECT with the used cells (primary diseased or iPSC-derived healthy and diseased) needed to be established and was quite challenging, resulting in low numbers of individual ECT for final analysis. Most data was available for ECT contraction and compaction, here also data of several casting experiments could be combined, making this data more valid. However, since first trials were only conducted with primary CFB ECT, data for iPSC-StC ECT is lower. Additionally, due to huge time and batch (e.g., collagen, 48-well plates) differences between the different casting experiments, data of destructive tensile strength measurement could not be combined but showed similar trends. Nevertheless, the shown data is only resulting from one casting experiment. To validate results shown in the following paragraphs, further ECT experiments are required in general.

5.10.3.1 FLNC-dependent decrease in ECT contraction and compaction

Over the time course of ECT culture, contraction was analyzed on a daily basis for each ECT by image analysis monitoring deflection of fluorescently labelled flexible poles around which the ECT were formed (3.3.2.2). These analyses showed a higher contraction of ECT harboring primary normal CFB and iPSC-derived control as well as DCM1_res StC, compared to ECT harboring primary DCM1 CFB or DCM1 iPSC-StC, respectively (Fig. 53 A, B). Interestingly, iPSC-derived control ECT could recapitulate contraction of primary normal CFB. Notably, DCM1_res iPSC-StC showed restored contraction capacity to control level (iPSC-StC and primary). In addition, ECT compaction was analyzed by determining CSA of the ECT at the days of destructive-tensile strength measurements (day 13 and 21). This analysis demonstrated significantly decreased ECT compaction in ECT harboring either primary DCM1 CFB or iPSC-derived DCM1 StC, whereas all other ECT showed similar and stronger ECT compaction (Fig. 54 C, D). Again, interestingly, iPSC-derived control ECT achieved comparable ECT compaction as primary normal ECT and DCM1_res iPSC-StC ECT showed restored compaction comparable to normal ECT. Analysis of ECT contraction and compaction hence revealed two major points. First, iPSC-derived StC can recapitulate both functional parameters – contraction and compaction – to a level of primary ECT. There are

even differences between normal and diseased ECT. This further supports the hypothesize, that indeed a CFB-like cell type was differentiated by the newly established protocol. Secondly, diseased ECT (primary and iPSC-derived) show decreased compaction and contraction in comparison to normal ECT, and this diseased phenotype is reversed by rescue of the FLNC variant back to control. This implicates that this diseased phenotype is based on the newly identified FLNC variant and hence highlights a role of FLNC within CFB. Since the key role of FLNC is crosslinking of actin filaments, the FLNC-dependent impairment leading to decreased ECT contraction and compaction, most likely is based on impaired formation of αSMA-containing stress fibers. The identified FLNC variant may lack the ability of proper crosslinking αSMA. To support this hypothesis, it is indispensable to analyze the structure of αSMA filaments e.g., by IF staining in normal, diseased, and rescued cells in the future. However, FLNC not only crosslinks actin filaments but is incorporated into highly complex interaction networks, at least in cardiomyocytes, which are important for locating actin filaments properly within the cell and also to tether them to the cell membrane (Gontier *et al.*, 2005; Mao and Nakamura, 2020; Popowicz *et al.*, 2006; Thompson *et al.*, 2000). Hence, FLNC might additionally function as a scaffolding protein within CFB, which might be important to coordinate fast dynamics of stress fibers, as reported for other actin-cross-linking proteins, like palladin acting as a scaffold for profilin and VASP (Boukhelifa *et al.*, 2006; Tojkander *et al.*, 2012). Impairment of these high dynamics, potentially based on disrupted protein interactions based on the FLNC variant, might result in decreased contraction of the CFB. Furthermore, FLNC is important for cell-cell communication, propagation of contraction and cell stability. Especially because FLNC also interacts with β-integrins (Loo *et al.*, 1998), which are important drivers for focal adhesion formation and communication between CFB and ECM, an impairment of this could also result in lower tissue contraction and compaction due to improper signaling from the CFB to the ECM. Regardless of the exact underlying mechanism being impaired, reduced ECT contraction and compaction driven by CFB might contribute to the DCM phenotype.

In general, ECT contraction and compaction revealed impairment of both in diseased CFB/iPSC-StC and hence identified a clearly diseased CFB phenotype contributing to DCM pathophysiology. Interestingly, decreased contraction and compaction of diseased ECT seems to be FLNC-dependent, pointing out a role of FLNC in CFB function. However, the exact molecular mechanism affected within the CFB based on the FLNC variant remains unknown and requires detailed investigation in the future.

5.10.3.2 Increased tissue stiffness and reduced elasticity in diseased ECT

In addition to analysis of ECT contraction and compaction ECT also were applied to destructive tensile strength measurement, where the ECT were stretched uniaxially until total ECT rupture. These measurements were conducted with ECT either after 13 days of culture or after 21 days. These measurements resulted in a stress-strain curve from which several mechanical/viscoelastic parameters could be retrieved. These include the Young`s modulus as a measure of ECT stiffness, as well as elasticity, characterized as the strain region in which the ECT deformation still is reversible, and the extensibility, characterized as the ultimate strain which can be applied to the ECT until rupture. These analyses showed

that ECT composed of primary CFB of the diseased father (DCM1) display significantly increased ECT stiffness (increased Young`s modulus), corresponding to a steeper slope of the curve during the elastic phase at both days of measurement (Fig. 55 C, D). The Young`s modulus and with it the resulting ECT stiffness of all other ECT is significantly and comparable lower compared to DCM1 CFB ECT (Fig. 55 C, D). Additionally, elasticity and extensibility of the ECT harboring primary diseased DCM1 CFB were significantly decreased compared to all other ECT at both time points (Fig. 55 C, D). This indicates that the DCM1 CFB ECT disrupt at lower strain already.

Our data have shown increased tissue stiffness of DCM1 ECT and increased fibrosis within DCM1 myocardium, this is in line with increased tissue stiffness as a classical marker of fibrotic tissue (Tschumperlin *et al.*, 2018). Fibrotic tissue in diseased hearts is characterized by extensive activation of myofibroblasts leading to increased deposition of ECM proteins, especially collagens, and excessive cross-linking of ECM molecules, initiated by lysyl oxidases (LOX) resulting in increased tissue stiffness, which in a positive feedback loop will further increase ECM deposition (Tschumperlin *et al.*, 2018). Increased tissue stiffness typically is accompanied by decreased tissue elasticity in fibrotic tissue and 3D ECT (Tschumperlin *et al.*, 2018), which is in line with the data shown in this project. However, the exact underlying mechanisms for this inverse regulation of stiffness and elasticity are still unclear. One theory for decreased elasticity might be, that collagen I is increasingly secreted in fibrotic areas in heart failure patients (Kasner *et al.*, 2011; Sweeney *et al.*, 2020). And collagen I was shown to have fewer elastic properties compared to other collagen subtypes like collagen III. This might decrease overall tissue elasticity (Collier *et al.*, 2012). Additionally, excessive ECM molecule crosslinking driven by LOX, might also contribute to a less elastic phenotype (Tschumperlin *et al.*, 2018). Based on the destructive tensile strength measurements, a diseased CFB phenotype could be confirmed, resembling a classical fibrotic phenotype with increased stiffness and decreased elasticity. This would have major implications on DCM progression towards a heart failure phenotype. To investigate the fibrotic phenotype in more detail large NGS and Western blot analysis of the diseased and normal ECT would shed light onto the exact ECM composition and expression e.g., of lysyl oxidases and would confirm the functional phenotype on a molecular level.

However, a similar phenotype shown in ECT composed of primary diseased CFB of the father (DCM1) could not be recapitulated in ECT composed of DCM1 iPSC-StC. This could have two reasons. (1) The generated iPSC-derived StC may not resemble the exact same CFB subtype which is enriched in actually diseased heart and hence lack any properties like ECM secretion or crosslinking not inducing increased stiffness and decreased elasticity. To analyze this possibility NGS analysis of primary CFB in comparison to iPSC-derived StC could unravel crucial differential expression of genes or activation of distinct pathways which could explain these functional differences. (2) The primary DCM1 CFB derive from a heart failure tissue with chronic fibrosis, whereas the DCM1 iPSC-StC were differentiated from iPSC reprogrammed from SFB not experiencing any chronic mechanical/fibrotic stress. Hence, it might be possible that the primary DCM1 CFB retained a “mechanical memory” which was imprinted due to the chronical stress as an epigenetic mark. This mechanism of

a mechanical memory retained by fibroblasts having long-term effects was already proposed by others (Heo *et al.*, 2015; Yang *et al.*, 2014a). This could have led to CFB characterized by chronic ECM deposition also in the absence of mechanical stress. This hypothesis is based on several findings that initiated fibrosis indeed has effects on the epigenetic landscape. This was shown to be driven by biochemical (O'Reilly, 2017; Tzouvelekis and Kaminski, 2015) as well as mechanical (Downing *et al.*, 2013; Lelievre, 2009) signals during fibrosis. To analyze this hypothesis further, analysis of the epigenetic landscape e.g. by epigenomic sequencing of primary and iPSC-derived cells and ECT could be performed to identify epigenetic alterations (Buenrostro *et al.*, 2015; Jeong *et al.*, 2016). Applying a higher mechanical co-stress to the generated ECT composed of DCM1_res iPSC-StC could induce a similar phenotype. This for example could be conducted by casting the ECT around one stiff pole (Santos *et al.*, 2019), instead of casting around two flexible poles. This will already apply a higher mechanical constrain to the ECT maybe triggering a fibrotic response. If this would be possible, the same experiments could be done with ECT harboring the FLNC rescue (DCM1_res iPSC-StC) to further evaluate if the FLNC variant might have any effects on stiffness and elasticity as well.

In summary, ECT harboring diseased CFB explanted from LV myocardium of the diseased father display increased stiffness and decreased elasticity, both being main characteristics of fibrotic tissue. Hence, this data indicates and further supports previous findings, that CFB have an effect on DCM pathophysiology since non-contracting, non-elastic fibrotic tissue will further impair systolic function and worsen DCM progression. This fibrotic phenotype could not be resembled in corresponding iPSC-StC. This could either be due to wrong subtype differentiation or due to epigenetic imprinting on the primary CFB acting as a mechanical memory maintaining a fibrotic phenotype even in the absence of mechanical stress. This mechanical memory would be absent in the iPSC-derived cells, as they were reprogrammed from SFB not experiencing mechanical stress of the failing heart. However, the exact underlying cause needs detailed future experiments.

5.11 Telomere shortening as a cause for DCM

Telomeres are short DNA repeats at the end of chromosomes acting as protective caps. However, these DNA repeats shorten by each cell division as a natural process important for cell senescence (Okamoto and Seimiya, 2019; Saliques *et al.*, 2010). Dysregulation of this telomere shortening was associated with oncogenic pathophysiological mechanisms for a long time, where telomeres do not shorten by cell division (Okamoto and Seimiya, 2019). Maintaining telomere length is a major hallmark of cancer and mostly mediated by upregulation of telomerase activity allowing unlimited numbers of cell division (Okamoto and Seimiya, 2019). Interestingly, recent studies identified a cardiomyocyte-specific telomere shortening in patients with genetically inherited, isolated, end-stage HCM and DCM associated with mutations in proteins important for contractile function (Chang and Blau, 2018; Chang *et al.*, 2018). This effect could also be modeled in iPSC-cardiomyocytes (Chang *et al.*, 2018). Hence, the role of telomere length in the pathophysiology of DCM within this family should be investigated. First, telomere length in iPSC and iPSC-derived cardiomyocytes of all family members was analyzed by qFISH (4.7.1) in collaboration with

the group of Dr. Christian Bär (Medizinische Hochschule Hannover). This data showed a general telomere shortening from iPSC to iPSC-cardiomyocytes in all four family members (Fig. 56). However, this telomere shortening is strongest in cells of diseased family members DCM1 and DCM3 (Fig. 56). In comparison, telomere shortening in healthy family members DCM2 and DCM4 is lower (Fig. 56). Additionally, DCM3 iPSC-cardiomyocytes also displayed the shortest iPSC-cardiomyocytes telomeres in general (Fig. 56). This observation gives a first hint of telomere shortening being associated with the analyzed DCM. To exclude that observed differences of telomere length are based on differences in telomerase activity between the analyzed cell lines, a TRAP assay was performed to elucidate telomerase activity. The TRAP assay could not identify differences in telomerase activity (Fig. 57). This suggests that observed stronger telomere shortening in diseased patients indeed might be a pathophysiological effect. So far, studies could not identify exact underlying mechanisms causing telomere shortening. However, two major hypotheses were postulated: either, as described by Chang and Blau, mechanical stress is the driving force inducing deprotection of telomere ends, which would explain observed downregulation of shelterin proteins as protectants of telomere length or an accumulation of oxidative stress inducing telomere shortening (Chang and Blau, 2018; Chang *et al.*, 2018). The oxidative stress-telomere axis was hypothesized several times, nevertheless, it is under debate if oxidative stress is inducing telomere shortening, or in fact it is the other way around (Chang and Blau, 2018). Within this study increased oxidative stress could only be observed in DCM1 patient (4.5.25.8) but not in DCM3 patient. As the telomere shortening is more prominent in DCM3 patient, most likely elevated ROS production is not the driving force within this DCM. Further experiments using ROS scavengers, such as *N*-acetyl-l-cysteine (NAC)(Halasi *et al.*, 2013) would give further insights into the contribution of ROS on telomere shortening. However, a key characteristic within this family is a FLNC-dependent sarcomeric disarray (4.2.15.5), which leads to impairment of contractile function. This is similar to reported effects in DCM patients with variants in key structural proteins, like *MYBPC3, MYH7, TNNT2,* and *TTN*, important for contraction being associated with cardiomyocyte-specific telomere shortening (Chang *et al.*, 2018). Hence, it could be hypothesized that dysregulated sarcomeric structure induces mechanical stress, leading to downregulation of shelterin proteins, causing deprotection of telomere ends, which eventually may result in cardiomyocyte-specific telomere shortening. To support this hypothesis, first telomere length of isogenic control cells should be analyzed by qFISH experiments. This would ideally restore telomere length. Additionally, expression analysis of shelterin proteins could be performed to test for downregulation. A contribution of a mechanical driver to induce telomere shortening, as described above, was further supported by studies also associating a disruption of sarcomere organization, decrease in force generation, presence of fibrosis and aberrant Ca^{2+} handling with shortening of telomeres in the context of heritable DCM, linked to mutations in the dystrophin protein (Chang *et al.*, 2021). Furthermore, this study provides evidence that in iPSC-derived cardiomyocytes the described telomere shortening occurs proliferation-independent and similar effects cannot be observed in normal control iPSC-cardiomyocytes (Chang *et al.*, 2021). This is in line with observations within the present project, also showing a FLNC-dependent sarcomeric disarray, associated with fibrosis in primary DCM1

myocardium and fibrotic-like processes in 3D ECT. Furthermore, 3D EHM demonstrated significantly impaired force generation and 2D analysis revealed slowed Ca^{2+} kinetics. Based on these reports and the previously described findings within this project, FLNC-dependent mechanical stress within the iPSC-cardiomyocytes might be directly associated with the observed telomere shortening.

In summary, a stronger telomere shortening from iPSC to iPSC-cardiomyocytes could be identified in DCM patients compared to external controls. This observation might point towards an association of cardiomyocyte-specific telomere shortening within this DCM family. It does not seem to be driven by oxidative stress. More likely, mechanical stress induced by a FLNC-dependent sarcomeric disarray could be causative. Further analysis of telomere length of isogenic controls and expression analysis of shelterin proteins would shed more light onto this hypothesis. However, more research is necessary to draw reliable conclusions.

5.12 Limitations of this work

In this study the patient-specific induced pluripotent stem cell system was used, which allows studying molecular mechanisms in a human rather than in an animal model making results more translatable from bench to bedside. Additionally, the iPSC system also holds advantages over the embryonic stem cell system as ethical issues are reduced and the iPSC represent the patients geno- and phenotype.

However, using the ps-iPSC system several disadvantages and limitations are implicated, which need to be considered in experimental design and evaluation of results. First, as already mentioned iPSC-derived cardiomyocytes only resemble a neonatal maturation state rather than resemble adult cardiomyocytes. Hence, it is possible that certain DCM phenotypes cannot be modeled by using the iPSC-cardiomyocytes system. Vice versa it is debatable that identified phenotypes only occur in the context of immature iPSC-cardiomyocytes, what would be absent in adult cardiomyocytes. Based on this, obtained results need to be assessed critically. Additionally, most experiments were conducted in 2D monolayer cell culture experiments and only few and isolated cell types (ventricular cardiomyocytes and CFB) were analyzed. However, especially the pathophysiology of the heart, as a multicellular organ, is largely influenced by the complex 3D interplay of several different cell types. Although 3D models of cardiomyocytes and CFB were generated for some readouts and 2D phenotypes could be resembled to some extent, the detailed interplay of these different cell types was not investigated and has to be done in the future. Furthermore, the huge genomic background variability of different patients and controls complicates the data interpretation. This is even worsened by the small sample size used in studies using the iPSC system, which is based on difficulties in recruiting suitable donors and the high effort in generation and maintenance of iPSC and their derived cells. At least the challenge of genomic background variability was partially circumvented by generation of isogenic controls to study the contribution of a certain variant.

5.13 Conclusion

Fig. 58 summarizes the findings within the present project. Within a four-member DCM family we could identify a new and “likely pathogenic” FLNC missense variant (p.R2187P) in diseased family members (father and daughter). With the help of isogenic control lines, FLNC-dependent disturbance of the sarcomeric regularity could be identified in both patients as the major disease mechanism. We show decreased contraction and increased stiffness of diseased 3D EHM, as well as impaired Ca^{2+} handling (i.e., decreased systolic [Ca^{2+}] and Ca^{2+} kinetics) of diseased iPSC-cardiomyocytes in 2D culture in both patients. Using isogenic control lines, we could link these phenotypes to the identified FLNC-variant. Based on these findings, we postulate the FLNC-dependent sarcomeric disarray as major underlying cause for the functional impairments shown. iPSC-cardiomyocytes of both patients display decreased CX43 expression, which is not restored upon FLNC rescue in isogenic control cells and needs further investigation. At least for the DCM1 patient we could identify FLNC-independent elevated levels of ROS, which can be reduced by ARNi treatment and might be involved in dysregulation of CX43 expression, as reported in the literature. Interestingly, we identified CaMKIIδ-dependent increased phosphorylation of RYR2-S2814 and PLN-T17 as potential compensatory mechanisms for slowed Ca^{2+} kinetics in DCM1 cells. In contrast to this, iPSC-cardiomyocytes of DCM3 displayed an unusual, FLNC-dependent increased expression and activity of SERCA, which might be compensatory for impaired Ca^{2+} handling in this patient. But it is still debatable, whether impaired Ca^{2+} handling or increased SERCA activity was the initial appearing phenotype. Nevertheless, different, potentially compensatory mechanisms in the two patients might be explanatory for varying disease onset and progression. Additionally, ECT composed of primary DCM1 CFB showed increased stiffness. Absence of increased stiffness in ECT harboring DCM1 iPSC-StC, points towards epigenetic changes of the primary CFB probably obtained upon mechanical stress within the chronically failing heart. Moreover, we could identify FLNC-dependent decreased compaction and contraction of diseased ECT. With this, we could – to our knowledge – for the first time demonstrate a role of FLNC within CFB and additionally could demonstrate a crucial contribution of the identified variant in CFB as an important player in the DCM pathophysiology. The underlying mechanisms being impaired in CFB based on the FLNC variant, however, need to be elucidated in detail in the future.

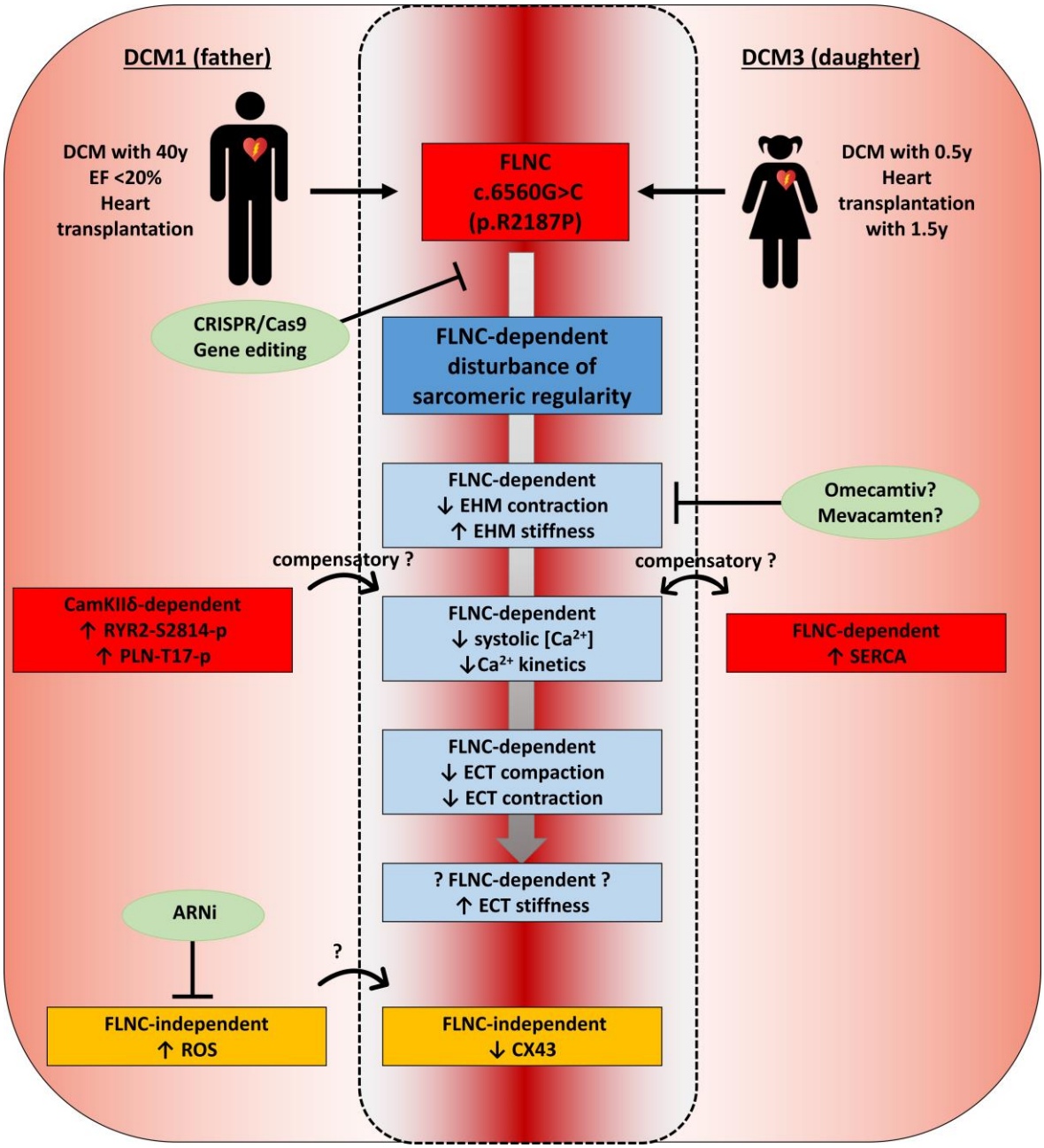

Fig. 58: Summary of DCM pathophysiology in index family. The father (DCM1) and the oldest daughter (DCM3) were diagnosed with sudden DCM and needed heart transplantation. Disease onset of the daughter was significantly earlier in life. Both harbor a newly identified FLNC variant (p.R2187P), localized in the important domain 20. With the help of CRISPR/Cas9 generated isogenic control lines, FLNC-dependent disturbance of the sarcomeric regularity could be identified in both patients as the major disease phenotype. FLNC-dependent sarcomeric irregularity led to decreased contraction in 3D EHM models and impaired Ca^{2+} handling in 2D iPSC-cardiomyocytes in both patients. DCM1 patient shows CaMKIIδ-dependent, but FLNC-independent RYR2 and PLN phosphorylation possibly to compensate for Ca^{2+} handling defects. DCM1 iPSC-cardiomyocytes display increased ROS production of unknown cause, which can be restored by ARNi treatment. DCM3 iPSC-cardiomyocytes show FLNC-dependent increased SERCA expression and activity as a potential mechanism to counteract Ca^{2+} handling defects. 3D ECT showed (FLNC-dependent) decreased compaction and contraction and increased stiffness of DCM1 CFB. Both patients show decreased CX43 expression, which is not FLNC-dependent and needs further investigation. It might be induced by increased ROS production of unknown cause in DCM1 patient, which can be restored upon ARNi treatment.

5.14 Outlook

Within this work, a patient-specific iPSC-cardiomyocytes model of a four-member DCM index family with diseased and healthy family members was established. Using this model system, a disease-causing missense variant in domain 20 of FLNC was identified. With the help of CRISPR/Cas9 generated isogenic controls, a FLNC-dependent sarcomeric disarray could be identified as major structural/cellular disease phenotype within this DCM family. Functional analysis directly associated the FLNC-dependent sarcomeric disarray with impaired Ca^{2+} homeostasis and impaired 3D mechanics. This highlights the CRISPR/Cas9 gene editing strategy, to rescue the FLNC variant, as a putative therapeutic approach to prevent DCM progressions in patients harboring the newly identified variant. However, CRISPR/Cas9 gene editing in *in vivo* studies still needs to be established reliably.

Identifying the FLNC variant and the resulting sarcomeric disarray as major disease drivers, it is necessary to unravel the exactly impaired FLNC function leading to the sarcomeric disarray. Due to the location of the FLNC variant in an interaction and phosphorylation hot-spot region two major, but overlapping, approaches could be conducted. On the one hand, phosphoproteomics, e.g., by using mass-spectrometry approaches, should analyze, whether the substituted arginine represents a potential phospho- or PTM site. Furthermore, directly impaired interactions of FLNC and its binding partners should be analyzed in more detail. For this, *in silico* binding predictions of wildtype and missense FLNC could be performed together with quantitative mass spectrometry approaches to identify changes in protein-protein interactions mediated by the FLNC variant on a global scale. These analyses could be supplemented and confirmed by pull down analysis, like co-immunoprecipitation, and Western blot analysis of predictably affected FLNC binding partners in iPSC-derived cardiomyocytes and the primary myocardium of DCM1.

To get further insights into the myofilament structure and function, analysis of the DCM1 primary myocardium should be conducted, to analyze for altered myofilament protein composition or posttranslational modifications. Additionally, differences in force modulation and Ca^{2+} sensitivity in primary DCM1 myocardium and single iPSC-cardiomyocytes might be investigated. Furthermore, the molecular driver for destabilization of the sarcomeric proteins should be identified and analyzed in the future. Preliminary data show increased expression of matrix metalloproteinase 2 (MMP2) in DCM1 and DCM3 (data not shown) hinting to a major role in cardiac disease progression and was demonstrated before in doxorubicin-dependent cardiomyopathies (Haupt *et al.*, 2022). Available MMP2 inhibitors should be tested in this context. Identifying the impaired structures and drives in more detail could reveal potential therapeutic target sites which could be tested in the future.

With analyzing Ca^{2+} handling we observed significantly upregulated expression and activity of SERCA within iPSC-cardiomyocytes of the diseased daughter only. Unraveling the underlying cause for this unusual pathogenic mechanism might shed more light onto the highly different disease onset of father and daughter. As we hypothesize a potential role of

an FLNC/ILK interaction affecting SERCA activity and we additionally identified an ILK variant within the diseased family members, focusing on the role of ILK would be the next step. This should include CRISPR/Cas9 gene editing to rescue the ILK variant to analyze the impact of this variant on SERCA activity. With these isogenic control cells potentially impaired ILK interactions could be unraveled e.g., by quantitative mass spectrometry approaches and pull-down assays in iPSC-derived cardiomyocytes and the primary myocardium of DCM1, as described for the FLNC variant as well. Furthermore, NGS analysis should identify altered signaling pathways based on the ILK variant. Additionally, IF staining should be performed to analyze localization of the ILK protein within the cell, to unravel potential mislocalization.

Additionally, we showed an increased ROS production, CaMKIIδ activity and a slight pro-arrhythmogenic potential in iPSC-cardiomyocytes of the diseased father as an isolated phenotype of this patient. As this observation might be an additional differing pathomechanism between the two patients it should be analyzed in the future. This would include more detailed analysis of the pro-arrhythmogenic potential by analyzing the oxidation of the CaMKIIδ, as a possible consequence of ROS production, explaining the increased CaMKIIδ activity. CaMKII inhibitors, as well as ROS scavengers would unravel the exact molecular players in DCM1 Ca^{2+} handling. MEA measurements would demonstrate a quantitative analysis of different arrhythmia types. Since a CX43 downregulation was demonstrated in this work for DCM1 and DCM3, which is reported to be induced by mitochondrial ROS production, mitochondrial ROS and general mitochondrial function should be analyzed in the future. This might unravel a direct link between increased ROS production, decreased CX43 expression and arrhythmia, as observed within this project, and possibly provide a potential therapeutic pathway. As we identified positive effects of Entresto treatment on ROS production in iPSC-cardiomyocytes of DCM1, role of Entresto treatment on CX43 expression and arrhythmia should be unraveled.

We used the iPSC-cardiomyocytes to generate 3D EHM. With this we were able to show impaired mechanics of the tissues, partially being restored in isogenic controls. First, these experiments need to be repeated to confirm the preliminary observations. However, these results suggest, that a restored sarcomere does not restore the mechanical function completely. As discussed, an altered Ca^{2+} sensitivity might play an additional role in impaired contractility of diseased tissues. Hence, this should be analyzed in 3D EHM, primary DCM1 myocardium, and iPSC-cardiomyocytes in more detail. This includes treatment with Mevacamten (myosin-inhibitor) to investigate a potentially increased Ca^{2+} sensitivity, as well as Omecamtiv (myosin-activator) (Fig. 58) to investigate a potentially decreased Ca^{2+} sensitivity. Analyzing the effects of Mevacamten and Omecamtiv on contractility, potential therapeutic strategies might be identified. Furthermore, single cell sequencing of the diseased and control EHM should be conducted to analyze possible different cardiomyocyte and CFB subpopulations. This for example could be based on impaired communication between cardiomyocytes and CFB due to observed FLNC-independent downregulation of CX43. This will be further analyzed in (1) EHM composed

of diseased and healthy cardiomyocytes and CFB in different combinations and (2) 2D co-culture experiments in which paracrine effects can be analyzed as well.

In line with this, we analyzed the role of single CFB in more detail. We identified decreased compaction and contraction of ECT composed of diseased CFB/iPSC-StC, which was restored to control level upon FLNC rescue. With this, we were able to identify a role of FLNC within CFB in general and a role of the FLNC variant in CFB on DCM pathophysiology in more detail. Based on this, the exact role of FLNC within CFB needs to be investigated in the future. This first would include IF staining to analyze for disruption of αSMA stress fibers, which would be similar to the sarcomeric disarray in cardiomyocytes. Additionally, as described before for cardiomyocytes, quantitative mass spectrometry, pull down assays and Western blots might be performed to analyze the function of FLNC in CFB in more detail.

Moreover, increased ECT stiffness was observed, which is, among others, an indicator for a fibrotic process, often shown in end-stage heart failure myocardium in general and observed in primary DCM1 LV myocardium as well. To investigate the fibrotic phenotype in more detail NGS and Western blot analysis of the diseased and normal ECT would shed light onto the exact ECM composition and expression e.g., of lysyl oxidases (cross-linking of ECM molecules) and would confirm the functional phenotype on a molecular level. So far, we were not able to recapitulate the increased ECT stiffness in ECT composed of diseased iPSC-StC. We postulate a mechanical memory mediated by epigenetic regulations upon chronic stress within the primary CFB, that induced the observed phenotype even in the absence of mechanical stress. Since iPSC-StC derive from iPSC reprogrammed from SFB not experiencing chronic stress within the heart, these cells lack the mechanical memory. In future experiments, iPSC-StC ECT could be casted around a stiff pole to apply a higher mechanical co-stress onto these tissues. This might trigger a fibrotic response in iPSC-StC ECT as shown for ECT composed of primary CFB. This would allow to evaluate if the FLNC variant might have any effects on stiffness and elasticity as well or if the observed phenotypes rather derived from e.g., cell-cell communication/signaling of cardiomyocytes and CFB in the heart. Moreover, absence of increased stiffness in iPSC-StC composed ECT might be based on a different CFB subtype or a rather immature phenotype, as shown for iPSC-cardiomyocytes as well. Hence, NGS analysis of the iPSC-derived cells in comparison to primary DCM1 CFB should be performed to analyze the exact CFB subtype and maturation stage.

Another aspect of this project was focusing on cardiomyocyte-specific telomere shortening in DCM patients. We indeed could demonstrate an increased telomere shortening in diseased iPSC-cardiomyocytes. However, the exact mechanism for this needs to be investigated in the future. Hypothesizing a role of the FLNC variant and the resulting sarcomeric disarray as underlying cause, which would be in line with other studies, analysis of telomere length of isogenic control iPSC-cardiomyocytes would be the next step. If this would be supportive, expression of shelterin proteins should be analyzed, which were shown to be downregulated upon deprotection of telomere ends induced by mechanical

stress (e.g., the sarcomeric disarray). Furthermore, inhibiting contraction by blebbistatin, as described by Chang *et al.* (Chang *et al.*, 2021), might reduce the mechanical-driven telomere shortening due to the sarcomeric disarray. This would give more evidence for the contribution of the FLNC variant onto telomere shortening.

6 References

Acharya, A., Baek, S.T., Huang, G., Eskiocak, B., Goetsch, S., Sung, C.Y., Banfi, S., Sauer, M.F., Olsen, G.S., Duffield, J.S., *et al.* (2012). The bHLH transcription factor Tcf21 is required for lineage-specific EMT of cardiac fibroblast progenitors. Development *139*, 2139-2149. 10.1242/dev.079970.

Adachi, K., and Scholer, H.R. (2012). Directing reprogramming to pluripotency by transcription factors. Curr Opin Genet Dev *22*, 416-422. 10.1016/j.gde.2012.07.001.

Ader, F., De Groote, P., Reant, P., Rooryck-Thambo, C., Dupin-Deguine, D., Rambaud, C., Khraiche, D., Perret, C., Pruny, J.F., Mathieu-Dramard, M., *et al.* (2019). FLNC pathogenic variants in patients with cardiomyopathies: Prevalence and genotype-phenotype correlations. Clin Genet *96*, 317-329. 10.1111/cge.13594.

Agarkova, I., Schoenauer, R., Ehler, E., Carlsson, L., Carlsson, E., Thornell, L.E., and Perriard, J.C. (2004). The molecular composition of the sarcomeric M-band correlates with muscle fiber type. Eur J Cell Biol *83*, 193-204. 10.1078/0171-9335-00383.

Agarwal, R., Paulo, J.A., Toepfer, C.N., Ewoldt, J.K., Sundaram, S., Chopra, A., Zhang, Q., Gorham, J., DePalma, S.R., Chen, C.S., *et al.* (2021). Filamin C Cardiomyopathy Variants Cause Protein and Lysosome Accumulation. Circ Res *129*, 751-766. 10.1161/CIRCRESAHA.120.317076.

Ahmad, S., Tirilomis, P., Pabel, S., Dybkova, N., Hartmann, N., Molina, C.E., Tirilomis, T., Kutschka, I., Frey, N., Maier, L.S., *et al.* (2019). The functional consequences of sodium channel NaV 1.8 in human left ventricular hypertrophy. ESC Heart Fail *6*, 154-163. 10.1002/ehf2.12378.

Ahmed, R.E., Anzai, T., Chanthra, N., and Uosaki, H. (2020). A Brief Review of Current Maturation Methods for Human Induced Pluripotent Stem Cells-Derived Cardiomyocytes. Front Cell Dev Biol *8*, 178. 10.3389/fcell.2020.00178.

Ai, X., Curran, J.W., Shannon, T.R., Bers, D.M., and Pogwizd, S.M. (2005). Ca2+/calmodulin-dependent protein kinase modulates cardiac ryanodine receptor phosphorylation and sarcoplasmic reticulum Ca2+ leak in heart failure. Circ Res *97*, 1314-1322. 10.1161/01.RES.0000194329.41863.89.

Akopian, A.N., Sivilotti, L., and Wood, J.N. (1996). A tetrodotoxin-resistant voltage-gated sodium channel expressed by sensory neurons. Nature *379*, 257-262. 10.1038/379257a0.

Ali, S.R., Ranjbarvaziri, S., Talkhabi, M., Zhao, P., Subat, A., Hojjat, A., Kamran, P., Muller, A.M., Volz, K.S., Tang, Z., *et al.* (2014). Developmental heterogeneity of cardiac fibroblasts does not predict pathological proliferation and activation. Circ Res *115*, 625-635. 10.1161/CIRCRESAHA.115.303794.

Ambrosi, C.M., Sadananda, G., Han, J.L., and Entcheva, E. (2019). Adeno-Associated Virus Mediated Gene Delivery: Implications for Scalable in vitro and in vivo Cardiac Optogenetic Models. Front Physiol *10*, 168. 10.3389/fphys.2019.00168.

Arnoldi, R., Chaponnier, C., Gabbiani, G., and Hinz, B. (2012). Chapter 88 - Heterogeneity of Smooth Muscle. In Muscle, J.A. Hill, and E.N. Olson, eds. (Academic Press), pp. 1183-1195. https://doi.org/10.1016/B978-0-12-381510-1.00088-0.

Ashpole, N.M., Herren, A.W., Ginsburg, K.S., Brogan, J.D., Johnson, D.E., Cummins, T.R., Bers, D.M., and Hudmon, A. (2012). Ca2+/calmodulin-dependent protein kinase II (CaMKII) regulates cardiac sodium channel NaV1.5 gating by multiple phosphorylation sites. J Biol Chem *287*, 19856-19869. 10.1074/jbc.M111.322537.

Aujla, P.K., and Kassiri, Z. (2021). Diverse origins and activation of fibroblasts in cardiac fibrosis. Cell Signal *78*, 109869. 10.1016/j.cellsig.2020.109869.

Badreldin, H.A., Aldosari, N., Alnashwan, L., Almutairi, T., Yousif, N., Alsulaiman, K., Aljuhani, O., Hafiz, A., and Alshaya, O. (2022). What the near Future Holds for Sacubitril/Valsartan: A Summary of Major Ongoing Studies. J Cardiovasc Dev Dis *9*. 10.3390/jcdd9020054.

Banerjee, I., Yekkala, K., Borg, T.K., and Baudino, T.A. (2006). Dynamic interactions between myocytes, fibroblasts, and extracellular matrix. Ann N Y Acad Sci *1080*, 76-84. 10.1196/annals.1380.007.

Bang, M.L., Bogomolovas, J., and Chen, J. (2022). Understanding the molecular basis of cardiomyopathy. Am J Physiol Heart Circ Physiol *322*, H181-H233. 10.1152/ajpheart.00562.2021.

Bao, X., Lian, X., Hacker, T.A., Schmuck, E.G., Qian, T., Bhute, V.J., Han, T., Shi, M., Drowley, L., Plowright, A., *et al.* (2016). Long-term self-renewing human epicardial cells generated from pluripotent stem cells under defined xeno-free conditions. Nat Biomed Eng *1*. 10.1038/s41551-016-0003.

Barrangou, R., and Doudna, J.A. (2016). Applications of CRISPR technologies in research and beyond. Nat Biotechnol *34*, 933-941. 10.1038/nbt.3659.

Batalov, I., and Feinberg, A.W. (2015). Differentiation of Cardiomyocytes from Human Pluripotent Stem Cells Using Monolayer Culture. Biomark Insights *10*, 71-76. 10.4137/BMI.S20050.

Begay, R.L., Graw, S.L., Sinagra, G., Asimaki, A., Rowland, T.J., Slavov, D.B., Gowan, K., Jones, K.L., Brun, F., Merlo, M., *et al.* (2018). Filamin C Truncation Mutations Are Associated With Arrhythmogenic Dilated Cardiomyopathy and Changes in the Cell-Cell Adhesion Structures. JACC Clin Electrophysiol *4*, 504-514. 10.1016/j.jacep.2017.12.003.

Begay, R.L., Tharp, C.A., Martin, A., Graw, S.L., Sinagra, G., Miani, D., Sweet, M.E., Slavov, D.B., Stafford, N., Zeller, M.J., *et al.* (2016). FLNC Gene Splice Mutations Cause Dilated Cardiomyopathy. JACC Basic Transl Sci *1*, 344-359. 10.1016/j.jacbts.2016.05.004.

Ben Jehuda, R., Shemer, Y., and Binah, O. (2018). Genome Editing in Induced Pluripotent Stem Cells using CRISPR/Cas9. Stem Cell Rev Rep *14*, 323-336. 10.1007/s12015-018-9811-3.

Bengel, P., Dybkova, N., Tirilomis, P., Ahmad, S., Hartmann, N., B, A.M., Krekeler, M.C., Maurer, W., Pabel, S., Trum, M., *et al.* (2021). Detrimental proarrhythmogenic interaction of Ca(2+)/calmodulin-dependent protein kinase II and NaV1.8 in heart failure. Nat Commun *12*, 6586. 10.1038/s41467-021-26690-1.

Benjamin, E.J., Blaha, M.J., Chiuve, S.E., Cushman, M., Das, S.R., Deo, R., de Ferranti, S.D., Floyd, J., Fornage, M., Gillespie, C., *et al.* (2017). Heart Disease and Stroke Statistics-2017 Update: A Report From the American Heart Association. Circulation *135*, e146-e603. 10.1161/CIR.0000000000000485.

Bers, D.M. (2002). Cardiac excitation-contraction coupling. Nature *415*, 198-205. 10.1038/415198a.

Bers, D.M. (2008). Calcium cycling and signaling in cardiac myocytes. Annu Rev Physiol *70*, 23-49. 10.1146/annurev.physiol.70.113006.100455.

Bers, D.M., and Borlaug, B.A. (2018). Mechanisms of Cardiac Contraction and Relaxation. Braunwald's Heart Disease: A Textbook of Cardiovascular Medicine. 11 ed. Elsevier.

Beuckelmann, D.J., Nabauer, M., and Erdmann, E. (1992). Intracellular calcium handling in isolated ventricular myocytes from patients with terminal heart failure. Circulation *85*, 1046-1055. 10.1161/01.cir.85.3.1046.

Bhaya, D., Davison, M., and Barrangou, R. (2011). CRISPR-Cas systems in bacteria and archaea: versatile small RNAs for adaptive defense and regulation. Annu Rev Genet *45*, 273-297. 10.1146/annurev-genet-110410-132430.

Bishop, S.P., Zhang, J., and Ye, L. (2022). Cardiomyocyte Proliferation from Fetal- to Adult- and from Normal- to Hypertrophy and Failing Hearts. Biology (Basel) *11*. 10.3390/biology11060880.

Blagova, O., Alieva, I., Kogan, E., Zaytsev, A., Sedov, V., Chernyavskiy, S., Surikova, Y., Kotov, I., and Zaklyazminskaya, E.V. (2020). Mixed Hypertrophic and Dilated Phenotype of Cardiomyopathy in a Patient With Homozygous In-Frame Deletion in the MyBPC3 Gene Treated as Myocarditis for a Long Time. Front Pharmacol *11*, 579450. 10.3389/fphar.2020.579450.

Bolotin, A., Quinquis, B., Sorokin, A., and Ehrlich, S.D. (2005). Clustered regularly interspaced short palindrome repeats (CRISPRs) have spacers of extrachromosomal origin. Microbiology (Reading) *151*, 2551-2561. 10.1099/mic.0.28048-0.

Borchert, T., Hubscher, D., Guessoum, C.I., Lam, T.D., Ghadri, J.R., Schellinger, I.N., Tiburcy, M., Liaw, N.Y., Li, Y., Haas, J., *et al.* (2017). Catecholamine-Dependent beta-Adrenergic Signaling in a Pluripotent Stem Cell Model of Takotsubo Cardiomyopathy. J Am Coll Cardiol *70*, 975-991. 10.1016/j.jacc.2017.06.061.

Bosman, F.T., and Stamenkovic, I. (2003). Functional structure and composition of the extracellular matrix. J Pathol *200*, 423-428. 10.1002/path.1437.

Boukhelifa, M., Moza, M., Johansson, T., Rachlin, A., Parast, M., Huttelmaier, S., Roy, P., Jockusch, B.M., Carpen, O., Karlsson, R., and Otey, C.A. (2006). The proline-rich protein palladin is a binding partner for profilin. FEBS J *273*, 26-33. 10.1111/j.1742-4658.2005.05036.x.

Bouzegrhane, F., and Thibault, G. (2002). Is angiotensin II a proliferative factor of cardiac fibroblasts? Cardiovasc Res *53*, 304-312. 10.1016/s0008-6363(01)00448-5.

Brauch, K.M., Karst, M.L., Herron, K.J., de Andrade, M., Pellikka, P.A., Rodeheffer, R.J., Michels, V.V., and Olson, T.M. (2009). Mutations in ribonucleic acid binding protein gene cause familial dilated cardiomyopathy. J Am Coll Cardiol *54*, 930-941. 10.1016/j.jacc.2009.05.038.

Bretherton, R., Bugg, D., Olszewski, E., and Davis, J. (2020). Regulators of cardiac fibroblast cell state. Matrix Biol *91-92*, 117-135. 10.1016/j.matbio.2020.04.002.

Brodehl, A., Ebbinghaus, H., Deutsch, M.A., Gummert, J., Gartner, A., Ratnavadivel, S., and Milting, H. (2019a). Human Induced Pluripotent Stem-Cell-Derived Cardiomyocytes as Models for Genetic Cardiomyopathies. Int J Mol Sci *20*. 10.3390/ijms20184381.

Brodehl, A., Ferrier, R.A., Hamilton, S.J., Greenway, S.C., Brundler, M.A., Yu, W., Gibson, W.T., McKinnon, M.L., McGillivray, B., Alvarez, N., *et al.* (2016). Mutations in FLNC are Associated with Familial Restrictive Cardiomyopathy. Hum Mutat *37*, 269-279. 10.1002/humu.22942.

Brodehl, A., Rezazadeh, S., Williams, T., Munsie, N.M., Liedtke, D., Oh, T., Ferrier, R., Shen, Y., Jones, S.J.M., Stiegler, A.L., *et al.* (2019b). Mutations in ILK, encoding integrin-linked kinase, are associated with arrhythmogenic cardiomyopathy. Transl Res *208*, 15-29. 10.1016/j.trsl.2019.02.004.

Buenrostro, J.D., Wu, B., Chang, H.Y., and Greenleaf, W.J. (2015). ATAC-seq: A Method for Assaying Chromatin Accessibility Genome-Wide. Curr Protoc Mol Biol *109*, 21 29 21-21 29 29. 10.1002/0471142727.mb2129s109.

Buggisch, M., Ateghang, B., Ruhe, C., Strobel, C., Lange, S., Wartenberg, M., and Sauer, H. (2007). Stimulation of ES-cell-derived cardiomyogenesis and neonatal cardiac cell

proliferation by reactive oxygen species and NADPH oxidase. J Cell Sci *120*, 885-894. 10.1242/jcs.03386.
Burgoyne, J.R., Mongue-Din, H., Eaton, P., and Shah, A.M. (2012). Redox signaling in cardiac physiology and pathology. Circ Res *111*, 1091-1106. 10.1161/CIRCRESAHA.111.255216.
Burridge, P.W., Keller, G., Gold, J.D., and Wu, J.C. (2012). Production of de novo cardiomyocytes: human pluripotent stem cell differentiation and direct reprogramming. Cell Stem Cell *10*, 16-28. 10.1016/j.stem.2011.12.013.
Burridge, P.W., Matsa, E., Shukla, P., Lin, Z.C., Churko, J.M., Ebert, A.D., Lan, F., Diecke, S., Huber, B., Mordwinkin, N.M., *et al.* (2014). Chemically defined generation of human cardiomyocytes. Nat Methods *11*, 855-860. 10.1038/nmeth.2999.
Burridge, P.W., and Zambidis, E.T. (2013). Highly efficient directed differentiation of human induced pluripotent stem cells into cardiomyocytes. Methods Mol Biol *997*, 149-161. 10.1007/978-1-62703-348-0_12.
Cadet, J.S., and Kamp, T.J. (2017). A Recipe for T-Tubules in Human iPS Cell-Derived Cardiomyocytes. Circ Res *121*, 1294-1295. 10.1161/CIRCRESAHA.117.312177.
Cahill, T.J., Ashrafian, H., and Watkins, H. (2013). Genetic cardiomyopathies causing heart failure. Circ Res *113*, 660-675. 10.1161/CIRCRESAHA.113.300282.
Canela, A., Vera, E., Klatt, P., and Blasco, M.A. (2007). High-throughput telomere length quantification by FISH and its application to human population studies. Proc Natl Acad Sci U S A *104*, 5300-5305. 10.1073/pnas.0609367104.
Chang, A.C., Ong, S.G., LaGory, E.L., Kraft, P.E., Giaccia, A.J., Wu, J.C., and Blau, H.M. (2016). Telomere shortening and metabolic compromise underlie dystrophic cardiomyopathy. Proc Natl Acad Sci U S A *113*, 13120-13125. 10.1073/pnas.1615340113.
Chang, A.C.Y., and Blau, H.M. (2018). Short telomeres - A hallmark of heritable cardiomyopathies. Differentiation *100*, 31-36. 10.1016/j.diff.2018.02.001.
Chang, A.C.Y., Chang, A.C.H., Kirillova, A., Sasagawa, K., Su, W., Weber, G., Lin, J., Termglinchan, V., Karakikes, I., Seeger, T., *et al.* (2018). Telomere shortening is a hallmark of genetic cardiomyopathies. Proc Natl Acad Sci U S A *115*, 9276-9281. 10.1073/pnas.1714538115.
Chang, A.C.Y., Pardon, G., Chang, A.C.H., Wu, H., Ong, S.G., Eguchi, A., Ancel, S., Holbrook, C., Ramunas, J., Ribeiro, A.J.S., *et al.* (2021). Increased tissue stiffness triggers contractile dysfunction and telomere shortening in dystrophic cardiomyocytes. Stem Cell Reports *16*, 2169-2181. 10.1016/j.stemcr.2021.04.018.
Chen, B., Dodge, M.E., Tang, W., Lu, J., Ma, Z., Fan, C.W., Wei, S., Hao, W., Kilgore, J., Williams, N.S., *et al.* (2009). Small molecule-mediated disruption of Wnt-dependent signaling in tissue regeneration and cancer. Nat Chem Biol *5*, 100-107. 10.1038/nchembio.137.
Chen, G., Gulbranson, D.R., Hou, Z., Bolin, J.M., Ruotti, V., Probasco, M.D., Smuga-Otto, K., Howden, S.E., Diol, N.R., Propson, N.E., *et al.* (2011). Chemically defined conditions for human iPSC derivation and culture. Nat Methods *8*, 424-429. 10.1038/nmeth.1593.
Chen, Q., Zhang, H., Liu, Y., Adams, S., Eilken, H., Stehling, M., Corada, M., Dejana, E., Zhou, B., and Adams, R.H. (2016). Endothelial cells are progenitors of cardiac pericytes and vascular smooth muscle cells. Nat Commun *7*, 12422. 10.1038/ncomms12422.
Chung, J.H., Biesiadecki, B.J., Ziolo, M.T., Davis, J.P., and Janssen, P.M. (2016). Myofilament Calcium Sensitivity: Role in Regulation of In vivo Cardiac Contraction and Relaxation. Front Physiol *7*, 562. 10.3389/fphys.2016.00562.

Chylinski, K., Makarova, K.S., Charpentier, E., and Koonin, E.V. (2014). Classification and evolution of type II CRISPR-Cas systems. Nucleic Acids Res *42*, 6091-6105. 10.1093/nar/gku241.

Ciarambino, T., Menna, G., Sansone, G., and Giordano, M. (2021). Cardiomyopathies: An Overview. Int J Mol Sci *22*. 10.3390/ijms22147722.

Cirino, A.L., and Ho, C. (1993). Hypertrophic Cardiomyopathy Overview. In GeneReviews((R)), M.P. Adam, G.M. Mirzaa, R.A. Pagon, S.E. Wallace, L.J.H. Bean, K.W. Gripp, and A. Amemiya, eds.

Clark, K.A., McElhinny, A.S., Beckerle, M.C., and Gregorio, C.C. (2002). Striated muscle cytoarchitecture: an intricate web of form and function. Annu Rev Cell Dev Biol *18*, 637-706. 10.1146/annurev.cellbio.18.012502.105840.

Cojan-Minzat, B.O., Zlibut, A., and Agoston-Coldea, L. (2021). Non-ischemic dilated cardiomyopathy and cardiac fibrosis. Heart Fail Rev *26*, 1081-1101. 10.1007/s10741-020-09940-0.

Collier, P., Watson, C.J., van Es, M.H., Phelan, D., McGorrian, C., Tolan, M., Ledwidge, M.T., McDonald, K.M., and Baugh, J.A. (2012). Getting to the heart of cardiac remodeling; how collagen subtypes may contribute to phenotype. J Mol Cell Cardiol *52*, 148-153. 10.1016/j.yjmcc.2011.10.002.

Cong, L., Ran, F.A., Cox, D., Lin, S., Barretto, R., Habib, N., Hsu, P.D., Wu, X., Jiang, W., Marraffini, L.A., and Zhang, F. (2013). Multiplex genome engineering using CRISPR/Cas systems. Science *339*, 819-823. 10.1126/science.1231143.

Correia, C., Koshkin, A., Duarte, P., Hu, D., Teixeira, A., Domian, I., Serra, M., and Alves, P.M. (2017). Distinct carbon sources affect structural and functional maturation of cardiomyocytes derived from human pluripotent stem cells. Sci Rep *7*, 8590. 10.1038/s41598-017-08713-4.

Crocini, C., and Gotthardt, M. (2021). Cardiac sarcomere mechanics in health and disease. Biophys Rev *13*, 637-652. 10.1007/s12551-021-00840-7.

Cyganek, L., Tiburcy, M., Sekeres, K., Gerstenberg, K., Bohnenberger, H., Lenz, C., Henze, S., Stauske, M., Salinas, G., Zimmermann, W.H., *et al.* (2018). Deep phenotyping of human induced pluripotent stem cell-derived atrial and ventricular cardiomyocytes. JCI Insight *3*. 10.1172/jci.insight.99941.

D'Oria, R., Schipani, R., Leonardini, A., Natalicchio, A., Perrini, S., Cignarelli, A., Laviola, L., and Giorgino, F. (2020). The Role of Oxidative Stress in Cardiac Disease: From Physiological Response to Injury Factor. Oxid Med Cell Longev *2020*, 5732956. 10.1155/2020/5732956.

Dal Ferro, M., Severini, G.M., Gigli, M., Mestroni, L., and Sinagra, G. (2019). Genetics of Dilated Cardiomyopathy: Current Knowledge and Future Perspectives. In Dilated Cardiomyopathy: From Genetics to Clinical Management, G. Sinagra, M. Merlo, and B. Pinamonti, eds. pp. 45-69. 10.1007/978-3-030-13864-6_5.

Danila, C.I., and Hamilton, S.L. (2004). Phosphorylation of ryanodine receptors. Biol Res *37*, 521-525. 10.4067/s0716-97602004000400005.

de Lange, F.J., Moorman, A.F., Anderson, R.H., Manner, J., Soufan, A.T., de Gier-de Vries, C., Schneider, M.D., Webb, S., van den Hoff, M.J., and Christoffels, V.M. (2004). Lineage and morphogenetic analysis of the cardiac valves. Circ Res *95*, 645-654. 10.1161/01.RES.0000141429.13560.cb.

De Paris, V., Biondi, F., Stolfo, D., Merlo, M., and Sinagra, G. (2019). Pathophysiology. In Dilated Cardiomyopathy: From Genetics to Clinical Management, G. Sinagra, M. Merlo, and B. Pinamonti, eds. pp. 17-25. 10.1007/978-3-030-13864-6_3.

Dedkova, E.N., and Blatter, L.A. (2013). Calcium signaling in cardiac mitochondria. J Mol Cell Cardiol *58*, 125-133. 10.1016/j.yjmcc.2012.12.021.

Deveau, H., Barrangou, R., Garneau, J.E., Labonte, J., Fremaux, C., Boyaval, P., Romero, D.A., Horvath, P., and Moineau, S. (2008). Phage response to CRISPR-encoded resistance in Streptococcus thermophilus. J Bacteriol *190*, 1390-1400. 10.1128/JB.01412-07.

Dick, E., Rajamohan, D., Ronksley, J., and Denning, C. (2010). Evaluating the utility of cardiomyocytes from human pluripotent stem cells for drug screening. Biochem Soc Trans *38*, 1037-1045. 10.1042/BST0381037.

Downing, T.L., Soto, J., Morez, C., Houssin, T., Fritz, A., Yuan, F., Chu, J., Patel, S., Schaffer, D.V., and Li, S. (2013). Biophysical regulation of epigenetic state and cell reprogramming. Nat Mater *12*, 1154-1162. 10.1038/nmat3777.

Dupont, E., Matsushita, T., Kaba, R.A., Vozzi, C., Coppen, S.R., Khan, N., Kaprielian, R., Yacoub, M.H., and Severs, N.J. (2001). Altered connexin expression in human congestive heart failure. J Mol Cell Cardiol *33*, 359-371. 10.1006/jmcc.2000.1308.

Dybkova, N., Ahmad, S., Pabel, S., Tirilomis, P., Hartmann, N., Fischer, T.H., Bengel, P., Tirilomis, T., Ljubojevic, S., Renner, A., *et al.* (2018). Differential regulation of sodium channels as a novel proarrhythmic mechanism in the human failing heart. Cardiovasc Res *114*, 1728-1737. 10.1093/cvr/cvy152.

Ebert, A.D., Liang, P., and Wu, J.C. (2012). Induced pluripotent stem cells as a disease modeling and drug screening platform. J Cardiovasc Pharmacol *60*, 408-416. 10.1097/FJC.0b013e318247f642.

Eden, M., and Frey, N. (2021). Cardiac Filaminopathies: Illuminating the Divergent Role of Filamin C Mutations in Human Cardiomyopathy. J Clin Med *10*. 10.3390/jcm10040577.

Ehrlich, H.P., Gabbiani, G., and Meda, P. (2000). Cell coupling modulates the contraction of fibroblast-populated collagen lattices. J Cell Physiol *184*, 86-92. 10.1002/(SICI)1097-4652(200007)184:1<86::AID-JCP9>3.0.CO;2-5.

Eijgenraam, T.R., Sillje, H.H.W., and de Boer, R.A. (2020). Current understanding of fibrosis in genetic cardiomyopathies. Trends Cardiovasc Med *30*, 353-361. 10.1016/j.tcm.2019.09.003.

Eisner, D., Bode, E., Venetucci, L., and Trafford, A. (2013). Calcium flux balance in the heart. J Mol Cell Cardiol *58*, 110-117. 10.1016/j.yjmcc.2012.11.017.

Eisner, D.A., Caldwell, J.L., Kistamas, K., and Trafford, A.W. (2017). Calcium and Excitation-Contraction Coupling in the Heart. Circ Res *121*, 181-195. 10.1161/CIRCRESAHA.117.310230.

Eisner, D.A., Caldwell, J.L., Trafford, A.W., and Hutchings, D.C. (2020). The Control of Diastolic Calcium in the Heart: Basic Mechanisms and Functional Implications. Circ Res *126*, 395-412. 10.1161/CIRCRESAHA.119.315891.

Eisner, D.A., Trafford, A.W., Diaz, M.E., Overend, C.L., and O'Neill, S.C. (1998). The control of Ca release from the cardiac sarcoplasmic reticulum: regulation versus autoregulation. Cardiovasc Res *38*, 589-604. 10.1016/s0008-6363(98)00062-5.

Elliott, P., Andersson, B., Arbustini, E., Bilinska, Z., Cecchi, F., Charron, P., Dubourg, O., Kuhl, U., Maisch, B., McKenna, W.J., *et al.* (2008). Classification of the cardiomyopathies: a position statement from the European Society Of Cardiology Working Group on Myocardial and Pericardial Diseases. Eur Heart J *29*, 270-276. 10.1093/eurheartj/ehm342.

Elliott, P., O'Mahony, C., Syrris, P., Evans, A., Rivera Sorensen, C., Sheppard, M.N., Carr-White, G., Pantazis, A., and McKenna, W.J. (2010). Prevalence of desmosomal protein gene mutations in patients with dilated cardiomyopathy. Circ Cardiovasc Genet *3*, 314-322. 10.1161/CIRCGENETICS.110.937805.

Emanuelli, G., Zoccarato, A., Reumiller, C.M., Papadopoulos, A., Chong, M., Rebs, S., Betteridge, K., Beretta, M., Streckfuss-Bomeke, K., and Shah, A.M. (2022). A roadmap for the characterization of energy metabolism in human cardiomyocytes derived from induced pluripotent stem cells. J Mol Cell Cardiol *164*, 136-147. 10.1016/j.yjmcc.2021.12.001.
Eschenhagen, T. (2018). A new concept of fibroblast dynamics in post-myocardial infarction remodeling. J Clin Invest *128*, 1731-1733. 10.1172/JCI121079.
Eschenhagen, T., and Carrier, L. (2019). Cardiomyopathy phenotypes in human-induced pluripotent stem cell-derived cardiomyocytes-a systematic review. Pflugers Arch *471*, 755-768. 10.1007/s00424-018-2214-0.
Evans, M.J., and Kaufman, M.H. (1981). Establishment in culture of pluripotential cells from mouse embryos. Nature *292*, 154-156. 10.1038/292154a0.
Feyen, D.A.M., McKeithan, W.L., Bruyneel, A.A.N., Spiering, S., Hormann, L., Ulmer, B., Zhang, H., Briganti, F., Schweizer, M., Hegyi, B., *et al.* (2020). Metabolic Maturation Media Improve Physiological Function of Human iPSC-Derived Cardiomyocytes. Cell Rep *32*, 107925. 10.1016/j.celrep.2020.107925.
Fineran, P.C., and Charpentier, E. (2012). Memory of viral infections by CRISPR-Cas adaptive immune systems: acquisition of new information. Virology *434*, 202-209. 10.1016/j.virol.2012.10.003.
Fomin, A., Gartner, A., Cyganek, L., Tiburcy, M., Tuleta, I., Wellers, L., Folsche, L., Hobbach, A.J., von Frieling-Salewsky, M., Unger, A., *et al.* (2021). Truncated titin proteins and titin haploinsufficiency are targets for functional recovery in human cardiomyopathy due to TTN mutations. Sci Transl Med *13*, eabd3079. 10.1126/scitranslmed.abd3079.
Frangoul, H., Altshuler, D., Cappellini, M.D., Chen, Y.S., Domm, J., Eustace, B.K., Foell, J., de la Fuente, J., Grupp, S., Handgretinger, R., *et al.* (2021). CRISPR-Cas9 Gene Editing for Sickle Cell Disease and beta-Thalassemia. N Engl J Med *384*, 252-260. 10.1056/NEJMoa2031054.
Frazier, A.H., Ramirez-Correa, G.A., and Murphy, A.M. (2011). Molecular mechanisms of sarcomere dysfunction in dilated and hypertrophic cardiomyopathy. Prog Pediatr Cardiol *31*, 29-33. 10.1016/j.ppedcard.2010.11.006.
Fu, S., Fu, C., Zhou, Q., Lin, R., Ouyang, H., Wang, M., Sun, Y., Liu, Y., and Zhao, Y. (2020). Widespread arginine phosphorylation in human cells—a novel protein PTM revealed by mass spectrometry. Science China Chemistry *63*, 341-346. 10.1007/s11426-019-9656-7.
Fu, X., Khalil, H., Kanisicak, O., Boyer, J.G., Vagnozzi, R.J., Maliken, B.D., Sargent, M.A., Prasad, V., Valiente-Alandi, I., Blaxall, B.C., and Molkentin, J.D. (2018). Specialized fibroblast differentiated states underlie scar formation in the infarcted mouse heart. J Clin Invest *128*, 2127-2143. 10.1172/JCI98215.
Funakoshi, S., Fernandes, I., Mastikhina, O., Wilkinson, D., Tran, T., Dhahri, W., Mazine, A., Yang, D., Burnett, B., Lee, J., *et al.* (2021). Generation of mature compact ventricular cardiomyocytes from human pluripotent stem cells. Nat Commun *12*, 3155. 10.1038/s41467-021-23329-z.
Furst, D.O., Goldfarb, L.G., Kley, R.A., Vorgerd, M., Olive, M., and van der Ven, P.F. (2013). Filamin C-related myopathies: pathology and mechanisms. Acta Neuropathol *125*, 33-46. 10.1007/s00401-012-1054-9.
Fusaki, N., Ban, H., Nishiyama, A., Saeki, K., and Hasegawa, M. (2009). Efficient induction of transgene-free human pluripotent stem cells using a vector based on Sendai virus, an RNA virus that does not integrate into the host genome. Proc Jpn Acad Ser B Phys Biol Sci *85*, 348-362. 10.2183/pjab.85.348.

Gando, I., Williams, N., Fishman, G.I., Sampson, B.A., Tang, Y., and Coetzee, W.A. (2019). Functional characterization of SCN10A variants in several cases of sudden unexplained death. Forensic Sci Int *301*, 289-298. 10.1016/j.forsciint.2019.05.042.

Gautel, M., and Djinovic-Carugo, K. (2016). The sarcomeric cytoskeleton: from molecules to motion. J Exp Biol *219*, 135-145. 10.1242/jeb.124941.

Gellens, M.E., George, A.L., Jr., Chen, L.Q., Chahine, M., Horn, R., Barchi, R.L., and Kallen, R.G. (1992). Primary structure and functional expression of the human cardiac tetrodotoxin-insensitive voltage-dependent sodium channel. Proc Natl Acad Sci U S A *89*, 554-558. 10.1073/pnas.89.2.554.

Giacomelli, E., Meraviglia, V., Campostrini, G., Cochrane, A., Cao, X., van Helden, R.W.J., Krotenberg Garcia, A., Mircea, M., Kostidis, S., Davis, R.P., *et al.* (2020). Human-iPSC-Derived Cardiac Stromal Cells Enhance Maturation in 3D Cardiac Microtissues and Reveal Non-cardiomyocyte Contributions to Heart Disease. Cell Stem Cell *26*, 862-879 e811. 10.1016/j.stem.2020.05.004.

Gomez, J., Lorca, R., Reguero, J.R., Moris, C., Martin, M., Tranche, S., Alonso, B., Iglesias, S., Alvarez, V., Diaz-Molina, B., *et al.* (2017). Screening of the Filamin C Gene in a Large Cohort of Hypertrophic Cardiomyopathy Patients. Circ Cardiovasc Genet *10*. 10.1161/CIRCGENETICS.116.001584.

Gontier, Y., Taivainen, A., Fontao, L., Sonnenberg, A., van der Flier, A., Carpen, O., Faulkner, G., and Borradori, L. (2005). The Z-disc proteins myotilin and FATZ-1 interact with each other and are connected to the sarcolemma via muscle-specific filamins. J Cell Sci *118*, 3739-3749. 10.1242/jcs.02484.

Gorska, A., and Mazur, A.J. (2022). Integrin-linked kinase (ILK): the known vs. the unknown and perspectives. Cell Mol Life Sci *79*, 100. 10.1007/s00018-021-04104-1.

Gottlich, B., Reichenberger, S., Feldmann, E., and Pfeiffer, P. (1998). Rejoining of DNA double-strand breaks in vitro by single-strand annealing. Eur J Biochem *258*, 387-395. 10.1046/j.1432-1327.1998.2580387.x.

Grassi, S., Campuzano, O., Coll, M., Cazzato, F., Sarquella-Brugada, G., Rossi, R., Arena, V., Brugada, J., Brugada, R., and Oliva, A. (2021). Update on the Diagnostic Pitfalls of Autopsy and Post-Mortem Genetic Testing in Cardiomyopathies. Int J Mol Sci *22*. 10.3390/ijms22084124.

Groen, M., Lopez-Davila, A.J., Zittrich, S., Pfitzer, G., and Stehle, R. (2020). Hypertrophic and Dilated Cardiomyopathy-Associated Troponin T Mutations R130C and DeltaK210 Oppositely Affect Length-Dependent Calcium Sensitivity of Force Generation. Front Physiol *11*, 516. 10.3389/fphys.2020.00516.

Grynkiewicz, G., Poenie, M., and Tsien, R.Y. (1985). A new generation of Ca2+ indicators with greatly improved fluorescence properties. J Biol Chem *260*, 3440-3450.

Guadix, J.A., Orlova, V.V., Giacomelli, E., Bellin, M., Ribeiro, M.C., Mummery, C.L., Perez-Pomares, J.M., and Passier, R. (2017). Human Pluripotent Stem Cell Differentiation into Functional Epicardial Progenitor Cells. Stem Cell Reports *9*, 1754-1764. 10.1016/j.stemcr.2017.10.023.

Guan, K., Nayernia, K., Maier, L.S., Wagner, S., Dressel, R., Lee, J.H., Nolte, J., Wolf, F., Li, M., Engel, W., and Hasenfuss, G. (2006). Pluripotency of spermatogonial stem cells from adult mouse testis. Nature *440*, 1199-1203. 10.1038/nature04697.

Guo, F., Sun, Y., Wang, X., Wang, H., Wang, J., Gong, T., Chen, X., Zhang, P., Su, L., Fu, G., *et al.* (2019). Patient-Specific and Gene-Corrected Induced Pluripotent Stem Cell-Derived Cardiomyocytes Elucidate Single-Cell Phenotype of Short QT Syndrome. Circ Res *124*, 66-78. 10.1161/CIRCRESAHA.118.313518.

Guo, T., Zhang, T., Mestril, R., and Bers, D.M. (2006). Ca2+/Calmodulin-dependent protein kinase II phosphorylation of ryanodine receptor does affect calcium sparks in mouse ventricular myocytes. Circ Res *99*, 398-406. 10.1161/01.RES.0000236756.06252.13.
Guo, Y., and Pu, W.T. (2020). Cardiomyocyte Maturation: New Phase in Development. Circ Res *126*, 1086-1106. 10.1161/CIRCRESAHA.119.315862.
Haas, J., Frese, K.S., Peil, B., Kloos, W., Keller, A., Nietsch, R., Feng, Z., Muller, S., Kayvanpour, E., Vogel, B., *et al.* (2015). Atlas of the clinical genetics of human dilated cardiomyopathy. Eur Heart J *36*, 1123-1135a. 10.1093/eurheartj/ehu301.
Halasi, M., Wang, M., Chavan, T.S., Gaponenko, V., Hay, N., and Gartel, A.L. (2013). ROS inhibitor N-acetyl-L-cysteine antagonizes the activity of proteasome inhibitors. Biochem J *454*, 201-208. 10.1042/BJ20130282.
Hall, C., Gehmlich, K., Denning, C., and Pavlovic, D. (2021). Complex Relationship Between Cardiac Fibroblasts and Cardiomyocytes in Health and Disease. J Am Heart Assoc *10*, e019338. 10.1161/JAHA.120.019338.
Hall, C.L., Gurha, P., Sabater-Molina, M., Asimaki, A., Futema, M., Lovering, R.C., Suarez, M.P., Aguilera, B., Molina, P., Zorio, E., *et al.* (2020). RNA sequencing-based transcriptome profiling of cardiac tissue implicates novel putative disease mechanisms in FLNC-associated arrhythmogenic cardiomyopathy. Int J Cardiol *302*, 124-130. 10.1016/j.ijcard.2019.12.002.
Hall, P.A., and Watt, F.M. (1989). Stem cells: the generation and maintenance of cellular diversity. Development *106*, 619-633. 10.1242/dev.106.4.619.
Hamrick, S.K., John Kim, C.S., Tester, D.J., Giudicessi, J.R., and Ackerman, M.J. (2022). Patient-specific, re-engineered cardiomyocyte model confirms the circumstance-dependent arrhythmia risk associated with the African-specific common SCN5A polymorphism p.S1103Y: Implications for the increased sudden deaths observed in black individuals during the COVID-19 pandemic. Heart Rhythm *19*, 822-827. 10.1016/j.hrthm.2021.12.029.
Hanna, J.H., Saha, K., and Jaenisch, R. (2010). Pluripotency and cellular reprogramming: facts, hypotheses, unresolved issues. Cell *143*, 508-525. 10.1016/j.cell.2010.10.008.
Hannigan, G.E., Coles, J.G., and Dedhar, S. (2007). Integrin-linked kinase at the heart of cardiac contractility, repair, and disease. Circ Res *100*, 1408-1414. 10.1161/01.RES.0000265233.40455.62.
Hassoun, R., Budde, H., Mugge, A., and Hamdani, N. (2021). Cardiomyocyte Dysfunction in Inherited Cardiomyopathies. Int J Mol Sci *22*. 10.3390/ijms222011154.
Haupt, L.P., Rebs, S., Maurer, W., Hubscher, D., Tiburcy, M., Pabel, S., Maus, A., Kohne, S., Tappu, R., Haas, J., *et al.* (2022). Doxorubicin induces cardiotoxicity in a pluripotent stem cell model of aggressive B cell lymphoma cancer patients. Basic Res Cardiol *117*, 13. 10.1007/s00395-022-00918-7.
Hayashi, K., Teramoto, R., Nomura, A., Asano, Y., Beerens, M., Kurata, Y., Kobayashi, I., Fujino, N., Furusho, H., Sakata, K., *et al.* (2020). Impact of functional studies on exome sequence variant interpretation in early-onset cardiac conduction system diseases. Cardiovasc Res *116*, 2116-2130. 10.1093/cvr/cvaa010.
He, J.Q., Ma, Y., Lee, Y., Thomson, J.A., and Kamp, T.J. (2003). Human embryonic stem cells develop into multiple types of cardiac myocytes: action potential characterization. Circ Res *93*, 32-39. 10.1161/01.RES.0000080317.92718.99.
He, L., Zhang, Q., Zhou, Y., and Huang, Y. (2018). Optogenetic Approaches to Control Calcium Entry in Non-Excitable Cells. In Calcium Entry Channels in Non-Excitable Cells, J.A. Kozak, and J.W. Putney, Jr., eds. pp. 145-160. 10.1201/9781315152592-8.

Henderson, C.A., Gomez, C.G., Novak, S.M., Mi-Mi, L., and Gregorio, C.C. (2017). Overview of the Muscle Cytoskeleton. Compr Physiol *7*, 891-944. 10.1002/cphy.c160033.
Heo, S.J., Thorpe, S.D., Driscoll, T.P., Duncan, R.L., Lee, D.A., and Mauck, R.L. (2015). Biophysical Regulation of Chromatin Architecture Instills a Mechanical Memory in Mesenchymal Stem Cells. Sci Rep *5*, 16895. 10.1038/srep16895.
Herman, D.S., Lam, L., Taylor, M.R., Wang, L., Teekakirikul, P., Christodoulou, D., Conner, L., DePalma, S.R., McDonough, B., Sparks, E., *et al.* (2012). Truncations of titin causing dilated cardiomyopathy. N Engl J Med *366*, 619-628. 10.1056/NEJMoa1110186.
Hershberger, R.E., Cowan, J., Morales, A., and Siegfried, J.D. (2009). Progress with genetic cardiomyopathies: screening, counseling, and testing in dilated, hypertrophic, and arrhythmogenic right ventricular dysplasia/cardiomyopathy. Circ Heart Fail *2*, 253-261. 10.1161/CIRCHEARTFAILURE.108.817346.
Hershberger, R.E., Hedges, D.J., and Morales, A. (2013). Dilated cardiomyopathy: the complexity of a diverse genetic architecture. Nat Rev Cardiol *10*, 531-547. 10.1038/nrcardio.2013.105.
Hershberger, R.E., and Jordan, E. (1993). Dilated Cardiomyopathy Overview. In GeneReviews((R)), M.P. Adam, G.M. Mirzaa, R.A. Pagon, S.E. Wallace, L.J.H. Bean, K.W. Gripp, and A. Amemiya, eds.
Hershberger, R.E., and Siegfried, J.D. (2011). Update 2011: clinical and genetic issues in familial dilated cardiomyopathy. J Am Coll Cardiol *57*, 1641-1649. 10.1016/j.jacc.2011.01.015.
Hill, M.C., Kadow, Z.A., Li, L., Tran, T.T., Wythe, J.D., and Martin, J.F. (2019). A cellular atlas of Pitx2-dependent cardiac development. Development *146*. 10.1242/dev.180398.
Himmel, M., Van Der Ven, P.F., Stocklein, W., and Furst, D.O. (2003). The limits of promiscuity: isoform-specific dimerization of filamins. Biochemistry *42*, 430-439. 10.1021/bi026501+.
Hofbauer, P., Jahnel, S.M., Papai, N., Giesshammer, M., Deyett, A., Schmidt, C., Penc, M., Tavernini, K., Grdseloff, N., Meledeth, C., *et al.* (2021). Cardioids reveal self-organizing principles of human cardiogenesis. Cell *184*, 3299-3317 e3222. 10.1016/j.cell.2021.04.034.
Hom, J.R., Quintanilla, R.A., Hoffman, D.L., de Mesy Bentley, K.L., Molkentin, J.D., Sheu, S.S., and Porter, G.A., Jr. (2011). The permeability transition pore controls cardiac mitochondrial maturation and myocyte differentiation. Dev Cell *21*, 469-478. 10.1016/j.devcel.2011.08.008.
Hong, B.K., Kwon, H.M., Byun, K.H., Kim, D., Choi, E.Y., Kang, T.S., Kang, S.M., Chun, K.J., Jang, Y., Kim, H.S., and Kim, M. (2000). Apoptosis in dilated cardiomyopathy. Korean J Intern Med *15*, 56-64. 10.3904/kjim.2000.15.1.56.
Horii, T., Tamura, D., Morita, S., Kimura, M., and Hatada, I. (2013). Generation of an ICF syndrome model by efficient genome editing of human induced pluripotent stem cells using the CRISPR system. Int J Mol Sci *14*, 19774-19781. 10.3390/ijms141019774.
Horikoshi, Y., Yan, Y., Terashvili, M., Wells, C., Horikoshi, H., Fujita, S., Bosnjak, Z.J., and Bai, X. (2019). Fatty Acid-Treated Induced Pluripotent Stem Cell-Derived Human Cardiomyocytes Exhibit Adult Cardiomyocyte-Like Energy Metabolism Phenotypes. Cells *8*. 10.3390/cells8091095.
Hu, H., Lin, S., Wang, S., and Chen, X. (2020). The Role of Transcription Factor 21 in Epicardial Cell Differentiation and the Development of Coronary Heart Disease. Front Cell Dev Biol *8*, 457. 10.3389/fcell.2020.00457.
Huxley, H.E. (1969). The mechanism of muscular contraction. Science *164*, 1356-1365. 10.1126/science.164.3886.1356.

Iborra-Egea, O., Galvez-Monton, C., Roura, S., Perea-Gil, I., Prat-Vidal, C., Soler-Botija, C., and Bayes-Genis, A. (2017). Mechanisms of action of sacubitril/valsartan on cardiac remodeling: a systems biology approach. NPJ Syst Biol Appl *3*, 12. 10.1038/s41540-017-0013-4.

Ishino, Y., Shinagawa, H., Makino, K., Amemura, M., and Nakata, A. (1987). Nucleotide sequence of the iap gene, responsible for alkaline phosphatase isozyme conversion in Escherichia coli, and identification of the gene product. J Bacteriol *169*, 5429-5433. 10.1128/jb.169.12.5429-5433.1987.

Ivey, M.J., and Tallquist, M.D. (2016). Defining the Cardiac Fibroblast. Circ J *80*, 2269-2276. 10.1253/circj.CJ-16-1003.

Iyer, D., Gambardella, L., Bernard, W.G., Serrano, F., Mascetti, V.L., Pedersen, R.A., Sinha, S., and Talasila, A. (2016). Robust derivation of epicardium and its differentiated smooth muscle cell progeny from human pluripotent stem cells. Development *143*, 904. 10.1242/dev.136143.

Jabbari, J., Olesen, M.S., Yuan, L., Nielsen, J.B., Liang, B., Macri, V., Christophersen, I.E., Nielsen, N., Sajadieh, A., Ellinor, P.T., *et al.* (2015). Common and rare variants in SCN10A modulate the risk of atrial fibrillation. Circ Cardiovasc Genet *8*, 64-73. 10.1161/HCG.0000000000000022.

Jaenisch, R., and Young, R. (2008). Stem cells, the molecular circuitry of pluripotency and nuclear reprogramming. Cell *132*, 567-582. 10.1016/j.cell.2008.01.015.

Jay, D., Garcia, E.J., Lara, J.E., Medina, M.A., and de la Luz Ibarra, M. (2000). Determination of a cAMP-dependent protein kinase phosphorylation site in the C-terminal region of human endothelial actin-binding protein. Arch Biochem Biophys *377*, 80-84. 10.1006/abbi.2000.1762.

Jeong, H.M., Lee, S., Chae, H., Kim, R., Kwon, M.J., Oh, E., Choi, Y.L., Kim, S., and Shin, Y.K. (2016). Efficiency of methylated DNA immunoprecipitation bisulphite sequencing for whole-genome DNA methylation analysis. Epigenomics *8*, 1061-1077. 10.2217/epi-2016-0038.

Jiang, W., Bikard, D., Cox, D., Zhang, F., and Marraffini, L.A. (2013). RNA-guided editing of bacterial genomes using CRISPR-Cas systems. Nat Biotechnol *31*, 233-239. 10.1038/nbt.2508.

Jinek, M., Chylinski, K., Fonfara, I., Hauer, M., Doudna, J.A., and Charpentier, E. (2012). A programmable dual-RNA-guided DNA endonuclease in adaptive bacterial immunity. Science *337*, 816-821. 10.1126/science.1225829.

Johnson, R.D., and Camelliti, P. (2018). Role of Non-Myocyte Gap Junctions and Connexin Hemichannels in Cardiovascular Health and Disease: Novel Therapeutic Targets? Int J Mol Sci *19*. 10.3390/ijms19030866.

Jung, C.B., Moretti, A., Mederos y Schnitzler, M., Iop, L., Storch, U., Bellin, M., Dorn, T., Ruppenthal, S., Pfeiffer, S., Goedel, A., *et al.* (2012). Dantrolene rescues arrhythmogenic RYR2 defect in a patient-specific stem cell model of catecholaminergic polymorphic ventricular tachycardia. EMBO Mol Med *4*, 180-191. 10.1002/emmm.201100194.

Jung, P., Seibertz, F., Fakuade, F.E., Ignatyeva, N., Sampathkumar, S., Ritter, M., Li, H., Mason, F.E., Ebert, A., and Voigt, N. (2022). Increased cytosolic calcium buffering contributes to a cellular arrhythmogenic substrate in iPSC-cardiomyocytes from patients with dilated cardiomyopathy. Basic Res Cardiol *117*, 5. 10.1007/s00395-022-00912-z.

Kajstura, J., Zhang, X., Liu, Y., Szoke, E., Cheng, W., Olivetti, G., Hintze, T.H., and Anversa, P. (1995). The cellular basis of pacing-induced dilated cardiomyopathy. Myocyte cell loss and

myocyte cellular reactive hypertrophy. Circulation *92*, 2306-2317. 10.1161/01.cir.92.8.2306.

Kamakura, T., Makiyama, T., Sasaki, K., Yoshida, Y., Wuriyanghai, Y., Chen, J., Hattori, T., Ohno, S., Kita, T., Horie, M., *et al.* (2013). Ultrastructural maturation of human-induced pluripotent stem cell-derived cardiomyocytes in a long-term culture. Circ J *77*, 1307-1314. 10.1253/circj.cj-12-0987.

Kamo, T., Akazawa, H., and Komuro, I. (2015). Cardiac nonmyocytes in the hub of cardiac hypertrophy. Circ Res *117*, 89-98. 10.1161/CIRCRESAHA.117.305349.

Kanisicak, O., Khalil, H., Ivey, M.J., Karch, J., Maliken, B.D., Correll, R.N., Brody, M.J., SC, J.L., Aronow, B.J., Tallquist, M.D., and Molkentin, J.D. (2016). Genetic lineage tracing defines myofibroblast origin and function in the injured heart. Nat Commun *7*, 12260. 10.1038/ncomms12260.

Karakikes, I., Stillitano, F., Nonnenmacher, M., Tzimas, C., Sanoudou, D., Termglinchan, V., Kong, C.W., Rushing, S., Hansen, J., Ceholski, D., *et al.* (2015). Correction of human phospholamban R14del mutation associated with cardiomyopathy using targeted nucleases and combination therapy. Nat Commun *6*, 6955. 10.1038/ncomms7955.

Karakikes, I., Termglinchan, V., and Wu, J.C. (2014). Human-induced pluripotent stem cell models of inherited cardiomyopathies. Curr Opin Cardiol *29*, 214-219. 10.1097/HCO.0000000000000049.

Kasner, M., Westermann, D., Lopez, B., Gaub, R., Escher, F., Kuhl, U., Schultheiss, H.P., and Tschope, C. (2011). Diastolic tissue Doppler indexes correlate with the degree of collagen expression and cross-linking in heart failure and normal ejection fraction. J Am Coll Cardiol *57*, 977-985. 10.1016/j.jacc.2010.10.024.

Kelly, S.J. (1977). Studies of the developmental potential of 4- and 8-cell stage mouse blastomeres. J Exp Zool *200*, 365-376. 10.1002/jez.1402000307.

Kim, D., Kim, C.H., Moon, J.I., Chung, Y.G., Chang, M.Y., Han, B.S., Ko, S., Yang, E., Cha, K.Y., Lanza, R., and Kim, K.S. (2009). Generation of human induced pluripotent stem cells by direct delivery of reprogramming proteins. Cell Stem Cell *4*, 472-476. 10.1016/j.stem.2009.05.005.

Kim, M., Ye, D., John Kim, C.S., Zhou, W., Tester, D.J., Giudicessi, J.R., and Ackerman, M.J. (2021). Development of a Patient-Specific p.D85N-Potassium Voltage-Gated Channel Subfamily E Member 1-Induced Pluripotent Stem Cell-Derived Cardiomyocyte Model for Drug-Induced Long QT Syndrome. Circ Genom Precis Med *14*, e003234. 10.1161/CIRCGEN.120.003234.

Kimura, K., Ieda, M., and Fukuda, K. (2012). Development, maturation, and transdifferentiation of cardiac sympathetic nerves. Circ Res *110*, 325-336. 10.1161/CIRCRESAHA.111.257253.

Klabunde, R. (2012). Cellular structure and function. In Cardiovascular physiology concepts (Baltimore, MD: Lippincott Williams & Wilkins), pp. 41-58.

Knoll, R., Postel, R., Wang, J., Kratzner, R., Hennecke, G., Vacaru, A.M., Vakeel, P., Schubert, C., Murthy, K., Rana, B.K., *et al.* (2007). Laminin-alpha4 and integrin-linked kinase mutations cause human cardiomyopathy via simultaneous defects in cardiomyocytes and endothelial cells. Circulation *116*, 515-525. 10.1161/CIRCULATIONAHA.107.689984.

Köhne, S. (2020). Involvement of cardiac fibroblasts in anthracycline-induced cardiotoxicity. University Medical Center Göttingen.

Koitabashi, N., Arai, M., Niwano, K., Watanabe, A., Endoh, M., Suguta, M., Yokoyama, T., Tada, H., Toyama, T., Adachi, H., *et al.* (2008). Plasma connective tissue growth factor is a

novel potential biomarker of cardiac dysfunction in patients with chronic heart failure. Eur J Heart Fail *10*, 373-379. 10.1016/j.ejheart.2008.02.011.
Koivumaki, J.T., Naumenko, N., Tuomainen, T., Takalo, J., Oksanen, M., Puttonen, K.A., Lehtonen, S., Kuusisto, J., Laakso, M., Koistinaho, J., and Tavi, P. (2018). Structural Immaturity of Human iPSC-Derived Cardiomyocytes: In Silico Investigation of Effects on Function and Disease Modeling. Front Physiol *9*, 80. 10.3389/fphys.2018.00080.
Kolanowski, T.J., Antos, C.L., and Guan, K. (2017). Making human cardiomyocytes up to date: Derivation, maturation state and perspectives. Int J Cardiol *241*, 379-386. 10.1016/j.ijcard.2017.03.099.
Kong, P., Christia, P., Saxena, A., Su, Y., and Frangogiannis, N.G. (2013). Lack of specificity of fibroblast-specific protein 1 in cardiac remodeling and fibrosis. Am J Physiol Heart Circ Physiol *305*, H1363-1372. 10.1152/ajpheart.00395.2013.
Kostin, S., Rieger, M., Dammer, S., Hein, S., Richter, M., Klovekorn, W.P., Bauer, E.P., and Schaper, J. (2003). Gap junction remodeling and altered connexin43 expression in the failing human heart. Mol Cell Biochem *242*, 135-144.
Koyanagi-Aoi, M., Ohnuki, M., Takahashi, K., Okita, K., Noma, H., Sawamura, Y., Teramoto, I., Narita, M., Sato, Y., Ichisaka, T., *et al.* (2013). Differentiation-defective phenotypes revealed by large-scale analyses of human pluripotent stem cells. Proc Natl Acad Sci U S A *110*, 20569-20574. 10.1073/pnas.1319061110.
Kramann, R., Schneider, R.K., DiRocco, D.P., Machado, F., Fleig, S., Bondzie, P.A., Henderson, J.M., Ebert, B.L., and Humphreys, B.D. (2015). Perivascular Gli1+ progenitors are key contributors to injury-induced organ fibrosis. Cell Stem Cell *16*, 51-66. 10.1016/j.stem.2014.11.004.
Kranias, E.G., and Hajjar, R.J. (2012). Modulation of cardiac contractility by the phospholamban/SERCA2a regulatome. Circ Res *110*, 1646-1660. 10.1161/CIRCRESAHA.111.259754.
Krenning, G., Zeisberg, E.M., and Kalluri, R. (2010). The origin of fibroblasts and mechanism of cardiac fibrosis. J Cell Physiol *225*, 631-637. 10.1002/jcp.22322.
LaBarge, W., Mattappally, S., Kannappan, R., Fast, V.G., Pretorius, D., Berry, J.L., and Zhang, J. (2019). Maturation of three-dimensional, hiPSC-derived cardiomyocyte spheroids utilizing cyclic, uniaxial stretch and electrical stimulation. PLoS One *14*, e0219442. 10.1371/journal.pone.0219442.
Lacey, S.F., and Fraietta, J.A. (2020). First Trial of CRISPR-Edited T cells in Lung Cancer. Trends Mol Med *26*, 713-715. 10.1016/j.molmed.2020.06.001.
Laflamme, M.A., Chen, K.Y., Naumova, A.V., Muskheli, V., Fugate, J.A., Dupras, S.K., Reinecke, H., Xu, C., Hassanipour, M., Police, S., *et al.* (2007). Cardiomyocytes derived from human embryonic stem cells in pro-survival factors enhance function of infarcted rat hearts. Nat Biotechnol *25*, 1015-1024. 10.1038/nbt1327.
Latysheva, N.S., Flock, T., Weatheritt, R.J., Chavali, S., and Babu, M.M. (2015). How do disordered regions achieve comparable functions to structured domains? Protein Sci *24*, 909-922. 10.1002/pro.2674.
Leber, Y., Ruparelia, A.A., Kirfel, G., van der Ven, P.F., Hoffmann, B., Merkel, R., Bryson-Richardson, R.J., and Furst, D.O. (2016). Filamin C is a highly dynamic protein associated with fast repair of myofibrillar microdamage. Hum Mol Genet *25*, 2776-2788. 10.1093/hmg/ddw135.
Lehman, W., Craig, R., and Vibert, P. (1994). Ca(2+)-induced tropomyosin movement in Limulus thin filaments revealed by three-dimensional reconstruction. Nature *368*, 65-67. 10.1038/368065a0.

Lelievre, S.A. (2009). Contributions of extracellular matrix signaling and tissue architecture to nuclear mechanisms and spatial organization of gene expression control. Biochim Biophys Acta *1790*, 925-935. 10.1016/j.bbagen.2009.03.013.
Lewandowski, J., Rozwadowska, N., Kolanowski, T.J., Malcher, A., Zimna, A., Rugowska, A., Fiedorowicz, K., Labedz, W., Kubaszewski, L., Chojnacka, K., *et al.* (2018). The impact of in vitro cell culture duration on the maturation of human cardiomyocytes derived from induced pluripotent stem cells of myogenic origin. Cell Transplant *27*, 1047-1067. 10.1177/0963689718779346.
Li, D., Zhou, H., and Zeng, X. (2019). Battling CRISPR-Cas9 off-target genome editing. Cell Biol Toxicol *35*, 403-406. 10.1007/s10565-019-09485-5.
Lian, X., Hsiao, C., Wilson, G., Zhu, K., Hazeltine, L.B., Azarin, S.M., Raval, K.K., Zhang, J., Kamp, T.J., and Palecek, S.P. (2012). Robust cardiomyocyte differentiation from human pluripotent stem cells via temporal modulation of canonical Wnt signaling. Proc Natl Acad Sci U S A *109*, E1848-1857. 10.1073/pnas.1200250109.
Lian, X., Zhang, J., Azarin, S.M., Zhu, K., Hazeltine, L.B., Bao, X., Hsiao, C., Kamp, T.J., and Palecek, S.P. (2013). Directed cardiomyocyte differentiation from human pluripotent stem cells by modulating Wnt/beta-catenin signaling under fully defined conditions. Nat Protoc *8*, 162-175. 10.1038/nprot.2012.150.
Liang, X., Potter, J., Kumar, S., Zou, Y., Quintanilla, R., Sridharan, M., Carte, J., Chen, W., Roark, N., Ranganathan, S., *et al.* (2015). Rapid and highly efficient mammalian cell engineering via Cas9 protein transfection. J Biotechnol *208*, 44-53. 10.1016/j.jbiotec.2015.04.024.
Lindner, D., Zietsch, C., Becher, P.M., Schulze, K., Schultheiss, H.P., Tschope, C., and Westermann, D. (2012). Differential expression of matrix metalloproteases in human fibroblasts with different origins. Biochem Res Int *2012*, 875742. 10.1155/2012/875742.
Linnemann, A., van der Ven, P.F., Vakeel, P., Albinus, B., Simonis, D., Bendas, G., Schenk, J.A., Micheel, B., Kley, R.A., and Furst, D.O. (2010). The sarcomeric Z-disc component myopodin is a multiadapter protein that interacts with filamin and alpha-actinin. Eur J Cell Biol *89*, 681-692. 10.1016/j.ejcb.2010.04.004.
Lino, C.A., Harper, J.C., Carney, J.P., and Timlin, J.A. (2018). Delivering CRISPR: a review of the challenges and approaches. Drug Deliv *25*, 1234-1257. 10.1080/10717544.2018.1474964.
Liu, C., Ma, N., Guo, Z., Zhang, Y., Zhang, J., Yang, F., Su, X., Zhang, G., Xiong, X., and Xing, Y. (2022a). Relevance of mitochondrial oxidative stress to arrhythmias: Innovative concepts to target treatments. Pharmacol Res *175*, 106027. 10.1016/j.phrs.2021.106027.
Liu, L., Ding, X., Han, Y., and Lv, J. (2022b). Effects and Safety of Sacubitril/Valsartan for Patients with Myocardial Infarction: A Systematic Review and Meta-Analysis. J Healthc Eng *2022*, 7840852. 10.1155/2022/7840852.
Loo, D.T., Kanner, S.B., and Aruffo, A. (1998). Filamin binds to the cytoplasmic domain of the beta1-integrin. Identification of amino acids responsible for this interaction. J Biol Chem *273*, 23304-23312. 10.1074/jbc.273.36.23304.
Lother, A., Bergemann, S., Deng, L., Moser, M., Bode, C., and Hein, L. (2018). Cardiac Endothelial Cell Transcriptome. Arterioscler Thromb Vasc Biol *38*, 566-574. 10.1161/ATVBAHA.117.310549.
Lou, Q., Janardhan, A., and Efimov, I.R. (2012). Remodeling of calcium handling in human heart failure. Adv Exp Med Biol *740*, 1145-1174. 10.1007/978-94-007-2888-2_52.

Louault, C., Benamer, N., Faivre, J.F., Potreau, D., and Bescond, J. (2008). Implication of connexins 40 and 43 in functional coupling between mouse cardiac fibroblasts in primary culture. Biochim Biophys Acta *1778*, 2097-2104. 10.1016/j.bbamem.2008.04.005.

Lozano, R., Naghavi, M., Foreman, K., Lim, S., Shibuya, K., Aboyans, V., Abraham, J., Adair, T., Aggarwal, R., Ahn, S.Y., *et al.* (2012). Global and regional mortality from 235 causes of death for 20 age groups in 1990 and 2010: a systematic analysis for the Global Burden of Disease Study 2010. Lancet *380*, 2095-2128. 10.1016/S0140-6736(12)61728-0.

Lynch, T.L.t., Sivaguru, M., Velayutham, M., Cardounel, A.J., Michels, M., Barefield, D., Govindan, S., dos Remedios, C., van der Velden, J., and Sadayappan, S. (2015). Oxidative Stress in Dilated Cardiomyopathy Caused by MYBPC3 Mutation. Oxid Med Cell Longev *2015*, 424751. 10.1155/2015/424751.

Ma, J., Guo, L., Fiene, S.J., Anson, B.D., Thomson, J.A., Kamp, T.J., Kolaja, K.L., Swanson, B.J., and January, C.T. (2011). High purity human-induced pluripotent stem cell-derived cardiomyocytes: electrophysiological properties of action potentials and ionic currents. Am J Physiol Heart Circ Physiol *301*, H2006-2017. 10.1152/ajpheart.00694.2011.

Maeder, M.L., Stefanidakis, M., Wilson, C.J., Baral, R., Barrera, L.A., Bounoutas, G.S., Bumcrot, D., Chao, H., Ciulla, D.M., DaSilva, J.A., *et al.* (2019). Development of a gene-editing approach to restore vision loss in Leber congenital amaurosis type 10. Nat Med *25*, 229-233. 10.1038/s41591-018-0327-9.

Makarova, K.S., Wolf, Y.I., Iranzo, J., Shmakov, S.A., Alkhnbashi, O.S., Brouns, S.J.J., Charpentier, E., Cheng, D., Haft, D.H., Horvath, P., *et al.* (2020). Evolutionary classification of CRISPR-Cas systems: a burst of class 2 and derived variants. Nat Rev Microbiol *18*, 67-83. 10.1038/s41579-019-0299-x.

Maltese, P.E., Aldanova, E., Kriuchkova, N., Averianov, A., Manara, E., Paolacci, S., Bruson, A., Miotto, R., Sartori, M., Guerri, G., *et al.* (2019). Putative role of Brugada syndrome genes in familial atrial fibrillation. Eur Rev Med Pharmacol Sci *23*, 7582-7598. 10.26355/eurrev_201909_18880.

Maltsev, V.A., Sabbah, H.N., Higgins, R.S., Silverman, N., Lesch, M., and Undrovinas, A.I. (1998). Novel, ultraslow inactivating sodium current in human ventricular cardiomyocytes. Circulation *98*, 2545-2552. 10.1161/01.cir.98.23.2545.

Mannhardt, I., Breckwoldt, K., Letuffe-Breniere, D., Schaaf, S., Schulz, H., Neuber, C., Benzin, A., Werner, T., Eder, A., Schulze, T., *et al.* (2016). Human Engineered Heart Tissue: Analysis of Contractile Force. Stem Cell Reports *7*, 29-42. 10.1016/j.stemcr.2016.04.011.

Manso, A.M., Kang, S.M., and Ross, R.S. (2009). Integrins, focal adhesions, and cardiac fibroblasts. J Investig Med *57*, 856-860. 10.2310/JIM.0b013e3181c5e61f.

Mao, Z., and Nakamura, F. (2020). Structure and Function of Filamin C in the Muscle Z-Disc. Int J Mol Sci *21*. 10.3390/ijms21082696.

Marjamaa, A., Laitinen-Forsblom, P., Lahtinen, A.M., Viitasalo, M., Toivonen, L., Kontula, K., and Swan, H. (2009). Search for cardiac calcium cycling gene mutations in familial ventricular arrhythmias resembling catecholaminergic polymorphic ventricular tachycardia. BMC Med Genet *10*, 12. 10.1186/1471-2350-10-12.

Maron, B.J., Towbin, J.A., Thiene, G., Antzelevitch, C., Corrado, D., Arnett, D., Moss, A.J., Seidman, C.E., Young, J.B., American Heart, A., *et al.* (2006). Contemporary definitions and classification of the cardiomyopathies: an American Heart Association Scientific Statement from the Council on Clinical Cardiology, Heart Failure and Transplantation Committee; Quality of Care and Outcomes Research and Functional Genomics and Translational Biology Interdisciplinary Working Groups; and Council on Epidemiology and Prevention. Circulation *113*, 1807-1816. 10.1161/CIRCULATIONAHA.106.174287.

Maruyama, T., Dougan, S.K., Truttmann, M.C., Bilate, A.M., Ingram, J.R., and Ploegh, H.L. (2015). Increasing the efficiency of precise genome editing with CRISPR-Cas9 by inhibition of nonhomologous end joining. Nat Biotechnol *33*, 538-542. 10.1038/nbt.3190.
Matsui, Y., Zsebo, K., and Hogan, B.L. (1992). Derivation of pluripotential embryonic stem cells from murine primordial germ cells in culture. Cell *70*, 841-847. 10.1016/0092-8674(92)90317-6.
Mattiazzi, A., Mundina-Weilenmann, C., Guoxiang, C., Vittone, L., and Kranias, E. (2005). Role of phospholamban phosphorylation on Thr17 in cardiac physiological and pathological conditions. Cardiovasc Res *68*, 366-375. 10.1016/j.cardiores.2005.08.010.
Maurer, W., Hartmann, N., Argyriou, L., Sossalla, S., and Streckfuss-Bomeke, K. (2022). Generation of homozygous Nav1.8 knock-out iPSC lines by CRISPR Cas9 genome editing to investigate a potential new antiarrhythmic strategy. Stem Cell Res *60*, 102677. 10.1016/j.scr.2022.102677.
Mayalu, M.N., Kim, M.C., and Asada, H.H. (2019). Multi-cell ECM compaction is predictable via superposition of nonlinear cell dynamics linearized in augmented state space. PLoS Comput Biol *15*, e1006798. 10.1371/journal.pcbi.1006798.
Meder, B., Haas, J., Keller, A., Heid, C., Just, S., Borries, A., Boisguerin, V., Scharfenberger-Schmeer, M., Stahler, P., Beier, M., *et al.* (2011). Targeted next-generation sequencing for the molecular genetic diagnostics of cardiomyopathies. Circ Cardiovasc Genet *4*, 110-122. 10.1161/CIRCGENETICS.110.958322.
Meyer, M., Schillinger, W., Pieske, B., Holubarsch, C., Heilmann, C., Posival, H., Kuwajima, G., Mikoshiba, K., Just, H., Hasenfuss, G., and *et al.* (1995). Alterations of sarcoplasmic reticulum proteins in failing human dilated cardiomyopathy. Circulation *92*, 778-784. 10.1161/01.cir.92.4.778.
Michel, J.B., Li, Z., and Lacolley, P. (2012). Smooth muscle cells and vascular diseases. Cardiovasc Res *95*, 135-137. 10.1093/cvr/cvs172.
Michels, V.V., Moll, P.P., Miller, F.A., Tajik, A.J., Chu, J.S., Driscoll, D.J., Burnett, J.C., Rodeheffer, R.J., Chesebro, J.H., and Tazelaar, H.D. (1992). The frequency of familial dilated cardiomyopathy in a series of patients with idiopathic dilated cardiomyopathy. N Engl J Med *326*, 77-82. 10.1056/NEJM199201093260201.
Mihl, C., Dassen, W.R., and Kuipers, H. (2008). Cardiac remodelling: concentric versus eccentric hypertrophy in strength and endurance athletes. Neth Heart J *16*, 129-133. 10.1007/BF03086131.
Miszalski-Jamka, K., Jefferies, J.L., Mazur, W., Glowacki, J., Hu, J., Lazar, M., Gibbs, R.A., Liczko, J., Klys, J., Venner, E., *et al.* (2017). Novel Genetic Triggers and Genotype-Phenotype Correlations in Patients With Left Ventricular Noncompaction. Circ Cardiovasc Genet *10*. 10.1161/CIRCGENETICS.117.001763.
Mitropoulou, P., Georgiopoulos, G., Figliozzi, S., Klettas, D., Nicoli, F., and Masci, P.G. (2020). Multi-Modality Imaging in Dilated Cardiomyopathy: With a Focus on the Role of Cardiac Magnetic Resonance. Front Cardiovasc Med *7*, 97. 10.3389/fcvm.2020.00097.
Mojica, F.J., Juez, G., and Rodriguez-Valera, F. (1993). Transcription at different salinities of Haloferax mediterranei sequences adjacent to partially modified PstI sites. Mol Microbiol *9*, 613-621. 10.1111/j.1365-2958.1993.tb01721.x.
Mollmann, H., Nef, H.M., Kostin, S., von Kalle, C., Pilz, I., Weber, M., Schaper, J., Hamm, C.W., and Elsasser, A. (2006). Bone marrow-derived cells contribute to infarct remodelling. Cardiovasc Res *71*, 661-671. 10.1016/j.cardiores.2006.06.013.
Molt, S., Buhrdel, J.B., Yakovlev, S., Schein, P., Orfanos, Z., Kirfel, G., Winter, L., Wiche, G., van der Ven, P.F., Rottbauer, W., *et al.* (2014). Aciculin interacts with filamin C and Xin and

is essential for myofibril assembly, remodeling and maintenance. J Cell Sci *127*, 3578-3592. 10.1242/jcs.152157.
Moore-Morris, T., Cattaneo, P., Puceat, M., and Evans, S.M. (2016). Origins of cardiac fibroblasts. J Mol Cell Cardiol *91*, 1-5. 10.1016/j.yjmcc.2015.12.031.
Moretti, A., Fonteyne, L., Giesert, F., Hoppmann, P., Meier, A.B., Bozoglu, T., Baehr, A., Schneider, C.M., Sinnecker, D., Klett, K., *et al.* (2020). Somatic gene editing ameliorates skeletal and cardiac muscle failure in pig and human models of Duchenne muscular dystrophy. Nat Med *26*, 207-214. 10.1038/s41591-019-0738-2.
Mouton, A.J., Ma, Y., Rivera Gonzalez, O.J., Daseke, M.J., 2nd, Flynn, E.R., Freeman, T.C., Garrett, M.R., DeLeon-Pennell, K.Y., and Lindsey, M.L. (2019). Fibroblast polarization over the myocardial infarction time continuum shifts roles from inflammation to angiogenesis. Basic Res Cardiol *114*, 6. 10.1007/s00395-019-0715-4.
Mummery, C.L., Zhang, J., Ng, E.S., Elliott, D.A., Elefanty, A.G., and Kamp, T.J. (2012). Differentiation of human embryonic stem cells and induced pluripotent stem cells to cardiomyocytes: a methods overview. Circ Res *111*, 344-358. 10.1161/CIRCRESAHA.110.227512.
Munoz-Chapuli, R., Perez-Pomares, J.M., Macias, D., Garcia-Garrido, L., Carmona, R., and Gonzalez-Iriarte, M. (2001). The epicardium as a source of mesenchyme for the developing heart. Ital J Anat Embryol *106*, 187-196.
Munzel, T., Gori, T., Keaney, J.F., Jr., Maack, C., and Daiber, A. (2015). Pathophysiological role of oxidative stress in systolic and diastolic heart failure and its therapeutic implications. Eur Heart J *36*, 2555-2564. 10.1093/eurheartj/ehv305.
Murray, J.T., Campbell, D.G., Peggie, M., Mora, A., and Cohen, P. (2004). Identification of filamin C as a new physiological substrate of PKBalpha using KESTREL. Biochem J *384*, 489-494. 10.1042/BJ20041058.
Nabeebaccus, A.A., Verma, S., Zoccarato, A., Emanuelli, G., Santos, C.X., Streckfuss-Bomeke, K., and Shah, A.M. (2021). Cardiomyocyte protein O-GlcNAcylation is regulated by GFAT1 not GFAT2. Biochem Biophys Res Commun *583*, 121-127. 10.1016/j.bbrc.2021.10.056.
Nag, A.C., and Zak, R. (1979). Dissociation of adult mammalian heart into single cell suspension: an ultrastructural study. J Anat *129*, 541-559.
Nagy, A., Gocza, E., Diaz, E.M., Prideaux, V.R., Ivanyi, E., Markkula, M., and Rossant, J. (1990). Embryonic stem cells alone are able to support fetal development in the mouse. Development *110*, 815-821. 10.1242/dev.110.3.815.
Natividad-Diaz, S.L., Browne, S., Jha, A.K., Ma, Z., Hossainy, S., Kurokawa, Y.K., George, S.C., and Healy, K.E. (2019). A combined hiPSC-derived endothelial cell and in vitro microfluidic platform for assessing biomaterial-based angiogenesis. Biomaterials *194*, 73-83. 10.1016/j.biomaterials.2018.11.032.
O'Reilly, S. (2017). Epigenetics in fibrosis. Mol Aspects Med *54*, 89-102. 10.1016/j.mam.2016.10.001.
Ogawa, M. (1993). Differentiation and proliferation of hematopoietic stem cells. Blood *81*, 2844-2853.
Oka, T., Akazawa, H., Naito, A.T., and Komuro, I. (2014). Angiogenesis and cardiac hypertrophy: maintenance of cardiac function and causative roles in heart failure. Circ Res *114*, 565-571. 10.1161/CIRCRESAHA.114.300507.
Okamoto, K., and Seimiya, H. (2019). Revisiting Telomere Shortening in Cancer. Cells *8*. 10.3390/cells8020107.

Okamoto, S., Amaishi, Y., Maki, I., Enoki, T., and Mineno, J. (2019). Highly efficient genome editing for single-base substitutions using optimized ssODNs with Cas9-RNPs. Sci Rep *9*, 4811. 10.1038/s41598-019-41121-4.
Okita, K., Nakagawa, M., Hyenjong, H., Ichisaka, T., and Yamanaka, S. (2008). Generation of mouse induced pluripotent stem cells without viral vectors. Science *322*, 949-953. 10.1126/science.1164270.
Olivetti, G., Abbi, R., Quaini, F., Kajstura, J., Cheng, W., Nitahara, J.A., Quaini, E., Di Loreto, C., Beltrami, C.A., Krajewski, S., *et al.* (1997). Apoptosis in the failing human heart. N Engl J Med *336*, 1131-1141. 10.1056/NEJM199704173361603.
Olivey, H.E., Mundell, N.A., Austin, A.F., and Barnett, J.V. (2006). Transforming growth factor-beta stimulates epithelial-mesenchymal transformation in the proepicardium. Dev Dyn *235*, 50-59. 10.1002/dvdy.20593.
Ortiz-Genga, M.F., Cuenca, S., Dal Ferro, M., Zorio, E., Salgado-Aranda, R., Climent, V., Padron-Barthe, L., Duro-Aguado, I., Jimenez-Jaimez, J., Hidalgo-Olivares, V.M., *et al.* (2016). Truncating FLNC Mutations Are Associated With High-Risk Dilated and Arrhythmogenic Cardiomyopathies. J Am Coll Cardiol *68*, 2440-2451. 10.1016/j.jacc.2016.09.927.
Paquet, D., Kwart, D., Chen, A., Sproul, A., Jacob, S., Teo, S., Olsen, K.M., Gregg, A., Noggle, S., and Tessier-Lavigne, M. (2016). Efficient introduction of specific homozygous and heterozygous mutations using CRISPR/Cas9. Nature *533*, 125-129. 10.1038/nature17664.
Park, I.H., Zhao, R., West, J.A., Yabuuchi, A., Huo, H., Ince, T.A., Lerou, P.H., Lensch, M.W., and Daley, G.Q. (2008). Reprogramming of human somatic cells to pluripotency with defined factors. Nature *451*, 141-146. 10.1038/nature06534.
Park, W.J., and Oh, J.G. (2013). SERCA2a: a prime target for modulation of cardiac contractility during heart failure. BMB Rep *46*, 237-243. 10.5483/bmbrep.2013.46.5.077.
Phillips, B.T., Gassei, K., and Orwig, K.E. (2010). Spermatogonial stem cell regulation and spermatogenesis. Philos Trans R Soc Lond B Biol Sci *365*, 1663-1678. 10.1098/rstb.2010.0026.
Piacentino, V., 3rd, Weber, C.R., Chen, X., Weisser-Thomas, J., Margulies, K.B., Bers, D.M., and Houser, S.R. (2003). Cellular basis of abnormal calcium transients of failing human ventricular myocytes. Circ Res *92*, 651-658. 10.1161/01.RES.0000062469.83985.9B.
Pickar-Oliver, A., and Gersbach, C.A. (2019). The next generation of CRISPR-Cas technologies and applications. Nat Rev Mol Cell Biol *20*, 490-507. 10.1038/s41580-019-0131-5.
Piek, A., de Boer, R.A., and Sillje, H.H. (2016). The fibrosis-cell death axis in heart failure. Heart Fail Rev *21*, 199-211. 10.1007/s10741-016-9536-9.
Pinto, A.R., Ilinykh, A., Ivey, M.J., Kuwabara, J.T., D'Antoni, M.L., Debuque, R., Chandran, A., Wang, L., Arora, K., Rosenthal, N.A., and Tallquist, M.D. (2016). Revisiting Cardiac Cellular Composition. Circ Res *118*, 400-409. 10.1161/CIRCRESAHA.115.307778.
Popowicz, G.M., Schleicher, M., Noegel, A.A., and Holak, T.A. (2006). Filamins: promiscuous organizers of the cytoskeleton. Trends Biochem Sci *31*, 411-419. 10.1016/j.tibs.2006.05.006.
Pruna, M., and Ehler, E. (2020). The intercalated disc: a mechanosensing signalling node in cardiomyopathy. Biophys Rev *12*, 931-946. 10.1007/s12551-020-00737-x.
Ramakrishna, S., Kwaku Dad, A.B., Beloor, J., Gopalappa, R., Lee, S.K., and Kim, H. (2014). Gene disruption by cell-penetrating peptide-mediated delivery of Cas9 protein and guide RNA. Genome Res *24*, 1020-1027. 10.1101/gr.171264.113.

Ranjha, L., Howard, S.M., and Cejka, P. (2018). Main steps in DNA double-strand break repair: an introduction to homologous recombination and related processes. Chromosoma *127*, 187-214. 10.1007/s00412-017-0658-1.

Raynaud, F., Jond-Necand, C., Marcilhac, A., Furst, D., and Benyamin, Y. (2006). Calpain 1-gamma filamin interaction in muscle cells: a possible in situ regulation by PKC-alpha. Int J Biochem Cell Biol *38*, 404-413. 10.1016/j.biocel.2005.09.020.

Rebs, S. (2021). Analysis of splice-defect associated cardiac diseases using a patient-specific iPSC-cardiomyocyte system. (Georg-August Universität Göttingen).

Regitz-Zagrosek, V., Petrov, G., Lehmkuhl, E., Smits, J.M., Babitsch, B., Brunhuber, C., Jurmann, B., Stein, J., Schubert, C., Merz, N.B., *et al.* (2010). Heart transplantation in women with dilated cardiomyopathy. Transplantation *89*, 236-244. 10.1097/TP.0b013e3181c35255.

Reimann, L., Schwable, A.N., Fricke, A.L., Muhlhauser, W.W.D., Leber, Y., Lohanadan, K., Puchinger, M.G., Schauble, S., Faessler, E., Wiese, H., *et al.* (2020). Phosphoproteomics identifies dual-site phosphorylation in an extended basophilic motif regulating FILIP1-mediated degradation of filamin-C. Commun Biol *3*, 253. 10.1038/s42003-020-0982-5.

Reimann, L., Wiese, H., Leber, Y., Schwable, A.N., Fricke, A.L., Rohland, A., Knapp, B., Peikert, C.D., Drepper, F., van der Ven, P.F., *et al.* (2017). Myofibrillar Z-discs Are a Protein Phosphorylation Hot Spot with Protein Kinase C (PKCalpha) Modulating Protein Dynamics. Mol Cell Proteomics *16*, 346-367. 10.1074/mcp.M116.065425.

Reinstein, E., Gutierrez-Fernandez, A., Tzur, S., Bormans, C., Marcu, S., Tayeb-Fligelman, E., Vinkler, C., Raas-Rothschild, A., Irge, D., Landau, M., *et al.* (2016). Congenital dilated cardiomyopathy caused by biallelic mutations in Filamin C. Eur J Hum Genet *24*, 1792-1796. 10.1038/ejhg.2016.110.

Reiser, P.J., Portman, M.A., Ning, X.H., and Schomisch Moravec, C. (2001). Human cardiac myosin heavy chain isoforms in fetal and failing adult atria and ventricles. Am J Physiol Heart Circ Physiol *280*, H1814-1820. 10.1152/ajpheart.2001.280.4.H1814.

Richards, S., Aziz, N., Bale, S., Bick, D., Das, S., Gastier-Foster, J., Grody, W.W., Hegde, M., Lyon, E., Spector, E., *et al.* (2015). Standards and guidelines for the interpretation of sequence variants: a joint consensus recommendation of the American College of Medical Genetics and Genomics and the Association for Molecular Pathology. Genet Med *17*, 405-424. 10.1038/gim.2015.30.

Richter, C., Chang, J.T., and Fineran, P.C. (2012). Function and regulation of clustered regularly interspaced short palindromic repeats (CRISPR) / CRISPR associated (Cas) systems. Viruses *4*, 2291-2311. 10.3390/v4102291.

Robinson, P., Griffiths, P.J., Watkins, H., and Redwood, C.S. (2007). Dilated and hypertrophic cardiomyopathy mutations in troponin and alpha-tropomyosin have opposing effects on the calcium affinity of cardiac thin filaments. Circ Res *101*, 1266-1273. 10.1161/CIRCRESAHA.107.156380.

Rodriguez-Sinovas, A., Sanchez, J.A., Valls-Lacalle, L., Consegal, M., and Ferreira-Gonzalez, I. (2021). Connexins in the Heart: Regulation, Function and Involvement in Cardiac Disease. Int J Mol Sci *22*. 10.3390/ijms22094413.

Roe, A.T., Frisk, M., and Louch, W.E. (2015). Targeting cardiomyocyte Ca2+ homeostasis in heart failure. Curr Pharm Des *21*, 431-448. 10.2174/1381612821041412041241 29.

Romagnuolo, R., Masoudpour, H., Porta-Sanchez, A., Qiang, B., Barry, J., Laskary, A., Qi, X., Masse, S., Magtibay, K., Kawajiri, H., *et al.* (2019). Human Embryonic Stem Cell-Derived Cardiomyocytes Regenerate the Infarcted Pig Heart but Induce Ventricular Tachyarrhythmias. Stem Cell Reports *12*, 967-981. 10.1016/j.stemcr.2019.04.005.

Rosenbaum, A.N., Agre, K.E., and Pereira, N.L. (2020). Genetics of dilated cardiomyopathy: practical implications for heart failure management. Nat Rev Cardiol *17*, 286-297. 10.1038/s41569-019-0284-0.

Rosenkranz, S. (2004). TGF-beta1 and angiotensin networking in cardiac remodeling. Cardiovasc Res *63*, 423-432. 10.1016/j.cardiores.2004.04.030.

Ruiz-Villalba, A., Simon, A.M., Pogontke, C., Castillo, M.I., Abizanda, G., Pelacho, B., Sanchez-Dominguez, R., Segovia, J.C., Prosper, F., and Perez-Pomares, J.M. (2015). Interacting resident epicardium-derived fibroblasts and recruited bone marrow cells form myocardial infarction scar. J Am Coll Cardiol *65*, 2057-2066. 10.1016/j.jacc.2015.03.520.

Ruppert, V., Nolte, D., Aschenbrenner, T., Pankuweit, S., Funck, R., and Maisch, B. (2004). Novel point mutations in the mitochondrial DNA detected in patients with dilated cardiomyopathy by screening the whole mitochondrial genome. Biochem Biophys Res Commun *318*, 535-543. 10.1016/j.bbrc.2004.04.061.

Sabri, A., Hughie, H.H., and Lucchesi, P.A. (2003). Regulation of hypertrophic and apoptotic signaling pathways by reactive oxygen species in cardiac myocytes. Antioxid Redox Signal *5*, 731-740. 10.1089/152308603770380034.

Sag, C.M., Mallwitz, A., Wagner, S., Hartmann, N., Schotola, H., Fischer, T.H., Ungeheuer, N., Herting, J., Shah, A.M., Maier, L.S., *et al.* (2014). Enhanced late INa induces proarrhythmogenic SR Ca leak in a CaMKII-dependent manner. J Mol Cell Cardiol *76*, 94-105. 10.1016/j.yjmcc.2014.08.016.

Saliques, S., Zeller, M., Lorin, J., Lorgis, L., Teyssier, J.R., Cottin, Y., Rochette, L., and Vergely, C. (2010). Telomere length and cardiovascular disease. Arch Cardiovasc Dis *103*, 454-459. 10.1016/j.acvd.2010.08.002.

Sam, F., Kerstetter, D.L., Pimental, D.R., Mulukutla, S., Tabaee, A., Bristow, M.R., Colucci, W.S., and Sawyer, D.B. (2005). Increased reactive oxygen species production and functional alterations in antioxidant enzymes in human failing myocardium. J Card Fail *11*, 473-480. 10.1016/j.cardfail.2005.01.007.

Samavarchi-Tehrani, P., Golipour, A., David, L., Sung, H.K., Beyer, T.A., Datti, A., Woltjen, K., Nagy, A., and Wrana, J.L. (2010). Functional genomics reveals a BMP-driven mesenchymal-to-epithelial transition in the initiation of somatic cell reprogramming. Cell Stem Cell *7*, 64-77. 10.1016/j.stem.2010.04.015.

Santos, G.L., Hartmann, S., Zimmermann, W.H., Ridley, A., and Lutz, S. (2019). Inhibition of Rho-associated kinases suppresses cardiac myofibroblast function in engineered connective and heart muscle tissues. J Mol Cell Cardiol *134*, 13-28. 10.1016/j.yjmcc.2019.06.015.

Santos, G.L., Meyer, T., Tiburcy, M., DeGrave, A., Zimmermann, W.H., and Lutz, S. (2021). Fibroblast Derived Human Engineered Connective Tissue for Screening Applications. J Vis Exp. 10.3791/62700.

Sasaki, K., Makiyama, T., Yoshida, Y., Wuriyanghai, Y., Kamakura, T., Nishiuchi, S., Hayano, M., Harita, T., Yamamoto, Y., Kohjitani, H., *et al.* (2016). Patient-Specific Human Induced Pluripotent Stem Cell Model Assessed with Electrical Pacing Validates S107 as a Potential Therapeutic Agent for Catecholaminergic Polymorphic Ventricular Tachycardia. PLoS One *11*, e0164795. 10.1371/journal.pone.0164795.

Schick, R., Mekies, L.N., Shemer, Y., Eisen, B., Hallas, T., Ben Jehuda, R., Ben-Ari, M., Szantai, A., Willi, L., Shulman, R., *et al.* (2018). Functional abnormalities in induced Pluripotent Stem Cell-derived cardiomyocytes generated from titin-mutated patients with dilated cardiomyopathy. PLoS One *13*, e0205719. 10.1371/journal.pone.0205719.

Schiro, J.A., Chan, B.M., Roswit, W.T., Kassner, P.D., Pentland, A.P., Hemler, M.E., Eisen, A.Z., and Kupper, T.S. (1991). Integrin alpha 2 beta 1 (VLA-2) mediates reorganization and contraction of collagen matrices by human cells. Cell *67*, 403-410. 10.1016/0092-8674(91)90191-z.

Schultheiss, H.P., Fairweather, D., Caforio, A.L.P., Escher, F., Hershberger, R.E., Lipshultz, S.E., Liu, P.P., Matsumori, A., Mazzanti, A., McMurray, J., and Priori, S.G. (2019). Dilated cardiomyopathy. Nat Rev Dis Primers *5*, 32. 10.1038/s41572-019-0084-1.

Schweizer, P.A., Darche, F.F., Ullrich, N.D., Geschwill, P., Greber, B., Rivinius, R., Seyler, C., Muller-Decker, K., Draguhn, A., Utikal, J., *et al.* (2017). Subtype-specific differentiation of cardiac pacemaker cell clusters from human induced pluripotent stem cells. Stem Cell Res Ther *8*, 229. 10.1186/s13287-017-0681-4.

Schwinger, R.H., Bohm, M., Schmidt, U., Karczewski, P., Bavendiek, U., Flesch, M., Krause, E.G., and Erdmann, E. (1995). Unchanged protein levels of SERCA II and phospholamban but reduced Ca2+ uptake and Ca(2+)-ATPase activity of cardiac sarcoplasmic reticulum from dilated cardiomyopathy patients compared with patients with nonfailing hearts. Circulation *92*, 3220-3228. 10.1161/01.cir.92.11.3220.

Sedaghat-Hamedani, F., Rebs, S., El-Battrawy, I., Chasan, S., Krause, T., Haas, J., Zhong, R., Liao, Z., Xu, Q., Zhou, X., *et al.* (2021). Identification of SCN5a p.C335R Variant in a Large Family with Dilated Cardiomyopathy and Conduction Disease. Int J Mol Sci *22*. 10.3390/ijms222312990.

Seferovic, P.M., Polovina, M., Bauersachs, J., Arad, M., Gal, T.B., Lund, L.H., Felix, S.B., Arbustini, E., Caforio, A.L.P., Farmakis, D., *et al.* (2019). Heart failure in cardiomyopathies: a position paper from the Heart Failure Association of the European Society of Cardiology. Eur J Heart Fail *21*, 553-576. 10.1002/ejhf.1461.

Sen, L., Cui, G., Fonarow, G.C., and Laks, H. (2000). Differences in mechanisms of SR dysfunction in ischemic vs. idiopathic dilated cardiomyopathy. Am J Physiol Heart Circ Physiol *279*, H709-718. 10.1152/ajpheart.2000.279.2.H709.

Severs, N.J., Coppen, S.R., Dupont, E., Yeh, H.I., Ko, Y.S., and Matsushita, T. (2004). Gap junction alterations in human cardiac disease. Cardiovasc Res *62*, 368-377. 10.1016/j.cardiores.2003.12.007.

Shiba, Y., Gomibuchi, T., Seto, T., Wada, Y., Ichimura, H., Tanaka, Y., Ogasawara, T., Okada, K., Shiba, N., Sakamoto, K., *et al.* (2016). Allogeneic transplantation of iPS cell-derived cardiomyocytes regenerates primate hearts. Nature *538*, 388-391. 10.1038/nature19815.

Skorska, A., Johann, L., Chabanovska, O., Vasudevan, P., Kussauer, S., Hillemanns, M., Wolfien, M., Jonitz-Heincke, A., Wolkenhauer, O., Bader, R., *et al.* (2022). Monitoring the maturation of the sarcomere network: a super-resolution microscopy-based approach. Cell Mol Life Sci *79*, 149. 10.1007/s00018-022-04196-3.

Smith, C.L., Baek, S.T., Sung, C.Y., and Tallquist, M.D. (2011). Epicardial-derived cell epithelial-to-mesenchymal transition and fate specification require PDGF receptor signaling. Circ Res *108*, e15-26. 10.1161/CIRCRESAHA.110.235531.

Song, Y., Shryock, J.C., and Belardinelli, L. (2008). An increase of late sodium current induces delayed afterdepolarizations and sustained triggered activity in atrial myocytes. Am J Physiol Heart Circ Physiol *294*, H2031-2039. 10.1152/ajpheart.01357.2007.

Sossalla, S., Wagner, S., Rasenack, E.C., Ruff, H., Weber, S.L., Schondube, F.A., Tirilomis, T., Tenderich, G., Hasenfuss, G., Belardinelli, L., and Maier, L.S. (2008). Ranolazine improves diastolic dysfunction in isolated myocardium from failing human hearts--role of late sodium current and intracellular ion accumulation. J Mol Cell Cardiol *45*, 32-43. 10.1016/j.yjmcc.2008.03.006.

Souders, C.A., Bowers, S.L., and Baudino, T.A. (2009). Cardiac fibroblast: the renaissance cell. Circ Res *105*, 1164-1176. 10.1161/CIRCRESAHA.109.209809.

Sovari, A.A., Rutledge, C.A., Jeong, E.M., Dolmatova, E., Arasu, D., Liu, H., Vahdani, N., Gu, L., Zandieh, S., Xiao, L., *et al.* (2013). Mitochondria oxidative stress, connexin43 remodeling, and sudden arrhythmic death. Circ Arrhythm Electrophysiol *6*, 623-631. 10.1161/CIRCEP.112.976787.

Spach, M.S., and Boineau, J.P. (1997). Microfibrosis produces electrical load variations due to loss of side-to-side cell connections: a major mechanism of structural heart disease arrhythmias. Pacing Clin Electrophysiol *20*, 397-413. 10.1111/j.1540-8159.1997.tb06199.x.

Spach, M.S., Heidlage, J.F., Barr, R.C., and Dolber, P.C. (2004). Cell size and communication: role in structural and electrical development and remodeling of the heart. Heart Rhythm *1*, 500-515. 10.1016/j.hrthm.2004.06.010.

Srivastava, M., Nambiar, M., Sharma, S., Karki, S.S., Goldsmith, G., Hegde, M., Kumar, S., Pandey, M., Singh, R.K., Ray, P., *et al.* (2012). An inhibitor of nonhomologous end-joining abrogates double-strand break repair and impedes cancer progression. Cell *151*, 1474-1487. 10.1016/j.cell.2012.11.054.

Staerk, J., Dawlaty, M.M., Gao, Q., Maetzel, D., Hanna, J., Sommer, C.A., Mostoslavsky, G., and Jaenisch, R. (2010). Reprogramming of human peripheral blood cells to induced pluripotent stem cells. Cell Stem Cell *7*, 20-24. 10.1016/j.stem.2010.06.002.

Stempien-Otero, A., Kim, D.H., and Davis, J. (2016). Molecular networks underlying myofibroblast fate and fibrosis. J Mol Cell Cardiol *97*, 153-161. 10.1016/j.yjmcc.2016.05.002.

Stossel, T.P., Condeelis, J., Cooley, L., Hartwig, J.H., Noegel, A., Schleicher, M., and Shapiro, S.S. (2001). Filamins as integrators of cell mechanics and signalling. Nature Reviews Molecular Cell Biology *2*, 138-145. 10.1038/35052082.

Streckfuss-Bomeke, K., Wolf, F., Azizian, A., Stauske, M., Tiburcy, M., Wagner, S., Hubscher, D., Dressel, R., Chen, S., Jende, J., *et al.* (2013). Comparative study of human-induced pluripotent stem cells derived from bone marrow cells, hair keratinocytes, and skin fibroblasts. Eur Heart J *34*, 2618-2629. 10.1093/eurheartj/ehs203.

Sun, N., Yazawa, M., Liu, J., Han, L., Sanchez-Freire, V., Abilez, O.J., Navarrete, E.G., Hu, S., Wang, L., Lee, A., *et al.* (2012). Patient-specific induced pluripotent stem cells as a model for familial dilated cardiomyopathy. Sci Transl Med *4*, 130ra147. 10.1126/scitranslmed.3003552.

Sweeney, M., Corden, B., and Cook, S.A. (2020). Targeting cardiac fibrosis in heart failure with preserved ejection fraction: mirage or miracle? EMBO Mol Med *12*, e10865. 10.15252/emmm.201910865.

Tajsharghi, H. (2008). Thick and thin filament gene mutations in striated muscle diseases. Int J Mol Sci *9*, 1259-1275. 10.3390/ijms9071259.

Takahashi, K., Tanabe, K., Ohnuki, M., Narita, M., Ichisaka, T., Tomoda, K., and Yamanaka, S. (2007). Induction of pluripotent stem cells from adult human fibroblasts by defined factors. Cell *131*, 861-872. 10.1016/j.cell.2007.11.019.

Takahashi, K., and Yamanaka, S. (2006). Induction of pluripotent stem cells from mouse embryonic and adult fibroblast cultures by defined factors. Cell *126*, 663-676. 10.1016/j.cell.2006.07.024.

Takahashi, K., and Yamanaka, S. (2016). A decade of transcription factor-mediated reprogramming to pluripotency. Nat Rev Mol Cell Biol *17*, 183-193. 10.1038/nrm.2016.8.

Tallquist, M.D., and Molkentin, J.D. (2017). Redefining the identity of cardiac fibroblasts. Nat Rev Cardiol *14*, 484-491. 10.1038/nrcardio.2017.57.

Taylor, M.R., Fain, P.R., Sinagra, G., Robinson, M.L., Robertson, A.D., Carniel, E., Di Lenarda, A., Bohlmeyer, T.J., Ferguson, D.A., Brodsky, G.L., *et al.* (2003). Natural history of dilated cardiomyopathy due to lamin A/C gene mutations. J Am Coll Cardiol *41*, 771-780. 10.1016/s0735-1097(02)02954-6.

Thomas, D., Choi, S., Alamana, C., Parker, K.K., and Wu, J.C. (2022a). Cellular and Engineered Organoids for Cardiovascular Models. Circ Res *130*, 1780-1802. 10.1161/CIRCRESAHA.122.320305.

Thomas, D., Cunningham, N.J., Shenoy, S., and Wu, J.C. (2022b). Human-induced pluripotent stem cells in cardiovascular research: current approaches in cardiac differentiation, maturation strategies, and scalable production. Cardiovasc Res *118*, 20-36. 10.1093/cvr/cvab115.

Thompson, T.G., Chan, Y.M., Hack, A.A., Brosius, M., Rajala, M., Lidov, H.G., McNally, E.M., Watkins, S., and Kunkel, L.M. (2000). Filamin 2 (FLN2): A muscle-specific sarcoglycan interacting protein. J Cell Biol *148*, 115-126. 10.1083/jcb.148.1.115.

Thomson, J.A., Itskovitz-Eldor, J., Shapiro, S.S., Waknitz, M.A., Swiergiel, J.J., Marshall, V.S., and Jones, J.M. (1998). Embryonic stem cell lines derived from human blastocysts. Science *282*, 1145-1147. 10.1126/science.282.5391.1145.

Tiburcy, M., Hudson, J.E., Balfanz, P., Schlick, S., Meyer, T., Chang Liao, M.L., Levent, E., Raad, F., Zeidler, S., Wingender, E., *et al.* (2017). Defined Engineered Human Myocardium With Advanced Maturation for Applications in Heart Failure Modeling and Repair. Circulation *135*, 1832-1847. 10.1161/CIRCULATIONAHA.116.024145.

Tiburcy, M., Meyer, T., Liaw, N.Y., and Zimmermann, W.H. (2020). Generation of Engineered Human Myocardium in a Multi-well Format. STAR Protoc *1*, 100032. 10.1016/j.xpro.2020.100032.

Tiemann, U., Sgodda, M., Warlich, E., Ballmaier, M., Scholer, H.R., Schambach, A., and Cantz, T. (2011). Optimal reprogramming factor stoichiometry increases colony numbers and affects molecular characteristics of murine induced pluripotent stem cells. Cytometry A *79*, 426-435. 10.1002/cyto.a.21072.

Tirziu, D., Giordano, F.J., and Simons, M. (2010). Cell communications in the heart. Circulation *122*, 928-937. 10.1161/CIRCULATIONAHA.108.847731.

Tohyama, S., Hattori, F., Sano, M., Hishiki, T., Nagahata, Y., Matsuura, T., Hashimoto, H., Suzuki, T., Yamashita, H., Satoh, Y., *et al.* (2013). Distinct metabolic flow enables large-scale purification of mouse and human pluripotent stem cell-derived cardiomyocytes. Cell Stem Cell *12*, 127-137. 10.1016/j.stem.2012.09.013.

Tojkander, S., Gateva, G., and Lappalainen, P. (2012). Actin stress fibers--assembly, dynamics and biological roles. J Cell Sci *125*, 1855-1864. 10.1242/jcs.098087.

Tomasek, J.J., Gabbiani, G., Hinz, B., Chaponnier, C., and Brown, R.A. (2002). Myofibroblasts and mechano-regulation of connective tissue remodelling. Nat Rev Mol Cell Biol *3*, 349-363. 10.1038/nrm809.

Traister, A., Li, M., Aafaqi, S., Lu, M., Arab, S., Radisic, M., Gross, G., Guido, F., Sherret, J., Verma, S., *et al.* (2014). Integrin-linked kinase mediates force transduction in cardiomyocytes by modulating SERCA2a/PLN function. Nat Commun *5*, 4533. 10.1038/ncomms5533.

Trevino, A.E., and Zhang, F. (2014). Genome editing using Cas9 nickases. Methods Enzymol *546*, 161-174. 10.1016/B978-0-12-801185-0.00008-8.

Tschumperlin, D.J., Ligresti, G., Hilscher, M.B., and Shah, V.H. (2018). Mechanosensing and fibrosis. J Clin Invest *128*, 74-84. 10.1172/JCI93561.

Tzouvelekis, A., and Kaminski, N. (2015). Epigenetics in idiopathic pulmonary fibrosis. Biochem Cell Biol *93*, 159-170. 10.1139/bcb-2014-0126.
Undrovinas, A.I., Maltsev, V.A., and Sabbah, H.N. (1999). Repolarization abnormalities in cardiomyocytes of dogs with chronic heart failure: role of sustained inward current. Cell Mol Life Sci *55*, 494-505. 10.1007/s000180050306.
Urban, P.L. (2016). Quantitative mass spectrometry: an overview. Philos Trans A Math Phys Eng Sci *374*. 10.1098/rsta.2015.0382.
Valdes-Mas, R., Gutierrez-Fernandez, A., Gomez, J., Coto, E., Astudillo, A., Puente, D.A., Reguero, J.R., Alvarez, V., Moris, C., Leon, D., *et al.* (2014). Mutations in filamin C cause a new form of familial hypertrophic cardiomyopathy. Nat Commun *5*, 5326. 10.1038/ncomms6326.
Valdivia, C.R., Chu, W.W., Pu, J., Foell, J.D., Haworth, R.A., Wolff, M.R., Kamp, T.J., and Makielski, J.C. (2005). Increased late sodium current in myocytes from a canine heart failure model and from failing human heart. J Mol Cell Cardiol *38*, 475-483. 10.1016/j.yjmcc.2004.12.012.
van der Flier, A., and Sonnenberg, A. (2001). Structural and functional aspects of filamins. Biochim Biophys Acta *1538*, 99-117. 10.1016/s0167-4889(01)00072-6.
van der Ven, P.F., Ehler, E., Vakeel, P., Eulitz, S., Schenk, J.A., Milting, H., Micheel, B., and Furst, D.O. (2006). Unusual splicing events result in distinct Xin isoforms that associate differentially with filamin c and Mena/VASP. Exp Cell Res *312*, 2154-2167. 10.1016/j.yexcr.2006.03.015.
van der Ven, P.F., Wiesner, S., Salmikangas, P., Auerbach, D., Himmel, M., Kempa, S., Hayess, K., Pacholsky, D., Taivainen, A., Schroder, R., *et al.* (2000). Indications for a novel muscular dystrophy pathway. gamma-filamin, the muscle-specific filamin isoform, interacts with myotilin. J Cell Biol *151*, 235-248. 10.1083/jcb.151.2.235.
Vartak, S.V., and Raghavan, S.C. (2015). Inhibition of nonhomologous end joining to increase the specificity of CRISPR/Cas9 genome editing. FEBS J *282*, 4289-4294. 10.1111/febs.13416.
Velychko, S., Adachi, K., Kim, K.P., Hou, Y., MacCarthy, C.M., Wu, G., and Scholer, H.R. (2019). Excluding Oct4 from Yamanaka Cocktail Unleashes the Developmental Potential of iPSCs. Cell Stem Cell *25*, 737-753 e734. 10.1016/j.stem.2019.10.002.
Verdonschot, J.A.J., Hazebroek, M.R., Derks, K.W.J., Barandiaran Aizpurua, A., Merken, J.J., Wang, P., Bierau, J., van den Wijngaard, A., Schalla, S.M., Abdul Hamid, M.A., *et al.* (2018). Titin cardiomyopathy leads to altered mitochondrial energetics, increased fibrosis and long-term life-threatening arrhythmias. Eur Heart J *39*, 864-873. 10.1093/eurheartj/ehx808.
Verdonschot, J.A.J., Vanhoutte, E.K., Claes, G.R.F., Helderman-van den Enden, A., Hoeijmakers, J.G.J., Hellebrekers, D., de Haan, A., Christiaans, I., Lekanne Deprez, R.H., Boen, H.M., *et al.* (2020). A mutation update for the FLNC gene in myopathies and cardiomyopathies. Hum Mutat *41*, 1091-1111. 10.1002/humu.24004.
Vuckovic, S., Dinani, R., Nollet, E.E., Kuster, D.W.D., Buikema, J.W., Houtkooper, R.H., Nabben, M., van der Velden, J., and Goversen, B. (2022). Characterization of cardiac metabolism in iPSC-derived cardiomyocytes: lessons from maturation and disease modeling. Stem Cell Res Ther *13*, 332. 10.1186/s13287-022-03021-9.
Walker, C.A., and Spinale, F.G. (1999). The structure and function of the cardiac myocyte: a review of fundamental concepts. J Thorac Cardiovasc Surg *118*, 375-382. 10.1016/S0022-5223(99)70233-3.

Wang, L., Yang, Y., Ma, H., Xie, Y., Xu, J., Near, D., Wang, H., Garbutt, T., Li, Y., Liu, J., and Qian, L. (2022a). Single-cell dual-omics reveals the transcriptomic and epigenomic diversity of cardiac non-myocytes. Cardiovasc Res *118*, 1548-1563. 10.1093/cvr/cvab134.

Wang, Q., Karvelsson, S.T., Kotronoulas, A., Gudjonsson, T., Halldorsson, S., and Rolfsson, O. (2022b). Glutamine-Fructose-6-Phosphate Transaminase 2 (GFPT2) Is Upregulated in Breast Epithelial-Mesenchymal Transition and Responds to Oxidative Stress. Mol Cell Proteomics *21*, 100185. 10.1016/j.mcpro.2021.100185.

Wang, Y., Yu, M., Hao, K., Lei, W., Tang, M., and Hu, S. (2022c). Cardiomyocyte Maturation-the Road is not Obstructed. Stem Cell Rev Rep. 10.1007/s12015-022-10407-y.

Warren, L., Manos, P.D., Ahfeldt, T., Loh, Y.H., Li, H., Lau, F., Ebina, W., Mandal, P.K., Smith, Z.D., Meissner, A., *et al.* (2010). Highly efficient reprogramming to pluripotency and directed differentiation of human cells with synthetic modified mRNA. Cell Stem Cell *7*, 618-630. 10.1016/j.stem.2010.08.012.

Weintraub, R.G., Semsarian, C., and Macdonald, P. (2017). Dilated cardiomyopathy. Lancet *390*, 400-414. 10.1016/S0140-6736(16)31713-5.

Wencker, D., Chandra, M., Nguyen, K., Miao, W., Garantziotis, S., Factor, S.M., Shirani, J., Armstrong, R.C., and Kitsis, R.N. (2003). A mechanistic role for cardiac myocyte apoptosis in heart failure. J Clin Invest *111*, 1497-1504. 10.1172/JCI17664.

Widyantoro, B., Emoto, N., Nakayama, K., Anggrahini, D.W., Adiarto, S., Iwasa, N., Yagi, K., Miyagawa, K., Rikitake, Y., Suzuki, T., *et al.* (2010). Endothelial cell-derived endothelin-1 promotes cardiac fibrosis in diabetic hearts through stimulation of endothelial-to-mesenchymal transition. Circulation *121*, 2407-2418. 10.1161/CIRCULATIONAHA.110.938217.

Williams, B., Lobel, W., Finklea, F., Halloin, C., Ritzenhoff, K., Manstein, F., Mohammadi, S., Hashemi, M., Zweigerdt, R., Lipke, E., and Cremaschi, S. (2020). Prediction of Human Induced Pluripotent Stem Cell Cardiac Differentiation Outcome by Multifactorial Process Modeling. Front Bioeng Biotechnol *8*, 851. 10.3389/fbioe.2020.00851.

Worku, M.G. (2021). Pluripotent and Multipotent Stem Cells and Current Therapeutic Applications: Review. Stem Cells Cloning *14*, 3-7. 10.2147/SCCAA.S304887.

Xu, X., Gao, D., Wang, P., Chen, J., Ruan, J., Xu, J., and Xia, X. (2018). Efficient homology-directed gene editing by CRISPR/Cas9 in human stem and primary cells using tube electroporation. Sci Rep *8*, 11649. 10.1038/s41598-018-30227-w.

Yang, C., Tibbitt, M.W., Basta, L., and Anseth, K.S. (2014a). Mechanical memory and dosing influence stem cell fate. Nat Mater *13*, 645-652. 10.1038/nmat3889.

Yang, K.C., Bonini, M.G., and Dudley, S.C., Jr. (2014b). Mitochondria and arrhythmias. Free Radic Biol Med *71*, 351-361. 10.1016/j.freeradbiomed.2014.03.033.

Yang, L., Soonpaa, M.H., Adler, E.D., Roepke, T.K., Kattman, S.J., Kennedy, M., Henckaerts, E., Bonham, K., Abbott, G.W., Linden, R.M., *et al.* (2008). Human cardiovascular progenitor cells develop from a KDR+ embryonic-stem-cell-derived population. Nature *453*, 524-528. 10.1038/nature06894.

Yang, X., Pabon, L., and Murry, C.E. (2014c). Engineering adolescence: maturation of human pluripotent stem cell-derived cardiomyocytes. Circ Res *114*, 511-523. 10.1161/CIRCRESAHA.114.300558.

Yang, X., Rodriguez, M., Pabon, L., Fischer, K.A., Reinecke, H., Regnier, M., Sniadecki, N.J., Ruohola-Baker, H., and Murry, C.E. (2014d). Tri-iodo-l-thyronine promotes the maturation of human cardiomyocytes-derived from induced pluripotent stem cells. J Mol Cell Cardiol *72*, 296-304. 10.1016/j.yjmcc.2014.04.005.

Yang, X., Rodriguez, M.L., Leonard, A., Sun, L., Fischer, K.A., Wang, Y., Ritterhoff, J., Zhao, L., Kolwicz, S.C., Jr., Pabon, L., *et al.* (2019). Fatty Acids Enhance the Maturation of Cardiomyocytes Derived from Human Pluripotent Stem Cells. Stem Cell Reports *13*, 657-668. 10.1016/j.stemcr.2019.08.013.

Ye, L., Zimmermann, W.H., Garry, D.J., and Zhang, J. (2013). Patching the heart: cardiac repair from within and outside. Circ Res *113*, 922-932. 10.1161/CIRCRESAHA.113.300216.

Yoshida, S., Miyagawa, S., Fukushima, S., Kawamura, T., Kashiyama, N., Ohashi, F., Toyofuku, T., Toda, K., and Sawa, Y. (2018). Maturation of Human Induced Pluripotent Stem Cell-Derived Cardiomyocytes by Soluble Factors from Human Mesenchymal Stem Cells. Mol Ther *26*, 2681-2695. 10.1016/j.ymthe.2018.08.012.

Yoshida, Y., and Yamanaka, S. (2017). Induced Pluripotent Stem Cells 10 Years Later: For Cardiac Applications. Circ Res *120*, 1958-1968. 10.1161/CIRCRESAHA.117.311080.

Young, C.S., Hicks, M.R., Ermolova, N.V., Nakano, H., Jan, M., Younesi, S., Karumbayaram, S., Kumagai-Cresse, C., Wang, D., Zack, J.A., *et al.* (2016). A Single CRISPR-Cas9 Deletion Strategy that Targets the Majority of DMD Patients Restores Dystrophin Function in hiPSC-Derived Muscle Cells. Cell Stem Cell *18*, 533-540. 10.1016/j.stem.2016.01.021.

Yu, J., Vodyanik, M.A., Smuga-Otto, K., Antosiewicz-Bourget, J., Frane, J.L., Tian, S., Nie, J., Jonsdottir, G.A., Ruotti, V., Stewart, R., *et al.* (2007). Induced pluripotent stem cell lines derived from human somatic cells. Science *318*, 1917-1920. 10.1126/science.1151526.

Yutzey, K.E. (2017). Cardiomyocyte Proliferation: Teaching an Old Dogma New Tricks. Circ Res *120*, 627-629. 10.1161/CIRCRESAHA.116.310058.

Zaglia, T., and Mongillo, M. (2017). Cardiac sympathetic innervation, from a different point of (re)view. J Physiol *595*, 3919-3930. 10.1113/JP273120.

Zeisberg, E.M., and Kalluri, R. (2010). Origins of cardiac fibroblasts. Circ Res *107*, 1304-1312. 10.1161/CIRCRESAHA.110.231910.

Zent, J., and Guo, L.W. (2018). Signaling Mechanisms of Myofibroblastic Activation: Outside-in and Inside-Out. Cell Physiol Biochem *49*, 848-868. 10.1159/000493217.

Zhang, H., Tian, L., Shen, M., Tu, C., Wu, H., Gu, M., Paik, D.T., and Wu, J.C. (2019). Generation of Quiescent Cardiac Fibroblasts From Human Induced Pluripotent Stem Cells for In Vitro Modeling of Cardiac Fibrosis. Circ Res *125*, 552-566. 10.1161/CIRCRESAHA.119.315491.

Zhang, J., Nuebel, E., Daley, G.Q., Koehler, C.M., and Teitell, M.A. (2012). Metabolic regulation in pluripotent stem cells during reprogramming and self-renewal. Cell Stem Cell *11*, 589-595. 10.1016/j.stem.2012.10.005.

Zhang, J., Wang, X., Vikash, V., Ye, Q., Wu, D., Liu, Y., and Dong, W. (2016). ROS and ROS-Mediated Cellular Signaling. Oxid Med Cell Longev *2016*, 4350965. 10.1155/2016/4350965.

Zhang, J., Wilson, G.F., Soerens, A.G., Koonce, C.H., Yu, J., Palecek, S.P., Thomson, J.A., and Kamp, T.J. (2009). Functional cardiomyocytes derived from human induced pluripotent stem cells. Circ Res *104*, e30-41. 10.1161/CIRCRESAHA.108.192237.

Zhang, Y., Ge, X., Yang, F., Zhang, L., Zheng, J., Tan, X., Jin, Z.B., Qu, J., and Gu, F. (2014). Comparison of non-canonical PAMs for CRISPR/Cas9-mediated DNA cleavage in human cells. Sci Rep *4*, 5405. 10.1038/srep05405.

Zhao, J., Cao, H., Tian, L., Huo, W., Zhai, K., Wang, P., Ji, G., and Ma, Y. (2017). Efficient Differentiation of TBX18(+)/WT1(+) Epicardial-Like Cells from Human Pluripotent Stem Cells Using Small Molecular Compounds. Stem Cells Dev *26*, 528-540. 10.1089/scd.2016.0208.

Zhao, M., Tang, Y., Zhou, Y., and Zhang, J. (2019). Deciphering Role of Wnt Signalling in Cardiac Mesoderm and Cardiomyocyte Differentiation from Human iPSCs: Four-

dimensional control of Wnt pathway for hiPSC-cardiomyocytess differentiation. Sci Rep *9*, 19389. 10.1038/s41598-019-55620-x.
Zhao, M.T., Shao, N.Y., and Garg, V. (2020a). Subtype-specific cardiomyocytes for precision medicine: Where are we now? Stem Cells *38*, 822-833. 10.1002/stem.3178.
Zhao, M.T., Ye, S., Su, J., and Garg, V. (2020b). Cardiomyocyte Proliferation and Maturation: Two Sides of the Same Coin for Heart Regeneration. Front Cell Dev Biol *8*, 594226. 10.3389/fcell.2020.594226.
Zheng, T., Hou, Y., Zhang, P., Zhang, Z., Xu, Y., Zhang, L., Niu, L., Yang, Y., Liang, D., Yi, F., *et al.* (2017). Profiling single-guide RNA specificity reveals a mismatch sensitive core sequence. Sci Rep *7*, 40638. 10.1038/srep40638.
Zhou, A.X., Hartwig, J.H., and Akyurek, L.M. (2010a). Filamins in cell signaling, transcription and organ development. Trends Cell Biol *20*, 113-123. 10.1016/j.tcb.2009.12.001.
Zhou, B., von Gise, A., Ma, Q., Hu, Y.W., and Pu, W.T. (2010b). Genetic fate mapping demonstrates contribution of epicardium-derived cells to the annulus fibrosis of the mammalian heart. Dev Biol *338*, 251-261. 10.1016/j.ydbio.2009.12.007.
Zhou, P., and Pu, W.T. (2016). Recounting Cardiac Cellular Composition. Circ Res *118*, 368-370. 10.1161/CIRCRESAHA.116.308139.
Zhou, W., and Freed, C.R. (2009). Adenoviral gene delivery can reprogram human fibroblasts to induced pluripotent stem cells. Stem Cells *27*, 2667-2674. 10.1002/stem.201.
Zhou, Y., Chen, Z., Zhang, L., Zhu, M., Tan, C., Zhou, X., Evans, S.M., Fang, X., Feng, W., and Chen, J. (2020). Loss of Filamin C Is Catastrophic for Heart Function. Circulation *141*, 869-871. 10.1161/CIRCULATIONAHA.119.044061.
Zhu, L., Liu, K., Feng, Q., and Liao, Y. (2022). Cardiac Organoids: A 3D Technology for Modeling Heart Development and Disease. Stem Cell Rev Rep. 10.1007/s12015-022-10385-1.
Zitzler, J., Link, D., Schafer, R., Liebetrau, W., Kazinski, M., Bonin-Debs, A., Behl, C., Buckel, P., and Brinkmann, U. (2004). High-throughput functional genomics identifies genes that ameliorate toxicity due to oxidative stress in neuronal HT-22 cells: GFPT2 protects cells against peroxide. Mol Cell Proteomics *3*, 834-840. 10.1074/mcp.M400054-MCP200.
Zuris, J.A., Thompson, D.B., Shu, Y., Guilinger, J.P., Bessen, J.L., Hu, J.H., Maeder, M.L., Joung, J.K., Chen, Z.Y., and Liu, D.R. (2015). Cationic lipid-mediated delivery of proteins enables efficient protein-based genome editing in vitro and in vivo. Nat Biotechnol *33*, 73-80. 10.1038/nbt.3081.

7 Appendix

In addition to the presented DCM project, the submitting PhD student contributed to additional work in collaboration with the group of Prof. Dr. Samuel Sossalla. As this work resulted in two significant publications, it is summarized below.

Voltage-gated sodium channels (Na_v) are crucial for cardiac conduction, since they open quickly upon action potential arrival, induce membrane depolarization, and hence allow cardiomyocyte contraction. Equally, Na_v close quickly after activation, important for repolarization and cardiomyocyte relaxation. However, in heart failure (HF) and other cardiac pathologies, some Na_v remain open and induce an enhanced persistent Na^+ current (late I_{Na} or I_{NaL}) (Song *et al.*, 2008; Sossalla *et al.*, 2008; Valdivia *et al.*, 2005). This I_{NaL} has huge consequences on cardiac electrophysiology and could induce arrhythmias (Maltsev *et al.*, 1998; Undrovinas *et al.*, 1999). The most prominent cardiac Na_v is the $Na_v1.5$ (Gellens *et al.*, 1992). Nevertheless, other Na_v isoforms are expressed in the heart. This includes expression of the largely non-cardiac $Na_v1.8$, encoded by the *SCN10A* gene, originally shown to be expressed in sensory neurons (Akopian *et al.*, 1996). Interestingly, expression of $Na_v1.8$ was shown to be increased in human failing myocardium and was associated with enhanced I_{NaL} and arrhythmogenesis (Ahmad *et al.*, 2019; Dybkova *et al.*, 2018). Further studies identified variants within the *SCN10A* gene ($Na_v1.8$) by genome wide association studies, to be associated with arrhythmias and sudden cardiac death (Jabbari *et al.*, 2015). Nevertheless, since $Na_v1.8$ originally was identified in sensory neurons it is still under debate whether these reported effects originate from cardiac ganglia or cardiomyocytes.
To investigate the role of $Na_v1.8$ in cardiomyocytes, CRISPR/Cas9 genome editing was applied to generate an iPSC line with a homozygous *SCN10A* knock-out (Maurer *et al.*, 2022). In brief, two crRNAs and the Cas9 enzyme were introduced into a previously described healthy iPSC line (Borchert *et al.*, 2017) by electroporation. These two crRNA were targeted the first exon of the *SCN10A* gene, where the Cas9 should introduce DSB, which by chance should be repaired by NHEJ, generating spontaneous insertions/deletions, eventually leading to frameshifts resulting in premature stop codons (Suppl. Fig. 1 A). This approach yielded two clones (K62.1, K62.4), originating form a mixed clone (K62), composed of edited and wildtype clones, after subsequent singularization. Both clones harbor identical frameshifts resulting in premature stop codons on both alleles (Suppl. Fig. 1 B). Maintained presence of the frameshifts was checked frequently by Sanger sequencing. Additionally, off-target sites predicted for both crRNAs were analyzed by Sanger sequencing as well, which did not identify any off-target cutting (data exemplarily shown in Suppl. Fig. 2). To prove origin of the knock-out (KO) lines from the healthy iPSC line of which they derive, STR analysis were performed (data not shown). G-banding analysis of both KO iPSC lines revealed a normal karyotype (Suppl. Fig. 1 C). Since genome editing like CRISPR/Cas9 has dramatic effects on the cells´ genome, the KO iPSC lines again were analyzed for full pluripotency. First, expression of classical pluripotency-specific genes, like *OCT4, SOX2, NANOG* and *LIN28,* in both KO lines was comparable to expression in the healthy iPSC line and significantly upregulated compared to fibroblasts from which the parental healthy iPSC line originally was derived (Suppl. Fig. 1 D). Additionally,

expression of similar pluripotency-specific markers (OCT4, SOX2, LIN28 and TRA1-60) was demonstrated on protein level by IF staining (Suppl. Fig. 1 E). Furthermore, the KO lines displayed classical iPSC morphology and expressed ALP (Fig. 1E). Both KO lines showed spontaneous differentiation capacity into all three germ layers, shown by expression of markers of all three germ layers on protein level, like α-SMA, AFP, and β-III-Tubulin (Suppl. Fig. 1 F). This was further supported by mRNA data, showing expression endodermal *AFP* and *ALB,* mesodermal *cTNT* and *αMHC,* as well as ectodermal *MAP2* and *PAX6* (Suppl. Fig. 1 F). In line with these findings, *OCT4* expression decreased during differentiation. It could also be shown by MLC2v expression, that the KO iPSC are able to differentiate into ventricular iPSC-cardiomyocytes (Suppl. Fig. 1 G).

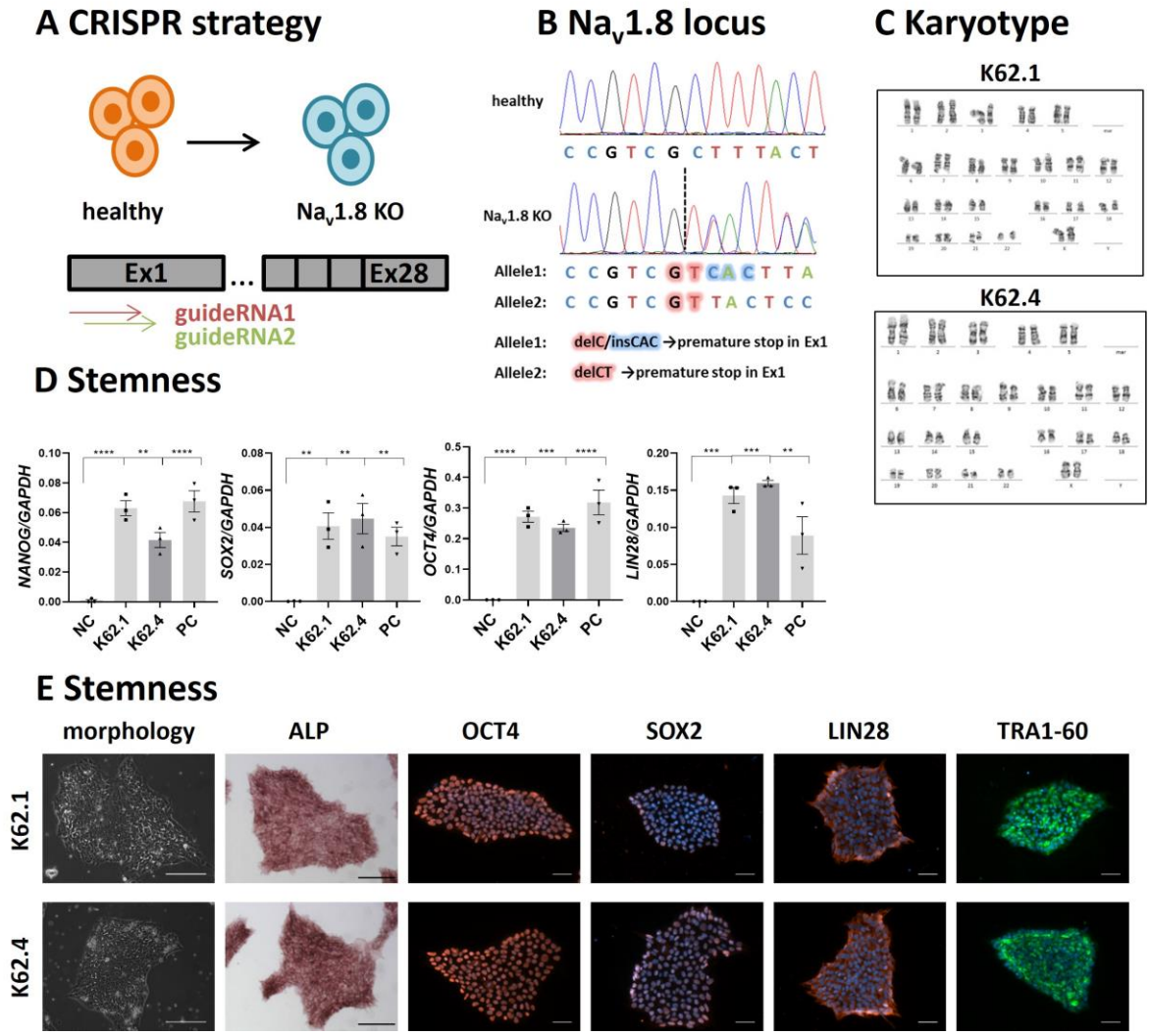

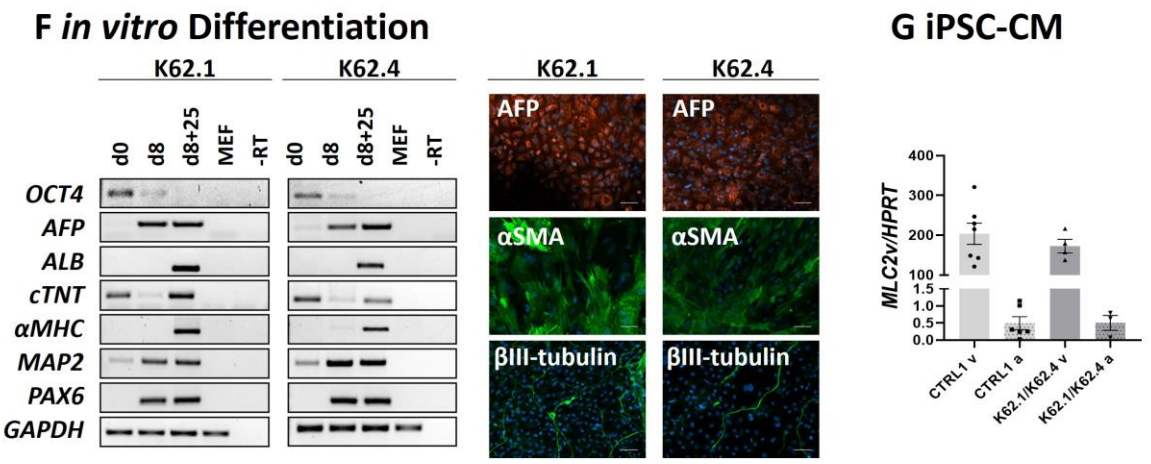

Suppl. Fig. 1: Summary of SCN10A knock-out iPSC lines and subsequent quality control analysis. A Shown is the CRISPR/Cas9 strategy, using two different guideRNAs to induce frameshifts resulting in premature stop codons. **B** Shown is the resulting sequence of obtained homozygous knock-out lines, displaying insertion and deletion on both alleles resulting in premature stop codons in SCN10A exon 1. **C** Shown are G-banding analysis to prove a normal karyotype. **D** Shown are qPCR analysis to demonstrate mRNA expression of pluripotency-specific genes, like NANOG, SOX2, OCT4 and LIN28. **E** Shown are images of classical iPSC morphology, expression of ALP and expression of pluripotency-specific proteins OCT4, SOX2, LIN28 and TRA1-60. **F** Shown is expression of markers of all three germ layers on mRNA level (endoderm: AFP, ALB: mesoderm: cTNT, αMHC; ectoderm: MAP2, PAX6) and on protein level (endoderm: AFP, mesoderm: α-SMA, ectoderm: β-III-Tubulin. **G** Shown is qPCR data of MLC2v expression to demonstrate successful differentiation into ventricular iPSC-cardiomyocytes. Figure from Maurer *et al.* (Maurer *et al.*, 2022).

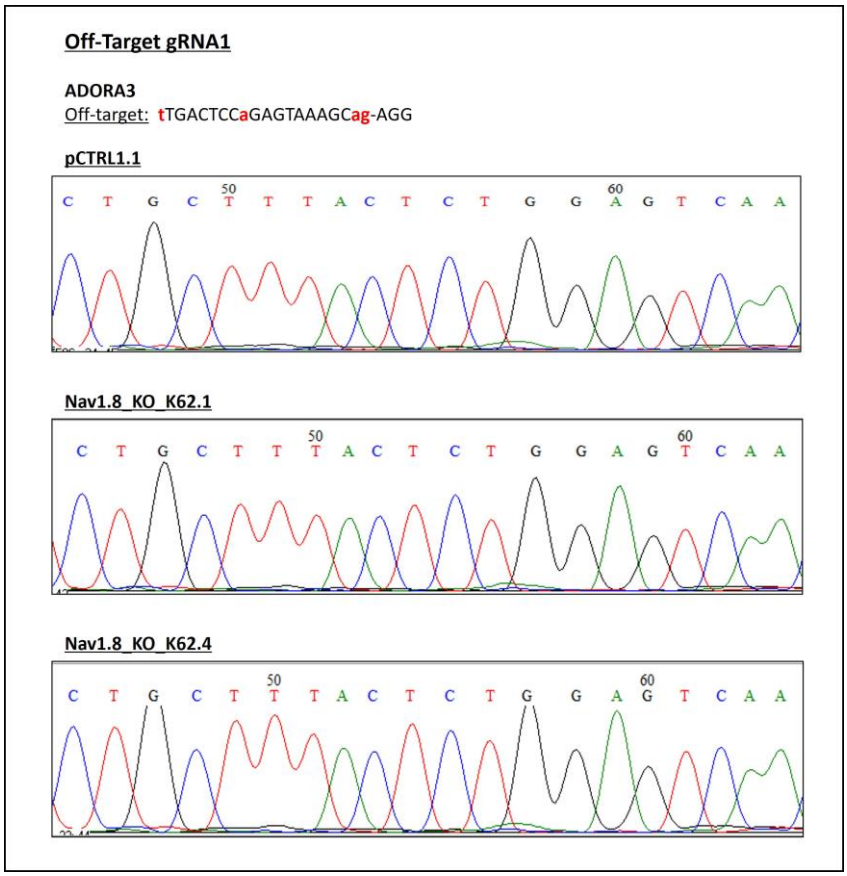

Suppl. Fig. 2: Off target analysis of $Na_v1.8$ KO gene edited iPSC clones. Sanger sequencing chromatograms of the ADORA3 as exemplarily chosen predicted off-target site (Jefferson Off-Spotter). Depicted are chromatograms of control iPSC lines before and after CRISPR/Cas9 to induce a $Na_v1.8$ KO (K62.1 and K62.4).

These generated homozygous *SCN10A* KO iPSC lines were used within a broader study to demonstrate that $Na_v1.8$ indeed plays a crucial role within cardiomyocytes by contributing to I_{NaL} formation (Bengel *et al.*, 2021). In short, previous studies reported an interplay of upregulated CaMKIIδ and I_{NaL}, which may induce cardiac arrhythmias in heart failure (Sag *et al.*, 2014). Additionally, interactions between CaMKIIδ and $Na_v1.5$ were demonstrated (Ashpole *et al.*, 2012). Based on this, an interaction between CaMKIIδ and $Na_v1.8$ was hypothesized maybe also driving I_{NaL} formation. Despite very low *SCN10A* mRNA expression compared to *SCN5A* ($Na_v1.5$) mRNA expression, indeed a direct interaction of CaMKIIδ and $Na_v1.8$ could be demonstrated (Bengel *et al.*, 2021). Functional experiments revealed decreased I_{NaL} upon genetical or pharmacological (autocamtide-2-related inhibitory peptide (AIP)) inhibition of CaMKIIδ as well as upon pharmacological inhibition of $Na_v1.8$ by PF-01247324 in murine and human cardiomyocytes (Bengel *et al.*, 2021). To clearly demonstrate the role of $Na_v1.8$ in cardiomyocytes and to support the specificity of PF-01247324 to specifically block $Na_v1.8$ and no other Na_v, the generated *SCN10A* KO iPSC lines were differentiated into ventricular iPSC-cardiomyocytes and the I_{NaL} was determined in basal *SCN10A* KO iPSC-cardiomyocytes, basal wildtype iPSC-cardiomyocytes and PF-01247324 treated KO and wildtype iPSC-cardiomyocytes. To enhance the I_{NaL}, which is low under healthy conditions, the iPSC-cardiomyocytes were treated with isoprenaline (Iso). Interestingly, these analyses revealed a ~60% reduction of I_{NaL} in Iso/PF-01247324-treated wildtype iPSC-cardiomyocytes compared to only Iso-treated wildtype iPSC-cardiomyocytes (Bengel *et al.*, 2021). A similar effect could be observed for Iso-treated *SCN10A* KO iPSC-cardiomyocytes compared to Iso-treated wildtype iPSC-cardiomyocytes, with a reduction of ~70% in I_{NaL} (Bengel *et al.*, 2021). This highlights an important role of cardiomyocyte expressed $Na_v1.8$ and its contribution to I_{NaL} formation. Since no further decrease in I_{NaL} could be observed upon PF-01247324 treatment of *SCN10A* KO iPSC-cardiomyocytes, the specificity of PF-01247324 could be further supported (Bengel *et al.*, 2021). Similar effects were demonstrated in $SCN10A^{-/-}$/$CaMKII\delta^{+/T}$ mice, showing decreased I_{NaL} in $SCN10A^{-/-}$/$CaMKII\delta^{+/T}$ compared to $CaMKII\delta^{+/T}$ mice with increased CaMKIIδ expression (Bengel *et al.*, 2021). These animals additionally were shown to have less ventricular arrhythmias and higher survival rates (Bengel *et al.*, 2021). Additionally, pharmacological inhibition of either CaMKIIδ or $Na_v1.8$ by AIP or PF-01247324, respectively, or parallel inhibition of both also reduced proarrhythmic potential (i.e. CaSpF) in human failing heart to a comparable level (Bengel *et al.*, 2021). In summary, this study demonstrated an interaction of CaMKIIδ and $Na_v1.8$ in cardiomyocytes, contributing to enhanced I_{NaL} formation in diseased and heart failure conditions, resulting in proarrhythmic events. This study showed that pharmacological inhibition or genetical knock-out of $Na_v1.8$ in different cell models can reverse the identified effects. Therefore, $Na_v1.8$ provides a promising CaMKIIδ downstream target for anti-arrhythmogenic treatment (Bengel *et al.*, 2021).

The submitting PhD student conducted CRISPR/Cas9 genome editing to generate homozygous *SCN10A* KO iPSC lines, analyzed and singularized promising clones, performed regular sequence control and did quality control and pluripotency characterization experiments. Additionally, all iPSC-cardiomyocytes differentiation experiments and quality control of iPSC-cardiomyocytes for functional experiments were performed by the PhD

student. Furthermore, mRNA expression analysis of *CaMKIIδ, SCN5A* and *SCN10A* from different tissues and cell systems were performed by the PhD student.

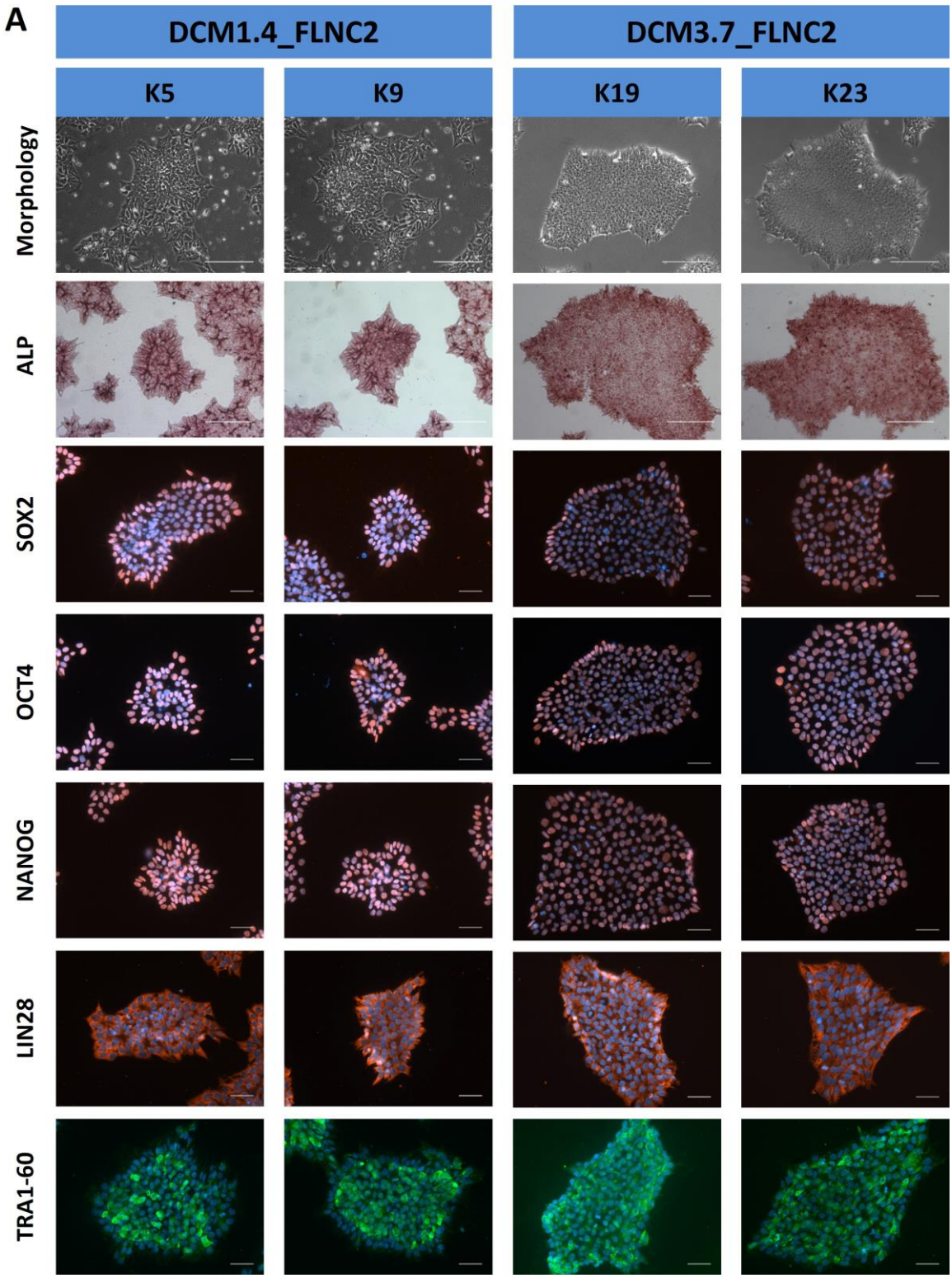

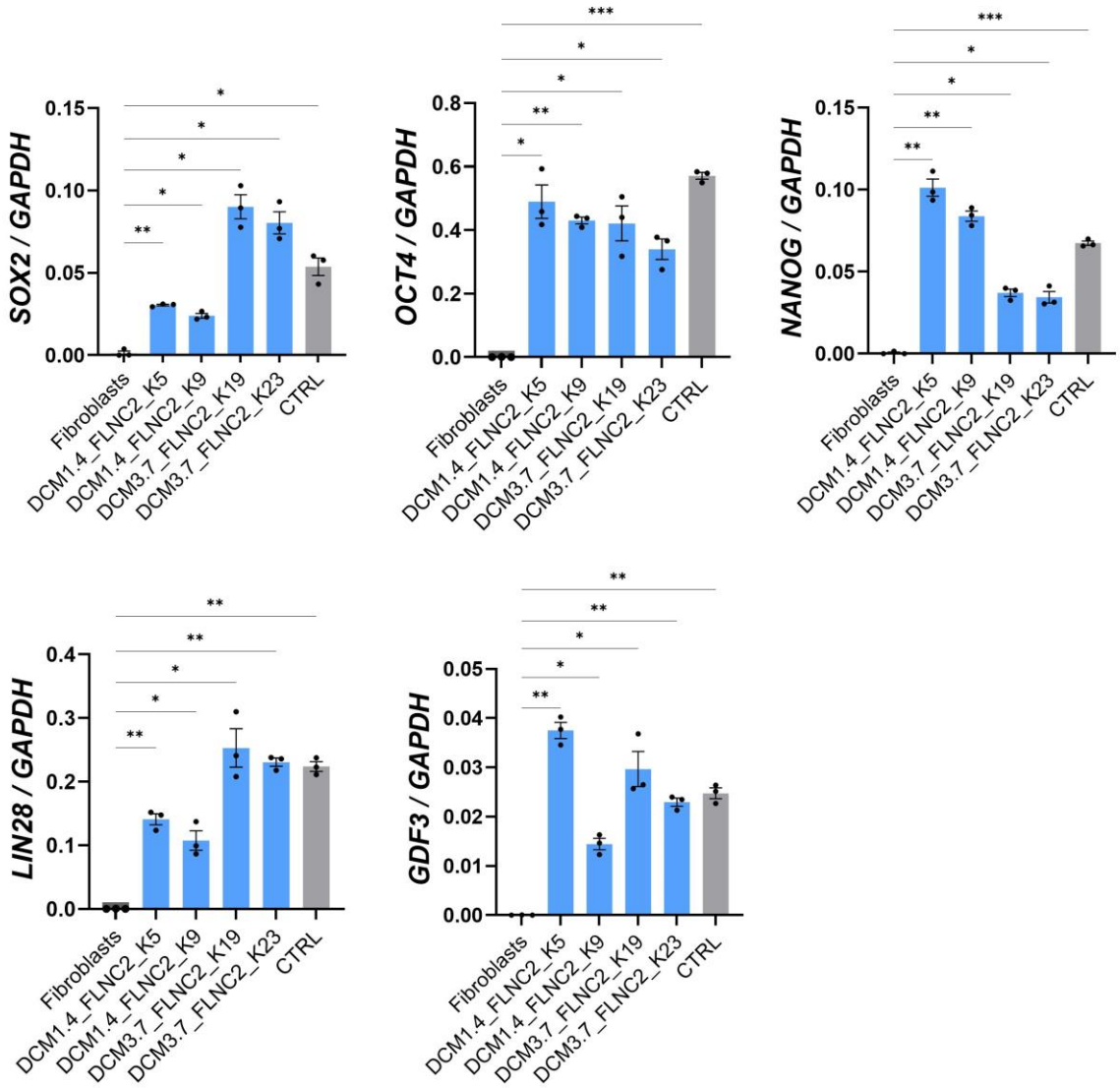

Suppl. Fig. 3: Pluripotency characterization of FLNC gene edited iPSC clones. Pluripotency characterization results of additional gene edited iPSC clones of DCM1 and DCM3 – K5, K9 and K19, K24, respectively. **A** Brightfield and ALP images of the generated iPSC lines of all family members. Images were taken with a Zeiss Axio Observer A1 inverted microscope. Scale bar=200µm. Additionally, images of the pluripotency markers SOX2 (red), OCT4 (red), NANOG (red), LIN28 (red) and TRA1-60 (green) are shown as merged images with the nuclear DAPI (blue) staining. All images were taken with a Zeiss Axio Observer A1 inverted microscope. Scale bar=50µm. **B** Quantitative PCR analyses of iPSC clones K5, K9, K19 and K23, fibroblasts and PBMCs (summarized as fibroblasts within the graphs) as negative control and control iPSC lines (all n=3 passages) to analyze the expression levels of different pluripotency-associated markers. Shown are analyses of *SOX2, OCT4, NANOG, LIN28* and *GDF3*. Expression levels of all markers were normalized by corresponding expression of *GAPDH,* and analyses were done using the ΔCt method. Statistical analysis (one-way ANONA with Tukey`s correction) compared fibroblasts/PBMCs (neg. control) with every other group. Data are presented as mean ± SEM. * = $p < 0.05$, ** = $p < 0.01$, *** = $p < 0.001$ and **** = $p < 0.0001$.

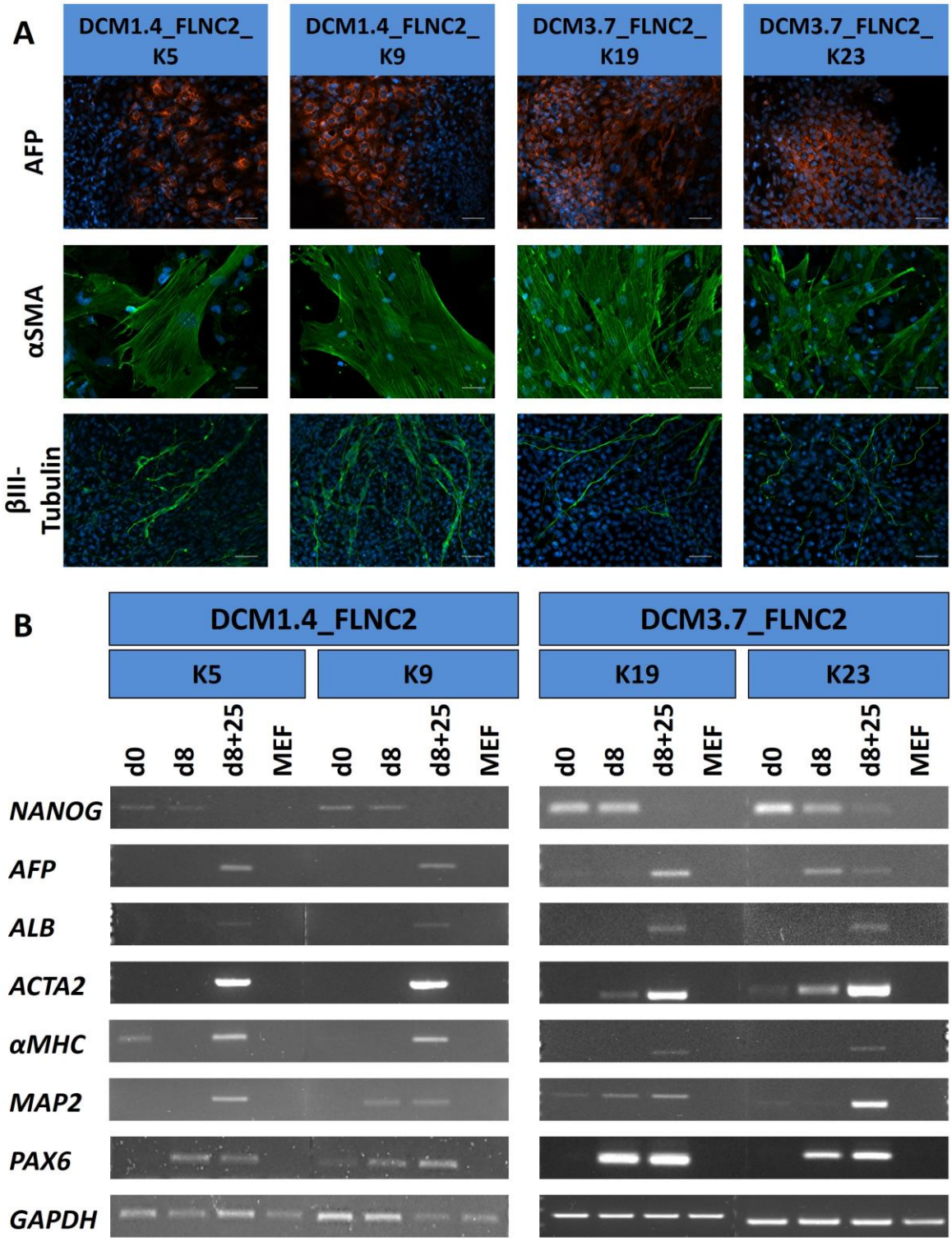

Suppl. Fig. 4: Spontaneous *in vitro* differentiation of FLNC gene edited iPSC clones. Shown are pluripotency characterization results of additional gene edited iPSC clones of DCM1 and DCM3 – K5, K9 and K19, K24, respectively. **A** Representative image of iPSC stained positive for AFP (red), αSMA (green) and βIII-tubulin (green), all shown as merged images with the nuclear stain DAPI (blue). All images were taken with a Zeiss Axio Observer A1 inverted microscope. Scale bar=50µm. **B** Results of semi-quantitative PCR of EBs of all family members at different time points. The iPSC showed *OCT4* expression at day 0. Over time, expression of markers of all germ layers, like *AFP* and *ALB* as endodermal, *ACTA2* and *αMHC* as mesodermal and *MAP2* and *PAX6* as ectodermal markers. *GAPDH* was used as housekeeping gene. MEFs, used as negative control, do not show expression of any of these markers.

Suppl. Tab. 1: Mean Ct values.

Gene	Cq value		
	iPSC	iPSC-cardiomyocytes	iPSC-cFB
18S	/	14	/
ACTA2	/	/	20.8
CaMKIIδ	/	24.5	/
COL1A1	/	/	19.8
CTGF	/	/	20
FLNC	/	23.5	/
FSP1	/	/	26
GAPDH	20	18	/
GDF3	24	/	/
GJA1	/	23.5	/
ILK	/	23.7	/
LIN28	22	/	/
MLC2v	/	20	/
MYH6	/	21.5	/
MYH7	/	19	/
MYOT	/	28.5	/
NANOG	22.5	/	/
NCX	/	20.5	/
OCT4	20	/	/
PGM5	/	25.5	/
PITX2	/	27	/
PLN	/	19.5	/
POSTN	/	/	25.3
SERCA	/	21	/
SOX2	23.8	/	/
SYNPO2	/	24	/
TCF21	/	/	30
TUBB5	/	/	20.5
XIN	/	25	/

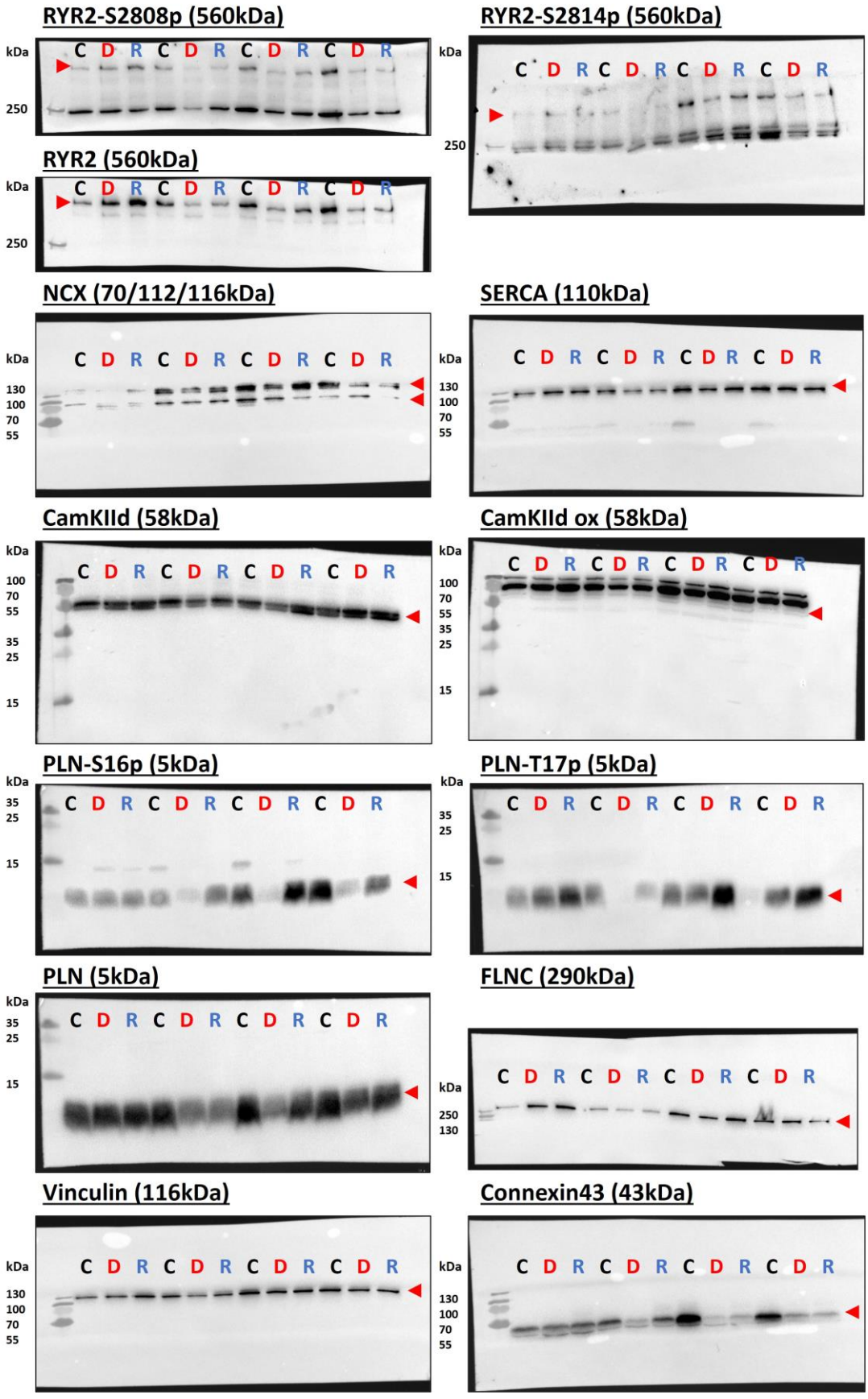

Suppl. Fig. 5: Full Western blot membranes for all DCM1/DCM1_res Western blots. Shown are imaged membranes of all markers shows. Each membrane was cut 2-3 times to obtain most markers. Red arrows mark the protein band used for quantification. C=control, D=DCM1, R=DCM1_res

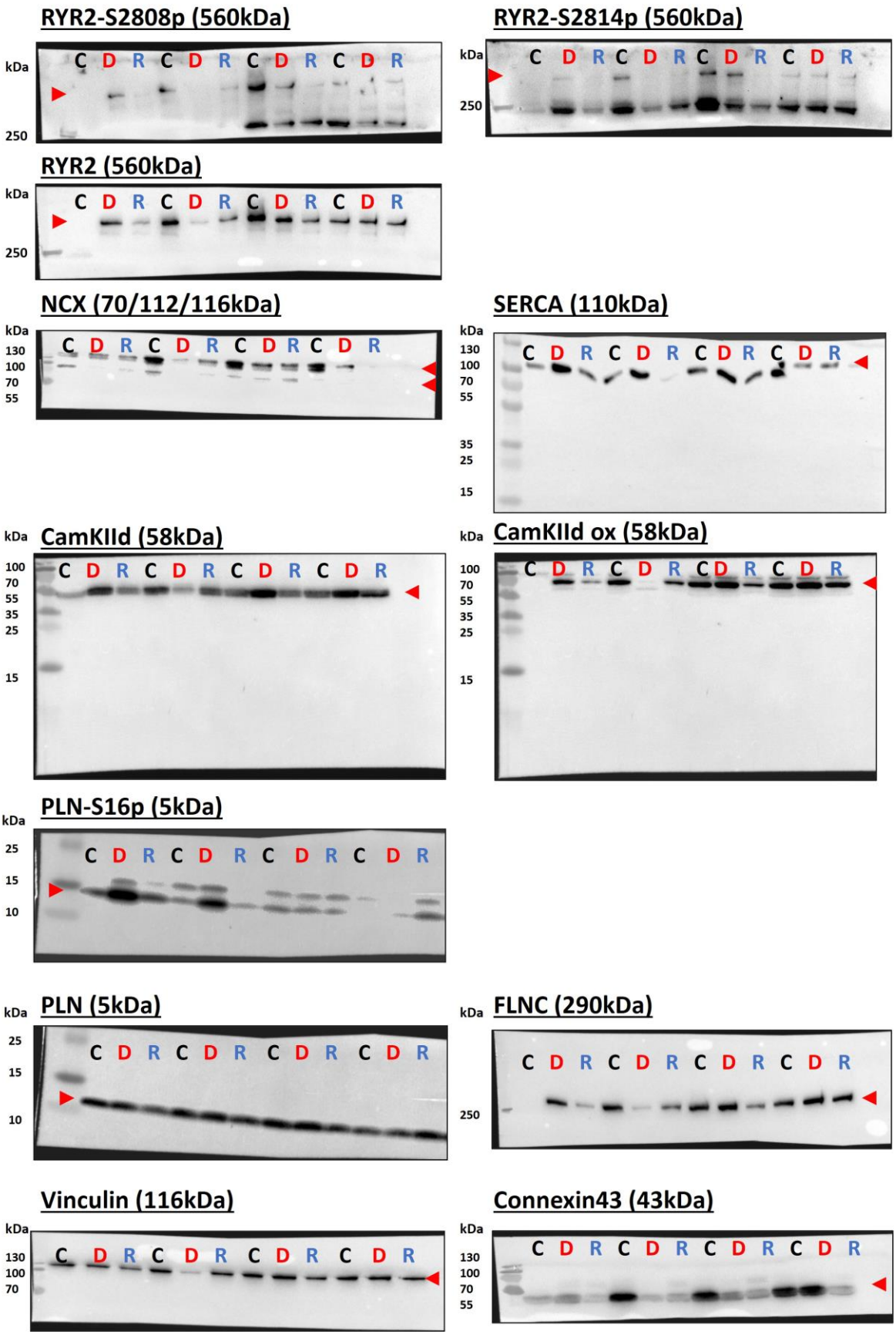

Suppl. Fig. 6: Full Western blot membranes for all DCM3/DCM3_res Western blots. Shown are imaged membranes of all markers shows. Each membrane was cut 2-3 times to obtain most markers. Red arrows mark the protein band used for quantification. C=control, D=DCM3, R=DCM3_res

Suppl. Tab. 2: Cell lines and differentiation ID-numbers used in experiments.

Experiment	Control	DCM1	DCM1_res	DCM3	DCM3_res	DCM2	DCM4
Sarcomere regularity analysis (iPSC-cardiomyocytes)	isWT4bld6_116 isWT4bld6_129 isWT4bld6_182 isWT4bld6_191	sDCM1.4_380 sDCM1.4_396 sDCM1.4-410	sDCM1.4_FLNC2_K1_11 sDCM1.4_FLNC2_K9_12 sDCM1.4_FLNC2_K5_31 sDCM1.4_FLNC2_K5_50 sDCM1.4_FLNC2_K9_51	sDCM3.7_142 sDCM3.7_148 sDCM3.7_155 sDCM3.7_156 sDCM3.7_168 sDCM3.7_179 DCM3.7_317 sDCM3.7_328 sDCM3.7_331 sDCM3.7_335	sDCM3.7_FLNC2_K23_15 sDCM3.7_FLNC2_K24_15 sDCM3.7_FLNC2_K23_24 sDCM3.7_FLNC2_K24_23 sDCM3.7_FLNC2_K23_27 sDCM3.7_FLNC2_K24_27 sDCM3.7_FLNC2_K23_31 sDCM3.7_FLNC2_K24_31	sDCM2F1_169 sDCM2F2_294 sDCM2F2_340	sDCM4A2_98 sDCM4A2_100 sDCM4A4_103 sDCM4A2_129 sDCM4A4_161 sDCM4A2_188
Cell Size (iPSC-cardiomyocytes)	pCTRL1.1_579 isWT4bld6_129 isWT4bld6_182	sDCM1.4-380 sDCM1.4_396 sDCM1.4-410	sDCM1.4_FLNC2_K1_11 sDCM1.4_FLNC2_K9_12 sDCM1.4_FLNC2_K1_23	sDCM3.7_142 sDCM3.7_148 sDCM3.7_155 sDCM3.7_156 sDCM3.7_168 sDCM3.7_179 sDCM3.7_331 sDCM3.7_335 sDCM3.7_342	sDCM3.7_FLNC2_K24_23 sDCM3.7_FLNC2_K23_27 sDCM3.7_FLNC2_K24_27 sDCM3.7_FLNC2_K23_31 sDCM3.7_FLNC2_K24_31 sDCM3.7_FLNC2_K23_35 sDCM3.7_FLNC2_K24_34 sDCM3.7_FLNC2_K23_38	sDCM2F2_340 sDCM2F2_389 sDCM2F2_389	sDCM4A2_129 sDCM4A4_161 sDCM4A2_188
qPCR of developmental and cardiac specific genes (iPSC-cardiomyocytes)	pCTRL1.1_708 pCTRL1.1_747 pCTRL1.1_796 isWT4bld6_334 isWT4bld6_338 isWT4bld6_357	sDCM1.4-416 sDCM1.4-455 sDCM1.4-474 sDCM1.4-540 sDCM1.4-620	sDCM1.4_FLNC2_K1_81 sDCM1.4_FLNC2_K1_94 sDCM1.4_FLNC2_K1_149 sDCM1.4_FLNC2_K1_183 sDCM1.4_FLNC2_K1_186	sDCM3.7_231 sDCM3.7_248 sDCM3.7_261 sDCM3.7_313 sDCM3.7_317	sDCM3.7_FLNC2_K24_15 sDCM3.7_FLNC2_K24_27 sDCM3.7_FLNC2_K24_34 sDCM3.7_FLNC2_K24_91 sDCM3.7_FLNC2_K23_15	/	/

Experiment	Control	DCM1	DCM1_res	DCM3	DCM3_res	DCM2	DCM4
qPCR of ILK, FLNC and interaction partners (iPSC-cardiomyocytes)	pCTRL1.1_579 pCTRL1.1_796 pCTRL1.1_848 isWT4bld6_282 isWT4bld6_292 isWT4bld6_300 sCTRL4.10_145	sDCM1.4_217 sDCM1.4_228 sDCM1.4_234 sDCM1.4_396 sDCM1.4_410 sDCM1.4_416 sDCM1.4_419 sDCM1.4_455	/	sDCM3.7_20 sDCM3.7_37 sDCM3.7_148 sDCM3.7_156 sDCM3.7_179 sDCM3.7_221 sDCM3.7_231 sDCM3.7_238 sDCM3.7_245	/	sDCM2F1_233 sDCM2F1_248 sDCM2F1_263 sDCM2F1_298 sDCM2F1_303 sDCM2F1_320 sDCM2F1_414 sDCM2F1_445	sDCM4A2_98 sDCM4A2_100 sDCM4A2_188 sDCM4A2_193 sDCM4A2_237 sDCM4A2_240
Western blot (iPSC-cardiomyocytes)	pCTRL1.1_708 pCTRL1.1_747 pCTRL1.1_796 pCTRL1.1_873	sDCM1.4-416 sDCM1.4-455 sDCM1.4-474 sDCM1.4-540	sDCM1.4_FLNC2_K1_81 sDCM1.4_FLNC2_K1_94 sDCM1.4_FLNC2_K1_149 sDCM1.4_FLNC2_K1_186	sCDM3.7_231 sCDM3.7_248 sCDM3.7-261 sDCM3.7_317	sDCM3.7_FLNC2_K24_15 sDCM3.7_FLNC2_K24_27 sDCM3.7_FLNC2_K24_34 sDCM3.7_FLNC2_K24_91	/	/
Calcium measurement with FURA-2 (iPSC-cardiomyocytes)	pCTRL1.1_789 pCTRL1.1_845 pCTRL1.1_913 pCTRL1.1_977 pCTRL1.1_981 pCTRL1.1_995 pCTRL1.1_991	sDCM1.4_396 sDCM1.4_455 sDCM1.4-585 sDCM1.4-626	sDCM1.4_FLNC2_K1_40 sDCM1.4_FLNC2_K1_81 sDCM1.4_FLNC2_K1_101 sDCM1.4_FLNC2_K1_149 sDCM1.4_FLNC2_K1_166	sDCM3.7_317 sDCM3.7_331 sDCM3.7_335 sDCM3.7_377 sDCM3.7_390	sDCM3.7_FLNC2_K24_15 sDCM3.7_FLNC2_K24_23 sDCM3.7_FLNC2_K24_27 sDCM3.7_FLNC2_K24_91 sDCM3.7_FLNC2_K24_115	/	/
Calcium measurement with Fluo-4 (iPSC-cardiomyocytes)	WTD2_879 pCTRL1.1_349 sCTRL4.8_21 sCTRL4.10_23	sDCM1.4-620 sDCM1.4-626 sDCM1.4-639 sDCM1.4-649a sDCM1.4-649c	sDCM1.4_FLNC2_K1_149 sDCM1.4_FLNC2_K1_183 sDCM1.4_FLNC2_K1_198 sDCM1.4_FLNC2_K1_206	sDCM3.7_354 sDCM3.7_419 sDCM3.7_434 sDCM3.7_445a sDCM3.7_445b	sDCM3.7_FLNC2_K24_115 sDCM3.7_FLNC2_K24_130	/	/

Experiment	Control	DCM1	DCM1_res	DCM3	DCM3_res	DCM2	DCM4
AmplexRed measurement (iPSC-cardiomyocytes)	pCTRL1.1_1052 pCTRL1.1_1061 isWT4bld6_532	sDCM1.4_646a sDCM1.4_646b sDCM1.4_649a sDCM1.4_649b sDCM1.4_649c sDCM1.4_660a sDCM1.4_660b	sDCM1.4_FLNC2_K5_31 sDCM1.4_FLNC2_K1_101 sDCM1.4_FLNC2_K5_100 sDCM1.4_FLNC_K1_220a sDCM1.4_FLNC2_K1_220b	sDCM3.7_331 sDCM3.7_335 sDCM3.7_342 sDCM3.7_347	sDCM3.7_FLNC2_K24_20 sDCM3.7_FLNC2_K23_20 sDCM3.7_FLNC2_K23_24 sDCM3.7_FLNC2_K24_27 sDCM3.7_FLNC2_K23_27 sDCM3.7_FLNC2_K24_30 sDCM3.7_FLNC2_K23_31 sDCM3.7_FLNC2_K24_34 sDCM3.7_FLNC2_K23_35 sDCM3.7_FLNC2_K23_40	/	/
EHM (iPSC-cardiomyocytes)	pCTRL1.1_981 pCTRL1.1_1057	sDCM1.4-598 sDCM1.4-657	sDCM1.4_FLNC2_K1_161 sDCM1.4_FLNC2_K1_217	sDCM3.7_385 sDCM3.7_434	sDCM3.7_FLNC2_K24_79 sDCM3.7_FLNC2_K24_138	sDCM2F1_414	sDCM4A2360
qPCR of cFB markers	CFB9-24 p6, CFB9-38-41 p6, CFB9-30-33 p9	**all iPSC-StC**: DCM1.4_531 p6, DCM1.4_531 p7 **all primary CFB**: CFB1, CFB2, CFB3 **all primary SFB**: SFB1, SFB2, SFB3 **all primary DCM_LV**: DCM1, ACT4, ACT5	/	iPSC-StC DCM3.7_292 p7	/	/	/

Experiment	Control	DCM1	DCM1_res	DCM3	DCM3_res	DCM2	DCM4
ECT	PromoCell (provided by AG Lutz) **iPSC-StC** isWT4bld6_455	**CFB** sDCM_LV_247 **iPSC-StC** DCM1.4_531	iPSC-StC DCM1.4_FLNC2_K1_127	/	/	/	/
qFISH (iPSC)	/	sDCM1.4_258 sDCM1.4_301 sDCM1.4_302	/	sDCM3.7_52 sDCM3.7_110 sDCM3.7_111	/	sDCM2F2_300 sDCM2F2_301 sDCM2F2_303	sDCM4A4_110 sDCM4A4_118 sDCM4A4_119
qFISH (iPSC-cardiomyocytes)	/	sDCM1.4_217 sDCM1.4_228 sDCM1.4_234	/	sDCM3.7_28 sDCM3.7_15 sDCM3.7_20	/	sDCM2F2_265 sDCM2F2_268 sDCM2F2_286	sDCM4A4_98 sDCM4A4_100 sDCM4A4_103
TRAP (iPSC)	/	sDCM1.4_526 sDCM1.4_527 sDCM1.4_528	sDCM1.4_FLNC2_K1_86 sDCM1.4_FLNC2_K1_87 sDCM1.4_FLNC2_K1_88	sDCM3.7_310 sDCM3.7_311 sDCM3.7_312	sDCM3.7_FLNC2_K23_9 sDCM3.7_FLNC2_K23_12 sDCM3.7_FLNC2_K23_13	sDCM2F1_341 sDCM2F1_343 sDCM2F1_344	sDCM4A2_297 sDCM4A2_298 sDCM4A2_301

8 Acknowledgments

Not only the heart and its vital functions are strongly dependent on a complex network of many different and important players, but also a PhD project and a PhD student need the support of many important people to finally be successful. I therefore would like to sincerely thank everyone who supported me throughout my journey.

First, I would like to thank Prof. Dr. Katrin Streckfuß-Bömeke for welcoming me in the lab of Translational Stem Cell research and offering such an interesting project. You guided me through this intense time of becoming an independent scientist by offering your time and knowledge, encouraging me to leave my comfort zone and improving myself and last but not least by providing the needed resources. I am very grateful for that.

I want to express my gratitude to my co-supervisor Prof. Dr. Susanne Lutz, for the fruitful discussions and advices during my annual committee meetings, for her time and her effort in answering all my questions regarding cardiac fibroblasts and 3D tissues.

I also want to extant my gratitude to Prof. Dr. Bernd Wollnik for being my third thesis advisory committee member and the helpful discussions and advices, as well as for his excellent help in identifying the *FLNC* variant. I also want to thank Prof. Dr. Ralf Dressel, PD Dr. Laura Zelarayán-Behrend and Prof. Dr. Rüdiger Behr for being part of my examination board, despite their busy schedule.

I thank Prof. Dr. Gerd Hasenfuß for giving me the opportunity to work in the Department of Cardiology and Pneumology.

A special thank you goes to the members of the DCM index family, who agreed to donate somatic material and to share a lot of information, without which this project would have been impossible.

A big “thank you” to all the people for taking time and effort to teach me and to conduct collaborative experiments important for this thesis to progress. This includes Dr. Malte Tiburcy and Branimir Berecic for generating and analyzing the EHM. Dr. Gabriela Santos and Bastian Bues for providing me with knowledge and excellent help in conducting ECT experiments. Dr. Shambhabi Chatterjee and Dr. Christian Bär for conducting and analyzing qFISH and TRAP assays. Dr. Laura Zelarayán-Behrend for sharing her secrets on IF staining on tissue sections. The whole group around Prof. Dr. Samuel Sossalla, especially Maria Knierim and Dr. Nico Hartmann, for giving me the opportunity to dive into the field of electrophysiology, for sharing their skills of Ca^{2+} measurements, for getting experienced with the CRISPR Cas technology within their project and for the chance to contribute to excellent scientific work beyond the narrowed scope of my own thesis project.

I also want to thank everyone involved in the International Research Training Group (IRTG) 1816, funded by the German Research Council (DFG) and the King’s College London and British Heart Foundation Centre of Research Excellence for providing such a powerful and supportive program. A special thank you to Prof. Dr. Dörthe M. Katschinski, Dr. Christina M. Würtz and Ms. Fulya M. Ören for excellent organization and help with every question throughout the entire time.

I owe special thanks to all colleagues from the *KSB* lab for all their emotional and scientific support. First of all, I have to thank Johanna, for teaching everything I need to know about iPS cell culture and differentiation, for always being there when I needed help, for running the lab like no other. I could always rely on you. You are an outstanding technician. Thank you for everything. A second particular thanks goes to Liese for enduring all my complains and doubts, for always cheering me up, for believing in me, for spending the best coffee breaks with me. Thank you for all the scientific discussions and advices. I would not have survived this time without you. Thanks for becoming a true friend. Thirdly, a special thanks goes to Eva, for being the best lab rotation and master`s student I could have asked for. I really enjoyed our time, discussing science and progressing the DCM project together. Thank you for your trust and giving me the opportunity to learn how to teach. I also would like to thank all the other members of the lab, Sabine, Yvonne and Anke for making the time enjoyable and for being supportive and teaching me everything I needed to know. I also thank all our apprentices, especially Christina, Leanne, and Emma for always helping me out. I am also thankful for meeting all our medical students – Gideon, Franzi, Tjark, Brisca, Lukas and Charlotte. It was a pleasure working with you, witnessing all your motivation and passion you have for what you do. Thanks for all the fruitful discussions, for all your time and for becoming a team. It was such a pleasure to work with so many extraordinary people throughout the last 3.5 years. Particular thanks to Liese, Brisca, Eva and Sabine for taking your time to proofread this thesis.

Special thanks to all my “private” friends supporting me throughout the time and taking care of a proper work-LIFE-balance I otherwise would have neglected for sure. Senni, Tamara, Nora and Conny, thank you for listening, for being supportive and simply for all your time.

My particular gratitude goes to Nala, my best friend. Thank you for always being the happiest little girl I know, for always making me happy and calming me down, no matter how sad, stressed or tired I have been. Thank you for immediately changing my thoughts and mood as soon as we have been together. There is nothing I enjoy more than spending my time with you outside in the woods.

Last but not least, I would like to express my deepest gratitude to my family for their unconditional love and unlimited support since the beginning. My parents for always being there, for the best childhood I could have imagined, which marked the start of becoming a curious scientist. Thank you for all your support and for enabling this educational path. Eric and Rike, thank you for being the best younger siblings, for all your support and all your joy. I am proud of being your sister. Eric, special thanks for proofreading this thesis. Rike, thank you for being my best friend. And to all other members of my family, thank you for the continuous support, guidance, and love.

9 Affidavit

I hereby declare that this submitted doctoral thesis entitled:

“Role of predisposing genetics, telomere signaling and crosstalk of cardiac fibroblasts and cardiomyocytes in a pluripotent stem cell model of dilated cardiomyopathy”

has been written independently with no other sources and aids than quoted.

_____

Wiebke Maurer

Göttingen, August 2022